# Developing a Combined In-vitro In-silico Model to Study the Interactionbetween Vascular Cells and Blood Flow in Aortic Aneurysms in theContext of Bicuspid Aortic Valve Disease

Lust, Suzie

*Awarding institution:*
King's College London

# Developing a Combined *In-vitro In-silico* Model to Study the Interaction between Vascular Cells and Blood Flow in Aortic Aneurysms in the Context of Bicuspid Aortic Valve Disease

Thesis Submitted for the Degree of Doctor of Philosophy

2023

King's College London

Suzette Lust

# Acknowledgements

This PhD has been without doubt one of the most fulfilling and enjoyable things I have done. I don't take my experience for granted and I know I could not have had such a wonderful time without all the amazing people around me.

Firstly, I want to thank my supervisors Eileen Gentleman and Pablo Lamata. I don't think I can say enough how lucky I feel to have been your student. Thank you for giving me such freedom in the project, supporting me beyond the lab and trusting a mechanical engineer with a pipette! I am very grateful for everything you have taught me scientifically and beyond. I also gratefully acknowledge Rebecca Shipley who has been providing support and encouragement since my undergraduate dissertation. It is thanks to you that I realised I love to do research.

I would like to thank the Medical Research Council for funding my PhD and the DTP team at Kings for all their help throughout. I would also like to thank all the administration and technical staff on floor 27 of Guys Tower.

A big thank you goes to my friends in the lab, particularly Michael Norman for his help when I was starting out and Geraldine Jowett who made me realise how wonderful biology really is. I also want to thank everyone else in the Gentleman and Lamata groups for their help and for making the lab a joyful and inspiring place. Sometimes the smallest conversations with colleagues can make the biggest of differences.

The wonderful collaborations I have been lucky enough to be a part of, have been an absolute highlight. Thank you to every author on our papers. Thank you to Claire Desalles not only for the experiments we did together but in general for being a mentor and helping so openly and supportively. Thank you also to Jean Cacheux and Yukiko Matsunaga for hosting me in Japan. Closer to home, Marco Antonazzi and the Shanahan group in general, thank you for your expertise in vascular biology.

Thank you to Malcolm Haddrick, my supervisor at the MDC during my internship. I learnt a great deal from you and your infectious enthusiasm for experimenting makes me hopeful that this feeling won't go away.

Thank you to my friends for all the laughs and the reminder not to take things too seriously. Josef Bowles, none of this would be possible if we hadn't found each other on day 1 of our

undergraduate degree. Your friendship means the world to me. Sam Suchal, thank you for all the adventures we get up to. Spending time together has been a real support, not to mention a lot of fun.

The support, care and love I have received from my family cannot be overestimated. Thank you to my mother Nicole Braham and my father Graham Lust for always championing what I want to do. Making you proud is always one of my biggest motivations. To my sisters Danielle and Chantal, thank you for always being at the end of the phone when I needed a chat. Being your little sister is the best, thank you for showing me what life goals are.

Lastly, my beloved David. I will never be able to articulate what you mean to me. Thank you for always being so supportive and proud. Thank you for understanding how important this all is to me. It means the most it possibly can to be married to someone who always supports my goals. I couldn't have done this without you.

# List of Publications and Poster Presentations

## Publications

Lust, S. T., Hoogland, D., Norman, M. D., Kerins, C., Omar, J., Jowett, G. M., ... and Gentleman, E. (2021). Selectively cross-linked tetra-PEG hydrogels provide control over mechanical strength with minimal impact on diffusivity.*ACS biomaterials science and engineering*, 7(9), 4293-4304.

Lust, S.T., Shanahan, C.M., Shipley, R.J., Lamata, P. and Gentleman, E., 2021. Design considerations for engineering 3D models to study vascular pathologies *in-vitro*. *Acta biomaterialia*, 132, pp.114-128.

Jowett, G. M., Norman, M. D., Yu, T. T., Rosell Arevalo, P., Hoogland, D., Lust, S. T., ... and Gentleman, E. (2021). ILC1 drive intestinal epithelial and matrix remodelling. *Nature materials*, 20(2), 250-259.

## Poster Presentations at Conferences

Investigating the Effects of Flow on Vascular Cell Matrix Remodelling and the Consequences for Aortic Aneurysm.S. T. Lust, I. Guri, M. Norman, G. Jowett, C. Desalles, C. Kerins, E. Gentleman, P. Lamata, R. J. Shipley. RIKEN BDR-CuSTOM Joint Organoid Symposium. Japan. 2023.

Investigating the Effects of Flow on Vascular Cell Matrix Remodelling and the Consequences for Aortic Aneurysm. S. T. Lust, I. Guri, M. Norman, G. Jowett, C. Desalles, C. Kerins, E. Gentleman, P. Lamata, R. J. Shipley. Kings College London BHF Centre of Excellence Anual Symposium. UK. 2022.

Developing a Combined *in-vitro in-silico* Model to Study the Interaction between Vascular Cells and Flow in Aortic Aneurysms. S. T. Lust, E. Gentleman, P. Lamata, R. J. Shipley. King's MRC DTP Symposium. UK. 2018, 2019, and 2020.

**Creating an *in-vitro* model to study the interaction between blood flow and vascular cells in aortic wall remodelling**

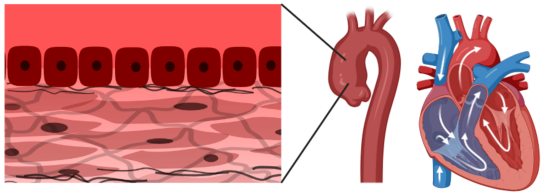

**Combining...**

Biomaterial Characterisation

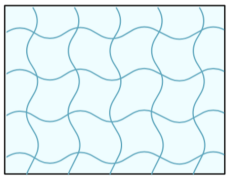

**Chapters 3 & 4**

3D Cultures of Vascular Cells

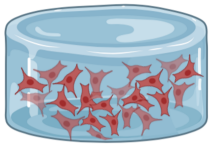

**Chapter 5**

Microfluidics

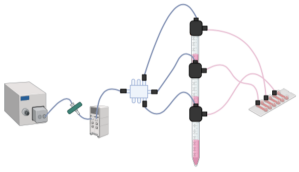

**Chapter 6**

**Which allows...**

Cell mediate matrix degradation

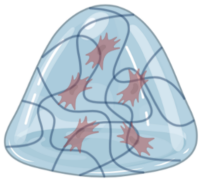

Nascent protein synthesis

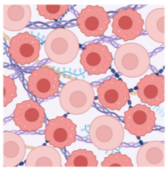

Cells to align to flow direction

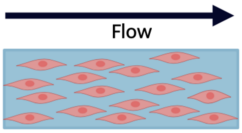


Made using Biorender.com

# Abstract

**Background**: Aortic aneurysms are estimated to account for 150 000 to 200 000 deaths per year world wide. As the vessel wall becomes enlarged its mechanical integrity is reduced exposing patients to risk of highly fatal aortic dissections or ruptures. This aortic dilatation is caused by breakdown of essential extra-cellular matrix proteins in the tissue mediated by aberrant vascular cell remodelling. Aneurysms are challenging to diagnose with symptoms presenting late in the disease progression. Furthermore, the rate of aneurysms in the population is rapidly increasing and there is therefore a pressing need to develop better metrics to stratify patient risk and new therapeutic strategies. Aneurysms are associated with a whole host of cardio-vascular diseases. In this work we are predominately focused on Bicuspid Aortic Valve disease (BAV), a congenital condition characterised by the malformation of the aortic valve resulting in only 2 leaflets. Indeed, BAV presents a high risk of thoracic aortic aneurysms (30-70%) but the mechanism driving their development is not well understood. Improvements in imaging techniques have now allowed pathological blood flow patterns to be correlated to aneurysm morphology and indeed there is increasing evidence that mechanotransduction from flow may be a driver of aneurysm development. Blood flow imparts mechanical forces to cells through stretching and frictional shear forces and these are known to regulate vascular cell behaviour. In particular, we are focused on interstitial flows through the vascular wall and their impact on vascular smooth muscle cell (VSMC) ECM interactions. We hypothesise that resulting interstitial fluid stresses may play a role in aberrant ECM remodelling and that this may be used to correlate disrupted flow patterns seen in patients to the morphology changes in their aortas.

**Aim**: To test this hypothesis we aimed to create a reductionist *in-vitro* model culturing VSMCs in 3D under interstitial flow. By creating a model that allows us to observe cell mediated matrix remodelling in these conditions, we may be able to infer the role, if any, that interstitial flows play in VSMC-ECM interaction.

**Methods**: To this end, we combined a synthetic PEG based ECM mimicking hydrogel with primary cultures of both bovine and human VSCMs with a microfludics setup. We used both experimental and modelling techniques to characterise the hydrogel's properties looking at degradability, permeability to flow and mass transport within the material. With these data in hand, we then sought to establish the optimum encapsulation conditions for our cultures of primary VSMCs

using imaging techniques to assess cell viability and morphology in different hydrogel conditions. We performed long term cultures of our cells and used immunostaining techniques to test cells' ability to synthesise nascent proteins within the hydrogels. Finally, we optimised a microfluidics setup to expose our cultures to interstitial flow and explored the impact these had on cell viability and morphology.

**Results**: We showed hydrogels doctored with degradable bioactive peptides could be broken down by exogenous MMPs as well our ability to control the rate of degradation by changing the number of these cross-links. We measured hydrogel permeability using 2 separate techniques which confirmed the material to have a low permeability compared to other standard hydrogels, on the order of $10^{-16}$ $m^2$. Furthermore, we characterised mass transport of solutes within hydrogels and were able to demonstrate a negligible impact of changing polymer solid content on diffusivity in hydrogels of up to 5% weight/volume for molecules up to 40 kDa in size. We identified that encapsulated cells preferred softer hydrogels of up to 3 kPa in stiffness, including 1 mM of degradable and adhesive bioactive peptides with cells encapsulated up to a density of $4 \times 10^6$ cells/ml. Via production of MMPs, VSMCs are able to break down the hydrogel and importantly by day 7 of culture, we detected newly synthesised fibronectin, collagen 1 and 4 proteins. Finally we showed we are able to stimulate encapsulated cells with interstitial flows demonstrating that cells align to the flow direction and remain rounder in morphology compared to in static controls. As an extension of this work, we also present a novel bioreactor design to impart a fuller range of mechanical forces to cell cultures in the future.

**Conclusion**: We have developed a novel *in-vitro* platform to study vascular cell-ECM interactions in response to flow, addressing the gap in the literature of studies in 3D focused on interstitial flows. Our experiments are underpinned by predictive mathematical models and can be extended to study multiple different vascular pathologies other than aneurysms. This type of reductionist model can be a powerful tool to elucidate the individual contributions of multiple factors involved in disease progression. Finally, these types of platforms combined with *in-vivo* studies may serve to identify new therapeutic targets and importantly identify novel markers to determine patient risk of disease.

# Contents

# List of Figures

# List of Tables

# Chapter 1

# Introduction

Aortic aneurysms are enlargements of the blood vessel diagnosed at a diameter increase of 50% [Mathur et al., 2016]. They are classified as either abdominal or thoracic depending on the location in the blood vessel, with the diaphragm as the point of demarcation between the two. Aortic aneurysms are estimated to account for 150 000 to 200 000 deaths per year worldwide [Wang et al., 2022] with cardiovascular disease as the leading cause of death in the United States [Ahmad et al., 2022]. The greatest clinical problem posed is the risk of potentially fatal ruptures of the aortic wall where it has become enlarged. In this case, patient fatalities are over 80% likely [Robinson et al., 2013], 50% of which occur before even arriving at a hospital [Wise et al., 2015].

Aneurysm diagnoses are often delayed due to the late presentation of symptoms which usually only occur once a significant enlargement is present posing an already high risk of rupture [Saeyeldin et al., 2019]. They are caused by a variety of conditions ranging from genetic diseases to injuries. In this thesis we are focused on Bicuspid Aortic Valve (BAV) disease, one of the main pathologies associated with thoracic aortic aneursym [Isselbacher, 2005]. A BAV has only 2 cusps or leaflets on the valve as opposed to the normal 3, as 2 are fused together. This in turn affects the movement of blood from the left ventricle up into the Aorta as normal opening of the valve is impaired. Subsequent dilatation of the ascending Aorta is one of the most prevalent and consistent markers of the disease affecting between 30 and 70% of patients [Losenno et al., 2012]. BAV is the most common congenital heart disease found in 0.5-2% of the population [Siu and Silversides, 2010], and importantly, these patients present an increased risk of rupture or dissection of their wall. Morphological changes in the valve and vessel dramatically change the pathway for blood flow exiting the heart to circulate to the rest of the body. The increase in vessel diameter or bulging is thought to be caused by a break down of the wall extracellular matrix (ECM) resulting in a weaker vessel wall less able to resist high pressure forces from blood flow. Indeed, maintenance of the aortic wall structure is regulated by a careful balance between synthesis and degradation of the vascular cell ECM. When an aneurysm begins to form, this balance is disrupted but the exact mechanism by which this pathological aortic remodelling

occurs is not well understood. The stimulus affecting tissue regulation in BAV is hotly contested. Historically, the literature has been focused on genetic causes however, emergence of new imaging techniques have allowed correlations between abnormal haemodynamics and aberrant ECM remodelling to be made, a factor which may previously have been overlooked. However, with the incidence of aortic aneurysms tripling in the United States in the past 30 years [Talk, 2014], there is a critical need to better characterise aortopathology development in order to develop preventative treatment strategies.

In this study we aim to better understand the haemodynamic contribution and better characterise the relationship between flow and aneurysm formation. This project aims to explore the potential causal link between abnormal flow patterns observed in patient data and wall degradation by directly correlating flow patterns to ECM mechanics. By strengthening the understanding of aortic morphological changes in response to flow, it may be possible to determine diagnostic criteria to help stratify patients for risk of developing aneurysms. Furthermore, thanks to advances in imaging techniques, these markers may be obtained using non-invasive cardiac flow characterisation.

## 1.1 Bicuspid Aortic Valve Disease

The defining feature of BAV is the malformation of the aortic valve, resulting in fusion of adjacent cusps as shown in Figure 1.1 [Andreassi and Della Corte, 2016]. This malformation alters how the valve opens affecting the cross-sectional area provided for flow to pass, and the eccentricity of the opening. This can have profound effects on the flow pathway potentially leading to stenosis, flow regurgitation and infection of the valve which often needs repairing or replacing [Yener et al., 2002]. Futhermore, BAV is associated with other non-valvular pathologies, though the degree to which these are totally independent is not well known. These are abnormalities of the aorta morphology which can lead to aortic dilations, aneurysms and dissections [Della Corte et al., 2007]. BAV does not always present alone but alongside other cardiac conditions. For example, 75% of patients with aortic coarctation (birth defect resulting in a narrowing of the Aorta) also present with BAV [Roos-Hesselink et al., 2003]. Therefore diagnosis and management of BAV can be difficult. Patients can display symptoms from infancy to late adulthood, but in most cases diagnosis happens later in life due to the late presentation of symptoms [Lewin and Otto, 2005, Saeyeldin et al., 2019]. A range of symptoms are displayed such as chest pain, fatigue, trouble when exercising, fainting, heart murmurs to name a few. Doctors usually conduct echocardiograms (though visualising the fused valve leaflets is difficult with this technique) and use family history, but BAV diagnosis is often hard to achieve until histological examination of excised tissue is performed [Fedak et al., 2002, Andreassi and Della Corte, 2016]. Furthermore, many of these symptoms overlap with other cardiac diseases which may have dif-

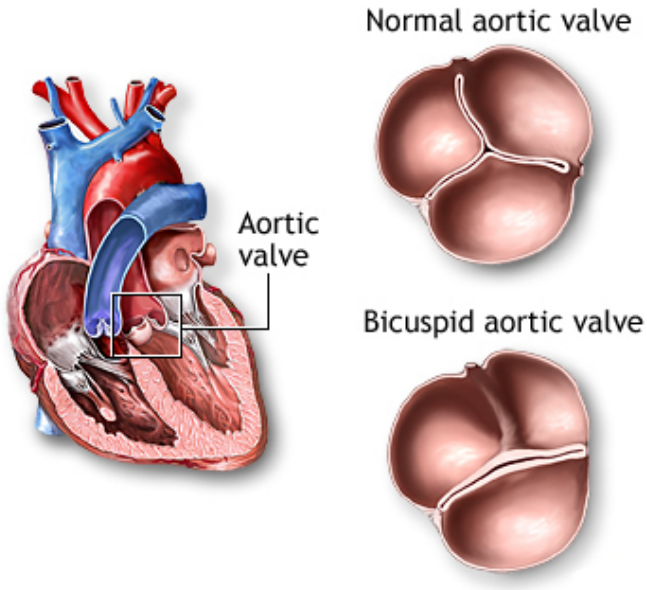


Figure 1.1: Figure showing a schematic of a Bicuspid Aortic Valve. Two of the 3 valve leaflets are fused resulting in a 2 leaflet opening. Image taken from [Medline, 1997].

ferent clinical statistics in terms of patient risk of aneurysm. Issues in diagnosis may incorrectly stratify patient risk for aneurysm or delay this process, an important issue with the time sensitivity of aneurysm growth. The current guidelines which stratify patients for risk of aneurysm are based on degree of dilatation. Prophylactic treatment using beta blockers is recommended for non-operative patients with dilatation of $>$ 4cm in the absence of significant flow regurgitation [Tadros et al., 2009]. However nearly all patients with BAV require valve surgery at some point [Lewin and Otto, 2005] with elective surgical repair suggested at a dilation of $>$ 5.5 cm. Using dilatation as a disease marker is fraught and indeed the current clinical guidelines have been shown to underestimate the number of patients who move on to develop dissections [Pape et al., 2007]. Therefore a better metric for patient stratification is required which can anticipate the need for surgery more successfully.

## 1.2 ECM Breakdown of Aortic Media

Dilatation of the Aorta is fundamentally caused by a mechanical failure of the vessel wall, due to the loss of essential structural proteins such elastin in the medial ECM accompanied by apoptosis of vascular cells as shown in Figure 1.2 [Dobrin and Mrkvicka, 1994, Rizzo et al., 1989, Quintana and Taylor, 2019, Lu et al., 2021, Michel et al., 2018]. Collagen is the most abundant structural protein in the Aorta providing stiffness and mechanical strength to the wall, with elastin giving the Aorta its elastic properties, formed in rings of fibres synthesised by vascular smooth muscle cells (VSMCs) during aortic development. Indeed VSMCS are predominantly responsi-

ble for maintaining the vessel wall ECM laying newly synthesised proteins [Michel et al., 2018]. Throughout our lifetime however, the vessel wall is required to remodel, in order to distend and constrict in accordance with the metabolic needs of tissue whilst attempting to reduce flow losses [Dolan et al., 2013]. Relaxation and remodelling of the wall is achieved by enzymatic degradation of structural proteins through release of matrix metalloproteinases (MMPs) and the relative production of their inhibitors, tissue inhibitors of metalloproteinases (TIMPs) [Newby, 2006].

MMPs are proteolytic enzymes which are involved in breaking down proteins in ECM as well as modulating cell-cell adhesion, cell migration and invasion, cell proliferation and apoptosis, tissue remodeling, growth factor and cytokine signaling [Brauer, 2006]. They are crucial not only in the maintenance of vascular tissue but also in cardiovascular development [Brauer, 2006]. They are produced by the 3 main cell types in the vascular wall: ECs, VSMCs and Fibroblasts (FBs) alongside immune cells [Wang and Khalil, 2018]. MMPs can be either secreted by cells or remain bound to the cellular membrane (membrane-type) [Raffetto and Khalil, 2008]. MMP-1, MMP-2, MMP-3, MMP-7, MMP-8, MMP-9, MMP-12, MMP-13, and MMP-14 and MMP-16 are all expressed within vascular tissues [Raffetto and Khalil, 2008, Galis et al., 1994]. MMPs 1, 8, 13 and 18 are collagenases implicated predominantly in the breakdown of interstitial collagen type I, II, and III [Raffetto and Khalil, 2008]. MMPs 2 and 9 are gelatinases which predominantly digest denatured collagens [Raffetto and Khalil, 2008]. MMP-12 is an elastase known to breakdown elastin in arteries [Liu et al., 2015]. MMP-3 is in the family of stromelysins and known to degrade a wide range of proteins including collagens, fibronectin, laminin and elastin. MMP-7 is a matrilysin which acts on proteoglycans, fibronection and gelatins [Raffetto and Khalil, 2008]. Finally, MMPs 14 and 16 are part of the membrane type subset of MMPs known to act on a range of ECM proteins as well as their role in activating other MMPs [Wang and Khalil, 2018]. The majority of MMPs are expressed as a pro-MMP inactive form which can be activated in 4 main ways: self-digestion, partial cleavage by plasmin, activation by membrane type MMPs or by other already active MMPs [Brauer, 2006]. For example, VSCMs are known to secrete membrane type MMPs which can activate proMMP-2 [Sinha and Frishman, 1998]. The overall activity of MMPs is therefore regulated by 4 main processes: (1) synthesis of MMPs by the cell, (2) movement of stored proteases (this is relatively small, the majority of MMPs being transcribed when needed), (3) post translational activation of MMPs and (4) ratio of TIMPs to MMPs and thus by both synthesis and activation [Chase and Newby, 2003]. Importantly, MMP regulation is heavily implicated in the progression of aberrant ECM remodelling in vascular disease .

The ECM is kept in balance by cyclic synthesis and degradation by the vascular cells of the vessel wall, through synthesis of proteins directly and activity of released MMPs [Annabi et al., 2002]. Over activity of MMPs is implicated in the progression of aortic aneurysms by causing an excessive breakdown of the vessel wall [Rabkin, 2017, Annabi et al., 2002, Thompson and Baxter, 1999, Lu et al., 2021]. Histological studies looking at excised aneurysm tissue from BAV patients have

confirmed this trend: decreased structural proteins and increased MMP levels, favouring degradation of the ECM. Luminex analysis measuring for MMP and TIMP concentration in ascending thoracic aortic aneurysm tissue from 46 patients with BAV compared to healthy controls revealed a global increase in MMPs concentration of 273% or more with MMP-9 accounting for the largest increase, and decreases in TIMP expression [Ikonomidis et al., 2012]. Interestingly, levels differed between groups with different valve fusion types, with each group presenting different MMP and TIMP concentration changes. A similar previous study by the same authors demonstrated a 34% increase in MMP-2 levels compared to tricuspid (TAV) (3 leaflet valve) aneurysm patients and healthy controls [Ikonomidis et al., 2006]. Similarly in a study by Boyum et al, MMP-2 and 9 levels were marked as increased compared to that of patients with TAV aneurysms ($43 \pm 11$ ng/ml vs $14 \pm 2$ ng/ml for MMP-2 and $4.0 \pm 0.9$ ng/ml vs $1.5 \pm 0.3$ ng/ml for MMP-9) [Boyum et al., 2004]. Indeed particularly associated with thoracic aortic aneurysms with BAV are MMPs 1, 9, 12, 14 and 2 [Rabkin, 2017] secreted predominantly by VSMCs and FBs [Quintana and Taylor, 2019]. .

The progression of aberrant ECM breakdown is dependent on both the activity of protesases within the tissue but also the microstructure of the tissue itself. The structural network of interconnected proteins dictates not only the chemistry of the matrix but also the relative ease or difficulty with which biomolecules released by the embedded cells can diffuse through. This in turn therefore affects the release of MMP activating molecules creating a feedback loop with the ECM structure. Additionally, changes to the permeability of the wall change the concentration of plasma proteins some of which can activate pro MMPs, further exacerbating the situation [Michel et al., 2018]. Altering cellular interaction or binding with the ECM can also modulate cell phenotype and proliferation, which in turn play a large role in matrix synthesis by the cell [Shapiro and Senior, 1999].

Alongside VSMCs, ECs and fibroblasts secrete MMPs in health, but in disease immune cells further exacerbate ECM degradation through additional secretion of MMPs as well as release of cytokines [Lu et al., 2021, Sinha and Frishman, 1998, Quintana and Taylor, 2019]. Indeed growth factors and cytokines produced by the VSMCs themselves and from recruited immune cells are implicated in the regulation of MMP transcription [Sinha and Frishman, 1998, Lu et al., 2021, Galis et al., 1994]. In particular, TGF$\beta$ has been implicated in matrix destruction in many aortic pathologies, affecting cell proliferation, differentiation and synthesis [Holm et al., 2011, Azhar et al., 2003, Daugherty et al., 2017]. In the aortic wall, TGF$\beta$ is secreted by VSMCs and stored in an inactive form in the ECM and activated upon release when the matrix is degraded or else when VSMCs exert contractile forces on the ECM [Michel et al., 2018, Hinz, 2015]. Impaired TGF$\beta$ has been demonstrated to be a key driver of thoracic aneurysm formation [Azhar et al., 2003, Bertoli-Avella et al., 2015]. In mice bred with TGF$\beta$ receptor gene deletion, embryos were observed to die during gestation due to severe abnormalities in aortic development along side other cardiac complications [Langlois et al., 2010, Jaffe et al., 2012].

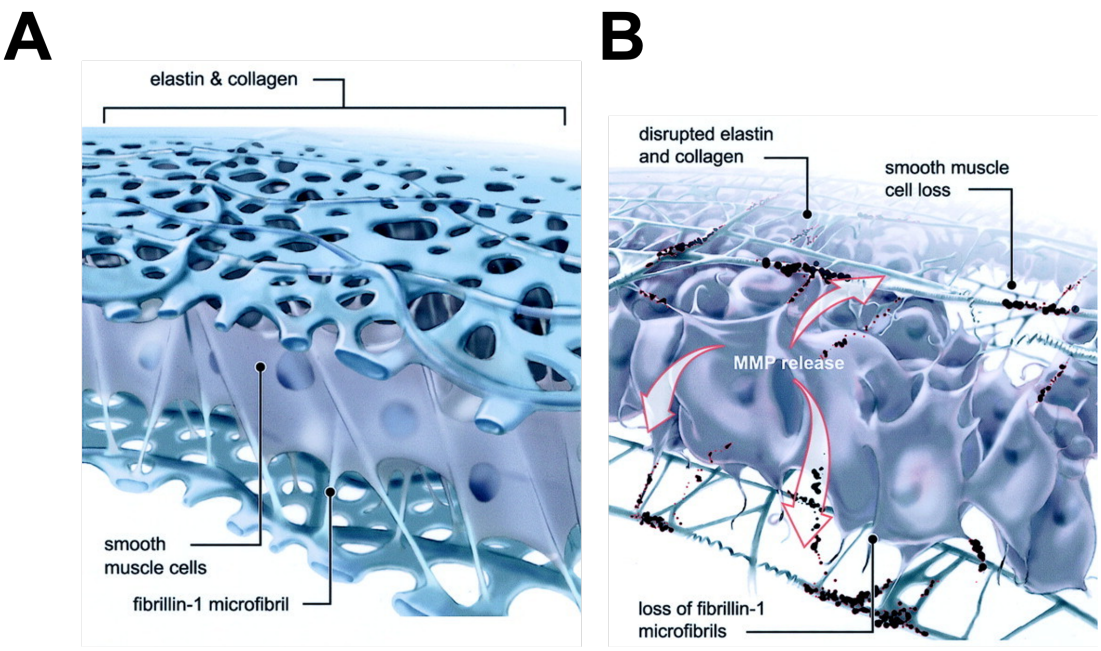


Figure 1.2: Schematic of the medial ECM in healthy (A) and BAV patients (B). In BAV, VSMCs detach from the surrounding ECM accompanied by MMP release, matrix remodeling, cell death, and a loss of vessel wall structure. Image adapted from [Fedak et al., 2002].

Jaffe et al observed that by knocking out TGF$\beta$R2 in mice, the resulting Aortas showed reduced protein synthesis in the vessel wall indicating that TGF$\beta$ is implicated in matrix regulation [Jaffe et al., 2012]. However the exact role of TGF$\beta$ in aneurysm development is still under debate [Daugherty et al., 2017].

Inflammation and the recruitment of immune cells is an important feature of abdominal aortic aneurysms though much less attributed to thoracic aneurysms associated with BAV [Lu et al., 2021]. Indeed studies suggest that the core characteristics of aneurysm, VSMC apoptosis and extracellular matrix degeneration happen in BAV related aneurysms without significant inflammatory response [Nataatmadja et al., 2003, Longo et al., 2002]. Rather, the matrix disregulation is potentially attributed to genetic abnormalities versus a result of injury.

## 1.3 Genetics

Statistical studies looking into familial clustering have shown evidence to support genetic causes of BAV, with the inheritability of the condition estimated to be as high as 0.89 [Cripe et al., 2004]. Furthermore a primary relative of a BAV patient is 10 times more likely to develop the condition compared to the general population [Siu and Silversides, 2010]. Affected genetic loci have been identified in the literature and include *TGFB* receptor genes *TGFBR*2 and *TGFBR*1, NOTCH signalling genes *NOTCH1* and genes associated with VSMCs markers

such as *ACTA*2 [Prakash et al., 2014, Martin et al., 2007, McBride et al., 2005, Goh et al., 2002]. However, since BAV presents heterogeneously and with confounding symptoms with other cardiac diseases, identifying exact genetic defects linked solely to BAV remains a challenge [Andreassi and Della Corte, 2016]. This has not been possible, with the exception of NOTCH1 mutations which have been associated both with familial and sporadic cases affecting valve calcification and subsequent stenosis [Andreassi and Della Corte, 2016]. However these show no link to malfunction of the Aorta itself [Prakash et al., 2014].

Genetic mutations clearly play an important role in BAV and undoubtedly untangling their contribution is an important consideration for developing therapeutic targets. However, in this thesis, we have focused solely on studying the importance of haemodynamics, whilst acknowledging the 2 factors may not be independent. Indeed genetic factors may alter the way in which cells respond to flow and the possibility of extending the work here by incorporating patient cells is discussed in the future work section.

## 1.4 The Role of Flow

The role of abnormal haemodynamics has been historically under played in the literature [Girdauskas et al., 2011]. Indeed multiple studies claim there to be no link between blood flow characteristics and aneurysm morphology. For example, in a study comparing BAV and TAV aneurysms, the correlation between degree of flow regurgitation and aortic dimensions is explored [Keane et al., 2000]. The authors highlight that whilst significant difference in both groups' aortic dimensions exist, both displayed comparable flow regimes and hence haemodynamics cannot be the root cause. Furthermore BAV can adopt many different pathologies not exclusively linked to valve malformation and thus this often leads to a theory of an underlying genetic defect affecting the entire structure of the valve and vessel, negating the possible contributions of flow [Kappetein et al., 1991].

Importantly however, studies claiming there to be no link between flow and aneurysm characteristics are heavily limited by their definition of what constitutes pathological flow. The metrics used such as peak flow velocities and pressure gradients often over simplify a more intricate flow profile. This is symptomatic of the restrictive imaging techniques most commonly available such as doppler echocardiography, the resolution capabilities of which do not allow analysis of complex flow patterns. However, with the increased feasibility of a technique known as 4D-MRI, allowing measurement of flow though the Aorta in 3 dimensions of space and in time (examples shown in Figure 1.3), more detailed analysis can be conducted [Girdauskas et al., 2011]. Indeed 4D-MRI scans have lead to more recent studies showing a clear correlation between flow and dilatation in BAV [Bissell et al., 2013, den Reijer et al., 2010, Guzzardi et al., 2015].

A consequence of leaflet fusion is that the valve may not fully open and the opening is therefore

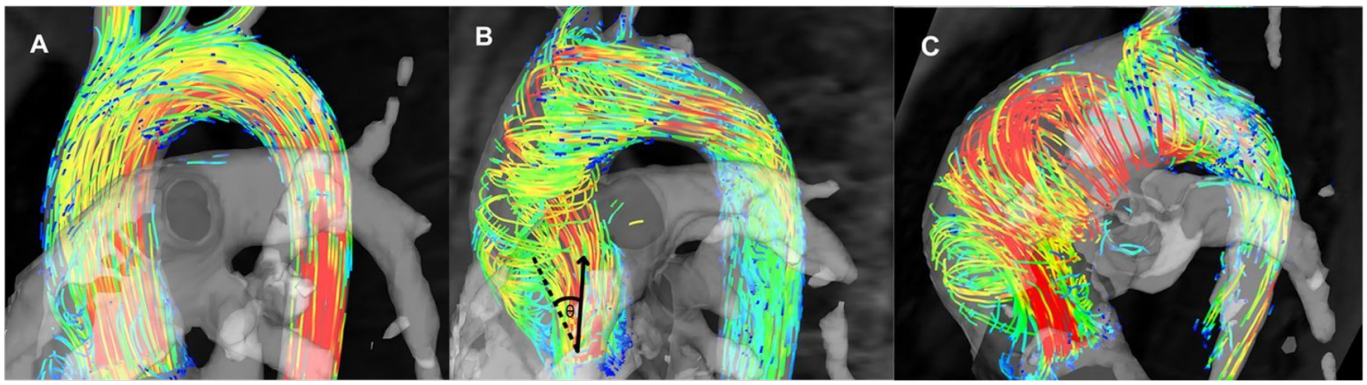


Figure 1.3: Figure showing 4D MRI scans of flow in healthy patients (A) compared to flow of BAV patients with examples of right handed (B) and left handed (C) helical flow. The angle $\theta$ between the main jet of flow and the aortic mid-line is shown in B. Image adapted from [Bissell et al., 2013].

often elliptical in shape, affecting the blood's pathway [Losenno et al., 2012]. The clinical maker used to detect abnormally functioning valves is the pressure drop across it. In a healthy patient, static pressure builds as blood collects behind the valve ready to be ejected. An ejection jet is then formed where streamlines are closely packed together which then develops into a full flow profile further upstream as dynamic pressure is recovered back into static pressure. Full pressure recovery is dependent on the geometry of the Aorta and the amount of losses from flow hitting the vessel wall [Richards et al., 2004]. In BAV patients, due to valve malformations, the flow jet is eccentric (Panel B in Figure 1.3) and therefore hits the aortic wall resulting in energy dissipation due to laminar viscous friction and turbulent friction from flow separation and vortices [Richards et al., 2004]. The central flow jet at peak systole comes out at an angle to the aortic mid-line [Bissell et al., 2013]. In clinical studies comparing BAV to TAV patients, this angle was found to be to be approximately 3 times greater in BAV [Richards et al., 2004]. The effect of this flow eccentricity is the formation of helical flow patterns (panels B and C Figure 1.3) and these are a defining feature BAV related aneurysms. In a study of 53 patients (20 with BAV, 25 TAV and 8 healthy volunteers) using 4D MRI, nested helical flow was observed during peak systole in the ascending Aorta of 15 of 20 patients with BAV but in none of the other groups [Hope et al., 2010]. BAV patients therefore displayed greater flow eccentricity and were the only group to demonstrate helical flow, thus indicating that these two factors may be linked. Indeed patients were divided into right handed and left handed helical flow groups, where right handed flow was correlated to larger aortic dimensions, and the degree of rotation was linked to increased angle of flow [Hope et al., 2010]. Furthermore, BAV patients also display a reduced effective flow area (the minimal cross-sectional area of the flow jet downstream of the aortic valve) which results in increased pressure build up and greater peak ejection velocities [Chandra et al., 2012] and this in turn can exacerbate pressure losses [Richards et al., 2004].

As the flow travels through a vessel shearing forces occur due to the friction between different

fluid layers, and the interaction between the fluid and the vessel. At the wall these are known as wall shear stresses (WSS) where the magnitude of these shearing forces is dependent on the viscosity and the rate of change of velocity in space in the direction of the shearing force. In helical flows observed in BAV patients, with fast changing flow directions, WSS may be increased. Indeed in [Bissell et al., 2013], measurements of wall shear stress showed that patients with BAV experience higher stress at the wall compared to TAV and healthy patients. Importantly Guzzardi et al analysed histological samples taken from patient Aortas combined with WSS maps [Guzzardi et al., 2015]. They showed that tissues taken with the highest increase in MMP levels and lowest concentration of elastin were co-localised with areas of high flow stimulation even within the same Aorta and therefore under the same genetic conditions. Furthermore with detached flow (regions where flow streamlines become separated and break away from the main flow bulk) there is the potential for fast changing values in shear giving rise to spatial and temporal WSS gradients and these have been studied in the context of atherosclerosis [Dolan et al., 2013].

There is therefore a clear case for the role that haemodynamics may play in aneurysm development and importantly, stimulation from flow is a known regulator of vascular cells. The shear and tensile forces exerted by blood on the Aorta wall affect the constituent cells in a range of different ways including cell paracrine and autocrine activity, cell orientation, phenotype, contractility and motility, all affecting vascular tissue remodelling [Gibbons and Dzau, 1994, Kamiya et al., 1984, Lehoux and Tedgui, 2003, Shi and Tarbell, 2011]. Receptors on the surface of both endothlial cells (ECs) and VSMCs sense flow changes which then activate mechanostransduction cascades [Lehoux and Tedgui, 2003]. One way this is mediated is by cytoskletal tension modulated by cell adhesions to surrounding ECM [Lehoux and Tedgui, 2003].

There has been extensive study of EC mechanotransduction. ECs are cultured in 2D and then exposed to shearing forces by passing cell culture medium over the cells at different flow rates. ECs are highly responsive to flow, aligning themselves in the direction of the shearing forces they are exposed to [Dewey Jr et al., 1981]. This in turn regulates cell proliferation and migration through cytoskeletal tension and indeed, shearing gradients that alter this tension have been associated with many vascular pathologies [White and Frangos, 2007]. Though less common, studies on VSMCs have also revealed effects of fluid forces. Expression of TGF$\beta$ has been shown to increase in 2D cultures of VSMCs exposed to shear [Ueba et al., 1997]. Shear has also been demonstrated to inhibit VSMC motility by decreasing levels of active MMP-2 in cells cultured under flow [Garanich et al., 2005]. Furthermore, growth factor release by VSMCs is affected by shear stresses of 3-25 dyn/cm2 promoting release of fibroblast growth factors (bFGF or FGF-2) [Rhoads et al., 2000].

Given the crucial role of VSMCs in maintaining vascular wall ECM, understanding the interaction between fluid forces and VSMCs may be of particular importance. Indeed whilst the majority of shear stress stimulation occurs through the luminal flow, due to pressure gradients

across the wall, a small proportion of flow is driven interstitially through the media where VSMCs reside [Wang and Tarbell, 1995]. Although the velocities of these flow are much smaller compared to those in the lumen, using analytical models considering tissue microstructure and cellular arrangement, these have been demonstrated to give rise to non negligible fluid stresses on the order of 1 dyn/cm$^2$ [Wang and Tarbell, 1995]. Furthermore, if the endothelial layer becomes disrupted for example in the case of injury or disease, this may lead to increased flow through the wall [Shi and Tarbell, 2011, Sill et al., 1995, Lopez-Quintero et al., 2009]. Between the endothelium and intima is a region known as the subendothlial intima made up of elastic lamina with leaky fenestral pores through which flow can enter [Tada and Tarbell, 2002]. These gaps concentrate the flow by forcing it through tight spaces. As a consequence, regions of higher fluid stresses occur near this layer compared to those developed downstream in the intima thus introducing a spatial variation in fluid stimulation throughout the intimal layer [Tada and Tarbell, 2002]. Indeed in [Tada and Tarbell, 2002], the authors extend on their original model in [Wang and Tarbell, 1995] estimating shear stresses in the intima, by including the influence of the elastic laminae. Numerical simulations revealed that fluid velocities near the entrance of the intima (near these elastic laminae) may be 100 times greater than average velocities in the fully developed flow downstream. The authors explore the impact of the total area of fenestral pores ie the surface area of the gaps between the elastic laminae and the distance between the pores and the resident VSMCs underneath. They conclude through their simulations that these impact the magnitude of the shear stresses experienced by the VSMCs but also the spatial gradient of these stresses in that region. The mechanostimulation within the intimal layer is therefore not uniform and by extension if these forces impact VSMC tissue interactions, ECM remodelling within this layer may also have a spatial variation. This in turn may further impact movement of flow through the layer by altering the geometry through which flow can move. Given that these estimates of shear stresses are known to impact VSMC behaviour and these parameters are further altered in disease (for example by endothelium denudation), it stands to reason that flow may be a contributor to intimal disease.

This interaction between flow and vascular cell behaviour is a possible link between the pathological flow in BAV patients and the changes in vessel shape mediated by cell driven tissue remodelling. It is this idea which forms the basis for the hypotheses in this thesis. In brief, our aim was to develop an *in-vitro* model to interrogate the role of flow in aberrant ECM remodelling. To this end we conducted a literature review on the current state of the art *in-vitro* models for studying vascular disease and published these findings in the review paper that follows [Lust et al., 2021b].

## 1.5 Design Considerations for Engineering 3D Models to Study Vascular Pathologies *in-vitro*

### 1.5.1 Author Contribution

All the research for the manuscript content was conducted by me. The manuscript was put together by me with my supervisors E. Gentleman and P. Lamata. I also gratefully thank our collaborators C. Shanahan and R. Shipley for their expertise and help.

### 1.5.2 Amendments

Reference 129 in the following paper is incorrectly dated as 2008 and was actually published in 1995.

Acta Biomaterialia 132 (2021) 114–128

Contents lists available at ScienceDirect

Acta Biomaterialia

journal homepage: www.elsevier.com/locate/actbio

Review article

# Design considerations for engineering 3D models to study vascular pathologies *in vitro*☆

Suzette T. Lust[a,b], Catherine M. Shanahan[c], Rebecca J. Shipley[d], Pablo Lamata[b], Eileen Gentleman[a,*]

[a] Centre for Craniofacial and Regenerative Biology, King's College London, London SE1 9RT, United Kingdom
[b] School of Biomedical Engineering and Imaging Sciences, King's College London, London SE1 7EH, United Kingdom
[c] School of Cardiovascular Medicine and Sciences, King's College London, London SE5 9NU, United Kingdom
[d] Institute of Healthcare Engineering and Department of Mechanical Engineering, University College London, London WC1E 7JE, United Kingdom

ARTICLE INFO

*Article history:*
Received 23 October 2020
Revised 28 January 2021
Accepted 18 February 2021
Available online 27 February 2021

*Keywords:*
Cardiovascular disease
Blood vessel remodelling
3D Vascular models
Biomaterials
Personalised disease modelling

ABSTRACT

Many cardiovascular diseases (CVD) are driven by pathological remodelling of blood vessels, which can lead to aneurysms, myocardial infarction, ischaemia and strokes. Aberrant remodelling is driven by changes in vascular cell behaviours combined with degradation, modification, or abnormal deposition of extracellular matrix (ECM) proteins. The underlying mechanisms that drive the pathological remodelling of blood vessels are multifaceted and disease specific; however, unravelling them may be key to developing therapies. Reductionist models of blood vessels created *in vitro* that combine cells with biomaterial scaffolds may serve as useful analogues to study vascular disease progression in a controlled environment. This review presents the main considerations for developing such *in vitro* models. We discuss how the design of blood vessel models impacts experimental readouts, with a particular focus on the maintenance of normal cellular phenotypes, strategies that mimic normal cell-ECM interactions, and approaches that foster intercellular communication between vascular cell types. We also highlight how choice of biomaterials, cellular arrangements and the inclusion of mechanical stimulation using fluidic devices together impact the ability of blood vessel models to mimic *in vivo* conditions. In the future, by combining advances in materials science, cell biology, fluidics and modelling, it may be possible to create blood vessel models that are patient-specific and can be used to develop and test therapies.

**Statement of significance**

Simplified models of blood vessels created *in vitro* are powerful tools for studying cardiovascular diseases and understanding the mechanisms driving their progression. Here, we highlight the key structural and cellular components of effective models and discuss how including mechanical stimuli allows researchers to mimic native vessel behaviour in health and disease. We discuss the primary methods used to form blood vessel models and their limitations and conclude with an outlook on how blood vessel models that incorporate patient-specific cells and flows can be used in the future for personalised disease modelling.



## 1. Introduction

Cardiovascular disease (CVD) is the leading cause of death worldwide [1]. One of the fundamental consequences of CVD is pathological remodelling of vascular tissues which can lead to complications such as aneurysms, myocardial infarction, ischaemia and stroke [2]. Studies using experimental animals and excised human tissues have proved invaluable in elucidating some of the mechanisms that drive pathological vascular remodelling. However, vascular dysregulation often involves multiple complex and dynamically interacting factors. As a result, confounding and/or redundant factors present in native tissues and whole experimental organisms can often hinder the discovery of the underlying mech-

☆ Part of the Special Issue on Biomaterials for Personalized Disease Models, guest-edited by Professors Kristopher Kilian and Stephanie Seidlits.

* Corresponding author.
*E-mail address:* eileen.gentleman@kcl.ac.uk (E. Gentleman).

https://doi.org/10.1016/j.actbio.2021.02.031

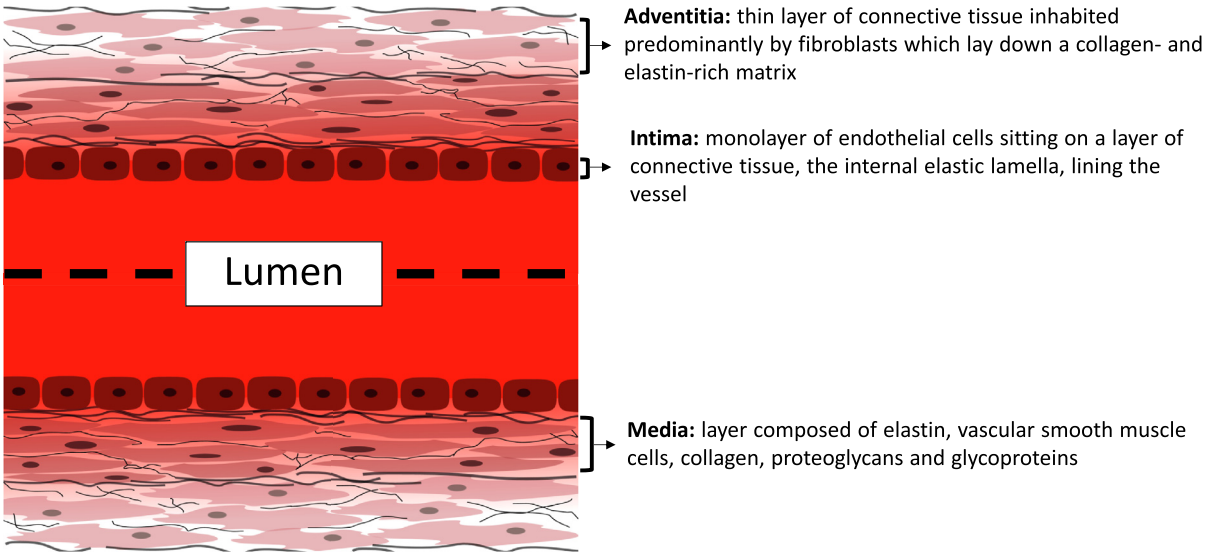


**Fig. 1.** Simplified diagram of the arterial wall showing the 3 main tissue layers. Endothelial cells form a confluent layer called the intima, which is supported by structural extracellular matrix proteins. Directly underneath is the media, which contains vascular smooth muscle cells embedded within a matrix containing elastin and collagen fibres. The outermost layer of the vessel wall, the adventitia, contains fibroblasts in a collagen and elastin-rich matrix.

anisms that govern these tissue-level changes, an understanding of which is likely essential in developing therapies.

Models of blood vessels built by combining cells with biomaterial scaffolds *in vitro* can serve as useful analogues to study some cell and tissue behaviours, in a reductionist manner [3]. By controlling experimental conditions, biological and mechanical factors can be introduced systematically, allowing study of how each impacts specific cell populations. Furthermore, such models can aid in reducing the use of animals in research [4]. *In vitro* models often rely on traditional 2D culture techniques; however, biomaterials, and in particular ECM-mimicking hydrogels may allow for more representative 3D cultures that are better able to recapitulate native cell behaviours in the 3D structure of the vessel wall [5–7]. Furthermore, advancements in the field of fluidics may also allow for the incorporation of fluid forces into models [8–11], which are vital in replicating the role of haemodynamics in driving vascular pathologies. In this review, we summarise some of the key considerations in developing *in vitro* models for vascular disease modelling by exploring the impact of biomaterials, culture methods and fluidic stimuli. We then explore how combining these factors may allow for the development of holistic models that can recapitulate the mechanisms of vascular disease progression. The purpose is to aid the reader in the design of 3D *in vitro* models tailored to study a range of vascular pathologies.

## 2. Designing engineered blood vessels

### 2.1. Pathological vascular remodelling

Mammalian vasculature is a highly dynamic tissue that constantly remodels throughout life. Balance is maintained through a tightly regulated network of complex inter- and intracellular behaviours regulated by biochemical and mechanical cues [2,12,13]. However, in disease, this intricate balance is often disrupted leading to vessel pathology. Causes of pathological remodelling can be classified into 3 main areas: changes in vascular cell phenotype, proliferation, or motility; degradation or modification of the extracellular matrix (ECM); and abnormal deposition of ECM [2]. These pathological changes can be driven by any combination of disrupted intercellular communication, changes in ECM composition, and/or abnormal haemodynamic stimulation of the vascular cells. Genetic factors potentially play a role in all of these mechanisms; however, discussion of this topic is omitted here.

Arteries, veins and arterioles are composed of 3 main cell types, endothelial cells (ECs), vascular smooth muscle cells (VSMCs) and fibroblasts (FBs) arranged in 3 layers (Fig. 1). The outermost layer, the adventitia, is a thin layer of connective tissue inhabited predominantly by FBs which lay down a collagen- and elastin-rich matrix to provide vessel mechanical strength [14]. Next is the tunica media that gives the elastic properties of the wall and is composed of elastin, VSMCs, collagen, proteoglycans and glycoproteins [14]. Finally, the intima is made up of a monolayer of ECs sitting on a layer of connective tissue, the internal elastic lamella, lining the vessel lumen. By comparison, capillaries are made up of a single layer of ECs which line a basement membrane [15,16]. Broadly speaking, veins are thin-walled compared to arteries [16]. Veins tend to support lower flow pressures and velocities compared to arteries [16]; however the composition and thickness of each layer differs depending on location, even within the same vessel [14]. For the purposes of this review, we refer to large vessels as veins and arteries that contain 3 layers.

Pathological vascular remodelling includes inward remodelling, which can drive vessel occlusion, structural changes in which vascular diameter is not altered, and outward remodelling resulting in vessel wall weakening [2]. Inward remodelling of the vessel wall is predominantly associated with intimal thickening caused by an increase in cell number and ECM deposition towards the vessel lumen [17]. This occurs through a combination of migration of cells from inside the vascular wall out into the lumen and recruitment of inflammatory cells. Such inward remodelling can occur in response to vessel injury and increased shearing forces due to the reduction of vessel calibre [18]. Outward remodelling is associated with loss of ECM proteins, cell death and ultimately weakening of the vessel wall. These changes in vessel morphology affect haemodynamics by disrupting the flow path. They also alter pressures, velocities, and flow profiles, both locally and systemically depending on the site. This aberrant vessel function has knock-on effects on the cardiovascular system as a whole causing flow insufficiency, regurgitations, increased frictional losses and pressure changes thereby increasing the overall cardiac burden, and in the worst cases, causing blockages or leaking of the system.

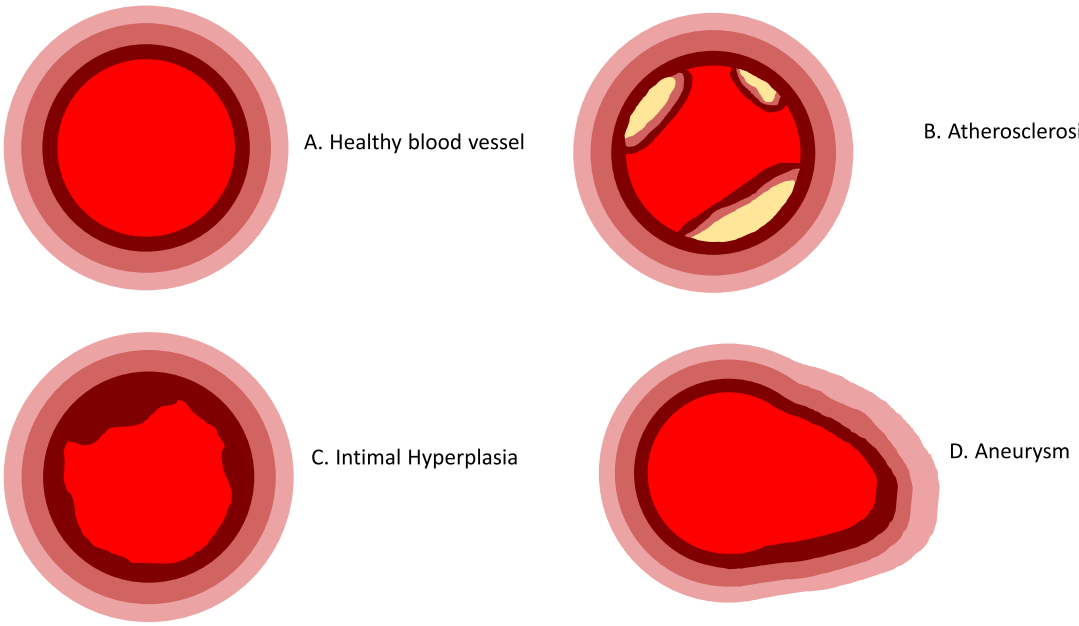


**Fig. 2.** Schematic representation of common pathologies marked by abnormal remodelling of the blood vessel. A) Healthy blood vessel in which 3 distinct tissue layers are observed. B) Atherosclerosis characterised by the accumulation of lipids and formation of plaques stabilised by fibrous caps. C) Intimal hyperplasia in which migration of vascular smooth muscle cells causes narrowing of the lumen. D) Aneurysm formation where the vessel diameter increases as the vessel wall becomes weakened and dilated.

One of the most common pathologies associated with aberrant vessel remodelling is atherosclerosis. Atherosclerotic plaques form through accumulation of lipids in the ECM, which prompts ECs to express adhesion molecules that can bind to and thus recruit leukocytes [19,20]. This leads to a vicious cycle of lipid accumulation, inflammation and cell death. Plaque formation also drives the recruitment of VSMCs into the vessel lumen which form a fibrous cap that stabilises the plaque (Fig. 2). Intimal hyperplasia (IH) is another pathological condition that can lead to vessel narrowing. However, unlike atherosclerosis, IH is associated with migration of VSMCs from within the vessel wall out towards the lumen, where they form an occluding lesion [21]. Increases in vessel diameter, on the other hand, is a distinctive feature of aneurysms. Dilatation is caused by a mechanical failure of the vessel wall due to matrix dysregulation, and consequently the loss of structural proteins such as collagen and elastin [22,23]. This is thought to be mediated by apoptosis of the VSMCs, which are responsible for depositing ECM proteins, and over-production of matrix degrading matrix metalloproteinases (MMPs), predominantly by VSMCs and FBs, which destroys ECM components that are vital for vessel tone and cell attachment [24–27].

### *2.2. Biomaterial scaffolds in in vitro models of the vasculature*

In engineered models of blood vessels, a key component is choice of scaffold material. The scaffold should support physiologically relevant cellular arrangements and be able to mimic tissue behaviours. Amongst other requirements, scaffolds should support long-term cell culture, allow the diffusion of nutrients and solutes involved in intercellular communications, and permit ECM remodelling. The intrinsic properties of the scaffold, such as its stiffness and the presentation of adhesion sites, should also allow for the maintenance of physiologically relevant cell phenotypes. Furthermore, as the material structure impacts interactions between embedded cells and applied mechanical forces, the biomaterial should both be able to withstand applied strain and stresses, but also impart mechanical cues to cells in a physiologically realistic and characterisable way.

Given the requirement of the matrix to deliver complex cues to embedded cells in a controllable manner, identifying an appropriate 3D material is not trivial. However, advances in materials science have produced platforms that can support cell survival, adhesion, and importantly, interaction with their environment, allowing cells to actively remodel and ultimately replace the matrix surrounding them [5,6,28]. Such materials are not only important in supporting long-term culture, but also in establishing disease models driven by matrix dysregulation, as they enable the study of how cells interact with their surrounding ECM.

Hydrogels are suitable for 3D cell encapsulation due to their two-phase composition with a solid polymer phase mimicking the ECM protein scaffold and a surrounding liquid phase available for transport of nutrients [7]. The first choice is between naturally derived or synthetic gels. Naturally derived gels offer an advantage as they contain natively occurring ECM proteins, and thus can recapitulate native tissue cues. Collagen gels are one of the most commonly used naturally derived hydrogels due to their high degree of biocompatibility, ability to support cell adhesion, availability, ease of use and ability to produce stable cross-linked networks [29]. Collagen is also the most abundant ECM protein in the media and adventitia [30], and so collagen gels, particularly formed from collagen type I, have been extensively employed in vascular studies [31,33–35]. Indeed, the ease with which cells can interact with naturally derived proteins has allowed important insights into cell-matrix interactions. For example, rat aortic SMCs, adventitial FBs and myofibroblasts encapsulated in rat tail tendon-derived collagen type I migrate through their surrounding matrix by upregulating MMP-1 production [33].

However, cells' interactions with native matrices have also been shown to modulate phenotype. Indeed, whilst collagen type I is abundant in vascular tissues, alone it may not support correct VSMC phenotypes whose regulation is mediated through complex interactions with many different proteins [28]. On the other hand, Matrigel, which is derived from a murine sarcoma and is abun-

dant in basement membrane proteins, provides cells with a multi-protein environment and is also often used for 3D cell culture. However, a comparison between VSMC behaviour in 3D culture using collagen type I and Matrigel revealed that, whilst proliferation of cells in Matrigel was slower, expression of typical phenotypic markers was progressively lost over time in both matrices [36]. This may be because batch-to-batch variability in Matrigel [37], and the presence of myriad undefined soluble factors and proteins may impact cell phenotype. For example, collagen type IV isolated from Matrigel can also present encapsulated cells with bound TGF$\beta$, which can regulate cellular responses [38]. Furthermore, these naturally derived hydrogels often lack the mechanical strength to withstand blood vessel pressures, and thus may not be suitable to deliver physiological mechanical cues to cells [35,39]. In short, biologically derived matrices offer advantages in terms of delivering biocompatibility and bioactivity with relative ease. However, these often lack mechanical strength, and it can be difficult to control how and which specific biomolecules are presented to encapsulated cells.

Synthetic gels are an alternative which may provide tighter control over matrix properties than biologically derived gels, with clearly defined properties and hence more inter-sample consistency. Synthetic hydrogels are often formed by cross-linking polymer macromers either via photo-polymerisation or through chemical or physical cross-linking, creating a lattice-like structure [40]. The dimensions of the lattice can be modulated by altering the polymer chain length and thus the mesh network size. This allows control over the diffusion of solutes through the gel. Moreover, changes in hydrogel structure alter flow passing through the gel, and by extension the shear it imparts on encapsulated cells. Control over these features is an advantage for recapitulating 3D mechanical and biochemical cues in a reproducible manner.

A major drawback of synthetic gels is their innate bio-inertness, and therefore sites for cellular interactions must be incorporated to make them hospitable for cells. This can be facilitated in synthetic gels by inclusion of bioactive peptides [40,41], which allow for control over the density and type of biological cues. Polymers can be modified to include peptides that contain the binding sites of native matrix proteins such as RGD, which mimics the fibronectin binding domain, as well as MMP-cleavable sequences, which allow cells to remodel and migrate through the 3D matrix. Inclusion of adhesive and degradable peptides can be tuned independently from matrix concentration, and by extension, stiffness, allowing orthogonal control of mechano-regulatory and biological cues [5].

Although not suitable for cell encapsulation, lactide and glycolide polymers have been proposed for blood vessel applications as they degrade by hydrolysis, and can be manufactured with high porosities, allowing for nutrient exchange [42]. Indeed, Polyglycolic acid (PGA) scaffolds have been shown to be replaced by SMC-derived ECM proteins, rendering the graft able to withstand pressures above 100-200 mmHg [43]. However, whilst PGA may improve upon the mechanical properties of collagen, studies have shown that PGA alone does not provide sufficient long-term mechanical strength unless progressively reinforced by native matrix synthesis [42]. Addition of other polymers to PGA such as poly-4-hydroxybutyrate (P4HB), poly-(lactic-co-glycolic acid) (PLGA), poly(L-lactic acid)(PLLA), poly(caprolactone) and polyethylene glycol (PEG) have been shown to improve their mechanical strength [42,44–47].

PEG has been identified as a suitable stand-alone material for vascular cell scaffolds due to its biocompatibility, hydrophilicity, resistance to protein adsorption, non-thrombogenic properties, high elasticity, and overall highly tunable properties [28,48–53]. PEG gels allow efficient and controllable diffusion of biomolecules. The diffusivity of species can be controlled by altering the length of the polymer chains in the PEG macromer, and by extension the mesh network size [53]. PEG gels are also amenable to incorporation of bioactive peptides through, for example, Michael-type addition reactions in which peptides are presented pendantly or used as cross-linkers between the PEG macromers [5,54,55]. Indeed, peptide-modified PEGDA hydrogels containing the RGD sequence are able to support the differentiation of human coronary artery SMCs toward a contractile phenotype equally well as when they are cultured on fibronectin or laminin [28] (Fig. 3).The high characterisability of PEG gels and thus control over important features, including diffusion of soluble factors and cell-matrix interaction, makes PEG-based gels especially suited to disease models designed to answer mechanistic questions. Furthermore, tight control over the matrix properties can also be crucial when incorporating other stimuli such as flow, enabling reliable prediction of the response of the matrix to mechanical force.

As both naturally derived and synthetic gels have drawbacks, it is also possible to create hybrid materials which combine the advantages of each [56–59]. For example, gelatin, collagen and elastin have been combined with synthetic poly(ε-caprolactone) to increase scaffold tensile strength compared to gelatin or collagen and elastin alone [57]. Furthermore, photocrosslinked gelatin methacryloyl (GelMA) in which naturally derived gelatin is modified with methacrylic anhydride has also been used to create vessel-like structures with separate layers encapsulating rat aortic SMCs and 3T3 fibroblasts and lined with a human umbilical vein endothelial cell layer [60].

### 2.3. Incorporating vascular cells: cellular arrangements and interactions

Blood vessels must withstand high pressures from fast blood flows whilst remaining compliant and adaptable to changing supply needs [61–63]. Regulation of vessel function is mediated through the contraction of the VSMCs, as well as composition of the ECM in each layer, and therefore is a combination of the passive structural and active cellular behaviours of the vessel. In disease and during vessel remodelling, VSMCs can change phenotype from that of a contractile cell to a “synthetic cell”. These cells lose their differentiated contractile properties and can migrate, proliferate and modify the ECM. For example, in aneurysms, loss of structural proteins in the medial ECM renders the vessel weak, making it prone to ballooning and rupture [64]. Conversely, in atherosclerosis, over-production of collagens and proteoglycans by VSMCs lead to areas of lipid accumulation, driving inflammation, necrosis and the formation of plaques, which encroach on the lumen, causing vessel stenosis [65].

*In vitro* setups for disease modelling should ideally recapitulate conditions that foster correct ECM maintenance to study the potential role of their disruption in disease progression. Indeed, at baseline, models should promote healthy cell function with the ability to monitor biomarkers which signal pathological behaviours. The geometry of the vessel model and choices in seeding methods determine the scope for physiological cell phenotypes, morphologies, and intercellular interactions. Next, we present a review of different *in vitro* setups, and a discussion of the key design choices impacting the fidelity of *in vitro* culture systems. In particular, we explore the impact of cell-ECM interactions and intercellular communication on maintaining correct cell phenotypes.

### 2.4. 2D versus 3D culture

Culturing cells on tissue culture plastic reduces complex 3D tissue structures into simplified cell monolayers. Whilst this has al-

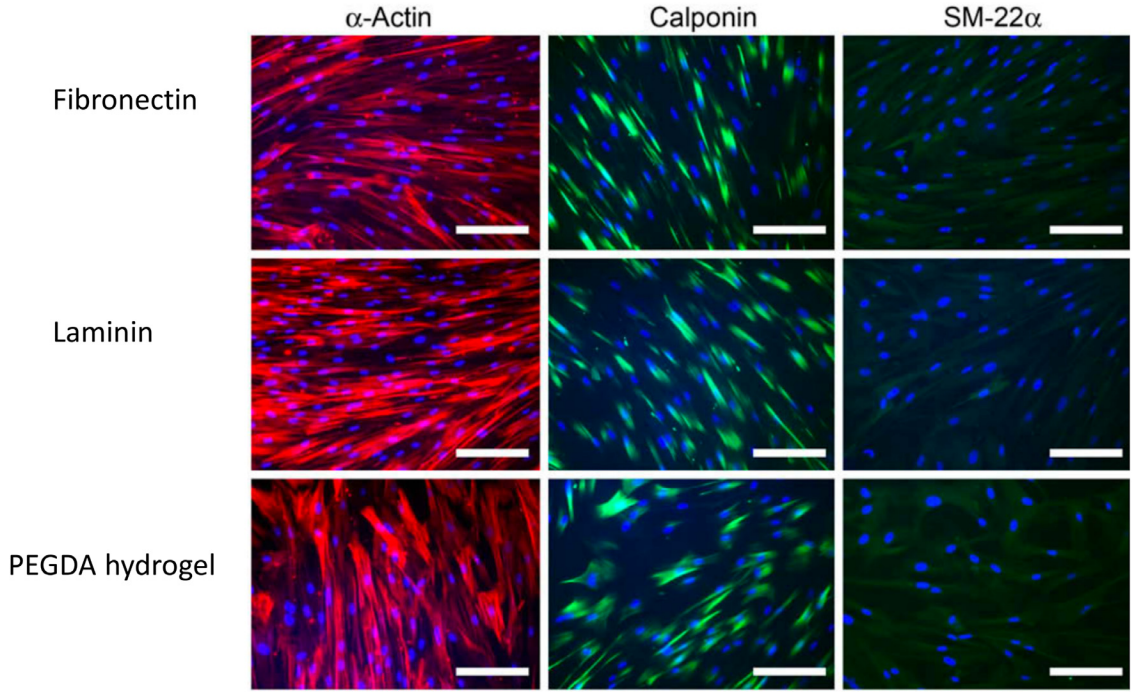


**Fig. 3.** Fluorescence staining of human coronary artery smooth muscle cells for alpha-actin, calponin and SM-22a protein after 6 days of culture on fibronectin, laminin and a RGD-bearing poly(ethylene glycol) diacrylate (PEGDA) hydrogel, cultured in low serum (2% FBS) and containing heparin (400 mg/ml) to induce differentiation. Scale bar=200 $\mu$m. RGD peptide-containing gels support equivalent levels of expression of the contractile markers compared to culture on fibronectin or laminin, indicating that RGD-modified PEGDA gels can support differentiation of SMCs toward a contractile phenotype. Figure adapted from [28].

lowed useful observations, cell behaviour in 2D is often markedly different from that *in vivo* [66,67]. Discrepancies between cell behaviour in 2D and 3D are not simply due to a change in dimensionality, but are rather also attributable to downstream impacts [68]. For example, in a 3D environment, cells are presented with adhesion sites in all directions, which alters their morphology [66,68]. Cells sense their environment through adhesions with their ECM. Thus, stiffness and mechanical stress are felt differently by cells in 3D than in 2D. The makeup of the ECM in which cells are surrounded is also a governing factor in directing cell phenotype. Indeed, cells respond differently to different ECM proteins in 2D compared to 3D [31]. Furthermore, transport of nutrients and soluble biomolecules is also altered in 3D, and therefore, studying the effect of disequilibrium of any of these factors is likely to be more faithful to that *in vivo* if studied in 3D. Importantly, whilst 2D endothelial cell culture may be appropriate due to their native monolayer presentation, VSMCs and FBs, which normally reside in an ECM-rich 3D structure, are known to be regulated by interactions with their 3D matrix [31,44,69–72].

VSMC-ECM interactions are an important regulator of vascular cell adhesion, migration, proliferation and phenotype [73]. Indeed, VSMCs lie on a phenotypic spectrum from synthetic to contractile and express different markers accordingly. Whilst distinction between contractile and synthetic cells is not always clear, in a healthy mature vessel the majority of cells are contractile. In a contractile state, VSMCs reinforce the vessel wall, enabling it to withstand fluid pressures. This is achieved through expression of dystrophin-glycoprotein complexes, which link actin filaments within the cell's cytoskeleton to the surrounding ECM [74]. Conversely, VSMC transdifferentiation or reversion to a synthetic state has been implicated in ECM dysregulation and disease progression [75]. Indeed, Chen *et al.* have shown that a subpopulation of VSMCs may themselves contribute to aneurysm formation by transdifferentiating into mesenchymal cells in response to loss of TGF$\beta$ signalling. Accumulation of these mesenchymal cells in the aortic wall of Apoe$^{-/-}$ mice on a hypercholesterolemic diet results in loss of the contractile VSMC and accumulation of lipid deposits and ossifications, which together contribute to aneurysm formation [76].

The presence of specific binding motifs and cellular engagement and disengagement with adhesion sites have been shown to govern VSMC phenotype [31,44,69–72]. Fibronectin and collagen type I have been implicated in driving the synthetic phenotype, whilst laminin and collagen type IV, promote the contractile. These relationships have been confirmed in disease models, such as atherosclerosis, where VSMC phenotypic changes are known to be mediated through interactions with fibronectin [77,78]. Given that the VSMC synthetic phenotype and ECM makeup are both markers of pathology, cell-ECM interactions and matrix composition should therefore be considerations in designing *in vitro* models. Furthermore, VSMC's response to ECM proteins differs in 2D and 3D setups. In a study using rat aortic SMCs, cells were cultured on a 2D collagen type I surface or embedded within collagen type I gels at the same polymer concentration and compared to cells cultured on tissue culture plastic [31]. Embedding the cells led to a downregulation of smooth muscle actin (SMA), a marker of VSMC contractility, as well as to a decrease in cell proliferation compared to the 2D collagen condition and tissue culture plastic controls. Levels of SMA and proliferation were no different in 2D collagen cultures compared to tissue culture plastic controls, leading the authors to conclude that the changes in cell phenotype were independent of matrix composition and could be attributed to cell response to 3D culture.

When VSMCs are isolated from tissue samples, they often lose their phenotype, with expression of relevant markers dropping with successive passages [31]. These studies highlight that both protein presentation and dimensionality impact VSMC's ability to retain contractile phenotypes. This highlights the importance of studying VSMCs in 3D environments to recapitulate *in vivo*-like responses.

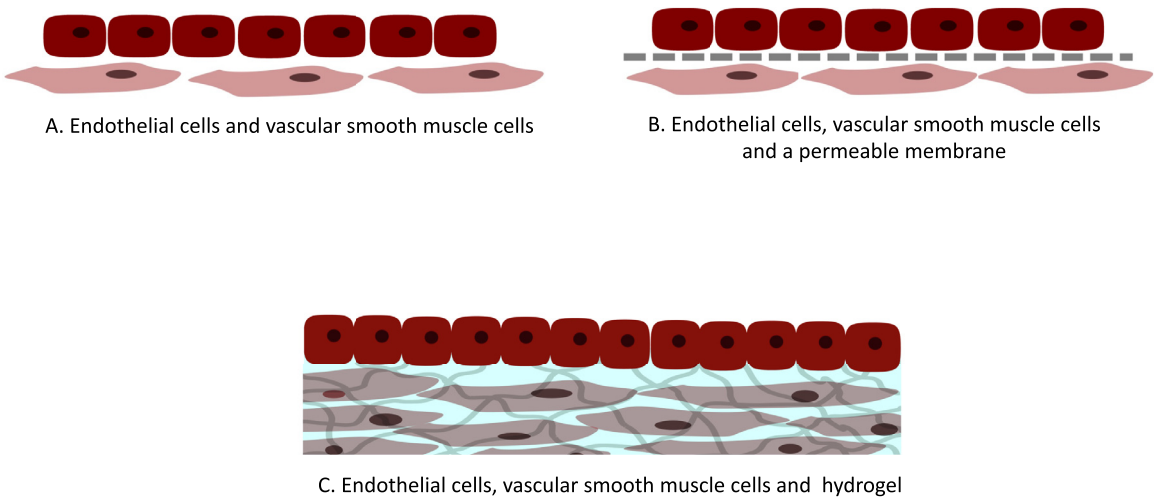


**Fig. 4.** Schematic representation outlining experimental setups for co-culturing endothelial cells with vascular smooth muscle cells. A) Culture of endothelial cells directly on top of vascular smooth muscle cells. B) Separation of both cell types by means of a permeable membrane. C) Culture of endothelial cells on 3D gels containing vascular smooth muscle cells.

### 2.5. VSMC-EC interactions

Despite its important role in regulating phenotype, VSMC interactions with ECM proteins alone may not be sufficient to retain VSMC contractility. Indeed, intercellular communication between VSMCs and ECs also regulates VSMC behaviours, including proliferation, quiescence, morphology, and by extension vasodilation and healthy vessel maintenance [67,79–88]. Co-culture of VSMCs with ECs has been shown to regulate SMC phenotype [87–89] and to prompt VSMCs to adopt a more contractile-like state, which makes including co-cultures in blood vessel models an important consideration.

The endothelial layer creates a selectively permeable barrier to the vascular wall by controlling transport of molecules and immune cells as well as by facilitating cell-cell communications through adherent junctions, tight junctions and gap junctions [90,91]. VSMC and EC communicate with one another both through direct cell-to-cell contact and through diffusion of secreted molecules [92–94]. Disruption of the endothelial barrier is thought to be the first step in the formation of atherosclerotic plaque [95]. For example, SMC proliferation in rat carotid arteries was studied by denuding the endothelium, both with and without causing damage to the media [96]. Here, denudation alone was sufficient to drive lesion formation, highlighting the role of the endothelial layer in vascular pathology. Such findings have been confirmed in *in vitro* injury models demonstrating how disruption of the EC layer can stimulate proliferation of the underlying VSMCs [97].

Maintenance of a healthy endothelium is therefore vital in a healthy vessel, and one key factor is facilitating correct EC regulation of VSMCs in a feedback loop. These cells communicate via gap junctions which require cell-cell contracts, and therefore culture systems which allow proximity may have advantages in retaining correct VSMC phenotype. There are 3 main ways in which co-cultures have been reported: culture of ECs directly on top of VSMCs [98,99], separation of both cell types with a permeable membrane [1,79,82,86,97], and culture of ECs on 3D gels containing encapsulated VSMCs [85,99] (Fig. 4). The main difference in each of these methods is the proximity that the different cell types have to each other, and the inclusion (or not) of a 3D cell niche for the VSMCs. The distance between cells impacts their ability to create gap junctions and hence the way in which they can interact. Furthermore, given that communication is also dependent on diffusion of soluble factors, the distance between the cells and the diffusivity through the layers may be key [100,101].

Taken together, these observations suggest that disease modelling should optimally start with a 3D culture with multiple cell types that allow for intercellular communication. In tissue engineered grafts that aim to replace whole sections of pathological tissue, these factors are often taken into account as the grafts are required to adopt the full function of vessels once implanted. Therefore, advances in tissue engineering have also provided important insights into the development of artificial layered constructs, which could be useful for disease modelling. The first engineered 3D vessel was created by Weinberg and Bell in 1986. In their model, a 3-layer construct composed of collagen gels laden with FBs and bovine VSMCs was created with a confluent monolayer of ECs lining the structure [35]. Whilst many physiological aspects of the native vessel were recapitulated with this model, it suffered from limitations in terms of vessel resistance to pressure as well as in the composition and morphology of the layers, as it lacked the elastin natively found in the intima.

Subsequent studies have improved on this original work by using materials with greater control over matrix properties, by improving manufacturing techniques, by including mechanical loading to simulate physiological strain, and importantly, as later discussed, by incorporating fluid force stimulation [43,45,48,102–106]. For example, Niklason *et al.*, created an artificial vessel by seeding bovine VSMCs on tubular biodegradable PGA scaffolds, which they cultured under pulsatile flow and in the presence of factors to support collagen synthesis and ECM protein cross-linking [43]. This created a graft with a smooth surface onto which EC could adhere, with the final structure able to withstand physiological pressures. Indeed, when implanted into a miniature swine model, the construct developed a highly organised structure with minimal signs of inflammation compared to a xenograft control.

In summary, the structure and composition of 3D vascular models will influence interactions between vascular cell types and with their ECM. Therefore, how these components are assembled in an *in vitro* model will impact its ability to recapitulate the native tissue's morphology, and its efficacy in mimicking native-like cell migration, proliferation, and ECM secretion/degradation, and by extension, vascular pathologies. Therefore, careful consideration is warranted in balancing simplicity against workability in the model to effectively capture particular aspects of disease or disease pathogenesis.

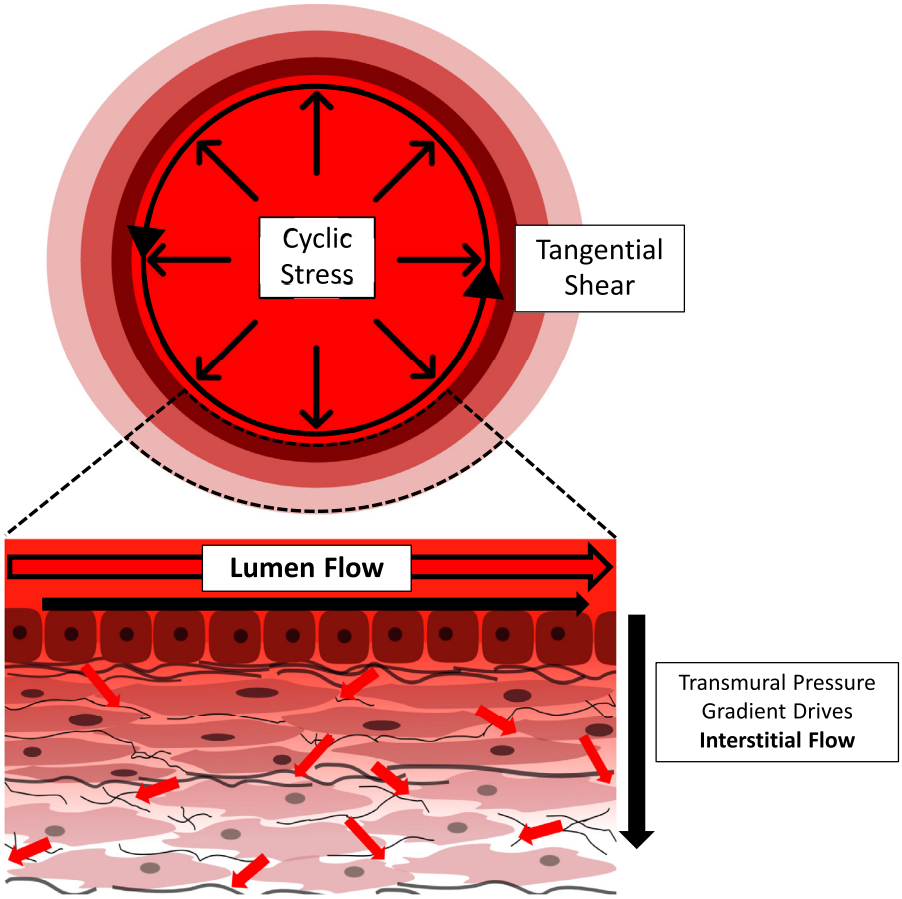


**Fig. 5.** Schematic of the 3 main axes of mechanical stimulation by flow in large vessels. Cyclic strain is developed in the wall as pulsatile flow develops normally, applying pressure forces that compress the vessel wall. Luminal shearing of endothelial cells is caused when blood flow passes over the cells. Finally, transmural pressure gradients drive interstitial flow through the vessel wall, which applies shear forces on embedded cells. Red arrows depict movement of flow through the lumen and interstitially in the vessel wall.

### *2.6. Incorporating mechano-stimulation: stress and strain*

Blood flow is pulsatile in nature, as pressure and velocity vary as the heart ejects blood and refills [107]. Haemodynamics within the system are determined by a combination of vessel geometry, driving pressures that force blood round the system, and the material properties of both vessels and blood itself. Therefore, blood flow profiles vary temporally and spatially along the circulatory system. Arteries and veins are exposed to continuous mechanical flow-mediated stimulation through two main mechanisms: deformation of the vessel wall due to blood pressure, and fluid shearing forces [62,108]. Pressure from the pulsatile flow acts normally to the vessel wall, delivering cyclic strains through circumferential stretching of the tissue [108] (Fig. 5), which the vessel wall resists by developing stresses [107]. Direct frictional shearing forces, on the other hand, act tangentially on the cells as a result of viscous flow passing over and around them [108,109] (Fig. 5).

The majority of blood flow passes through the lumen and delivers a shearing force to the ECs lining the vessel. ECs are highly mechanosensitive to blood flow cues, which they sense through their cytoskeleton as the cell deforms in response to fluid forces [110]. Indeed, luminal shear is a key regulator of vessel tone, prompting adaptive dilatation of the vessel wall [111–114]. It also regulates cell morphology, proliferation, protein expression and importantly for atherosclerosis research, the ability of ECs to attract monocytes [114–116]. ECs achieve regulation of the medial wall by producing vasoconstrictors and dilators, and in healthy vessels, maintain a non-adhesive lumen that has antithrombotic and anti-coagulant properties [117]. They also communicate to the matrix-synthesising cells embedded in the wall below [93,118–120].

In pathologies in which the vessel diameter is changed, healthy blood flow patterns are altered, and by extension, so are the mechanical forces imparted on the constituent cells. Given the crucial regulatory role of blood flow, it is therefore not surprising that pathological endothelial function precipitated by abnormal haemodynamics has been highlighted in many vascular pathologies [63,121,122]. Much effort has therefore focussed on understanding the mechanisms by which lumen flow disrupts endothelial function and its implications for disease progression. These include, but are not limited to, shear stress-driven development of atherosclerosis [63,123] and IH [124]. Moreover, flow eccentricity and high wall shear stress have been linked to dilatation in bicuspid aortic valve disease [125–128].

In addition to the luminal flow, transmural pressure gradients between the lumen and the outermost layer of the aortic wall drive a small amount of flow interstitially around the VSMCs and FBs (Fig. 5). The effect of this interstitial flow is often neglected due to slow flow velocities in this region (~$10^{-6}$ cm/s) [129]. However, due to the small interstitial spaces in the media wall, although flow is slow, the resultant forces have been shown to be non-negligible [129]. Using an analytical model, these velocities have been estimated to result in a shear stress of ~1 dyn/$cm^2$ [129]. Furthermore, in the case of injury or disease in which the luminal layer becomes disrupted or the ECM composition changes, the permeability of the EC layer may increase, exacerbating this effect [118,130,131]. *In vitro* studies have revealed that interstitial

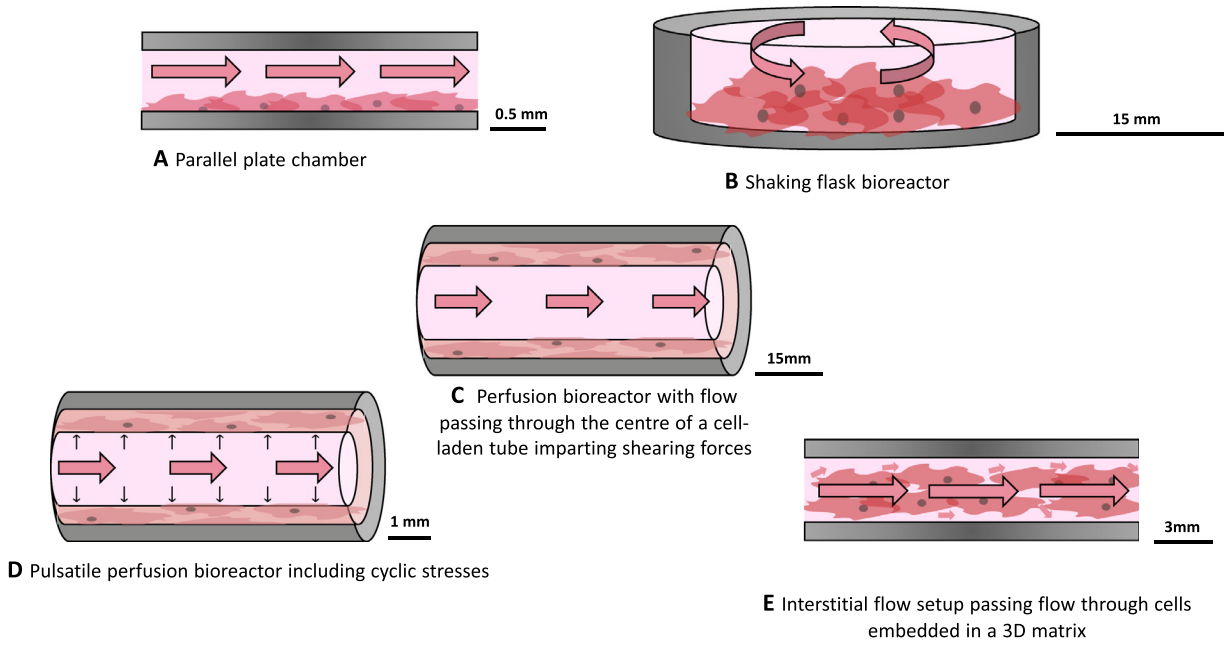


**Fig. 6.** Schematic of different bioreactor setups showing the movement of flow in each (pink arrows). A) A flat parallel plate chamber in which flow is passed over monolayers of cells delivers shear stresses to cells cultured along the wall. B) A shaking flask bioreactor in which the cell culture is rotated to stimulate motion of the cell culture media above imparts shear stresses on the cells. C) A perfusion bioreactor with flow passing through a central tubular channel surrounded by cells cultured in 2D or 3D applies shear to the cells in contact with the moving media. D) By incorporating pulsatile flow into a perfusion bioreactor, cells experience strain both from normally acting pressure forces as well as tangential shear. E) A parallel plate bioreactor can also deliver flow directly through a 3D matrix containing embedded cells, stimulating them with interstitial shear.

flow is able to impact SMC and FB migration, proliferation, and survival; as well as SMC alignment, contraction, phenotype and signalling [118]. It may therefore be important to include flow effects both luminally and interstitially in vascular models. Recapitulating *in vivo* interstitial stresses on VSMCs and FBs will likely require the use of 3D constructs. The structure of the interstitial tissue, driving pressure gradient, and the cellular arrangement inside the wall determine the nature of the flow, and therefore, 2D setups are unlikely to account for these effects. Indeed, with VSMC and FB dysregulation heavily implicated in vascular pathology, inclusion of 3D flow in disease modelling may be essential. Therefore, we next discuss models to recapitulate the 3 main axes of stimulation: cyclic stress, lumen stresses and interstitial stresses.

### 2.7. Providing mechanostimulation in in vitro models

Flow stimulation is imparted on cell cultures *in vitro* using fluidic devices known as bioreactors or flow chips, in which cells are placed in the path of flow (Fig. 6). Design criteria of these constructs are determined by considering the physiologically relevant forces to impart, and by extension the properties of *in vivo* flow to be recapitulated, as well as practical laboratory constraints.

The vascular system contains flows of different scales and regimes dependent on the size, geometry and location of a vessel. The distinction is made between macro and micro-scale flows and the relative contributions of inertial, viscous and pulsatile forces. These factors can be quantified numerically using the Reynolds and Wormsley numbers, dimensionless parameters calculated using flow velocities and vessel dimensions which provide the ratio of inertial to viscous forces, and pulsatile to viscous forces, respectively [15,107]. The Reynolds number also evaluates whether the flow is laminar or turbulent. In microvessels, viscous forces dominate, and the pulsatile nature of aortic flow is dampened, whereas in the macro circulation inertial terms become dominant with Reynolds number ranging from 1 in small arterioles to approximately 4000 in the aorta [107]. Pulsatile flow is highly relevant for the aorta and arterial components of the macro circulation due to the cyclical beating of the heart [15,107]. Pressure variation along the vessels and throughout the cardiac cycle also varies the circumferential strain as the vessel stretches in response.

Inevitably, the full complexity of *in vivo* flow is exceptionally challenging to capture *in vitro*, so careful consideration must be made as to the balance of building a system which is limited by over-complexity, versus careful tuning of specific flow parameters. Mechanical shear and strains are dependent on many different parameters and so there is an opportunity to control design criteria to provide controlled flow characteristics. The properties of the flowing medium as well as the geometry and substrate over or through which the fluid is moving influence the mechanical shear as flow passes over ECs and around embedded VSMCs. Pressures resulting from high flow velocities compact the tissue circumferentially, with the resistance of the matrix determining the degree of deformation. In the case of shearing forces, the magnitude of the mechanical force is dependent on the flow profile as well as the viscosity of fluid determining the friction between the flow and the vessel wall or interstitial matrix.

Determining exact values for these forces *in vivo* is challenging. Shear and strain cannot be directly measured *in vivo*. Instead, estimations are made using imaging techniques or patient catheterisation, often extrapolated or interpreted using mathematical models. For example, estimates of local velocity gradients are obtained using imaging techniques such as Doppler echocardiography or MRI, and these are then used to infer values of shearing force [132–134]. However, capturing all the intricacies of the full flow profile is challenging due to resolution limitations, and in particular estimates near the wall are hindered by difficulties in accurately tracking the moving vessel boundaries [132]. Furthermore, the assumptions required to apply mathematical models to these data can often simplify the complex *in vivo* environment. Nevertheless, advances continue to improve the robustness and accuracy of these estimates by improving the detail with which velocities are captured and the complexity of the models used [133,135].

When translating *in vivo* mechanical stimuli into *in vitro* systems, concessions in terms of operating medium, scale and geometry must be made. A major difference in *in vitro* models versus *in vivo* is the use of cell culture medium in place of blood. Blood is highly viscous, with a complex rheology due to suspended particulates, and so even in larger vessels, blood flows impart high shear stresses. To recapitulate this *in vitro* with culture medium, faster flows or increased spatial velocity variability is needed to maintain the same flow resistance, and there is a compromise to be struck balancing viscosity, flow velocity and geometry to reach physiological levels of shear. Importantly, as balancing these factors determines the regime of the flow, careful consideration must be made when changing flow velocities and chamber dimensions to ensure flow is representative of the pathology to be studied. By passing flow through smaller channels, the spatial variation in velocity is increased, and therefore with slower or less viscous forces, high levels of shear can still be achieved.

Furthermore, practical considerations in terms of scale may have to be made with most laboratory setups by sizing down. Microfluidics (devices with largest dimension of order 1mm) offers many advantages, including reducing the number of cells, amount of reagents needed and enabling high throughput [8–11,136–138]. Furthermore, with increasing ease of small-scale manufacture, microfluidic devices are able to impart specific mechanical cues with high tolerance [137]. Importantly, the smaller dimensions of microfluidic devices ensure flows remain laminar [10], which may be advantageous as fluid behaviour is more easily characterised and predicted in laminar regimes [10]. However, this could be a drawback for recapitulating pathological flow at higher Reynolds numbers.

Though predominantly used for the study of microvasculatures, microfluidics illustrate that spatial complexity can be introduced when using small scale flow chambers. Indeed, as physiological flow is highly heterogeneous, microfluidic systems lend themselves to precise patterning of fluid pathways [10]. Development of micro-physiological models to study whole organ pathology are often used to create “organ-on-a-chip” models [139–142]. To this end, microfluidic chambers have been designed not only to impart fluid forces to cells, but also to create microvascular networks for disease modelling and drug-screening assays [143–145]. For example, PDMS chambers combining cancer cells and ECs embedded in matrix surrounded by microfluidic channels have been designed to deliver arteriole and venule flow regimes [144]. Here, ECs migrate out to the fluid channels, eventually lining and sealing them to create a lumen through which flow passes. Then, by incorporating different cancer cells, a vascularised microtumour model can be developed. Studying tumours in the presence of vasculature can not only be used to model tumour development and response to drugs, but also cancer metastasis, through a process called extravasation by which cancer cells move through the endothelium and into the bloodstream [146,147].

Using cancer cell extravasation models, human mammary adenocarcinoma cells movement has been shown to be impacted by the surrounding matrix. Indeed, osteogenic-cell conditioned gels promote more movement than un-treated collagen type I gels, thus highlighting the impact of the tissue environment in cancer progression [148]. However, such devices model the blood vessel wall as a monolayer of ECs, and therefore can fall short in representing the complex vascular networks surrounding tumours *in vivo*. To improve on these studies, microvasculature models developed for organ-on-a-chip tumours can be incorporated into extravasation studies [149]. For example, micro-vasculatures have been formed by co-culturing primary human bone marrow-derived stromal cells differentiated towards the smooth muscle cell lineage with ECs. This resulted in more physiologically relevant blood vessel structures compared to those formed with ECs alone [150]. Moreover, using this model, the authors were further able to explore the impact of shear force on extravasation by passing flow through the vascular network, resulting in wall shear stresses of 0.25 dyn/cm$^2$ on ECs. The presence of flow decreased the permeability of the vasculature by tightening cell-cell junctions between the ECs. This in turn impacted extravasation rates, which were lower in flow conditions.

However, despite many advantages of using small scale devices to apply shear to cells, mircofluidics are not necessarily more physiologically representative [10]. Use of macro scale bioreactors should thus not be disregarded, particularly when studying vessel pathologies in larger vessels. Furthermore, when recapitulating large vessel events in which the Reynolds number is typically higher than for flows in microfluidic devices, fidelity to the flow regime may be important depending on the mechanism driving the shearing forces.

### 2.8. Towards the complete recapitulation of all factors

Thus far, we have highlighted the importance of co-culture systems within 3D materials, and fluid flow that captures all 3 axes of stimulation to recapitulate important aspects of blood vessel structure and the stimuli that act on it *in vivo*. Whilst models incorporating all these aspects combined do not yet exist, there are examples in which these factors have been incorporated individually using step-by-step approaches (Table 1).

A number of methods have been described to pass flow over monolayers of cells, including passing flow in a channel above the cells or shaking culture flasks [151–156]. Using such setups, 2D cultures of VSMC exposed to shear have been shown to upregulate expression of TGF$\beta$ [156], and downregulate MMP-2 expression, which inhibited cell migration [157]. Similarly, 3-25 dyn/cm$^2$ of shear stress have been shown to prompt increased VSMC secretion of FGF-2 [155]. Some studies have also combined shear stress with pressure and stretch by seeding EC on a thin concave polymer film which was stretched to mimic pulsatile flow [158]. The authors were able to show that their device was able to deliver both physiological and pathological pressure, flow, strain, and shear stress whilst allowing cells to align correctly and maintain barrier integrity compared to static cultures. Nevertheless, the shear stress levels on VSMCs in many studies are often higher than normal physiological levels and can be more than what cells are exposed to, even in the case of extreme pathologies [159].

There have also been efforts to incorporate cell-cell interactions into blood vessel models stimulated with flow. For example, in [160] the authors separated co-cultures of ECs and VSMCs using a medial layer containing a variety of adhesion proteins that were exposed to flow using a parallel plate flow chamber. Similarly, Van Engeland *et al.* combined ECs with embedded VSMCs to create an “artery-on-a-chip” device [1]. In this setup, ECs and VSMCs were seeded in a culture channel separated by a membrane intended to simulate the porous internal elastic lamina found between these cell layers *in vivo*. This model allows for cell-cell contact, whilst simultaneously exposing them to physiological luminal shear stresses, and was able to support ECs and VSMCs to maintain expression of phenotypic markers and normal cell morphologies. In particular, ECs expressed higher levels of von Willebrand factor, and VSMCs expressed more SMA when cultured in the device compared to in 2D. However, in this model, VSMCs were cultured in 2D and interstitial fluid flowing through the 3D matrix was not taken into account.

Simulation of fluid stresses can also be achieved using perfusion bioreactors. Here, 2D or 3D cell cultures are seeded in annular structures and flow is passed through a central lumen [4,43,161–165]. Such setups typically focus solely on shear; however, they have also been modified to pass flow through a 3D VSMC-seeded

**Table 1**
Table summarising the factors included and missing in some of the example blood vessel models described, highlighting that no one model includes all the factors necessary to comprehensively model vessel pathology.

| Brief Description | Example Reference | Co-culture of VSMCs and ECs | Intercellular communication | 3D culture of VSMCs | Cyclic Strain | Luminal shear | Interstitial shear through 3D matrix |
|---|---|---|---|---|---|---|---|
| Pulsatile flow passed over a layer of endothelial cells cultured on a stretchable membrane | [158] | | | | x | x | |
| Monolayer of endothelial cells cultured on top of a layer of vascular smooth muscle cells separated by a layer of medial adhesion protein in a parallel plate biorector | [160] | x | x | | | x | |
| Monolayer of endothelial cells cultured on top of a layer of vascular smooth muscle cells separated by a porous membrane with flow passed over the cell cultures either side of the membrane. | [1] | x | x | | x | x | |
| Tubular scaffold seeded with vascular smooth muscle cells centered in a glass tube, pressurised from the inside to generate circumferential stretch, and perfused through the channel between the scaffold and glass wall to generate wall shear stress | [165] | | | x | x | x | |
| Flow driven through a 3D culture of cells embedded in a collagen matrix | [32,33] | | | x | | | x |

tubular structure with a surrounding channel, allowing the setup to then be pressurised to deform and thus strain the culture [165]. This allows independent control of circumferential stress and shear stress. Whilst this type of setup allows for study of fluid stresses and strains on 3D cocultures, transmural flow was not taken into account. Indeed, this component is often overlooked due to underestimation of the resultant mechanical forces on the inter-mural cells.

Although limited, there are a few studies that have incorporated interstitial flows into blood vessel models. Strategies to achieve this generally involve the culture of VSMCs and/or FBs in a 3D matrix across which a pressure gradient is applied to drive flow through the gel [32,33,152]. For example, Wang *et al.* perfused a SMC-laden collagen gel by applying hydrostatic pressure and found that encapsulated SMCs upregulated production of prostaglandins compared to 2D controls under the same level of shear [32]. Using a similar approach, Shi *et al.* studied cell migration within 3D cultures to model neointima formation. They combined vascular FBs, myofibroblasts, and SMCs and found that motility was driven by upregulation of MMP-1 in interstitial flow compared to no-flow conditions [33].

In studies that apply interstitial flows, the forces imparted on the cells are often estimated using laws that govern flow through porous media by considering pressures applied across cultures and the average flow velocities through the matrix. As the relationship between velocity and stress is more complex for flow through a matrix compared to tangential shear, approximations are often made assuming average velocities and homogenous matrix properties throughout the 3D structure. However, whilst these approximations have served to good use, their underlying assumptions (which often treat the matrix as a bulk material) may oversimplify the spatial variation in shear acting on embedded cells. Estimates which consider the finer structural heterogeneity may give more realistic predictions of the forces experienced by the embedded cells. Synthetic materials in which matrix properties can be more robustly predicted may lend themselves more easily to these quantifications. We therefore suggest that advances in biomaterials may allow for more accurate predictions of 3D flows within the structure.

Furthermore, pathological flow has been implicated in tissue dysregulation, prompting cells to remodel their surrounding ECM. This includes excessive destruction of the tissue in aneurysm and abnormal luminal deposition in atherosclerosis. The composition of the ECM in turn alters the interstitial fluid mechanics, affecting the transport of solutes to embedded cells. Systems in which this interplay between matrix changes in response to mechanostimulation and the subsequent altering of these mechanical cues may be important to capture these bi-directional effects [166,167]. Therefore, advances in biomaterials, which allow for representative cell-matrix interaction in the presence of flow is vital, once again highlighting the role of material properties for both meaningful static and dynamic disease modelling.

Building towards more representative *in vitro* experiments, the optimal way to simulate pathologies in arteries is likely to include all the pertinent stresses and strains with representative cell cultures in one setup (Fig. 7). Design of such a model is complex and requires careful consideration of how to incorporate these forces whilst retaining the ability to quantify them and control stimuli independently. Advances in the techniques outlined above may allow simultaneous 2D and 3D flow with different cell types to become increasingly feasible allowing for reductionist models which can incorporate all the major stimuli to vascular cells.

## 3. Future perspectives

Reductionist blood vessel models are proving to be useful tools in vascular disease modelling. These simplified setups may allow researchers to uncover underlying mechanisms that contribute to vessel pathologies, which can often be challenging to study in native tissue. However, by reducing the complexity of the cues in the *in vitro* environment, fidelity is limited, and potentially key stimuli may be overlooked. Therefore, conclusions should be critically appraised in the context of these limitations and verified using other approaches, if possible.

Undoubtedly, the mechanisms that underlie complex vascular diseases are multi-faceted and involve complex interactions between the factors highlighted in this review. Whilst studying cell-cell interactions, cell-ECM interactions, or flow mechanotransduc-

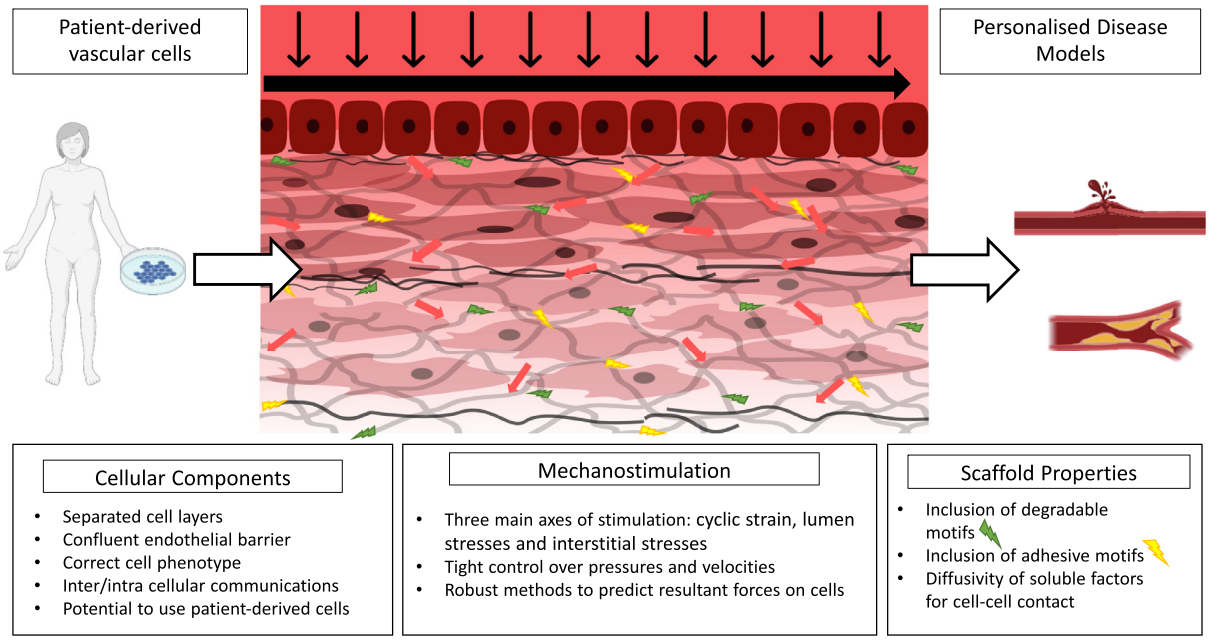


**Fig. 7.** Schematic showing an ideal *in vitro* blood vessel model, which includes patient-derived vascular cells to study the effects of pathological stimuli for personalised disease modelling. Created with BioRender.com.

tion independently may not be able to fully explain disease aetiology, by combining results obtained from *in vivo* studies with carefully constructed disease models, it may be possible to uncover factors that influence disease pathogenesis or progression. Indeed, elucidating the underlying mechanisms that drive vascular diseases may not only be important for understanding disease pathogenesis, but also key for identifying future therapeutic targets.

Not only can disease modelling potentially uncover underlying disease mechanisms, but the high controllability of the experimental conditions lends itself to use with techniques that may not be possible in tissue studies. Most notably, experimentally informed mathematical models are increasingly being applied in the fields of tissue engineering and disease modelling [168–170]. The concept underpinning such models is often the construction of a digital twin, whereby mathematical models constructed using experimental data predict biological behaviours, building in complexity as more experimental results are considered. *In silico* models can then be used to generate and test mechanistic hypotheses, study sensitivity to uncontrolled factors, and eventually produce *in silico* data that informs experimental decisions. Conversely, empirical data is used to parameterise and validate or extend the *in silico* models. A robust relationship can then be established between stimuli and cell behaviour through mathematical relations, and this can prove an extremely valuable tool for testing hypotheses around the mechanisms which underpin specific pathological behaviours. This combined approach, spanning *in vitro* experiments and mathematical models therefore not only serves to quantifiably characterise cell behaviours, but by building models capable of making validated predictions, can be used to reduce the number of experimental conditions required, ultimately expediting and reducing waste in *in vitro* work [168].

Furthermore, and particularly in the case of fluid forces, neither tangential nor interstitial shear can be experimentally measured. Therefore, quantification of mechanical forces is reliant on *in silico* work. However, creating robust mathematical models is reliant on reproducible, tightly controlled and characterisable setups. Given the need to work in 3D configurations, biomaterials are central to these models. The material's ability to facilitate cell-matrix interactions is one of the limiting factors in creating viable 3D cultures and so creating bioactive synthetic hydrogels may be key.

Vessel models for studying disease progression may also allow the use of vascular cells differentiated from patient-derived induced pluripotent stem cells (iPSCs). Advances in cell differentiation techniques and organoid derivation and culture have led to an increase in the use of patient-specific cells for disease modelling, particularly in gastrointestinal, cardiac, neural, hepatic and renal disease [5,141,171–174]. Indeed, use of human iPSC to derive ECs for use in microvasculature have also emerged for use in organ-on-a-chip models [142,175–178].

Patient-specific models offer obvious advantages in disease modelling, considering the role of genetics in cellular response to stimuli. Although some work has been made with use of iPSCs in cardiovascular applications, there is a paucity of work looking specifically at vessel disease [52,179]. We suggest that advances in this research area may lead to an understanding of pathological stimuli in large vessel diseases specific to patient genetics and make strides towards personalised disease modelling.

## 4. Conclusion

This paper highlights the main techniques used to create *in vitro* blood vessels for disease modelling and their limitations. As of yet, no one model exists that takes into account all the pertinent factors present in vascular disease. Looking forward, there is a need to develop more comprehensive models combining the best advances in biomaterials, fluidic devices, computational models and stem cell research. Reductionist *in vitro* models using iPSC-derived patient cells could serve to advance personalised medicine and develop therapeutic interventions.

## Declaration of Competing Interest

The authors declare no competing interests.

## Acknowledgements

S.T.L. gratefully acknowledges the UK Medical Research Council (MR/N013700/1) for funding through the MRC Doctoral Training Partnership in Biomedical Sciences at King's College London. PL holds a Wellcome Trust Senior Research Fellowship (209450/Z/17/Z) and is grateful to support from the Wellcome/EPSRC Centre for Medical Engineering (WT203148/Z/16/Z) and the BHF Centre for Research Excellence (RE/18/2/34213), both at King's College London. RJS is grateful for funding from the EPSRC (EP/R004463/1).

## References

[1] N.C.A. van Engeland, A.M.A.O. Pollet, J.M.J. den Toonder, C.V.C. Bouten, O.M.J.A. Stassen, C.M. Sahlgren, A biomimetic microfluidic model to study signalling between endothelial and vascular smooth muscle cells under hemodynamic conditions, Lab on a Chip 18 (2018) 1607–1620, doi:10.1039/c8lc00286j.

[2] B.J. van Varik, R.J.M.W. Rennenberg, C.P. Reutelingsperger, A.A. Kroon, P.W. de Leeuw, L.J. Schurgers, Mechanisms of arterial remodeling: Lessons from genetic diseases, Front. Genet. 3 (2012) 1–10, doi:10.3389/fgene.2012.00290.

[3] K.H. Benam, S. Dauth, B. Hassell, A. Herland, A. Jain, K.J. Jang, K. Karalis, H.J. Kim, L. MacQueen, R. Mahmoodian, S. Musah, Y.S. Torisawa, A.D. van der Meer, R. Villenave, M. Yadid, K.K. Parker, D.E. Ingber, Engineered in vitro disease models, Annu. Rev. Pathol. (2015), doi:10.1146/annurev-pathol-012414-040418.

[4] J. Robert, B. Weber, L. Frese, M.Y. Emmert, D. Schmidt, A. von Eckardstein, L. Rohrer, S.P. Hoerstrup, A three-dimensional engineered artery model for in vitro atherosclerosis research, PLoS ONE 8 (2013), doi:10.1371/journal.pone.0079821.

[5] G.M. Jowett, M.D.A. Norman, T.T.L. Yu, P. Rosell Arévalo, D. Hoogland, S.T. Lust, E. Read, E. Hamrud, N.J. Walters, U. Niazi, M.W.H. Chung, D. Marciano, O.S. Omer, T. Zabinski, D. Danovi, G.M. Lord, J. Hilborn, N.D. Evans, C.A. Dreiss, L. Bozec, O.P. Oommen, C.D. Lorenz, R.M.P. da Silva, J.F. Neves, E. Gentleman, ILC1 drive intestinal epithelial and matrix remodelling, Nat. Mater. 20 (2021) 250–259, doi:10.1038/s41563-020-0783-8.

[6] S.A. Ferreira, P.A. Faull, A.J. Seymour, T.T.L. Yu, S. Loaiza, H.W. Auner, A.P. Snijders, E. Gentleman, Neighboring cells override 3D hydrogel matrix cues to drive human MSC quiescence, Biomaterials 176 (2018) 13–23, doi:10.1016/j.biomaterials.2018.05.032.

[7] D.A. Foyt, M.D.A. Norman, T.T.L. Yu, E. Gentleman, Exploiting Advanced Hydrogel Technologies to Address Key Challenges in Regenerative Medicine, Adv. Healthcare Mater. 7 (2018), doi:10.1002/adhm.201700939.

[8] V. van Duinen, S.J. Trietsch, J. Joore, P. Vulto, T. Hankemeier, Microfluidic 3D cell culture: From tools to tissue models, Curr. Opin. Biotech. 35 (2015) 118–126, doi:10.1016/j.copbio.2015.05.002.

[9] P.S. Dittrich, A. Manz, Lab-on-a-chip: Microfluidics in drug discovery, Nat. Rev. Drug Discov. 5 (2006) 210–218, doi:10.1038/nrd1985.

[10] K.H.K. Wong, J.M. Chan, R.D. Kamm, J. Tien, Microfluidic models of vascular functions, Annu. Rev. Biomed. Eng. 14 (2012) 205–230, doi:10.1146/annurev-bioeng-071811-150052.

[11] A.D. van der Meer, A.A. Poot, M.H.G. Duits, J. Feijen, I. Vermes, Microfluidic technology in vascular research, J. Biomed. Biotech. 2009 (2009), doi:10.1155/2009/823148.

[12] E.A. Logsdon, S.D. Finley, A.S. Popel, F. MacGabhann, A systems biology view of blood vessel growth and remodelling, J. Cell. Mol. Med. 18 (2014) 1491–1508, doi:10.1111/jcmm.12164.

[13] M.F. O'Rourke, J. Hashimoto, Mechanical factors in arterial aging. A clinical perspective, J. Am. Coll. Cardiol. 50 (2007) 1–13, doi:10.1016/j.jacc.2006.12.050.

[14] J.R. Barbour, F.G. Spinale, J.S. Ikonomidis, Proteinase systems and thoracic aortic aneurysm progression, J. Surg. Res. 139 (2007) 292–307.

[15] Y.C Fung, Micro- and Macrocirculation, Biomechanics Motion, Flow, Stress and Growth, Springer, New York, 1990.

[16] Standring Susan, Cells, Tissues and Systems, Gray's Anatomy, Churchill Livingstone., 2009 40th edition.

[17] A.C. Newby, A.B. Zaltsman, Molecular mechanisms in intimal hyperplasia, J. Pathol. 190 (2000) 300–309, doi:10.1002/(SICI)1096-9896(200002)190:3⟨300::AID-PATH596⟩3.0.CO;2-I.

[18] A.C. Newby, Dual role of matrix metalloproteinases (matrixins) in intimal thickening and atherosclerotic plaque rupture, Physiol. Rev. 85 (2005) 1–31, doi:10.1152/physrev.00048.2003.

[19] P. Libby, P.M. Ridker, A. Maseri, Inflammation and atherosclerosis, Circulation 105 (2002) 1135–1143, doi:10.1161/hc0902.104353.

[20] R. Paoletti, A.M. Gotto, D.P. Hajjar, Inflammation in atherosclerosis and implications for therapy, Circulation 109 (2004) 20–26, doi:10.1161/01.cir.0000131514.71167.2e.

[21] M.G. Davies, P.-O. Hagen, Pathobiology of intimal hyperplasia, Br. J. Surg. (1994) 1254–1269, doi:10.1016/0741-5214(89)90153-5.

[22] P.B. Dobrin, R. Mrkvicka, Failure of elastin or collagen as possible critical connective tissue alterations underlying aneurysmal dilatation, Cardiovasc. Surg. 2 (1994) 484–488.

[23] R.J. Rizzo, W.J. McCarthy, S.N. Dixit, M.P. Lilly, V.P. Shively, W.R. Flinn, J.S.T. Yao, Collagen types and matrix protein content in human abdominal aortic aneurysms, J. Vasc. Surg. 10 (1989) 365–373.

[24] K.L. Losenno, R.L. Goodman, M.W.A. Chu, Bicuspid aortic valve disease and ascending aortic aneurysms: Gaps in knowledge, Cardiol. Res. Pract. 2012 (2012).

[25] P.W.M. Fedak, T.E. David, R.L. Leask, R.D. Weisel, J. Butany, Clinical and pathophysiological implications of a bicuspid aortic valve, Circulation (2002).

[26] W.R.W. Wilson, M. Anderton, E.C. Schwalbe, J.L. Jones, P.N. Furness, P.R.F. Bell, M.M. Thompson, Matrix metalloproteinase-8 and -9 are increased at the site of abdominal aortic aneurysm rupture, Circulation 113 (2006) 438–445, doi:10.1161/CIRCULATIONAHA.105.551572.

[27] V. Davis, R. Persidskaia, L. Baca-Regen, Y. Itoh, H. Nagase, Y. Persidsky, A. Ghorpade, B.Timothy Baxter, Matrix metalloproteinase-2 production and its binding to the matrix are increased in abdominal aortic aneurysms, Arterioscler. Thromb. Vasc. Biol. 18 (1998) 1625–1633, doi:10.1161/01.ATV.18.10.1625.

[28] J.A. Beamish, A.Y. Fu, A. jin Choi, N.A. Haq, K. Kottke-Marchant, R.E. Marchant, The influence of RGD-bearing hydrogels on the re-expression of contractile vascular smooth muscle cell phenotype, Biomaterials 30 (2009) 4127–4135, doi:10.1016/j.biomaterials.2009.04.038.

[29] C.H. Lee, A. Singla, Y. Lee, Biomedical applications of collagen, Int. J. Pharmaceut. 221 (2001) 1–22, doi:10.1016/S0378-5173(01)00691-3.

[30] M.J. Chow, R. Turcotte, C.P. Lin, Y. Zhang, Arterial extracellular matrix: A mechanobiological study of the contributions and interactions of elastin and collagen, Biophys. J. 106 (2014) 2684–2692, doi:10.1016/j.bpj.2014.05.014.

[31] J.P. Stegemann, R.M. Nerem, Altered response of vascular smooth muscle cells to exogenous biochemical stimulation in two- and three-dimensional culture, Exp. Cell Res. 283 (2003) 146–155, doi:10.1016/S0014-4827(02)00041-1.

[32] S. Wang, J.M. Tarbell, Effect of fluid flow on smooth muscle cells in a 3-dimensional collagen gel model, Arterioscler. Thromb. Vasc. Biol. 20 (2000) 2220–2225, doi:10.1161/01.ATV.20.10.2220.

[33] Z.-D. Shi, X.-Y. Ji, H. Qazi, J.M. Tarbell, Interstitial flow promotes vascular fibroblast, myofibroblast, and smooth muscle cell motility in 3-D collagen I via upregulation of MMP-1, Am. J. Physiol.-Heart Circulat. Physiol. 297 (2009) H1225–H1234, doi:10.1152/ajpheart.00369.2009.

[34] S. Li, J. Lao, B.P.C. Chen, Y. Li, Y. Zhao, J. Chu, K.-D. Chen, T.C. Tsou, K. Peck, S. Chien, Genomic analysis of smooth muscle cells in 3-dimensional collagen matrix, FASEB J. 17 (2003) 97–99, doi:10.1096/fj.02-0256fje.

[35] C.B. Weinberg, E. Bell, A blood vessel model constructed from collagen and cultured vascular cells, Science 231 (1986) 397–400, doi:10.1126/science.2934816.

[36] J. Song, B.E. Rolfe, I.P. Hayward, G.R. Campbell, J.H. Campbell, Reorganization of structural proteins in vascular smooth muscle cells grown in collagen gel and basement membrane matrices (Matrigel): A comparison with their in situ counterparts, J. Struct. Biol. 133 (2001) 43–54, doi:10.1006/jsbi.2001.4327.

[37] C.S. Hughes, L.M. Postovit, G.A. Lajoie, Matrigel: a complex protein mixture required for optimal growth of cell culture, Proteomics 10 (2010) 1886–1890, doi:10.1002/pmic.200900758.

[38] S. Vukicevic, H.K. Kleinman, F.P. Luyten, A.B. Roberts, N.S. Roche, A.H. Reddi, Identification of multiple active growth factors in basement membrane matrigel suggests caution in interpretation of cellular activity related to extracellular matrix components, Exp. Cell Res. 202 (1992) 1–8, doi:10.1016/0014-4827(92)90397-Q.

[39] J.D. Berglund, M.M. Mohseni, R.M. Nerem, A. Sambanis, A biological hybrid model for collagen-based tissue engineered vascular constructs, Biomaterials 24 (2003) 1241–1254, doi:10.1016/S0142-9612(02)00506-9.

[40] R. Cruz-Acuña, A.J. García, Synthetic hydrogels mimicking basement membrane matrices to promote cell-matrix interactions, Matrix Biol. 57-58 (2017) 324–333, doi:10.1016/j.matbio.2016.06.002.

[41] M. Guvendiren, J.A. Burdick, Engineering synthetic hydrogel microenvironments to instruct stem cells, Curr. Opin. Biotech. 24 (2013) 841–846, doi:10.1016/j.copbio.2013.03.009.

[42] D.J. Mooney, C.L. Mazzoni, C. Breuer, K. McNamara, D. Hern, J.P. Vacanti, R. Langer, Stabilized polyglycolic acid fibre-based tubes for tissue engineering, Biomaterials 17 (1996) 115–124, doi:10.1016/0142-9612(96)85756-5.

[43] L.E. Niklason, J. Gao, W.M. Abbott, K.K. Hirschi, S. Houser, R. Marini, R. Langer, Functional arteries grown in vitro, Science 284 (1999) 489–493, doi:10.1126/science.284.5413.489.

[44] B.S. Kim, J. Nikolovski, J. Bonadio, E. Smiley, D.J. Mooney, Engineered smooth muscle tissues: Regulating cell phenotype with the scaffold, Exp. Cell Res. 251 (1999) 318–328, doi:10.1006/excr.1999.4595.

[45] S.P. Hoerstrup, G. Zünd, R. Sodian, A.M. Schnell, J. Grünenfelder, M.I. Turina, Tissue engineering of small caliber vascular grafts, Eur. J. Cardio-Thoracic Surg. 20 (2001) 164–169, doi:10.1016/S1010-7940(01)00706-0.

[46] X. Wang, S. Sui, Pulsatile culture of a poly(DL-lactic-co-glycolic acid) sandwiched cell/hydrogel construct fabricated using a step-by-step mold/extraction method, Artificial Organs 35 (2011) 645–655, doi:10.1111/j.1525-1594.2010.01137.x.

[47] H. Bramfeldt, P. Sarazin, P. Vermette, Smooth muscle cell adhesion in surface-modified three-dimensional copolymer scaffolds prepared from co-continuous blends, J. Biomed. Mater. Res. Part A 91 (2009) 305–315, doi:10.1002/jbm.a.32244.

[48] M.S. Hahn, M.K. McHale, E. Wang, R.H. Schmedlen, J.L. West, Physiologic pulsatile flow bioreactor conditioning of poly(ethylene glycol)-based tissue en-

gineered vascular grafts, Ann. Biomed. Eng. 35 (2007) 190–200, doi:10.1007/s10439-006-9099-3.
[49] M.H. Fittkau, P. Zilla, D. Bezuidenhout, M.P. Lutolf, P. Human, J.A. Hubbell, N. Davies, The selective modulation of endothelial cell mobility on RGD peptide containing surfaces by YIGSR peptides, Biomaterials 26 (2005) 167–174, doi:10.1016/j.biomaterials.2004.02.012.
[50] S.R. Peyton, C.B. Raub, V.P. Keschrumrus, A.J. Putnam, The use of poly(ethylene glycol) hydrogels to investigate the impact of ECM chemistry and mechanics on smooth muscle cells, Biomaterials 27 (2006) 4881–4893, doi:10.1016/j.biomaterials.2006.05.012.
[51] B.K. Mann, A.S. Gobin, A.T. Tsai, R.H. Schmedlen, J.L. West, Smooth muscle cell growth in photopolymerized hydrogels with cell adhesive and proteolytically degradable domains: Synthetic ECM analogs for tissue engineering, Biomaterials 22 (2001) 3045–3051, doi:10.1016/S0142-9612(01)00051-5.
[52] M.R. Zanotelli, H. Ardalani, J. Zhang, Z. Hou, E.H. Nguyen, S. Swanson, B.K. Nguyen, J. Bolin, A. Elwell, L.L. Bischel, A.W. Xie, R. Stewart, D.J. Beebe, J.A. Thomson, M.P. Schwartz, W.L. Murphy, Stable engineered vascular networks from human induced pluripotent stem cell-derived endothelial cells cultured in synthetic hydrogels, Acta Biomaterialia 35 (2016) 32–41, doi:10.1016/j.actbio.2016.03.001.
[53] A.W. Watkins, K.S. Anseth, Investigation of molecular transport and distributions in poly(ethylene glycol) hydrogels with confocal laser scanning microscopy, Macromolecules 38 (2005) 1326–1334, doi:10.1021/ma0475232.
[54] M.P. Lutolf, N. Tirelli, S. Cerritelli, L. Cavalli, J.A. Hubbell, Systematic modulation of Michael-type reactivity of thiols through the use of charged amino acids, Bioconjugate Chemistry 12 (2001) 1051–1056, doi:10.1021/bc015519e.
[55] M.P. Lutolf, J.A. Hubbell, Synthesis and physicochemical characterization of end-linked poly(ethylene glycol)-co-peptide hydrogels formed by Michael-type addition, Biomacromolecules 4 (2003) 713–722, doi:10.1021/bm025744e.
[56] A.M.J. Coenen, K. V. Bernaerts, J.A.W. Harings, S. Jockenhoevel, S. Ghazanfari, Elastic materials for tissue engineering applications: Natural, synthetic, and hybrid polymers, Acta Biomaterialia 79 (2018) 60–82, doi:10.1016/j.actbio.2018.08.027.
[57] S. Heydarkhan-Hagvall, K. Schenke-Layland, A.P. Dhanasopon, F. Rofail, H. Smith, B.M. Wu, R. Shemin, R.E. Beygui, W.R. MacLellan, Three-dimensional electrospun ECM-based hybrid scaffolds for cardiovascular tissue engineering, Biomaterials (2008), doi:10.1016/j.biomaterials.2008.03.034.
[58] J.W. Nichol, S.T. Koshy, H. Bae, C.M. Hwang, S. Yamanlar, A. Khademhosseini, Cell-laden microengineered gelatin methacrylate hydrogels, Biomaterials (2010), doi:10.1016/j.biomaterials.2010.03.064.
[59] C. Chen, J. Tang, Y. Gu, L. Liu, X. Liu, L. Deng, C. Martins, B. Sarmento, W. Cui, L. Chen, Bioinspired Hydrogel Electrospun Fibers for Spinal Cord Regeneration, Adv. Funct. Mater. (2019), doi:10.1002/adfm.201806899.
[60] A. Hasan, A. Paul, A. Memic, A. Khademhosseini, A multilayered microfluidic blood vessel-like structure, Biomedical Microdevices (2015), doi:10.1007/s10544-015-9993-2.
[61] F. Tronc, Z. Mallat, S. Lehoux, M. Wassef, B. Esposito, A. Tedgui, Role of matrix metalloproteinases in blood flow–induced arterial enlargement, Arterioscler. Thromb. Vasc. Biol. 20 (2000), doi:10.1161/01.atv.20.12.e120.
[62] S. Lehoux, A. Tedgui, Cellular mechanics and gene expression in blood vessels, J. Biomech. (2003), doi:10.1016/S0021-9290(02)00441-4.
[63] J.M. Dolan, J. Kolega, H. Meng, High wall shear stress and spatial gradients in vascular pathology: A review, Ann. Biomed. Eng. (2013), doi:10.1007/s10439-012-0695-0.
[64] D.A. Vorpe, J.P. Vande Geest, Biomechanical determinants of abdominal aortic aneurysm rupture, Arterioscler. Thromb. Vasc. Biol. 25 (2005) 1558–1566, doi:10.1161/01.ATV.0000174129.77391.55.
[65] M.D. Rekhter, Collagen synthesis in atherosclerosis: Too much and not enough, Cardiovasc. Res. 41 (1999) 376–384, doi:10.1016/S0008-6363(98)00321-6.
[66] E. Cukierman, R. Pankov, D.R. Stevens, K.M. Yamada, Taking cell-matrix adhesions to the third dimension, Science 294 (2001) 1708–1712, doi:10.1126/science.1064829.
[67] K.G. Battiston, J.W.C. Cheung, D. Jain, J.P. Santerre, Biomaterials in co-culture systems: Towards optimizing tissue integration and cell signaling within scaffolds, Biomaterials 35 (2014) 44654476, doi:10.1016/j.biomaterials.2014.02.023.
[68] B.M. Baker, C.S. Chen, Deconstructing the third dimension-how 3D culture microenvironments alter cellular cues, J. Cell Sci. 125 (2012) 3015–3024, doi:10.1242/jcs.079509.
[69] G.K. Owens, Regulation of differentiation of vascular smooth muscle cells, Physiol. Rev. 75 (1995) 487–517, doi:10.1152/physrev.1995.75.3.487.
[70] J. Thyberg, U. Hedin, M. Sjöiund, L. Palmberg, B.A. Bottger, Regulation of differentiated properties and proliferation of arterial smooth muscle cells, Arterioscler. Thromb. Vasc. Biol. 10 (1990) 966–990, doi:10.1161/01.ATV.10.6.966.
[71] R.K. Assoian, E.E. Marcantonio, The extracellular matrix as a cell cycle control element in atherosclerosis and restenosis, J. Clin. Invest. 100 (1997) 2436–2439.
[72] J.P. Stegemann, H. Hong, R.M. Nerem, Mechanical, biochemical, and extracellular matrix effects on vascular smooth muscle cell phenotype, J. Appl. Physiol. 98 (2005) 2321–2327, doi:10.1152/japplphysiol.01114.2004.
[73] J. Xu, G.P. Shi, Vascular wall extracellular matrix proteins and vascular diseases, Biochimica et Biophysica Acta - Molecular Basis of Disease 1842 (2014) 2106–2119, doi:10.1016/j.bbadis.2014.07.008.
[74] E.P. Moiseeva, Adhesion receptors of vascular smooth muscle cells and their functions, Cardiovasc. Res. 52 (2001) 372–386, doi:10.1016/S0008-6363(01)00399-6.
[75] A. Frismantiene, M. Philippova, P. Erne, T.J. Resink, Smooth muscle cell-driven vascular diseases and molecular mechanisms of VSMC plasticity, Cellular Signalling 52 (2018) 48–64, doi:10.1016/j.cellsig.2018.08.019.
[76] P.Y. Chen, L. Qin, G. Li, J. Malagon-Lopez, Z. Wang, S. Bergaya, S. Gujja, A.W. Caulk, S. Murtada, X. Zhang, Z.W. Zhuang, D.A. Rao, G. Wang, Z. Tobiasova, B. Jiang, R.R. Montgomery, L. Sun, H. Sun, E.A. Fisher, J.R. Gulcher, C. Fernandez-Hernando, J.D. Humphrey, G. Tellides, T.W. Chittenden, M. Simons, Smooth muscle cell reprogramming in aortic aneurysms, Cell Stem Cell 26 (2020) 542–557 e11, doi:10.1016/j.stem.2020.02.013.
[77] J. Thyberg, K. Blomgren, J. Roy, P.K. Tran, U. Hedin, Phenotypic modulation of smooth muscle cells after arterial injury is associated with changes in the distribution of laminin and fibronectin, J. Histochem. Cytochem. 45 (1997) 837–846, doi:10.1177/002215549704500608.
[78] Y. Huo, A. Hafezi-Moghadam, K. Ley, Role of vascular cell adhesion molecule-1 and fibronectin connecting segment-1 in monocyte rolling and adhesion on early atherosclerotic lesions, Circulat. Res. 87 (2000) 153–159, doi:10.1161/01.RES.87.2.153.
[79] M.K. Ganesan, R. Finsterwalder, H. Leb, U. Resch, K. Neumüller, R. de Martin, P. Petzelbauer, Three-dimensional coculture model to analyze the cross talk between endothelial and smooth muscle cells, Tissue Eng. Part C Methods 23 (2017) 38–49, doi:10.1089/ten.tec.2016.0299.
[80] Y. Xia, A. Bhattacharyya, E.E. Roszell, M. Sandig, K. Mequanint, The role of endothelial cell-bound Jagged1 in Notch3-induced human coronary artery smooth muscle cell differentiation, Biomaterials 33 (2011) 2462–2472, doi:10.1016/j.biomaterials.2011.12.001.
[81] M.H. Nam, H.S. Lee, Y. Seomun, Y. Lee, K.W. Lee, Monocyte-endothelium-smooth muscle cell interaction in co-culture: Proliferation and cytokine productions in response to advanced glycation end products, Biochimica et Biophysica Acta - General Subjects 1810 (2011) 907–912, doi:10.1016/j.bbagen.2011.06.005.
[82] G.B. Nackman, F.R. Bech, M.F. Fillinger, R.J. Wagner, J.L. Cronenwett, Endothelial cells modulate smooth muscle cell morphology by inhibition of transforming growth factor-beta1 activation, Surgery 120 (1996) 418–426, doi:10.1016/S0039-6060(96)80318-7.
[83] G.A. Truskey, Endothelial cell vascular smooth muscle co-culture assay for high throughput screening assays, Int. J. High Throughput Screen 2010 (2011) 171–181, doi:10.2147/IJHTS.S13459.Endothelial.
[84] M.F. van Buul-Wortelboer, H.J.M. Brinkman, K.P. Dingemans, P.G. de Groot, W.G. van Aken, J.A. van Mourik, Reconstitution of the vascular wall in vitro. A novel model to study interactions between endothelial and smooth muscle cells, Exp. Cell Res. 162 (1986) 151158, doi:10.1016/0014-4827(86)90433-7.
[85] T. Ziegler, R.W. Alexander, R.M. Nerem, An endothelial cell-smooth muscle cell co-culture model for use in the investigation of flow effects on vascular biology, Ann. Biomed. Eng. 23 (1995) 216–225, doi:10.1007/BF02584424.
[86] H.Q. Wang, L. Bai, B.R. Shen, Z.Q. Yan, Z.L. Jiang, Coculture with endothelial cells enhances vascular smooth muscle cell adhesion and spreading via activation of $\beta$1-integrin and phosphatidylinositol 3-kinase/Akt, Eur. J. Cell Biol. 86 (2007) 51–62, doi:10.1016/j.ejcb.2006.09.001.
[87] R.J. Powell, J.L. Cronenwett, M.F. Fillinger, R.J. Wagner, L.N. Sampson, Endothelial cell modulation of smooth muscle cell morphology and organizational growth pattern, Ann. Vasc. Surg. 10 (1996) 4–10, doi:10.1007/BF02002334.
[88] R.J. Powell, J. Bhargava, M.D. Basson, B.E. Sumpio, Coculture conditions alter endothelial modulation of TGF-$\beta$1 activation and smooth muscle growth morphology, Am. J. Physiol. Heart Circulat. Physiol. 274 (1998) 642–649, doi:10.1152/ajpheart.1998.274.2.h642.
[89] E.M. Rzucidlo, K.A. Martin, R.J. Powell, Regulation of vascular smooth muscle cell differentiation, J. Vasc. Surg. 45 (2007) A25–A32, doi:10.1016/j.jvs.2007.03.001.
[90] T. Hirase, K. Node, Endothelial dysfunction as a cellular mechanism for vascular failure, Am. J. Physiol. Heart Circulat. Physiol. 302 (2012) 499–505, doi:10.1152/ajpheart.00325.2011.
[91] G. Bazzoni, E. Dejana, Endothelial cell-to-cell junctions: Molecular organization and role in vascular homeostasis, Physiol. Rev. 84 (2004) 869–901, doi:10.1152/physrev.00035.2003.
[92] B. Lilly, We have contact: Endothelial cell-smooth muscle cell interactions, Physiology 29 (2014) 234–241, doi:10.1152/physiol.00047.2013.
[93] M. Li, M. Qian, K. Kyler, J. Xu, Endothelial–Vascular Smooth Muscle Cells Interactions in Atherosclerosis, Front. Cardiovasc. Med. 5 (2018), doi:10.3389/fcvm.2018.00151.
[94] M.J.A. van Kempen, H.J. Jongsma, Distribution of connexin37, connexin40 and connexin43 in the aorta and coronary artery of several mammals, Histochem. Cell Biol. 112 (1999) 479–486, doi:10.1007/s004180050432.
[95] B. Zheng, W. Yin, T. Suzuki, X. Zhang, Y. Zhang, L. Song, L. Jin, H. Zhan, H. Zhang, J. Li, J. Wen, Exosome-mediated miR-155 transfer from smooth muscle cells to endothelial cells induces endothelial injury and promotes atherosclerosis, Molecular Therapy 25 (2017) 1279–1294, doi:10.1016/j.ymthe.2017.03.031.
[96] J. Fingerle, Y.P.T. Au, A.W. Clowes, M.A. Reidy, Intimal lesion formation in rat carotid arteries after endothelial denudation in absence of medial injury, Arteriosclerosis 10 (1990) 1082–1087, doi:10.1161/01.atv.10.6.1082.
[97] J.G. Jacot, J.Y. Wong, Endothelial injury induces vascular smooth muscle cell proliferation in highly localized regions of a direct contact co-culture system, Cell Biochem. Biophys. 52 (2008) 37–46, doi:10.1007/s12013-008-9023-6.

[98] K. Niwa, T. Kado, J. Sakai, T. Karino, The effects of a shear flow on the uptake of LDL and acetylated LDL by an EC monoculture and an EC-SMC coculture, Ann. Biomed. Eng. 32 (2004) 537–543, doi:10.1023/B:ABME.0000019173.79939.54.
[99] A. Tan, K. Fujisawa, Y. Yukawa, Y.T. Matsunaga, Bottom-up fabrication of artery-mimicking tubular co-cultures in collagen-based microchannel scaffolds, Biomater. Sci. 4 (2016) 1503–1514, doi:10.1039/c6bm00340k.
[100] M.W. Vaughn, L. Kuo, J.C. Liao, Effective diffusion distance of nitric oxide in the microcirculation, Am. J. Physiol. Heart Circulat. Physiol. 274 (1998) 1705–1714, doi:10.1152/ajpheart.1998.274.5.h1705.
[101] Y. Pang, X. Wang, A.A. Ucuzian, E.M. Brey, W.H. Burgess, K.J. Jones, T.D. Alexander, H.P. Greisler, Local delivery of a collagen-binding FGF-1 chimera to smooth muscle cells in collagen scaffolds for vascular tissue engineering, Biomaterials 31 (2010) 878–885, doi:10.1016/j.biomaterials.2009.10.007.
[102] S.J. Lee, D.N. Heo, J.S. Park, S.K. Kwon, J.H. Lee, J.H. Lee, W.D. Kim, I.K. Kwon, S.A. Park, Characterization and preparation of bio-tubular scaffolds for fabricating artificial vascular grafts by combining electrospinning and a 3D printing system, Phys. Chem. Chem. Phys. 17 (2015) 2996–2999, doi:10.1039/c4cp04801f.
[103] D. Shum-Tim, U. Stock, J. Hrkach, T. Shinoka, J. Lien, M.A. Moses, A. Stamp, G. Taylor, A.M. Moran, W. Landis, R. Langer, J.P. Vacanti, J.E. Mayer, Tissue engineering of autologous aorta using a new biodegradable polymer, Ann. Thorac. Surg. 68 (1999) 2298–2304, doi:10.1016/S0003-4975(99)01055-3.
[104] J. Luo, L. Qin, L. Zhao, L. Gui, M.W. Ellis, Y. Huang, M.H. Kural, J.A. Clark, S. Ono, J. Wang, Y. Yuan, S.M. Zhang, X. Cong, G. Li, M. Riaz, C. Lopez, A. Hotta, S. Campbell, G. Tellides, A. Dardik, L.E. Niklason, Y. Qyang, Tissue-engineered vascular grafts with advanced mechanical strength from human iPSCs, Cell Stem Cell 26 (2020) 251-261.e8, doi:10.1016/j.stem.2019.12.012.
[105] T. Aper, M. Wilhelmi, C. Gebhardt, K. Hoeffler, N. Benecke, A. Hilfiker, A. Haverich, Novel method for the generation of tissue-engineered vascular grafts based on a highly compacted fibrin matrix, Acta Biomaterialia 29 (2016) 21–32, doi:10.1016/j.actbio.2015.10.012.
[106] N.L. Heureux, S. Pâquet, R. Labbé, L. Germain, F.A. Auger, A completely biological tissue-engineered human blood vessel, FASEB J. 12 (1998) 47–56, doi:10.1096/fsb2fasebj.12.1.47.
[107] D.N. Ku, Blood flow in arteries, Annu. Rev. Fluid Mech. 29 (1997) 399–434, doi:10.1146/annurev.fluid.29.1.399.
[108] C. Hahn, M.A. Schwartz, Mechanotransduction in vascular physiology and atherogenesis, Nat. Rev. Mol. Cell Biol. 10 (2009) 53–62, doi:10.1038/nrm2596.
[109] C.R. White, J.A. Frangos, The shear stress of it all: The cell membrane and mechanochemical transduction, Philos. Trans. R. Soc. B Biol. Sci. 362 (2007) 1459–1467, doi:10.1098/rstb.2007.2128.
[110] B.P. Helmke, P.F. Davies, The cytoskeleton under external fluid mechanical forces: Hemodynamic forces acting on the endothelium, Ann. Biomed. Eng. 30 (2002) 284–296, doi:10.1114/1.1467926.
[111] A. Kamiya, T. Togawa, Adaptive regulation of wall shear stress to flow change in the canine carotid artery, Am. J. Physiol. Heart Circulat. Physiol. 8 (1980) 14–21, doi:10.1152/ajpheart.1980.239.1.h14.
[112] J. Gimbrone, A. Michael, K.R. Anderson, J.N. Topper, The critical role of mechanical forces in blood vessel development, physiology and pathology, J. Vasc. Surg. (1999) 1104–1151.
[113] D. Kaiser, M.A. Freyberg, P. Friedl, Lack of hemodynamic forces triggers apoptosis in vascular endothelial cells, Biochem. Biophys. Res. Commun. 231 (1997) 586–590, doi:10.1006/bbrc.1997.6146.
[114] P.F. Davies, Flow-Mediated Endothlial Mechanotransduction, Physiol. Rev. 75 (1995).
[115] S. Chien, Mechanotransduction and endothelial cell homeostasis: The wisdom of the cell, Am. J. Physiol. Heart Circulat. Physiol. (2007) 292, doi:10.1152/ajpheart.01047.2006.
[116] M.L. Kutys, C.S. Chen, Forces and mechanotransduction in 3D vascular biology, Curr. Opin. Cell Biol. 42 (2016) 73–79, doi:10.1016/j.ceb.2016.04.011.
[117] G.M. Rubanyi, The role of endothelium in cardiovascular homeostasis and diseases, J. Cardiovasc. Pharmacol. 22 (1993).
[118] Z.-D. Shi, J.M. Tarbell, Fluid flow mechanotransduction in vascular smooth muscle cells and fibroblasts, Ann. Biomed. Eng. (2011), doi:10.1007/s10439-011-0309-2.
[119] M. Peng, X. Liu, G. Xu, Extracellular vesicles as messengers in atherosclerosis, J. Cardiovasc. Translat. Res. 13 (2020) 121–130, doi:10.1007/s12265-019-09923-z.
[120] S. Kourembanas, T. Morita, Y. Liu, H. Christou, Mechanisms by which oxygen regulates gene expression and cell-cell interaction in the vasculature, Kidney Int. 51 (1997) 438–443, doi:10.1038/ki.1997.58.
[121] J. Edlin, P. Youssefi, R. Bilkhu, C.A. Figueroa, R. Morgan, J. Nowell, M. Jahangiri, Haemodynamic assessment of bicuspid aortic valve aortopathy: A systematic review of the current literature, Eur. J. Cardio-Thorac. Surg. 55 (2019) 610–617, doi:10.1093/ejcts/ezy312.
[122] M.A. Gimbrone Jr., G. García-Cardeña, Vascular endothelium, hemodynamics, and the pathobiology of atherosclerosis, Cardiovasc. Pathol. 22 (2013) 9–15, doi:10.1016/j.carpath.2012.06.006.
[123] V. Peiffer, S.J. Sherwin, P.D. Weinberg, Does low and oscillatory wall shear stress correlate spatially with early atherosclerosis? A systematic review, Cardiovasc. Res. 99 (2013) 242–250, doi:10.1093/cvr/cvt044.
[124] Y. Zhang, X. He, X. Chen, H. Ma, D. Liu, J. Luo, Z. Du, Y. Jin, Y. Xiong, J. He, D. Fang, K. Wang, W.E. Lawson, J.C.K. Hui, Z. Zheng, G. Wu, Enhanced external counterpulsation inhibits intimal hyperplasia by modifying shear stress-responsive gene expression in hypercholesterolemic pigs, Circulation 116 (2007) 526–534, doi:10.1161/CIRCULATIONAHA.106.647248.
[125] M.D. Hope, T.A. Hope, A.K. Meadows, K.G. Ordovas, T.H. Urbania, M.T. Alley, C.B. Higgins, Bicuspid aortic valve: Four-dimensional MR evaluation of ascending aortic systolic flow patterns, Radiology 255 (2010) 53–61, doi:10.1148/radiol.09091437.
[126] L. Dux-Santoy, A. Guala, G. Teixido-Tura, A. Ruiz-Munoz, G. Maldonado, N. Villalva, L. Galian, F. Valente, L. Gutierrez, T. Gonzalez-Alujas, A. Sao-Aviles, K. M. Johnson, O. Wieben, M. Huguet, D. Garcia-Dorado, A. Evangelista, J. F. Rodriguez-Palomares, Increased rotational flow in the proximal aortic arch is associated with its dilation in bicuspid aortic valve disease, Eur. Heart J. Cardiovasc. Imaging 20 (2019) 1407–1417.
[127] M.M. Bissell, A.T. Hess, L. Biasiolli, S.J. Glaze, M. Loudon, A. Pitcher, A. Davis, B. Prendergast, M. Markl, A.J. Barker, others, Aortic dilation in bicuspid aortic valve disease: flow pattern is a major contributor and differs with valve fusion type, Circulat. Cardiovasc. Imaging. 6 (2013).
[128] P. van Ooij, M. Markl, J.D. Collins, J.C. Carr, C. Rigsby, R.O. Bonow, S.C. Malaisrie, P.M. McCarthy, P.W.M. Fedak, A.J. Barker, Aortic valve stenosis alters expression of regional aortic wall shear stress: New insights from a 4-dimensional flow magnetic resonance imaging study of 571 subjects, J. Am. Heart Assoc. (2017) 6, doi:10.1161/JAHA.117.005959.
[129] D.M. Wang, J.M. Tarbell, Modeling interstitial flow in an artery wall allows estimation of wall shear stress on smooth muscle cells, J. Biomech. Eng. 117 (2008) 358, doi:10.1115/1.2794192.
[130] H.W. Sill, Y.S. Chang, J.R. Artman, J.A. Frangos, T.M. Hollis, J.M. Tarbell, Shear stress increases hydraulic conductivity of cultured endothelial monolayers, Am. J. Physiol. 268 (1995) H535–543.
[131] S.v. Lopez-Quintero, R. Amaya, M. Pahakis, J.M. Tarbell, The endothelial glycocalyx mediates shear-induced changes in hydraulic conductivity, Am. J. Physiol. Heart Circulat. Physiol. 296 (2009) 1451–1456, doi:10.1152/ajpheart.00894.2008.
[132] T.G. Papaioannou, C. Stefanadis, Vascular wall shear stress: Basic principles and methods, Hellenic J. Cardiol. 46 (2005) 9–15.
[133] S. Petersson, P. Dyverfeldt, T. Ebbers, Assessment of the accuracy of MRI wall shear stress estimation using numerical simulations, J. Magnet. Resonan. Imaging 36 (2012) 128–138, doi:10.1002/jmri.23610.
[134] M. Markl, P.J. Kilner, T. Ebbers, Comprehensive 4D velocity mapping of the heart and great vessels by cardiovascular magnetic resonance, J. Cardiovasc. Magnet. Resonan. 13 (2011) 1–22 http://www.doaj.org/doaj?func=abstract&id=704300.
[135] F. Donati, S. Myerson, M.M. Bissell, N.P. Smith, S. Neubauer, M.J. Monaghan, D.A. Nordsletten, P. Lamata, Beyond Bernoulli: Improving the accuracy and precision of noninvasive estimation of peak pressure drops, Circulat. Cardiovasc. Imaging (2017), doi:10.1161/CIRCIMAGING.116.005207.
[136] M.H.W. Chin, M.D.A. Norman, E. Gentleman, M.-O. Coppens, R.M. Day, A hydrogel-integrated culture device to interrogate T cell activation with physicochemical cues, ACS Appl. Mater. Interfaces 12 (42) (2020) 47355–47367, doi:10.1021/acsami.0c16478.
[137] K.M. Gray, K.M. Stroka, Vascular endothelial cell mechanosensing: New insights gained from biomimetic microfluidic models, Semin. Cell Dev. Biol. 71 (2017) 106–117, doi:10.1016/j.semcdb.2017.06.002.
[138] Y.-H.V.Ma, K.Middleton, L.You, Y.Sun, A review of microfluidic approaches for investigating cancer extravasation during metastasis, Microsystems & Nanoengineering. 4 (2018) 1-13. 10.1038/micronano.2017.104.
[139] M.L. Moya, Y.-H. Hsu, A.P. Lee, C.W.H. Christopher, S.C. George, In vitro perfused human capillary networks, Tissue Eng. Part C Methods 19 (2013) 730–737, doi:10.1089/ten.tec.2012.0430.
[140] L.A. Low, D.A. Tagle, Tissue chips-innovative tools for drug development and disease modeling, Lab on a Chip 17 (2017) 3026–3036, doi:10.1039/c7lc00462a.
[141] R. Passier, V. Orlova, C. Mummery, Complex tissue and disease modeling using hiPSCs, Cell Stem Cell 18 (2016) 309–321, doi:10.1016/j.stem.2016.02.011.
[142] A.D. van der Meer, V. v. Orlova, P. ten Dijke, A. van den Berg, C.L. Mummery, Three-dimensional co-cultures of human endothelial cells and embryonic stem cell-derived pericytes inside a microfluidic device, Lab on a Chip (2013), doi:10.1039/c3lc50435b.
[143] X. Wang, D.T.T. Phan, A. Sobrino, S.C. George, C.C.W. Hughes, A.P. Lee, Engineering anastomosis between living capillary networks and endothelial cell-lined microfluidic channels, Lab on a Chip 16 (2016) 282–290, doi:10.1039/c5lc01050k.
[144] A. Sobrino, D.T.T. Phan, R. Datta, X. Wang, S.J. Hachey, M. Romero-López, E. Gratton, A.P. Lee, S.C. George, C.C.W. Hughes, 3D microtumors in vitro supported by perfused vascular networks, Sci. Rep. 6 (2016) 1–11, doi:10.1038/srep31589.
[145] D.T.T. Phan, X. Wang, B.M. Craver, A. Sobrino, D. Zhao, J.C. Chen, L.Y.N. Lee, S.C. George, A.P. Lee, C.C.W. Hughes, A vascularized and perfused organ-on-a-chip platform for large-scale drug screening applications, Lab on a Chip 17 (2017) 511–520, doi:10.1039/c6lc01422d.
[146] B. Strilic, S. Offermanns, Intravascular survival and extravasation of tumor cells, Cancer Cell 32 (2017) 282–293, doi:10.1016/j.ccell.2017.07.001.
[147] G.P. Gupta, J. Massagué, Cancer Metastasis: Building a Framework, Cell 127 (2006) 679–695, doi:10.1016/j.cell.2006.11.001.
[148] S. Bersini, J.S. Jeon, G. Dubini, C. Arrigoni, S. Chung, J.L. Charest, M. Moretti, R.D. Kamm, A microfluidic 3D invitro model for specificity of breast can-

cer metastasis to bone, Biomaterials 35 (2014) 2454–2461, doi:10.1016/j.biomaterials.2013.11.050.
[149] J.S. Jeon, S. Bersini, M. Gilardi, G. Dubini, J.L. Charest, M. Moretti, R.D. Kamm, Human 3D vascularized organotypic microfluidic assays to study breast cancer cell extravasation (Proc Natl Acad Sci USA (2015) 112:1, 214–219, doi:10.1073/pnas.1501426112.
[150] J.S. Jeon, S. Bersini, J.A. Whisler, M.B. Chen, G. Dubini, J.L. Charest, M. Moretti, R.D. Kamm, Generation of 3D functional microvascular networks with human mesenchymal stem cells in microfluidic systems, Integrat. Biol. 6 (2014) 555–563 United Kingdom, doi:10.1039/c3ib40267c.
[151] A. Dardik, L. Chen, J. Frattini, H. Asada, F. Aziz, F.A. Kudo, B.E. Sumpio, Differential effects of orbital and laminar shear stress on endothelial cells, J. Vasc. Surg. 41 (2005) 869–880, doi:10.1016/j.jvs.2005.01.020.
[152] J.S. Garanich, M. Pahakis, J.M. Tarbell, Shear stress inhibits smooth muscle cell migration via nitric oxide-mediated downregulation of matrix metalloproteinase-2 activity, Am. J. Physiol. Heart Circulat. Physiol. 288 (2005) H2244–H2252, doi:10.1152/ajpheart.00428.2003.
[153] H. Ueba, M. Kawakami, T. Yaginuma, Shear stress as an inhibitor of vascular smooth muscle cell proliferation arteriosclerosis, Arterioscler. Thromb. Vasc. Biol. 17 (1997) 1512–1516, doi:10.1161/01.ATV.17.8.1512.
[154] C.F. Dewey Jr., S.R. Bussolari, M.A. Gimbrone Jr., P.F. Davies, The dynamic response of vascular endothelial cells to fluid shear stress, J. Biomech. Eng. 103 (1981) 177–185, doi:10.1115/1.3138276.
[155] D.N. Rhoads, S.G. Eskin, L.V. McIntire, Fluid flow releases fibroblast growth factor-2 from human aortic smooth muscle cells, Arterioscler. Thromb. Vasc. Biol. 20 (2000) 416–421.
[156] H. Ueba, M. Kawakami, T. Yuginuma, Shear stress as an inhibitor of vascular smooth muscle cell proliferation role of transforming growth factor-$\beta$1 and tissue-type plasminogen activator, Arterioscler. Thromb. Vasc. Biol. 17 (1997) 1512–1516.
[157] J.S. Garanich, M. Pahakis, J.M. Tarbell, Shear stress inhibits smooth muscle cell migration via nitric oxide-mediated downregulation of matrix metalloproteinase-2 activity, Am. J. Physiol. Heart Circulat. Physiol. 288 (2005) 2244–2252, doi:10.1152/ajpheart.00428.2003.
[158] R. Estrada, G.A. Giridharan, M.-D. Nguyen, T.J. Roussel, M. Shakeri, V. Parichehreh, S.D. Prabhu, P. Sethu, Endothelial cell culture model for replication of physiological profiles of pressure, flow, stretch, and shear stress in vitro, Anal. Chem. 83 (2011) 3170–3177, doi:10.1021/ac2002998.
[159] V. Rizzo, Enhanced interstitial flow as a contributing factor in neointima formation: (Shear) stressing vascular wall cell types other than the endothelium, Am. J. Physiol. Heart Circulat. Physiol. 297 (2009) 1196–1197, doi:10.1152/ajpheart.00499.2009.
[160] M.D. Lavender, Z. Pang, C.S. Wallace, L.E. Niklason, G.A. Truskey, A system for the direct co-culture of endothelium on smooth muscle cells, Biomaterials 26 (2005) 4642–4653, doi:10.1016/j.biomaterials.2004.11.045.
[161] C. Williams, T.M. Wick, Endothelial cell-smooth muscle cell co-culture in a perfusion bioreactor system, Ann. Biomed. Eng. 33 (2005) 920–928, doi:10.1007/s10439-005-3238-0.
[162] F. Zhao, R. Chella, T. Ma, Effects of shear stress on 3-D human mesenchymal stem cell construct development in a perfusion bioreactor system: Experiments and hydrodynamic modeling, Biotech. Bioeng. (2007), doi:10.1002/bit.21184.
[163] S.I. Jeong, J.H. Kwon, J.I. Lim, S.-W. Cho, Y. Jung, W.J. Sung, S.H. Kim, Y.H. Kim, Y.M. Lee, B.-S. Kim, C.Y. Choi, S.-J. Kim, Mechano-active tissue engineering of vascular smooth muscle using pulsatile perfusion bioreactors and elastic PLCL scaffolds, Biomaterials (2005), doi:10.1016/j.biomaterials.2004.04.036.
[164] S. Shinohara, T. Kihara, S. Sakai, M. Matsusaki, M. Akashi, M. Taya, J. Miyake, Fabrication of in vitro three-dimensional multilayered blood vessel model using human endothelial and smooth muscle cells and high-strength PEG hydrogel, J. Biosci. Bioeng. 116 (2013) 231–234, doi:10.1016/j.jbiosc.2013.02.013.
[165] E.E. van Haaften, T.B. Wissing, M.C.M. Rutten, J.A. Bulsink, K. Gashi, M.A.J. van Kelle, A.I.P.M. Smits, C.V.C. Bouten, N.A. Kurniawan, Decoupling the effect of shear stress and stretch on tissue growth and remodeling in a vascular graft, Tissue Eng. Part C Methods 24 (2018) 418–429, doi:10.1089/ten.tec.2018.0104.
[166] U. Blache, M.M. Stevens, E. Gentleman, Harnessing the secreted extracellular matrix to engineer tissues, Nat. Biomed. Eng. 4 (2020) 357–363, doi:10.1038/s41551-019-0500-6.
[167] S.A. Ferreira, M.S. Motwani, P.A. Faull, A.J. Seymour, T.T.L. Yu, M. Enayati, D.K. Taheem, C. Salzlechner, T. Haghighi, E.M. Kania, O.P. Oommen, T. Ahmed, S. Loaiza, K. Parzych, F. Dazzi, O.P. Varghese, F. Festy, A.E. Grigoriadis, H.W. Auner, A.P. Snijders, L. Bozec, E. Gentleman, Bi-directional cell-pericellular matrix interactions direct stem cell fate, Nat. Commun. 9 (2018) 1–12, doi:10.1038/s41467-018-06183-4.
[168] R.H. Coy, O.R. Evans, J.B. Phillips, R.J. Shipley, An integrated theoretical-experimental approach to accelerate translational tissue engineering, J. Tissue Eng. Regenerat. Med. 12 (2018) e53–e59, doi:10.1002/term.2346.
[169] J. Corral-Acero, F. Margara, M. Marciniak, C. Rodero, F. Loncaric, Y. Feng, A. Gilbert, J.F. Fernandes, H.A. Bukhari, A. Wajdan, M.V. Martinez, M.S. Santos, M. Shamohammdi, H. Luo, P. Westphal, P. Leeson, P. DiAchille, V. Gurev, M. Mayr, L. Geris, P. Pathmanathan, T. Morrison, R. Cornelussen, F. Prinzen, T. Delhaas, A. Doltra, M. Sitges, E.J. Vigmond, E. Zacur, V. Grau, B. Rodriguez, E.W. Remme, S. Niederer, P. Mortier, K. McLeod, M. Potse, E. Pueyo, A. Bueno-Orovio, P. Lamata, The 'Digital Twin' to enable the vision of precision cardiology, Eur. Heart J. (2020) 1–11, doi:10.1093/eurheartj/ehaa159.
[170] A. Carusi, K. Burrage, B. Rodríguez, Bridging experiments, models and simulations: An integrative approach to validation in computational cardiac electrophysiology, Am. J. Physiol. Heart Circulat. Physiol. 303 (2012) 144–155, doi:10.1152/ajpheart.01151.2011.
[171] B. Talug, Z. Tokcaer-Keskin, Induced pluripotent stem cells in disease modelling and regeneration, Adv. Exp. Med. Biol. 1144 (2018) 91–99, doi:10.1007/5584_2018_290.
[172] Z.E. Clayton, S. Sadeghipour, S. Patel, Generating induced pluripotent stem cell derived endothelial cells and induced endothelial cells for cardiovascular disease modelling and therapeutic angiogenesis, Int. J. Cardiol. 197 (2015) 116–122, doi:10.1016/j.ijcard.2015.06.038.
[173] L. Atchison, H. Zhang, K. Cao, G.A. Truskey, A tissue engineered blood vessel model of Hutchinson-Gilford progeria syndrome using human iPSC-derived smooth muscle cells, Sci. Rep. 7 (2017) 1–12, doi:10.1038/s41598-017-08632-4.
[174] A.D. Ebert, P. Liang, J.C. Wu, Induced pluripotent stem cells as a disease modeling and drug screening platform, J. Cardiovasc. Pharmacol. 60 (2012) 408–416, doi:10.1097/FJC.0b013e318247f642.
[175] Y.K. Kurokawa, R.T. Yin, M.R. Shang, V.S. Shirure, M.L. Moya, S.C. George, Human induced pluripotent stem cell-derived endothelial cells for three-dimensional microphysiological systems, Tissue Eng. Part C Methods 23 (2017) 474–484, doi:10.1089/ten.tec.2017.0133.
[176] S.L. Natividad-Diaz, S. Browne, A.K. Jha, Z. Ma, S. Hossainy, Y.K. Kurokawa, S.C. George, K.E. Healy, A combined hiPSC-derived endothelial cell and in vitro microfluidic platform for assessing biomaterial-based angiogenesis, Biomaterials 194 (2019) 73–83, doi:10.1016/j.biomaterials.2018.11.032.
[177] A. Cochrane, H.J. Albers, R. Passier, C.L. Mummery, A. van den Berg, V.v. Orlova, A.D. van der Meer, Advanced in vitro models of vascular biology: Human induced pluripotent stem cells and organ-on-chip technology, Adv. Drug Deliv. Rev. 140 (2019) 68–77, doi:10.1016/j.addr.2018.06.007.
[178] J. Ribas, Y.S. Zhang, P.R. Pitrez, J. Leijten, M. Miscuglio, J. Rouwkema, M.R. Dokmeci, X. Nissan, L. Ferreira, A. Khademhosseini, Biomechanical strain exacerbates inflammation on a Progeria-on-a-Chip model, Small 13 (2017) 1–13, doi:10.1002/smll.201603737.
[179] K. Narsinh, K.H. Narsinh, J.C. Wu, Derivation of human induced pluripotent stem cells for cardiovascular disease modeling, Circulat. Res. 108 (2011) 1146–1156, doi:10.1161/CIRCRESAHA.111.240374.

# Chapter 2

# Hypotheses and Aims

The goal of this project was to build a model to determine the haemodynamic contribution to pathological remodelling of the vascular ECM. Our review paper highlights the paucity of research on mechanotransduction from interstitial flow and the importance of studying this on cells in 3D. Given the importance VSMCs have in maintaining the ECM of the medial wall and their fundamental role in aneurysm development we aimed to address this gap by developing a platform to interrogate the role if any of interstitial flow in VSMC-ECM remodelling and the wider implications for aneurysm development.

We hypothesised that fluid forces can modulate cellular behaviour in 3D *in-vitro* models of the vessel wall, stimulating the breakdown of ECM, leading to aneurysm-like behaviour. By extension we hypothesised that these models can then be used to highlight the contribution of pathological flow seen in BAV patients to aneurysm development. In particular we hypothesised that:

- Interstitial shearing forces on VSMCs are non negligible. Their impact on ECM remodelling can be recapitulated by encapsulating VSMCs in ECM mimicking hydrogels and exposing them to flow
- A significant amount of mechanotransduction-mediated ECM remodelling is independent of signalling between ECs and VSMCs and by extension, independent of luminal flow
- A proportion of ECM regulation failure can be stimulated by fluid stresses alone, independently of genetic contributions in BAV disease
- Thresholds of fluid stresses/gradients prompting pathological cell behaviour can be identified to help stratify patients for aneurysm risk in the future

To test these hypotheses, we aimed to develop a model combining 3D culture of VSMCs in ECM mimicking hydrogels combined with microfluidics to impart fluid stresses. Specifically we aimed to:

1. Determine a suitable biomaterial in which to encapsulate VSMCs cultures in 3D, characterising mass transport within the material, material degradability and permeability to flow

2. Develop a suitable static *in-vitro* baseline model to study VSCM cell ECM interaction exploring VSMC viability, ability to remodel their surrounding matrix and lay down newly synthesised proteins

3. Develop a method to include fluid flow mechanostimulation into these models using a microfluidics setup

## 2.1 Thesis Structure

There are 3 main areas of work in this thesis: characterising the biomaterial used to encapsulate cells in the model (Aim 1), developing the 3D culture of cells (Aim 2) and incorporating flow into the system (Aim 3). Chapters 3 and 4 of this thesis focus on Aim 1, with Chapter 3 characterising biomaterial degradability and permeability to flow and Chapter 4 focusing on predicting mass transport of molecules through the matrix. In Chapter 5 we introduce cell cultures into the model and explore the viability of primary VSMCs and their ability to remodel the biomaterial. Finally in Chapter 6, microfluidics systems to include flow into the model are introduced. The model as a whole is then discussed looking at limitations and areas for future work.

# Chapter 3

# PEG-peptide Hydrogel Characterisation: Exploring Degradability and Permeability

## Chapter Abstract

**Background**: To develop a reductionist *in-vitro* model of vascular cell ECM remodelling, a hydrogel with encapsulated cells can be used in place of tissue samples. For the specific purposes of studying cell-matrix interactions in the presence of flow, the hydrogel at baseline needs to be degradable by cells, be permeable to flow and allow for effective mass transport to and from cells. The first two chapters of this thesis serve to characterise these properties of the selected hydrogel before cell cultures are introduced.

**Aim**: The aim of this first chapter is to present the synthetic PEG-peptide hydrogel chemistry, assess the hydrogel degradation behaviour and ascertain the hydrogel's Darcy permeability.

**Methods**: Hydrogel degradability was assessed in the presence of exogenous MMPs 1 and 9 by incubating samples of different percentages of degradable cross-links with MMPs in solution and measuring the concentration over time of the tryptophan group found on cleaved peptide fragments. Permeability was assessed using two separate methods to track flow through the hydrogel under pressure: particle tracking velocimetry (PTV) and Micro Electro-Mechanical System (MEMS) based pressure measurements. Permeabilities of hydrogels of different polymer contents were made as well as measurements at different pressures.

**Results**: Hydrogels with greater numbers of cleavable cross-links were degraded at a faster rate in the presence of MMPs. Both PVT and MEMS methods proved to be suitable for measuring hydrogel permeability which was found to be on the order of $10^{-16}\mathrm{m}^2$. Permeability decreased with increasing applied pressure.

**Conclusion**: The data in this chapter confirms that degradability of the PEG-peptide hydrogel can be altered by changing the number of MMP-cleavable cross-links. Furthermore, the methods presented show 2 suitable assays for measuring the permeability of relatively impermeable hydrogels. Permeability of different hydrogels can be assessed to predict the flow velocities through the matrix under known applied pressured.

## 3.1 Introduction

To create our 3D reductionist *in-vitro* model, a biomaterial is used to encapsulate cells in lieu of using tissue samples. As previously described in Chapter 1, this allows us to reduce the complexity of our models and study independently how specific cues impact cellular behaviours by stripping back the multitude of factors at play *in-vivo*. Hydrogels are suitable materials for this purpose due to their dual phase nature: a cross-linked solid polymer phase mimicking the ECM and the liquid phase in between available for mass transport. Synthetic hydrogels in particular offer a high degree of control over the chemical and mechanical environment, compared to their naturally derived counterparts. Parameters can be individually tuned thus making these hydrogels highly amenable for mechanotransduction studies.

For our *in-vitro* model we chose to use a fully synthetic poly(ethylene glycol) (PEG) hydrogel cross-linked with bioactive peptides, hereon in referred to as the PEG-peptide hydrogel system. The PEG-peptide system has been extensively described and characterised in two publications from our lab. This hydrogel was first published with by Jowett et al where it was used to study the impact of ILC1 immune cells on ECM remodelling by intestinal organoids and the consequences for inflammatory bowel disease. Some of the work presented in this chapter contributed to the hydrogel characterisation section of that paper. The hydrogel is further characterised in the publication in Chapter 4 [Lust et al., 2021a]. Information on the hydrogel is reproduced here for clarity but some of the detail is omitted for the sake of avoiding repetition. This hydrogel's chemistry was previously developed before the work of this thesis by previous lab group members. All the work presented here is characterising the material properties or using the system for *in-vitro* culture.

Synthetic hydrogels without modification to include bioactive peptides are not hospitable to cells. Traditionally introducing bioactive motifs is not trivial and can often lead to defects in the hydrogel. The main method for incorporating peptides into hydrogels is by cross-linking peptides with cysteine groups on both ends to PEG macromers with alkene-containing groups on the end of the PEG macromer arm. Since both ends of the peptide can indiscriminately react with any end of the PEG macromer, this can lead to defects due to primary loops (in which both ends of the peptide react to the same PEG thus not contributing to the cross-linking of the overall system) or dangling PEG ends which have not been reacted with. These inhomogeneities are detrimental to the cross-linking efficiency, thus increasing the amount of polymer needed in order to achieve hydrogel formation. They also introduce unknown defects into the system reducing reproducibility and the degree to which it can be represented by theoretical estimates with assumed homogeneous properties. To overcome this in our system, peptides have differently reacting ends and are first reacted with a four-arm 10 kDa PEG-NPC (JenKem Technology, USA) to form PEG–peptide conjugates as shown in Figure 3.1. This is then mixed with a 10 or 20 kDa PEG tetramer with

a vinyl-sulphone end group (JenKem Technology, USA) to form the hydrogel network. Each end of the peptide can only react with either the NPC or VS group. This two stage cross-linking has been shown to reduce the number of defects within the system, thus allowing hydrogels at polymer solid contents as low as 2% weight/volume (W/V) to form [Jowett et al., 2021]. In our system we have 3 peptides which can be cross-linked into the hydrogel: a non functional peptide Ac-KDW-ERC-NH2, an RGD based adhesive peptide, (RGDSGD)K–GDQGIAGF–ERC–NH2) and an MMP cleavable sequence DEG (Ac–GRDSGK–GPQGIWGQ–ERC–NH2). These are referred to from hereon in as non-functional, adhesive and degradable respectively. All peptides are custom synthesised by Peptide Protein Research, Ltd. (UK),> 98% purity. Stiffness of the hydrogel is altered by altering the total number of PEG macromers (VS and conjugate) in the reaction thus altering the polymer solid content. The properties of the hydrogel are altered by changing the proportion of conjugates with adhesive, degradable or non-functional peptides. Each conjugate has the same peptide on all 4 arms and the ratio of each conjugate type is then changed. The non-functional peptide serves to act as a "filler" peptide which makes a cross-link without changing the bioactivity. Thus for the same number of cross-links (polymer content), degradability or adhesiveness can be altered meaning these properties can be independently tuned from stiffness. Full details of the chemistry are provided in Chapter 4.

For our purpose of using this biomaterial to study vascular cell-ECM interaction in the presence of interstitial flow, the following criteria need to be met:

- Allow for active transport of nutrients and other molecules to and from encapsulated cells (this is addressed in Chapter 4)
- Allow cell mediated degradability ie for hydrogel cross-links to be MMP cleavable
- Allow flow to be passed through the material around 3D encapsulated cells ie to be permeable
- Support long-term culture of encapsulated vascular cells (this is addressed in Chapter 5)

For the work in [Jowett et al., 2021] we characterised the degradation behaviour of the hydrogel in the presence of exogenous MMPs and this work is reproduced for this thesis in this chapter. The bulk of the work in this chapter however, relates to assessing hydrogel permeability which as it turns out was very challenging to characterise.

### 3.1.1 Hydrogel Permeability

In the aim of delivering fluid cues to embedded cells, the mechanics of flow moving through the hydrogel needs to be considered. Indeed the way in which fluid can move through the matrix inpacts the mechanical forces imparted, internal pressures in the structure, as well as affecting mass transport to and from embedded cells. Darcy permeability ($\kappa$) referred to simply as permeability

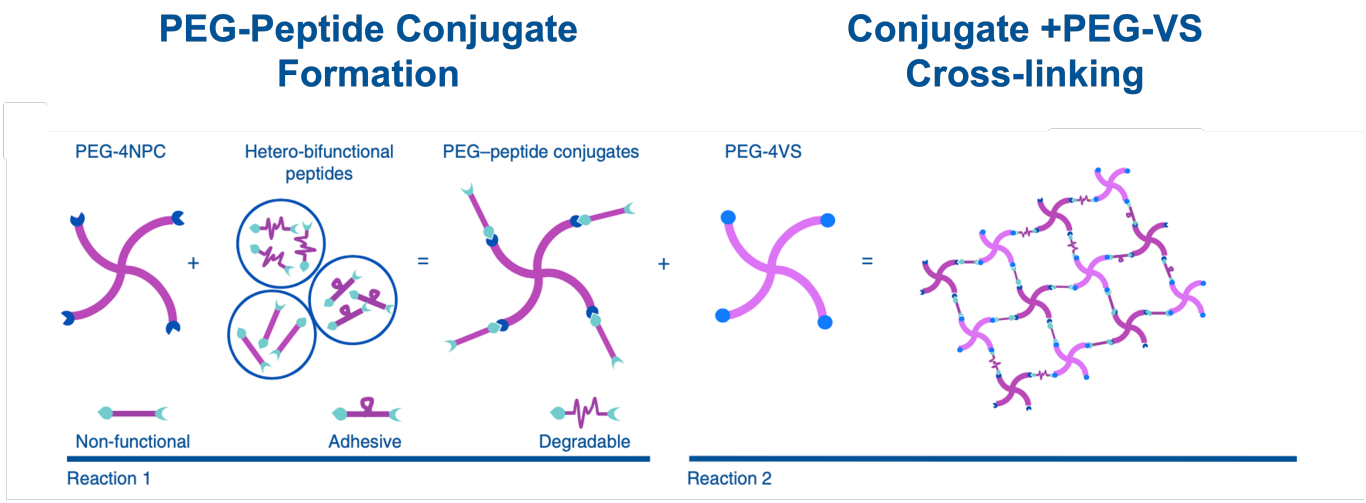


Figure 3.1: Diagram showing the 2 stage reaction used to form the PEG-peptide hydrogel system. PEG-4NPC is first conjugated with degradable, adhesive or non-functional peptides to form a peg-peptide conjugate. This conjugate is then reacted at 1:1 ratio with PEG-4VS. This image is reproduced from [Jowett et al., 2021] and credit is given to G. Jowett.

hereon in, is a macroscopic property used to characterise this fluid movement and is defined as the ease with which a porous material can transmit flow through it [Dias et al., 2012]. It is affected by the degree of free space in the material (porosity or void volume fraction), as well as the orientation and inter-connectivity of these spaces (tortuosity) [Dias et al., 2012]. In essence, the structure of the material is as important as how much free space there is for flow to get through, meaning a highly porous material is not necessarily a highly permeable one. Independently assessing hydrogel porosity and tortuosity can be challenging and unreliable due to limitations in measurement techniques [Chor and Li, 2006]. Furthermore estimates of these parameters have lead to incorrect conclusions where more porous scaffolds were expected to allow easier mass transport within the hydrogel but did not [Chor and Li, 2006]. To overcome this, techniques have been developed to measure permeability directly. Darcy's law states that the rate of flow through a material is proportional to the applied pressure across it given by:

$$Q = \frac{\kappa A}{\mu L} \triangle P, \tag{3.1}$$

where $Q$ is the volumetric flow rate through the material (in $m^3/s$), A is the cross-sectional area of the material in the direction of flow (in $m^2$), L is the length of the material in the direction of flow (in m), $\mu$ is the dynamic viscosity of the fluid (in Pa·s), $\triangle P$ is the pressure gradient applied (in Pa) and $\kappa$ the material permeability (in $m^2$).

The most direct way to measure permeability is to apply a pressure across a known volume of material and measure the flow rate of the fluid coming out. There are 2 main ways to apply pressure to the material: using a pump or hydro-static pressure [Pennella et al., 2013]. In

the former, a peristaltic or constant pressure pump is connected to a reservoir via tubing and then this is connected to a chamber containing the material through which the flow must pass [Ochoa et al., 2009, Wang and Tarbell, 2000, Truscello et al., 2012, Shimko and Nauman, 2007].

In hydrostatic pressure setups, instead of using a pump, a static head of water is used to generate pressure [Bagarello et al., 2004, Sanz-Herrera et al., 2008, Shimko et al., 2005]. The hydrostatic pressure is given by:

$$P = \rho g H, \tag{3.2}$$

where $\rho$ is the density of the fluid (in kg/m$^2$), g is the acceleration due to gravity (in m/s$^2$) and h the height of the column of fluid (in m).

In order to measure permeability with these techniques, the applied pressure and the flow rate of liquid through the material need to be accurately measured. Applied pressure is usually ascertained by measuring the pressure differential either side of the material using a pressure gauge. The more challenging aspect is measuring the rate of the resultant flows. With highly permeable materials, lower pressures can be applied to achieve large flow rates which can easily be measured by for example collecting the fluid volume over a set period of time as in [Shimko et al., 2005]. However in the case where slower flows need to be detected, alternative methods are required. In [Wang and Tarbell, 2000], Wang et al measure flow rate by tracking the movement of an airbubble positioned in the tubing after the material using a spectro-photometer to record the displacement of the bubble over time. Another possible method is to infer the volumetric flow rate by measuring the pressure increase caused by this displacement into a closed cavity using a pressure gauge as in [Cacheux et al., 2022]

Estimates of hydrogel permeability can also be obtained by using theoretical relationships between properties of the material microstructure such as porosity, to permeability itself as in [Dias et al., 2012, Sanz-Herrera et al., 2008]. The microstructure characteristics are either assumed from theoretical estimates or experimental values can be obtained by imaging the material microstructure. This is usually achieved using micro computed tomography ($\mu$CT) [Pennella et al., 2013]. The structure of the material is reconstructed from images and then simulations are run to resolve for unknown parameters [Sanz-Herrera et al., 2008]. These simulations use numerical methods for geometries for which equations cannot analytically be resolved, by descretising the total geometry into simpler volumes. More details on these methods are given in Chapter 6.

Although estimates based on these imaging techniques have been shown to be capable of faithfully capturing permeability compared to direct methods for materials such as Sponceram (a ceramic) in [Sanz-Herrera et al., 2008], capturing the necessary data to use these methods remain a challenge with hydrogels. The preparation involved for $\mu$CT likely de-

forms or alters the hydrogel microstructure during freeze-drying steps [Rahman et al., 2013, Dušková-Smrčková et al., 2021] although advances are being made to address these issues [Varley et al., 2016, Offeddu et al., 2016]. We therefore decided to measure permeability directly.

In this chapter we present 2 separate methods we used to determine the permeability of our PEG-peptide hydrogel system and discuss why some other methods were unsuccessful.

### 3.1.2 Chapter Aims

The data in this chapter address Aim 1: assessing the suitability of the PEG-peptide hydrogel system to study cell-mediated remodelling. The specific aims of this chapter were to:

- Assess hydrogel degradation behaviour
- Determine the permeability of the hydrogel to flow

## 3.2 Methods

### 3.2.1 Hydrogel Synthesis

The PEG-peptide hydrogel is formed by reacting PEG-peptide conjugates with the desired peptides with a 10 or 20 kDa PEG tetramer with a vinyl-sulphone (PEG-VS) end group (JenKem Technology, USA) in a 1-1 ratio. Both the PEG-VS and PEG conjugate components are first dissolved to the correct concentration in basic HEPES buffer (30 mM PH8) to favour the cross-linking reaction before both solutions are mixed thoroughly to allow homogeneous cross-linking. The peptide sequences in the conjugates have a thiol containing cysteine group on their ends and thus when mixed in hepes, free negative ions in the buffer can accept protons from the thiol group which is then negatively charged. This group is then able to react with the VS group on the second PEG through nucleophilic substitution (Michael type addition).

Samples are then incubated at 37°C for 45 mins to fully form before media or PBS is added around the hydrogels to keep them hydrated. All cross-linking is performed with low protein binding tips and eppendorf tubes to minimise loses. This is important as hydrogels of relatively low polymer content are made (down to 2% W/V) and thus maximum retention is needed. The required mass of each PEG component is calculated by considering the total desired polymer solid content for a particular volume of hydrogel. To simplify this process, as part of this PhD project a MATLAB script was written which computes the required masses by first asking the user to specify the total volume of hydrogel to be made, the polymer content of the hydrogel, and the ratio of peptides desired. A "recipe" is then printed with the correct masses and volumes in which to dissolve the respective components. This MATLAB code is given in Appendix 3.6.

Before hydrogels can be formed, the PEG-peptide conjugates are made in a 2-day conjugation process. Peptide salts provided by the manufacturer are designed with a lysine group at one end and a cysteine group at the other. The primary amine in the lysine group is protected by a trifluoroacetic acid (TFA) group. The peptides are then first dissolved in DMSO and mixed with triethylamine (TEA) which through an acid-base reaction removes the TFA group to expose the primary amine. A PEG tetramer with nitrophenyl carbonate (NPC) end groups are added to the peptide DMSO solution at a molar ratio of 12:1 for the non functional peptide, 8:1 for the adhesive peptide and 10:1 for the degradable sequence. These molarities have been optimised for the highest conjugation efficiency tested using size exclusion chromatography to determine the proportion of modified arms on the PEG tetramer previously by T. T. L. Yu. The PEG-NPC is added drop-wise to ensure the peptide is in excess compared to the PEG to further maximise conjugation efficiency. In this reaction, the NPC group on the PEG NPC is replaced by the peptide through nucleophilic substitution in which the primary amine on the peptide lysine conjugates attaches to the exposed carbon on the PEG where the NPC group was cleaved off. Free NPC and DMSO are removed by liophilisation.

The conjugates are then purified to remove any unreacted PEG-NPC before being aliquoted, snap frozen and lyophilised prior to storage at $-20°C$. Quality control on each batch is performed by first estimating the amount of peptide conjugated using the nanodrop and quantifying the available free thiol groups using Elmmans reagent assay. In this assay 5,5-Dithiobis(2-nitrobenzoic acid) (DTNB) reacts with free thiols to produce a measurable yellow product whose quantity is assessed using a plate reader to measure sample absorption at 412 nm. The details of this protocol are also given in [Jowett et al., 2021]. This protocol was established before the work in this PhD and thus other than some minor optimisation, the steps were only reproduced here to generate conjugates.

### 3.2.2 Assessing hydrogel degradability

Our hydrogel system is designed to allow encapsulated cells to break down degradable cross-links via MMP secretion. This degradable sequence contains a tryptophan, which can be detected using absorbance measurements at 280 nm. Therefore we developed an assay to measure hydrogel degradation through tryptophan release.

Thirty $\mu$L hydrogels were cast at the bottom of 96 well plates and once formed were topped up with PBS and allowed to swell for 24 hrs. Subsequently the PBS was replaced with either 84.6 nM human recombinant MMP1 (Abcam 124850) or 89.5-nM human MMP9 (Sigma SAE0078) in Tris Buffer (50 mM Tris, 100 mM NaCl, 10 mM CaCl2, at pH 7.5). The salts in the buffer help to maintain the activity of the MMP enzyme in solution. These concentrations of MMPs were decided on after trial incubations to determine concentrations which would lead to a degradation time scale that was fast enough to be captured in a reasonable time but at a slow enough rate so that the precise degradation profile could be obtained. At regular time intervals, 30 $\mu$L samples of solution were taken from above each sample. The solution was thoroughly pipetted to ensure homogenous concentration of tryptophan groups and disrupt any clumps whilst ensuring to do this gently to avoid breaking up the degrading hydrogel. The 30 $\mu$L was then transferred to a UV vis plate and the tryptophan absorption was measured on a plate reader (BMG Labtech CLARIOstar) at discreet wavelength of 280 nm and normalised to buffer alone (with MMP) . The solution was then transferred back to the hydrogel samples. We tested 2.5% W/V hydrogels of varying degradability using 0, 25, 45, 75 or 100% of PEG-peptide conjugates containing a degradable sequence (all other cross-links formed using non-functional peptides). This work was conducted for the publication of [Jowett et al., 2021] and was done in collaboration with M. Norman and D. Marciano. The work was divided equally.

### 3.2.3 Particle Tracking Velocimetry - Collaboration with the Ecole Polytechnique

This work was conducted as a collaboration with C. Desalles from the Ecole Polytechnique and the work was divided evenly. A commercially available microfluidics chip (Ibidi $\mu$-Slide VI 0.4) was filled with hydrogel to create a 30 $\mu$L solid channel of hydrogel (17 mm $\times$ 3.8 mm $\times$ 0.4 mm) and connected to another empty identical channel. These were then connected to a reservoir containing a suspension of 1 $\mu$m diameter beads (Polysciences Fluoresbrite ®YG Microspheres) at a density of $4.55\times10^8$ beads/ml. The suspension was driven through the channels by a compressor which can generate up to 2 Bar of pressure (Fluigent Microfluidic Low Pressure Generator FLPG Plus) and a pressure controller (Fluigent Microfluidic flow controller Flow E$^{TM}$). The empty channel before the hydrogel was used in order to easily image the beads moving. The setup is shown in Figure 3.2. The empty channel was placed under the microscope at 20X magnification and 30 second videos of 2 images/second were taken for flows through the channel. Videos of bead movement were analysed using the Trackmate interface in ImageJ [Ershov et al., 2022]. The simple LAP tracker was used with a max distance linking 2 particles of 15 $\mu$m and a gap closing distance of 5 $\mu$m if particles are lost from one frame to the next. Beads were automatically segmented using the DoG detector with a particle diameter of 2 $\mu$m. Tracks were then imported into MATLAB and analysed using the written script in Appendix 3.7. Flow rates were calculated only considering the x-displacement of each bead and dividing over the recording time, from which then permeability can be calculated using the applied pressure as in Equation 3.1. Recordings were made for flow through hydrogels at different applied pressures.

### 3.2.4 MEMS Based Pressure Sensor Method - Collaboration with the University of Tokyo

Whilst the PTV method yielded good results for determining hydrogel permeability as discussed in the results section, we wanted to confirm our readings using an alternative method. Furthermore, for reasons which are discussed later in this chapter, certain limitations with the PTV method meant we wanted to use a technique with a a potentially higher degree of precision in order to be able to measure small changes in permeability. A postdoc in the Matsunaga lab at the University of Tokyo, J. Cacheux, had developed a permeability assay using a pressurised closed cavity to precisely determine hydrogel permeability [Cacheux et al., 2023]. With this method, permeability is estimated by determining the volume passed through the hydrogel as the increase of pressure caused by the entry of this flow into a closed chamber. The device was setup as shown in Panel A and C of Figure 3.3. Pressure measurements are made using a Micro Electro-Mechanical System (MEMS) based pressure sensor. The chip shown in Panel A of Figure 3.3 is connected to a pressure controller (Fluigent MFCS) to control the flow passing through the hydrogel sample. The closed

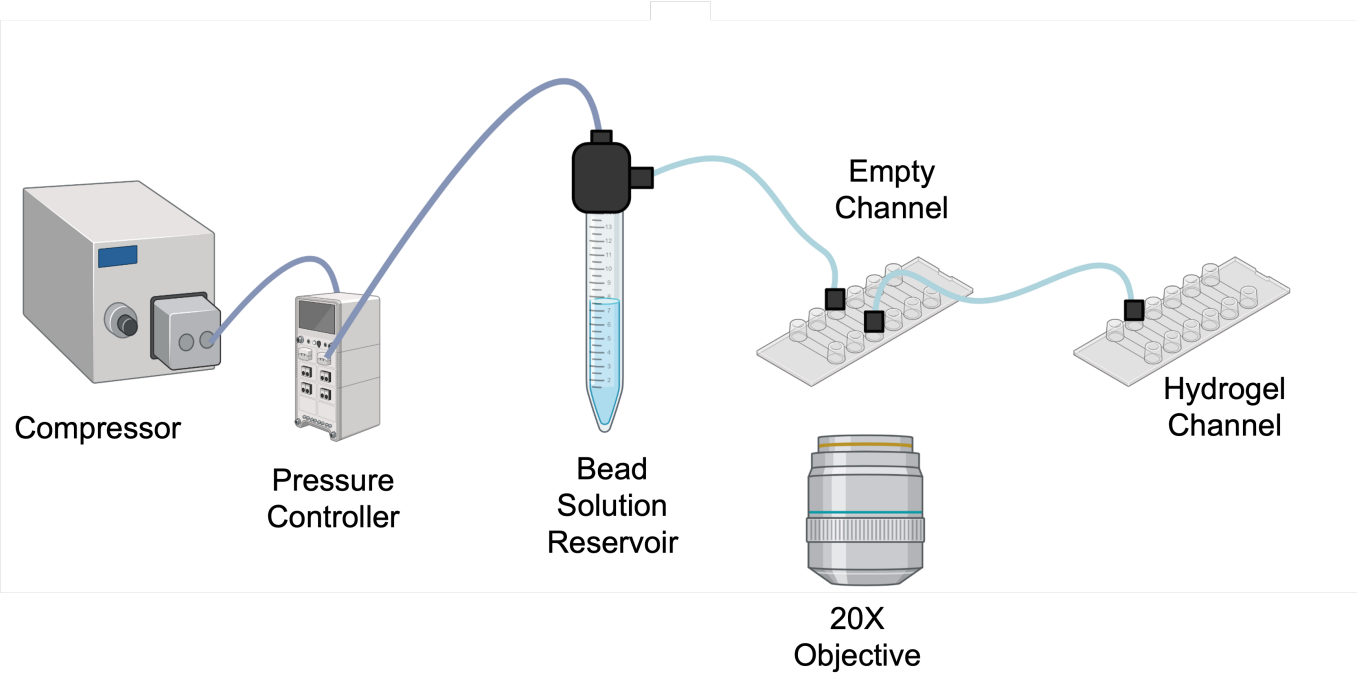


Figure 3.2: Figure showing the particle tracking velocimetry setup used to measure hydrogel permeability. A compressor and pressure controller are used to pressurise a reservoir containing a suspension of micro beads which are then driven through an empty channel connected to a channel filled with hydrogel. The motion of the beads is captured recording 30 second videos using a 20X objective to measure velocity and hence flow rate for each applied pressure from which permeability can be calculated. Image made using Biorender.com.

pressure cavity is connected to a pressure sensor (Merit Sensor LP series) in which deflection of a strain gauge caused by increased pressure is converted into an electrical signal recorded as change in voltage by a digital multi-meter (Agilent, 34401A), with pressures and voltages recorded using LabVIEW software. The sensor is contained on a 3D printed mechanical piece (Elegoo Mars 3, water washable resin) [Cacheux et al., 2023]. This setup was entirely designed from scratch by J. Cacheux previously and the work we conducted in Tokyo was optimising the setup for the PEG-peptide system and data collection.

Silicon moulds were cut to house the hydrogel in as shown in Panel B of Figure 3.3. A 7 mm diameter hole was punched into 1 mm thick silicon sheet to make the hydrogel mould. Hydrogels were formed in the mould resting on glass slides treated with Sigmacote®siliconising agent (Sigma). Since the glass was then hydrophobic samples were able to be lifted and stay in tact. These were then placed in the chip with a 40 $\mu$m nylon mesh on the top to act as permeable barrier to keep the hydrogel in place. On top of the mesh, another silicon sheet with a 5 mm diameter hole was placed as shown in Panel D3 of Figure 3.3. The chamber was then pressurised at different values and the readings from the pressure gauge recorded.

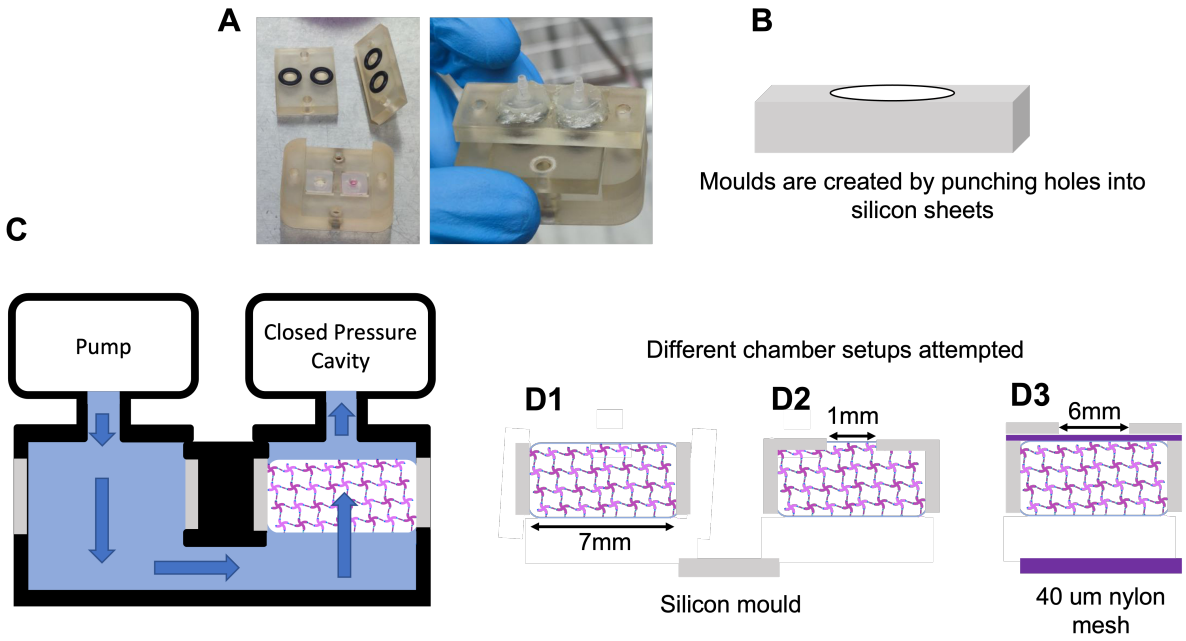


Figure 3.3: Figure showing the MEMS setup for measuring hydrogel permeability. Panel A shows a photograph of the chamber in which silicon moulds are enclosed and flow is passed through the samples. Panel B shows an example of the mould shape in which a hole is punched and the hole is filled with hydrogel. Panel C shows a schematic of the device and the path of the flow pumped up through the hydrogel sample and into a closed pressure cavity. Pressure changes are then measured and used to calculate flow rate. Finally Panel D1-D3 show examples of different configurations attempted. In D1, the hydrogel is simply in the silicon mould but the sample was seen to detach from the walls and thus flow was able to bypass the hydrogel. In D2 a second mould with a smaller hole was placed on top of the hydrogel to clamp the sample in but the material was seen to extrude and then break at high pressures. Finally, in D3, the setup was tested with a larger hole in the silicon on the top of the hydrogel but with a permeable 40 $\mu$m nylon mesh to keep the sample from moving up into the cavity. This design was the most suitable and the method carried forward for measurements.

## 3.3 Results

### 3.3.1 Hydrogels with a higher degree of degradable cross-links degrade faster in the presence of exogenous MMPs

Hydrogels of different percentage degradability were incubated with exogenous MMP-1 or MMP-9 and the absorption of tryptophan found on cleaved peptides was measured. Results were then calculated as a percentage of the total peptide content in the initial hydrogel as shown in Figure 3.4. The chosen MMP concentrations allowed for the initial rapid rate of bond cleavage to be captured by sampling over the hours time scale but by continuing the experiment over the course of several days we were able to see the reduction in rate of cleavage as hydrogels tended towards total degradation. As predicted, hydrogels which included a higher degree of degradable cross-links degraded faster in the presence of MMPs (Anova with Tukey's multiple comparison test at t=8 hrs for MMP-9 showed: p=0.0015 0% vs 25%, $p < 0.0001$ 0% vs 75% or 100%, p=0.0073 25% vs 75% and p=0.0015 25% vs 100%, no difference between 75% and 100%; at t=6 hrs for MMP-1: p=0.0077 0% vs 75%, p=0.0129 0% vs 100%, p=0.0097 25% vs 75% and p=0.0169 25% vs 100%, no difference between 0% and 25% or 75% and 100%). Degradation in the presence of MMP-1 appeared to happen at a faster rate than with MMP-9. Since similar concentrations were used (84.6 nM vs 89.5 nM respectively) this indicates that MMP-1 may act at a faster rate on our degradable sequence. Indeed this is in accordance with predictions made in [Nagase and Fields, 1996] in which the relative activity rates are given for different MMPs on different cleavable sequences.

### 3.3.2 Measurements by PTV can be used to determine hydrogel permeability

The permeability hydrogels of 2, 2.5, 5 and 10% polymer solid content were measured at pressures ranging from 200 to 900 mBar as shown in Figure 3.5. The permeability of the PEG-peptide hydrogel is on the order of $10^{-16}\text{m}^2$. Differences in permeabilities between hydrogels of differing solid content appear to reduce as pressure increases as shown in Figure 3.5. Kruskal-Wallis with Dunn's multiple comparison statistical test revealed that for 2% and 2.5% hydrogels permeability significantly decreased for fixed solid content with increasing applied pressure between 200 and 800 mBar (for 2% p=0.0259; for 2.5% p=0.0099). However, differences between measurements at different pressures were not observed for higher solid content hydrogels ($p > 0.5$). Furthermore, we would expect to see a decrease in permeability with increasing polymer content due to a reduction in available spaces in which fluid can move but the variability in data obtained using the PTV method did not allow us to determine significant differences between different polymer contents.

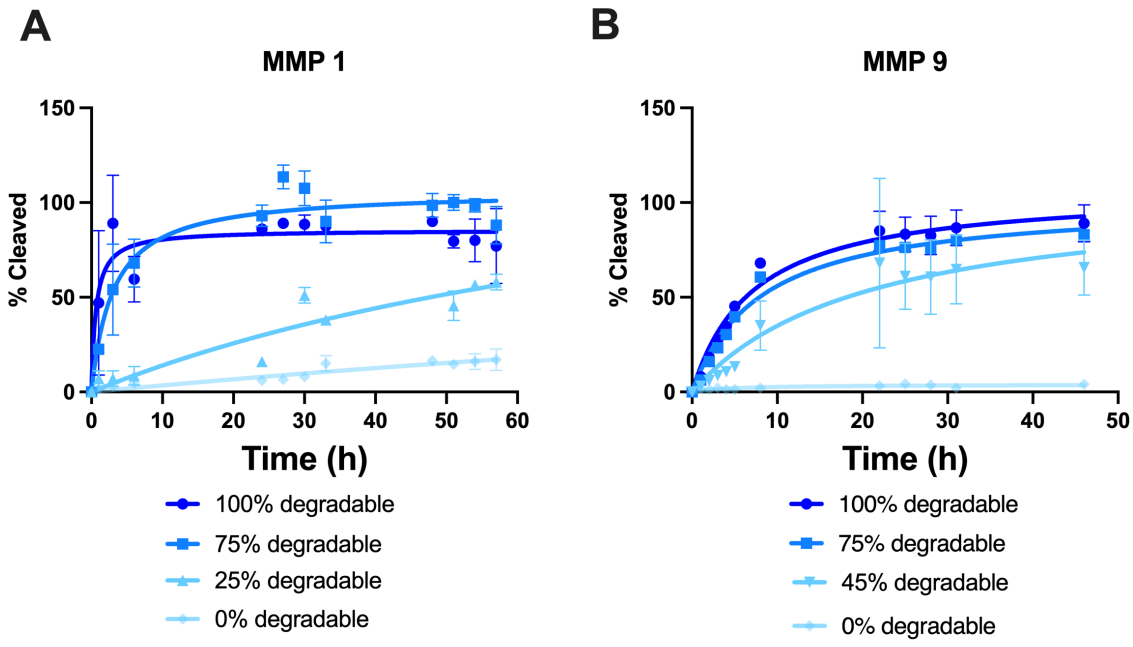


Figure 3.4: Figure showing the percentage of cleaved cross-links over time for hydrogels of different percentage degradabilities in the presence of exogenous MMP-1 (A) and MMP-9 (B). A hyperbola is used to fit mean values based on 2 technical replicates (independent hydrogels) in A and 3 for B.

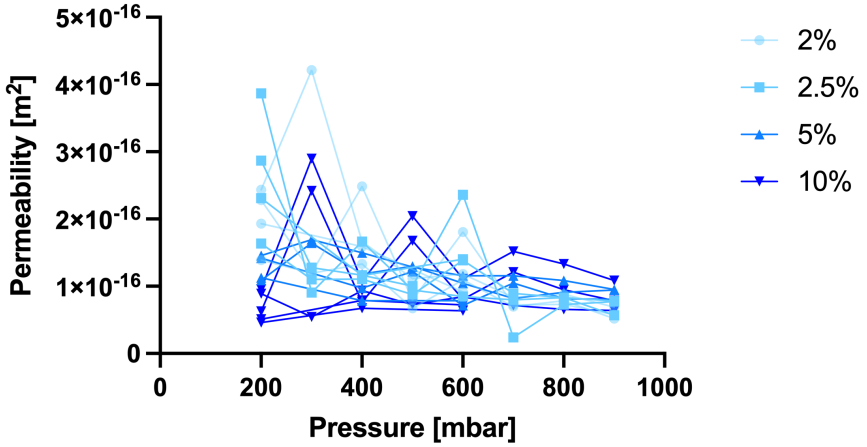


Figure 3.5: Figure showing the permeability at different pressures for hydrogels of different polymer solid content as measured by PTV. Three technical replicates (independent hydrogels) are measured for each polymer solid content.

### 3.3.3 Measurements made with MEMS confirm permeability values obtained using PTV

The permeability hydrogels of 2, 3 and 4% polymer solid content were measured at pressures of 100, 200 and 300 mBar as shown in Figures 3.6 and 3.7. The permeability was found to be on the order of $10^{-16}$ $m^2$. Kruskal-Wallis with Dunn's multiple comparison statistical test revealed that permeability decreases with increasing pressure for 2 and 3% hydrogels (for 2% p=0.0219 100 vs 300 mBar; for 3% p=0.0219 100 vs 300 mBar; (4% not tested).

In order to compare the results obtained using the PTV and MEMS method, we plot permeability against pressure gradient to account for the fact that the applied pressure is over a different distance in both setups. Indeed an applied pressure of for example 200 mBar over a 17 mm length of hydrogel in the PTV method, results in a different pressure gradient over the length of the material than when applied over the 1 mm thickness in the MEMS setup. Results are plotted together in Figure 3.8. Data with both methods found the permeability of the hydrogel to be on the order of $10^{-16}$ $m^2$. Only the 2% hydrogel has been measured using both methods at this stage but the combined data followed the same trend whereby permeability decreases with increasing pressures. The results indicate that both methods are reliable for determining permeability and yield similar values for permeability.

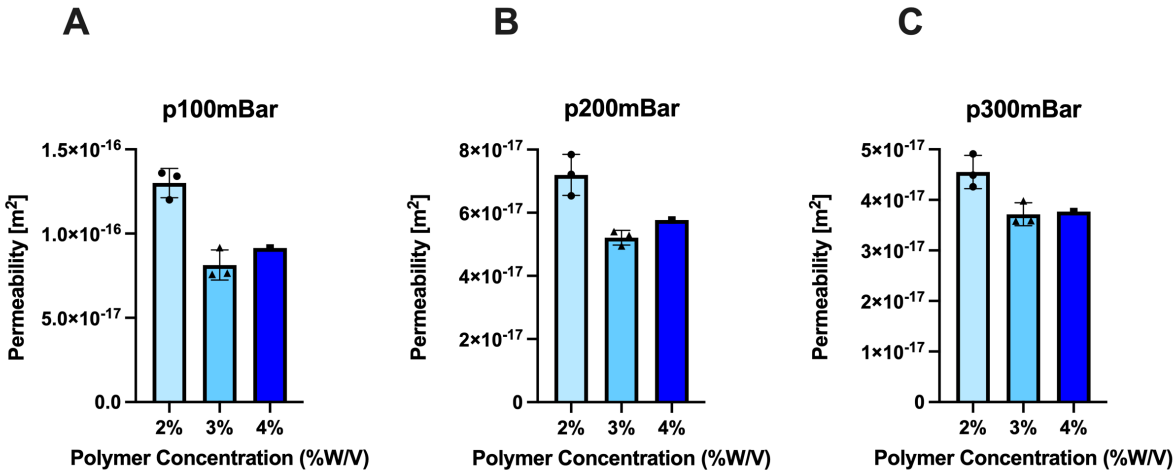


Figure 3.6: Figure showing the comparison of permeability of hydrogels of different polymer solid content at 3 different pressures using the MEMS method. Statistical analysis: Mann-Whitney test for 2 and 3% conditions only (insufficient n numbers at 4%). Three technical replicates (independent hydrogels) are measured for each polymer solid content.

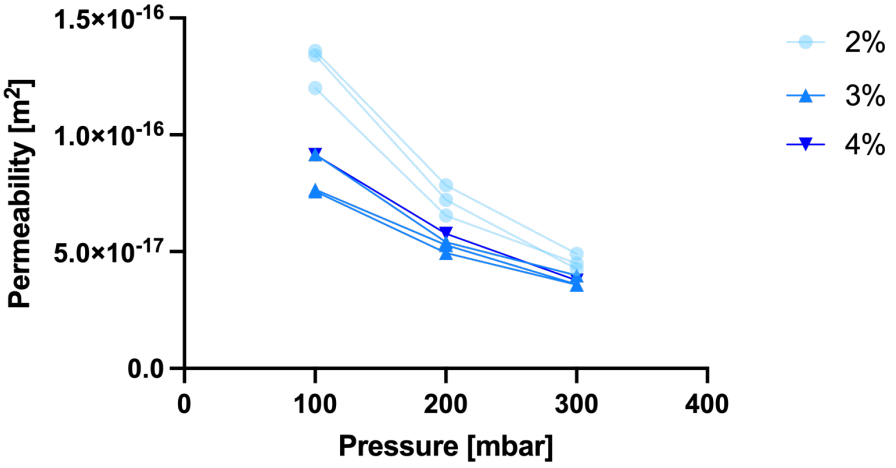


Figure 3.7: Figure showing the permeability at different pressures for hydrogels of different polymer solid content as measured by MEMS. A second order polynomial is used to fit mean values based on three technical replicates (independent hydrogels) other than the 4% hydrogel data which is only of 1 replicate.

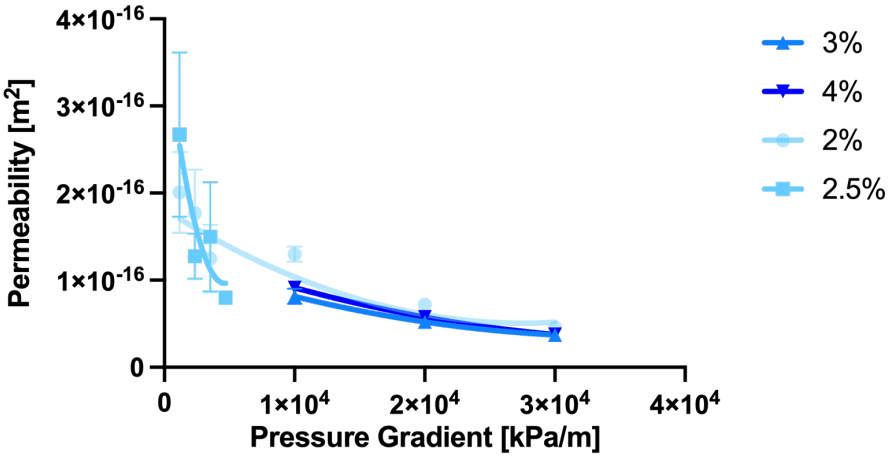


Figure 3.8: Figure showing the combined permeability values obtained using the PTV (2 and 2.5%) and MEMS (2, 3 and 4%) plotted against pressure gradient. A second order polynomial is used to fit mean values based on at least three technical replicates (independent hydrogels) other than the 4% hydrogel data which is only of 1 replicate.

## 3.4 Discussion

In this chapter we aimed to characterise the PEG-peptide hydrogel for use in our *in-vitro* vascular model. Specifically we looked to show that the matrix degradability can be controlled and that the material is permeable to flow. Other important properties such as material swelling behaviour and stiffness measurements have been performed previously in [Jowett et al., 2021] and [Lust et al., 2021a].

Results from the degradation assay show that by altering the number of MMP cleavable cross-links we can indeed control the rate of degradation by exogenous MMPs. By extension, MMP producing encapsulated cells should then be able to break down the matrix and therefore this material is suitable to study cell mediated ECM breakdown in our model (discussed further in Chapter 5).

We then sought to characterise the hydrogel's permeability using direct relations between pressure and flow rate from Darcy's law. We encountered difficulties attempting to assess permeability using standard techniques reported in the literature [Pennella et al., 2013]. We first attempted to determine hydrogel permeability using both the pump driven and hydro-static pressure methods, and collecting the resultant flow to measure volumetric flow rates. In these two setups, shown in Figure 3.9 Panel A and B, custom 3D printed discs of varying thickness were made using an Ultimaker 3 printer, shown in Figure 3.9 Panel C1. Discs were fabricated by gluing nylon from 40 $\mu$m cell strainers to the underside. The nylon induced enough surface tension to keep liquid hydrogel in place on top of the strainer during the cross-linking process until formed but was permeable enough not to affect readings. These 3D printed rings were then placed and screwed

into a brass fitting as shown in Figure 3.9 Panel C2. Tubing was connected to the fitting with either a raised reservoir to generate a hydro-static head or a peristaltic pump.

In either setup, there appeared to be no consistent flow coming through the hydrogel or else in the case with the pump the pressure was increased to a point where either a leak would develop or the hydrogel would puncture. With these results we realised that our hydrogel was likely highly impermeable as these techniques which work for hydrogels such as collagen were unable to yield reliable results. Furthermore we realised that the setup would need to be tighter, with fewer connections and moving parts in order to ensure water was not passing through by avoiding the hydrogel and simply through a lose connection or gap. We therefore concluded from these failed attempts that we would need to apply much higher pressures but also develop more precise methods for measuring the resultant flows as these were likely to be much smaller than we first anticipated.

To address this we then sought a collaboration with C. Desalles from the Ecole Polytechnique. Claire developed a microvessel model as part of her PhD thesis in which she makes micro channels in collagen hydrogels. These are then seeded with endothelial cells and flow is passed through the channel to stimulate them with shear [Dessalles et al., 2021]. The flow rate through the channel is measured by particle tracking velocimetry (PTV) in which the movement of micro beads suspended in the flowing solution is tracked to infer the flow rate. Claire noticed that her flow rate through the channel was smaller than expected as some flow was seeping out of the channel into the surrounding collagen. She used this data to estimate the permeability of her hydrogel and after seeing her present at a conference I contacted her to see if we could apply this technique to the PEG-peptide system. We collaborated for 2 weeks of experiments, one week in her lab in Paris and one in the lab in London. We realised early on that it was not possible to create a microchannel in our hydrogel system as the hydrogels were too soft and the channel collapsed or else the hydrogel was torn when the needle used to make the channel was removed. We decided then to devise an alternative method to use PTV to measure flow through the hydrogel and eventually settled on using the Ibidi channels as described in the methods. We found the permeability of the PEG-peptide hydrogel to be on the order of $10^{-16}$ $m^2$ with values decreasing with increasing applied pressure.

We sought to confirm and improve upon our PVT measurements. To this end, we applied to the Royal Society for funding for a collaboration with the Matsunaga Lab at the University of Tokyo to conduct the MEMS permeability measurements. A postdoc in this lab J. Cacheux, had developed an assay using a pressurised closed cavity to precisely determine hydrogel permeability [Cacheux et al., 2022]. We were awarded the Royal Society International Exchanges 2022 grant and I was lucky enough to be able to travel to Tokyo for 2 weeks of experiments. In Jean's setup, a hollow tube is created in a silicon chamber filled with hydrogel (collagen for his study) which is chemically cross-linked to the silicon walls using glutaraldehyde treatment to clamp the collagen in

place. The hollow tube is then pressurised with flow which permeates the hydrogel and increases the pressure in a cavity above the hydrogel. The pressure increase is 2-fold, an initial deformation of the hydrogel up into the cavity and then the increase from flow entering. A mathematical model in COMSOL mulitphysics is used to decouple these 2 effects by first predicting the expected deformation of the hydrogel into the cavity based on material properties such as Young's modulus.

From the work attempted with Claire in Paris, we knew that creating a channel would not work and so our initial experiments in Tokyo were spent adapting the setup for our specific material. Furthermore, glutaraldehyde does not cross-link with the PEG-based system and thus we needed to find alternative ways to keep the material in place. We attempted 3 different moulds as shown in Panels D1-D3 of Figure 3.3. In the first (Panel D1), a disc of hydrogel is made in a silicon mould and we hypothesised that the PEG may stick enough to the silicon walls. However this was not the case and the hydrogel pulled away from the walls and the flow was able to bypass the hydrogel. In our second attempt (D2), we sandwiched the hydrogel between 2 silicon surfaces one with a much smaller hole. In this setup we observed extrusion of the hydrogel through the smaller hole where the pressure distended the material up into the cavity. The surface area through which the flow could get through was so reduced that in order to achieve flow rates we could measure, forces were so concentrated that the hydrogel tore. In essence, either the pressures were so low the resolution of the pressure gauge was not high enough to measure changes or so high we pierced the hydrogel. Through this work we realised that we needed a large surface area of thin hydrogel to maximise the flow rates for a given pressure. Furthermore, the PEG-peptide hydrogel was highly deformable and so we wanted to try and constrain it to ensure pressure changes recorded truly resulted from movement of flow rather than material deformation. Thus in our final attempt, we also used a method to constrain the hydrogel which would not reduce surface area for flow using a 40 $\mu$m nylon mesh (Figure 3.3 Panel D3).

The data we were eventually able to obtain now explain why we encountered issues using standard permeability assays. Both the PVT and MEMS methods place the PEG-peptide hydrogel permeability on the order of $10^{-16}$ m$^2$. By comparison, estimates for collagen-1 hydrogels are on the order of $10^{-10}$ m$^2$ to $10^{-15}$ m$^2$ depending on concentration [Serpooshan et al., 2013, Cacheux et al., 2022, Cross et al., 2010], $10^{-10}$ m$^2$ for matrigel [Ng and Pun, 2008] and $10^{-9}$ m$^2$ [Sanz-Herrera et al., 2008] for Sponceram®. Therefore our material is 1 to 7 orders of magnitude less permeable than materials for which standard methods are usually used. Pressures which could reasonably be applied without causing leaks or else breaking the material thus resulted in slow flow rates on the order of tens of nanolitres per minute which could not be measured using standard techniques such as flow collection. Therefore, in both the PVT and MEMS assays, methods with a higher precision for measuring small scale flows were used.

In PVT, tracking of microspheres to infer flow velocities through the hydrogel proved to be

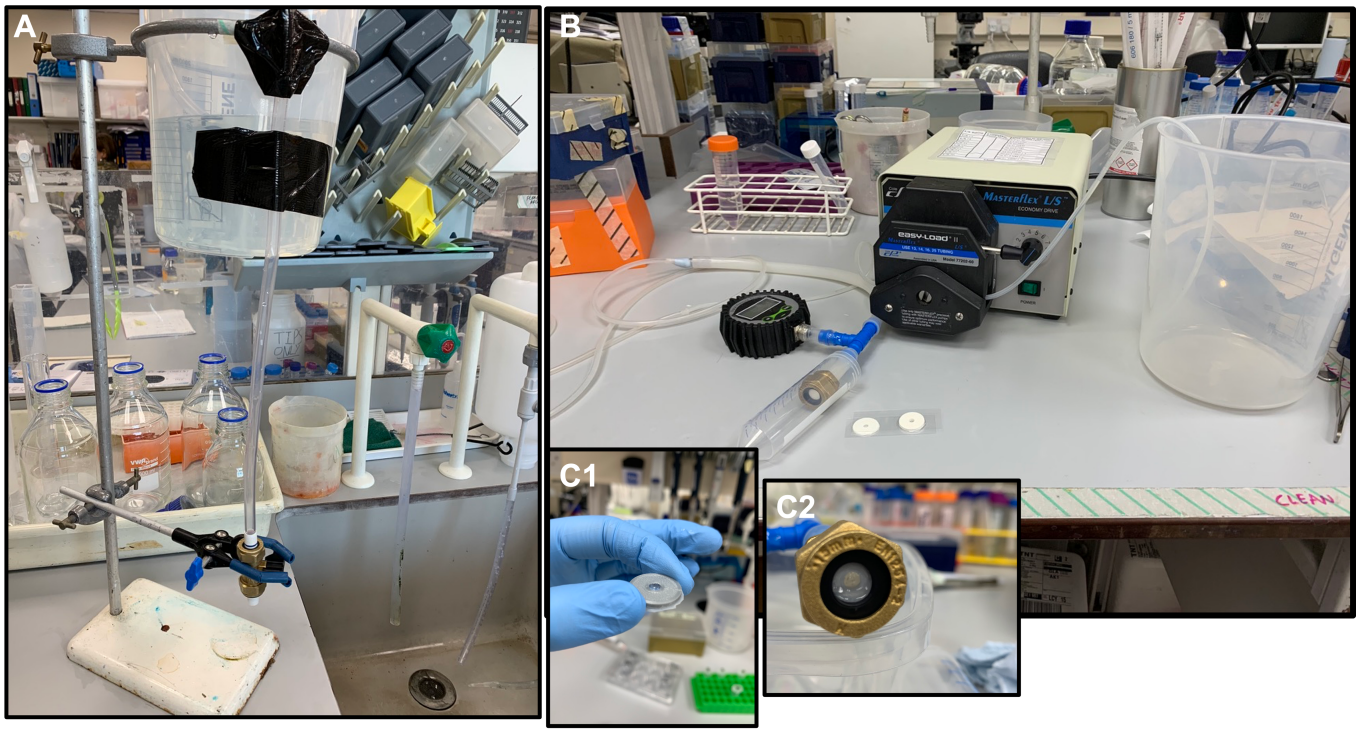


Figure 3.9: Figure showing the first setups attempted for determining hydrogel permeability. In A a hydro-static head is developed above the hydrogel to try and push flow through. In B a peristaltic pump is used instead. In each setup, the hydrogel is formed into a custom 3D printed disc on top of 40 $\mu$m nylon mesh (C1) before being fixed into the brass fitting (C2).

an effective method to determine the approximate permeability of our hydrogels. The setup was relatively straight forward requiring no new equipment outside of a standard microfluidics setup. It is therefore an easy and cheap method which can be setup up relatively easily in any lab. Another big advantage of this setup is that the hydrogel is heavily constrained within the fluidics chip and therefore the material is less prone to bulk deformation under pressure. However, whilst reliable estimates of permeability were obtained there are limitations with this method. The data we collected had a relatively large variability associated and we unable to detect significant changes in permeability with polymer content. We hypothesise that the main source of error comes from accurately tracking the motion of the beads with slower flow rates. There is a random motion of the beads in all directions (Brownian motion) and whilst we only consider the net displacement in the direction of the flow, this motion is likely different to that of the fluid in which the beads are suspended alone. The impact of this effect is likely greater at lower pressures. Indeed measurements at lower pressures than 200 mBar (data not shown) were unable to give reliable results. This is further exacerbated by the fact that the fluidic device used is relatively long at 17 mm with a small cross-sectional area. This means there is high resistance to flow from the long thin material sample. Consequently, same pressures result in slower velocities than in a shorter sample with larger cross-sectional area and this is a potential area of improvement for this assay. Manufacturing a chip is possible with a simple geometry however manufacturing it at a high enough tolerance to withstand high pressures without leaking is challenging.

Using the MEMS method, the volume flow rate is inferred by measuring the pressure difference in a closed cavity and calculating the volume of liquid which would result in this pressure change. Therefore errors associated with tracking slow velocities are avoided. Furthermore, the size of the cavity can be reduced simply by pre-filling with liquid so that smaller volumes of flow result in higher pressure changes and are thus more easily measured. The measurements are therefore limited by the precision of the pressure gauge and indeed using this method we obtained data with smaller variation then that from PTV readings. However we were unable to detect the smaller flows through 5 and 10% hydrogels and thus with the current setup we are limited to measurements on softer hydrogels. Whilst obtaining data for a fuller range of samples would be useful, significant cell death is seen when encapsulated in hydrogels above a polymer content of 5% as discussed in Chapter 5. Therefore this limitation in studying stiffer hydrogels is likely not an issue for future work involving cells.

With both experiments we obtained similar values and were thus able to validate these methods for assessing permeability of hydrogels. Both methods also revealed similar relationships between pressure and permeability. It would be expected expected that hydrogels of increased polymer content, with a greater number of cross-links within the system creates a more tortuous path for flow with reduced void fraction and thus a reduction in permeability [Byun et al., 2008, Cross et al., 2010]. However we were not able to detect significant differences between hydrogels

of different solid content with our data at this stage. By comparison to the PTV method, MEMS produced data with less variability and we hypothesise that by collecting readings for more samples it may be possible to detect significant differences between hydrogels of differing polymer content in the future. In these assays we used applied pressures from 100 to 900 mBar. By comparison, estimates for peak systolic blood pressure in human Aortas range between approximately 150 to 200 mBar [Takazawa et al., 2007, Chen et al., 1997].

Permeability decreased with increasing pressure gradient for a fixed solid content. This behaviour suggests that under pressure the microstructure of the hydrogel is altered and thus with changes in pressure, the ease with which flow can move through the material is changed. Indeed the pressure under flow developed in poroelastic materials such as hydrogels (materials with the interaction of multiple immiscible phases [Hassanizadeh and Gray, 1979]), is a combination of the fluid pressures and the elastic stress due to deformation of the solid phase [MacMinn et al., 2015]. When the material is under pressure, the deformation of the polymer phase changes the arrangement of the pore structure, pore connectivity and thus by extension the permeability of the material [MacMinn et al., 2016, Fiori et al., 2022]. When pressure is applied, the material internally deforms and this is dependent on how the material is constrained with the polymer network compressed against rigid boundaries. Indeed Macminn et all develop a macroscopic model of this poroelastic behaviour using spherical, polyacrylamide hydrogel beads sandwiched between two glass disks [MacMinn et al., 2015]. Fluid is then injected into the centre of the discs which in turn setups a pressure gradient from the centre to the edge where the beads are unconstrained. The subsequent deformation or rearrangement of the hydrogel beads is then captured and shown to be non uniform with larger deformations observed near where the fluid enters.

Not only is there spatial variation in polymer deformation under pressure, but there is also a time dependency. When the driving pressure is initially applied a high pressure gradient across the material exists with the closest area to the pressure compressing more than regions further away [MacMinn et al., 2016]. Steady state is reached when the elastic tension cause by polymer deformation is matched by fluid strain and thus changes in structure stop. Indeed we noticed this effect qualitatively. When we first pressurised the hydrogels, a certain amount of time was needed for readings to settle before steady measurements can be made. With the PVT method this was done by eye but with the MEMS, a clear pressure increase caused by initial material deformation could easily be distinguished from increases due to flow, due to the rate of increase. Furthermore, we developed a method to constrain the material to minimise this effect. Without this implemented, we observed continuous deformation under pressure until breaking point. The material deformations are larger under higher pressures and we therefore hypothesise that differences in permeability with pressure are caused by this pressure strain relationship impacting the hydrogel microstructure.

Permeability is therefore dependent on the shape the material, how it is constrained and the

pressure applied. In both setups, the degree to which the hydrogel is constrained and the length over which pressure gradients are developed are very different. Nonetheless both techniques used allowed us to obtain similar results and thus assess the order of magnitude of permeability for the material.

Interestingly, the permeability of our material is closer than other commonly used hydrogels, to that of theoretical estimates for the aortic media which is estimated to be on the order of $10^{-18}$ $m^2$ [Prosi et al., 2005, Huang and Tarbell, 1997, Sun et al., 2006, Olgac et al., 2008]. Our permeability measures do not yet include the presence of cells which these models account for. We hypothesise that introducing cells into the system would further reduce the permeability and might therefore match these values more closely but we have not conducted any experiments to confirm this. In any event, since the movement of flow through the material is governed by both the amount of free space and the arrangement of it, matching permeability values does not necessarily lead to the same flow movement. However, the lower permeability of our material does suggest that the matrix is densely packed and the path of flow tortuous and thus we may be able to generate high levels of shear stimulation to the cells with relatively low pressures and flow rates as is discussed further in Chapter 6.

## 3.5 Conclusion

The work in this chapter has allowed us to characterise the degradation and permeability properties of the PEG-peptide hydrogel. We showed the degradation rate of the hydrogel can be tuned by altering the number of cleavable cross-links which we demonstrated using both exogenous MMP1 and 9. We determined the permeability of the hydrogel using 2 independent methods obtaining similar results and showed permeability values to be dependent on applied pressure gradient. In summary:

- Hydrogels made with MMP cleavable cross-links degrade in the presence of exogenous MMPs
- The rate of degradation is changed by altering the number of cleavable cross-links
- The hydrogel permeability is measured to be on the order of $10^{-16}$ $m^2$
- Hydrogel permeability is dependent on applied pressure gradient
- Both PVT and MEMS assays have been demonstrated to be effective methods for measuring low permeability materials

At this stage, we have shown the PEG-peptide system to be suitable for the purposes of our model, allowing us to alter polymer content and degradability independently. Furthermore, we are able to measure the impact of changing polymer content on hydrogel permeability and determine flow rates through the material for different pressures. In the next chapter, we address another important consideration, whether changing hydrogel polymer content and thus stiffness also alters mass transport through the material.

# Chapter 4

# PEG-peptide Hydrogel Characterisation: Exploring Mass Transport

## Chapter Abstract

**Background**: Synthetic hydrogels are suitable materials in which to encapsulate cells for studying their behaviour in 3D. One advantage of such materials is the ability to modulate matrix stiffness by increasing the polymer solid content. However, introducing a greater number of polymers and hence cross-links into the system, reduces the size of the gaps in the polymer mesh (mesh network size), through which molecules can diffuse.

**Aim**: The aim of this chapter is to determine the impact of changing hydrogel polymer solid content on mass transport and explore whether modulating stiffness slows movement of molecules within the matrix.

**Methods**: Hydrogel diffusivity was assessed using predictive models underpinned by experimental data to characterise the hydrogel's permissiveness to diffusion of molecules of biologically relevant size. Diffusion of encapsulated fluorescent FITC-dextran molecules of size 10, 40 and 70 kDa within hydrogels of 2.5, 5 and 10% polymer solid content was measured by monitoring the absolute fluorescence of solution around the hydrogel over time. Diffusion models were setup considering theoretical estimates of network mesh size based on swelling data to determine the relative diffusivity of the hydrogel network. Modelling data was then fitted to experimental data to predict network diffusivity.

**Results**: Diffusion rates of molecules were shown to negligibly change with increasing polymer solid content for hydrogels of up to 5% polymer solid content for all but the largest molecule size. Thus we are able to make hydrogels of stiffness up to approximately 6.5 kPa without significantly

hindering diffusion of molecules within the material.

**Conclusion**: The data in this chapter confirms that solid content and hence stiffness of the PEG-peptide hydrogel system can be modulated over a wide range without introducing significant changes in mass transport to and from encapsulated cells.

## 4.1 Introduction

In the previous chapter we introduced the PEG-peptide hydrogel system which is used to create our *in-vitro* models. When hydrogels are used create 3D cultures of cells, it is crucial to understand mass transport of molecules to and from the cells within the network, not only to understand transport of nutrients and waste but also movement of any molecules of interest produced by cells for analysis [Weber et al., 2009]. This ability of a material to allow passive movement of molecules from areas of high to low concentration (diffusion) is known as diffusivity. The purpose of this chapter is then to characterise hydrogel diffusivity in our PEG-peptide system.

As described in Chapter 3, our hydrogel is formed using a 2 step cross-linking process which results in more efficient network formation with the ability to form hydrogels at polymer solid contents as low as 2% [Jowett et al., 2021]. Whilst this helps to create hydrogels with fewer defects and hence more controllable mechanical properties, the increased network connectivity likely reduces the number of gaps in the system. This in turn may reduce the ease of movement through the network via the liquid phase and indeed, results from Chapter 3 did place our hydrogel's permeability to flow several orders of magnitude lower than that of other common hydrogels. Permeability and diffusivity are intrinsically linked as both depend on the microstructure of the porous material, notably the pore size or overall void fraction in the solid phase but also the arrangement and path through this void fraction [Offeddu et al., 2018]. Permeability and diffusivity increase with increasing pore size, and decrease with path tortuosity [Hadjiev and Amsden, 2015, O'Brien et al., 2007, Offeddu et al., 2018].

Given the relatively low permeability of our hydrogel we wanted to characterise the system's diffusivity and importantly, ensure that by modulating polymer stiffness we would not introduce an extra variable by also changing diffusion. Indeed increasing polymer solid content and thus the number of cross-links per unit volume, reduces the gaps in the solid phase if efficient network formation occurs [Zustiak and Leach, 2010]. In order to understand the potential impact of this effect in our system, we characterised mass transport of molecules of different sizes through PEG-peptide hydrogels of different polymer contents using both modelling and experimental techniques. This work was published in 2021 in a publication entitled "Selectively Cross-Linked Tetra-PEG Hydrogels Provide Control over Mechanical Strength with Minimal Impact on Diffusivity" and is presented in full in this thesis.

### 4.1.1 Chapter Aims

The data in this chapter address Aim 1: assessing the suitability of the PEG-peptide hydrogel system to study cell-mediated remodelling. The specific aims of this chapter were to:

- Assess mass transport within the hydrogels

### 4.1.2 Author Contribution

This paper was a collaborative effort but for the purpose of this thesis I am highlighting my individual contribution. All modelling of solute diffusivity and theoretical mesh size calculations were performed by me. Experimental measurements of FITC dextran diffusion were also performed by me but I gratefully acknowledge the efforts of G.M.Jowett, M.Norman and C. Kerins in helping me develop the assay. Swelling experiments were performed by M.Norman with help from D. Marciano and rheological characterisation by D. Hoogland with help from J.Omar. The PEG-peptide hydrogel system was developed before this paper and the majority of this work was conducted by T. L. Yu. The project was conceived by me and my supervisors E. Gentleman and P. Lamata, and my collaborator R. J. Shipley. The manuscript was predominately written by me and E. Gentleman.

ACS Biomaterials SCIENCE & ENGINEERING

pubs.acs.org/journal/abseba

Article

# Selectively Cross-Linked Tetra-PEG Hydrogels Provide Control over Mechanical Strength with Minimal Impact on Diffusivity

Suzette T. Lust, Dominique Hoogland, Michael D. A. Norman, Caoimhe Kerins, Jasmin Omar, Geraldine M. Jowett, Tracy T. L. Yu, Ziqian Yan, Jessie Z. Xu, Daniele Marciano, Ricardo M. P. da Silva, Cécile A. Dreiss, Pablo Lamata, Rebecca J. Shipley, and Eileen Gentleman*

Cite This: *ACS Biomater. Sci. Eng.* 2021, 7, 4293–4304

Read Online

ACCESS | Metrics & More | Article Recommendations



**ABSTRACT:** Synthetic hydrogels formed from poly(ethylene glycol) (PEG) are widely used to study how cells interact with their extracellular matrix. These *in vivo*-like 3D environments provide a basis for tissue engineering and cell therapies but also for research into fundamental biological questions and disease modeling. The physical properties of PEG hydrogels can be modulated to provide mechanical cues to encapsulated cells; however, the impact of changing hydrogel stiffness on the diffusivity of solutes to and from encapsulated cells has received only limited attention. This is particularly true in selectively cross-linked "tetra-PEG" hydrogels, whose design limits network inhomogeneities. Here, we used a combination of theoretical calculations, predictive modeling, and experimental measurements of hydrogel swelling, rheological behavior, and diffusion kinetics to characterize tetra-PEG hydrogels' permissiveness to the diffusion of molecules of biologically relevant size as we changed polymer concentration, and thus hydrogel mechanical strength. Our models predict that hydrogel mesh size has little effect on the diffusivity of model molecules and instead predicts that diffusion rates are more highly dependent on solute size. Indeed, our model predicts that changes in hydrogel mesh size only begin to have a non-negligible impact on the concentration of a solute that diffuses out of hydrogels for the smallest mesh sizes and largest diffusing solutes. Experimental measurements characterizing the diffusion of fluorescein isothiocyanate (FITC)-labeled dextran molecules of known size aligned well with modeling predictions and suggest that doubling the polymer concentration from 2.5% (w/v) to 5% produces stiffer gels with faster gelling kinetics without affecting the diffusivity of solutes of biologically relevant size but that 10% hydrogels can slow their diffusion. Our findings provide confidence that the stiffness of tetra-PEG hydrogels can be modulated over a physiological range without significantly impacting the transport rates of solutes to and from encapsulated cells.

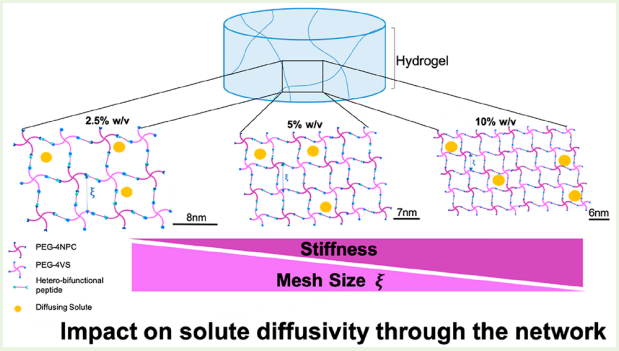


**KEYWORDS:** *hydrogel, diffusivity, mass transport, PEG, mesh size, rheology, diffusion modeling, obstruction theory*

## INTRODUCTION

Cells' interactions with their local environment are known to play central roles in regulating processes including proliferation, migration, differentiation, and phenotypic maintenance.[1−3] By extension, these interactions are also involved in dysregulation of cell behavior in pathologies. Thus, understanding the impact of mechanical and biological cues cells receive from their surroundings is key in both disease modeling and the development of regenerative therapies.[4,5] While the ability of whole organisms and tissue explants to provide physiologically relevant environments to cells are unrivalled, there is also a need for simpler reductionist models that allow for studies into how specific cues impact cellular behaviors. Such models have the potential to identify underlying mechanisms that govern complex tissue pathologies, can reveal fundamental insights into cell-matrix interactions, and may inform methods to engineer tissues for regenerative applications.

While *in vitro* cell cultures have revolutionized our understanding of mammalian biology, cells respond differently when within 3D structures akin to tissues compared to on 2D surfaces.[6,7] Indeed, among other factors, the transport of molecules to and from cells is markedly changed in 3D. Hydrated polymer networks called hydrogels can mimic many

**Special Issue:** Advanced Biomedical Hydrogels

**Received:** December 11, 2020
**Accepted:** April 27, 2021
**Published:** June 20, 2021

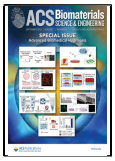

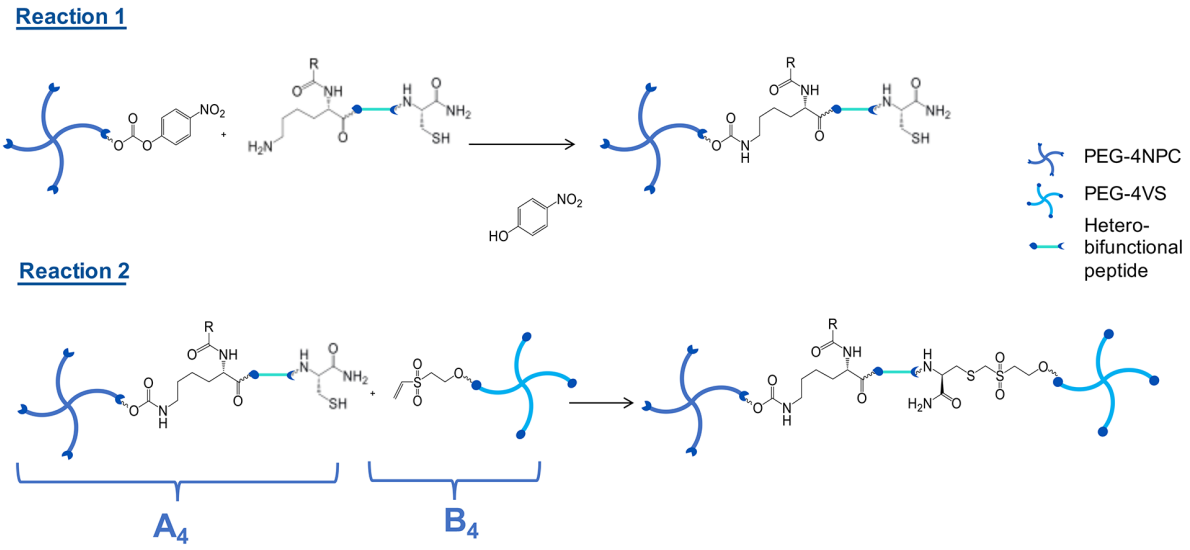


**Figure 1.** Diagram of the reaction schemes used to form hydrogels. Reaction 1 conjugates peptides with PEG-4NPC. Reaction 2 selectively cross-links PEG-peptide conjugates ($A_4$) with PEG-4VS ($B_4$) using a Michael-type addition.

aspects of the 3D environment cells inhabit *in vivo*. Their compatibility hinges on their two-phase nature, with a solid polymer scaffold mimicking the extracellular matrix (ECM) and the liquid phase available for transport of nutrients.[8] Moreover, the properties of the hydrogel network can be tuned to mimic characteristics of the native tissue, including their stiffness, which is known to regulate a range of cellular behaviors, including fate specification.[1−3]

Synthetic hydrogels formed from poly(ethylene glycol) (PEG) are suitable for cell encapsulation due to PEG's stability, hydrophilicity, and resistance to protein adsorption.[9] Furthermore, the versatility with which PEG macromers can be cross-linked allows control over theoretical mesh size by simply changing polymer concentration, macromer arm size, and the number of arms. And, while native biochemical cues are missing in PEG hydrogels, the polymer can be modified to include ECM-mimicking anchorage sites. Furthermore, cross-linking the network with matrix metalloproteinase (MMP)-sensitive peptides allows encapsulated cells to actively remodel and migrate through them.[10,11] However, the introduction of bioactive motifs often leads to network inhomogeneities.[12] These irregularities are caused by missing cross-links, internal loops within individual polymer macromers, and dangling polymer ends.[13,14] Such inhomogeneities, although potentially useful as means to permit diffusion, can lead to reduced stiffness.[15,16] Moreover, as inhomogeneities push gel structures further from the ideal network, theoretical characterizations fall short, making predictions of hydrogel properties more complex and attributing them to biological outcomes more fraught.[17] Therefore, hydrogel designs that reduce inhomogeneities may provide a more effective and controlled platform for studying cellular behaviors in 3D.

Many covalently cross-linked hydrogel networks rely on Michael-type additions between a cysteine residue at the end of a peptide and an alkene-containing end group on the PEG macromer arm (either 4-arm or 8-arm, $B_4$/$B_8$). Peptide sequences susceptible to enzymatic degradation are then created with cysteine groups at both termini ($A_2$), creating $A_2$+$B_4$/$B_8$ designs. In such designs, homobifunctional cross-linking peptides react with the polymer chain ends indiscriminately. In this scenario, primary loops in which one peptide reacts at both ends on the same macromer are likely to form, particularly at low polymer concentrations. Adhesive motifs, on the other hand, typically have a single cysteine group, and thus are incorporated in a pendant fashion. In the latter arrangement, as more pendant groups are introduced, the number of arms available for cross-linking is reduced, increasing gel inhomogeneities.

To circumvent these issues, it is possible to selectively functionalize end groups of both the polymer backbone and peptides, ensuring that each can only react in a desired manner. Indeed, the Shibayama group has reported on highly homogeneous, high-strength "tetra-PEG" hydrogels that form upon mixing two polymer macromers with different reactive terminal groups ($A_4$+$B_4$).[15] We hypothesized that it would also be possible to create efficiently cross-linked $A_4$+$B_4$ hydrogels suitable for supporting live cells. However, the implications of the $A_4$+$B_4$ design on mass transport to and from encapsulated cells has not been investigated thoroughly.

To create $A_4$+$B_4$/tetra-PEG hydrogels, we created hetero-bifunctional peptides and reacted an amine at the peptides' N-terminus with nitrophenyl carbonate (NPC) end-functionalized four-arm PEG (PEG-4NPC, $A_4$), creating PEG−peptide conjugates. We then formed hydrogels by reacting a free thiol from a cysteine residue located at the peptides' C-terminus with vinyl sulfone (VS) end-functionalized four-arm PEG (PEG-4VS, $B_4$). We have previously shown that when adhesive (RGD) and MMP-degradable peptide sequences are used to cross-link the PEG network, this design supports the viability of encapsulated human induced pluripotent stem cell-derived intestinal organoids.[11] Importantly, even within these soft matrices (elastic modulus, ∼ 1 kPa), gelation was quick enough that organoids did not fall to the bottom of the hydrogel prior to gelation, suggesting that network formation was more effective at polymer concentrations as low as 2.5% compared to similar $A_2$+$B_4$ designs.[18]

The tetra-PEG design allows physical and biological properties of the hydrogel to be tuned independently, while maintaining network connectivity. Indeed, as MMP-susceptible and adhesive peptides both participate in cross-linking, cellular


https://doi.org/10.1021/acsbiomaterials.0c01723
ACS Biomater. Sci. Eng. 2021, 7, 4293−4304

response to mechanical stiffness can be studied without altering adhesiveness or degradability. However, at higher polymer concentrations, the space between cross-links in the polymer phase, known as the mesh size, is reduced. It therefore follows that higher polymer concentrations may not only change cells' mechanical environment but also impact the mass transport of solutes. Indeed, others have shown that for some hydrogel systems, increasing polymer concentration impacts diffusivity.[19,20] For both *in vitro* models and regenerative applications, the ability of nutrients to reach encapsulated cells over a reasonable time scale is crucial. Diffusivity will also impact researchers' ability to detect secreted molecules in the culture supernatant, which may be of interest for monitoring cell behaviors. Moreover, time scales for diffusion of biomolecules can impact cell−cell communication,[21,22] which may play a role in regulating autocrine versus paracrine signaling effects.

Here, we combined predictive models with experimental characterization to study how altering polymer concentration in tetra-PEG hydrogels impacts the network's permissiveness to the diffusion of molecules. Our findings show that hydrogel stiffness can be modulated over a large range while only impacting diffusivity negligibly, as we only observed significant changes in diffusion at high polymer concentrations that are less suitable for encapsulating cells.

## MATERIALS AND METHODS

**PEG−Peptide Conjugate Synthesis and Hydrogel Formation.** PEG−peptide conjugates were synthesized as described previously.[11] Briefly, peptide Ac-KDW-ERC-NH2 (custom synthesis Peptide Protein Research, Ltd. (UK), >98% purity) with an N-terminal primary amine (lysine side chain) and C-terminal thiol (cysteine) were reacted with a four-arm 10 kDa PEG-NPC (JenKem Technology, USA) to form PEG−peptide conjugates (Figure 1). Twenty or 15 μL (depending on end volume) of purified conjugate solution was then cross-linked with 20 or 15 μL of 10 kDa PEG tetramer solution with a vinyl-sulphone end group (JenKem Technology, USA) at the required concentrations at 37 °C through a base-catalyzed (pH 8) Michael-type addition. This strategy was used to make 2.5%, 5%, and 10% (w/v) hydrogels.

**Swelling.** First, 30 μL hydrogels were formed in Sigmacote (Sigma UK)-treated 6-mm-diameter glass cylindrical molds and submerged in PBS. Hydrogel wet weight was measured once swelling equilibrium had been achieved (after 48 h). Hydrogels were lyophilized to determine dry weight and the mass swelling ratio calculated using

$$Q_m = \frac{\text{wet weight}}{\text{dry weight}} \tag{1}$$

The mass swelling ratio was then used to calculate the volumetric swelling ratio $Q_v$ using the following relation:

$$Q_v = 1 + \left(\frac{\rho_p}{\rho_s} \times (Q_m - 1)\right) \tag{2}$$

where $\rho_p$ and $\rho_s$ are the polymer and solvent densities, respectively. This parameter describes the amount of water within the hydrogel in the swollen state and can be used to infer network connectivity. Data were analyzed for significance using one-way Anova with Tukey's multiple comparison test.

**Rheological Measurements of Hydrogel Gelation and Mechanical Properties.** Hydrogel gelation was assessed on a strain-controlled ARES from TA Instruments using a 25 mm cone with a 0.02-rad angle and plate by carrying out small-amplitude oscillatory time-sweep measurements at a strain of 5% and a constant angular frequency of 1 rad $s^{-1}$. All measurements were carried out at 37 °C, depositing paraffin oil on the edges of the sample to prevent evaporation. To perform measurements, 86 μL of hydrogel precursor solution was placed in the instrument, and storage modulus $G'$ and loss modulus $G''$ were recorded as a function of time (Orchestrator software, version 7.2.0.2). Subsequently, an amplitude sweep was carried out, recording $G'$ and $G''$ over the range 1−100% shear strain for 2.5 and 5% gels and 1-25% for the 10% gel, at a fixed frequency of 1 rad $s^{-1}$; this range was found to be within the linear viscoelastic region. Finally, a frequency sweep was recorded, measuring $G'$ and $G''$ as a function of shear frequency in the range 100−0.1 rad $s^{-1}$ at a fixed strain of 5%. To assess whether storage and loss moduli were significantly different between samples with varying polymer concentration, a one-way ANOVA with Tukey's multiple comparison correction was performed.

**Theoretical Estimations of Mesh Size.** Hydrogels can be modeled as polymer strands that cross-link to form a network, where mesh size, $\xi$, is the distance between cross-links. In this scenario, $\xi$ is the size of the spaces between polymer chains through which liquid and solutes can move. Therefore, mesh size influences the diffusivity of the network and the time scales taken to reach equilibrium for any solute diffusing through it. It can be challenging to directly measure mesh size without dehydrating the polymer network.[23,24] Therefore, theoretical estimates are obtained by estimating the molecular weight between cross-links and thus the length of these chains. Mesh size can be estimated using a variety of experimental techniques including dynamic light scattering, small angle neutron scattering, and small-angle X-ray scattering.[25] However, because of experimental limitations, it is most often estimated using simpler methods based on experimental parameters gathered from (1) rheological data, (2) swelling data, and (3) direct measurements of diffusivity.[24]

We make our estimates for network size here using swelling data. We consider $\xi$ as the average distance between cross-links, and hence a measure of the distance between two adjacent polymer strands in a hydrogel network in its equilibrium swollen state. Equilibrium swelling theory balances the thermal energy due to interactions between polymer and liquid molecules and the elastic tension in the polymer arms in the swollen state.[24,26] This relation has been shown to faithfully predict PEG gel swelling[27] and has been used previously to calculate mesh size in hydrogels used for *in vitro* cell cultures.[28−30] The Flory−Rehner theory states that the change in the potential energy in the system during transition from its preswollen to swollen state is equal to the increase in elastic forces in the system and that these two terms are equal at equilibrium. Therefore, when the expressions for the thermal mixing energy and the elastic energy in the polymer strands are used, the average molecular weight between cross-links $\bar{M}_c$ in g/mol is given by

$$\frac{1}{\bar{M}_c} = \frac{2}{\bar{M}_n} - \frac{\frac{\bar{v}}{V_1}(\ln(1 - v_2) + v_2 + \chi_1 v_2^2)}{v_2^{1/3} - \frac{v_2}{2}} \tag{3}$$

where $\bar{M}_n$ is the molecular weight of the polymer chains in the absence of the cross-linking agent in g/mol, $\bar{v}$ is the specific volume of the polymer and is defined as the ratio of polymer density to solute density (dimensionless), $V_1$ is the molar volume of the solvent in $cm^3$/mol,[31] $v_2$ is the polymer volume fraction in the swollen state (reciprocal of $Q_v$ obtained from swelling measurements) (dimensionless), and $\chi_1$ is the polymer−solvent interaction parameter (a measure of the degree of interaction between the polymer chains and the surrounding solution; dimensionless). Methods for determining these parameters, and in particular that for $\chi_1$, have improved understanding of the swelling equilibrium in hydrogels.[24] The values for each parameter for the $A_4$+$B_4$ hydrogels examined in this study are given in Table 1.

Once the average molecular weight between cross-links is found, this must be converted to an estimate of the end-to-end distance to predict $\xi$. The end-to-end distance between two adjacent cross-links before the network is stretched is given by $\sqrt{r_0^{1/2}}$ and obtained in nanometers using

$$\sqrt{r_0^{1/2}} = l\sqrt{NC_n} \tag{4}$$



https://doi.org/10.1021/acsbiomaterials.0c01723
ACS Biomater. Sci. Eng. 2021, 7, 4293−4304

**Table 1. Parameters Used in Theoretical Mesh Size Estimations**

| parameter name | explanation | value |
|---|---|---|
| $\bar{M}_n$ | molecular weight of the polymer chains in the absence of the cross-linking agent | $2.94 \times 10^3$ [g/mol] |
| $v$ | specific volume of the polymer | 0.9 |
| $V_1$ | molar volume of water | 18 [$cm^3$/mol] |
| $V_2$ | polymer volume fraction in the swollen state (reciprocal of $Q_v$ obtained from swelling data) | 0.024 for 2.5% hydrogels, 0.034 for 5% hydrogels, and 0.051 for 10% hydrogels |
| $X_1$ | the polymer solvent interaction parameter | 0.426[49] |
| $l$ | average bond length between repeating units | 0.146 [nm][32] |
| $C_n$ | Flory characteristic ratio | 4[32] |
| $M_r$ | molecular weight of repeating unit | 44 [g/mol][32] |

in which $l$ is the average bond length between repeating units in nanometers in the polymer chain, $N$ is the number of links between monomers in the chain (dimensionless), and $C_n$ is the Flory characteristic ratio (dimensionless value of 4 for long PEG chains).[24,32] This parameter $C_n$ is defined as the ratio of polymer chain length to the theoretical length when each section is considered to be freely jointed and can be randomly oriented with no influence from external forces, taking into account steric interference (nonbonded interactions between molecules). Further, $N$ is given by

$$N = 2\frac{\bar{M}_c}{M_r} \tag{5}$$

where $M_r$ is the molecular mass of the repeating unit in g/mol.[33]

When the polymer chain becomes stretched at the swelling equilibrium, the end-to-end distance is increased in the direction of the net stretching force.[34] A measure of this distance increase is given by the elongation ratio, which is the ratio of the new polymer chain length once the force has been applied to that of the unstretched end-to-end distance. This ratio is approximated for polymers which swell in all directions equally (isotropic).[26] The mesh size can then be expressed as

$$\xi = Q_v^{1/3}\sqrt{r_0^2} \tag{6}$$

**Modeling Solute Diffusion out of the Hydrogel.** We set up a diffusion model to simulate transport of solutes out of our tetra-PEG hydrogels and into the surrounding solution to assess the impact of mesh size on the diffusivity of molecules of relevant size. The model was established to mimic a standard experimental setup in which molecules of known size diffuse from hydrogels. This allowed for direct comparison between our theoretical predictions and experimental measurements.

Diffusion of solutes through a hydrogel is hindered by the presence of the polymer chains creating a mesh through which the solutes must move. This diffusibility is therefore determined by the relative size of the solute compared to the mesh size, the mobility of the polymer chains, and the potential steric interactions between solutes and polymer chains.[19] Models have been reported that predict solute transport through hydrated polymer networks with differing emphasis on the main obstruction mechanism.[19,24] We represented the solute molecules by hard spheres. The polymer chains were assumed to be immobile, and we neglected steric interactions between these and the solute. In such models, the presence of the polymer phase results in an increased path length for diffusing molecules slowing their transport. Similar models have been shown to effectively predict mass transport phenomena in hydrogels.[19,35]

Our model assumed the hydrogel to be a homogeneous porous network of fixed mesh size $\xi$, using theoretical estimates calculated for $A_4$+$B_4$ hydrogels with polymer concentrations of 2.5%, 5%, and 10%,

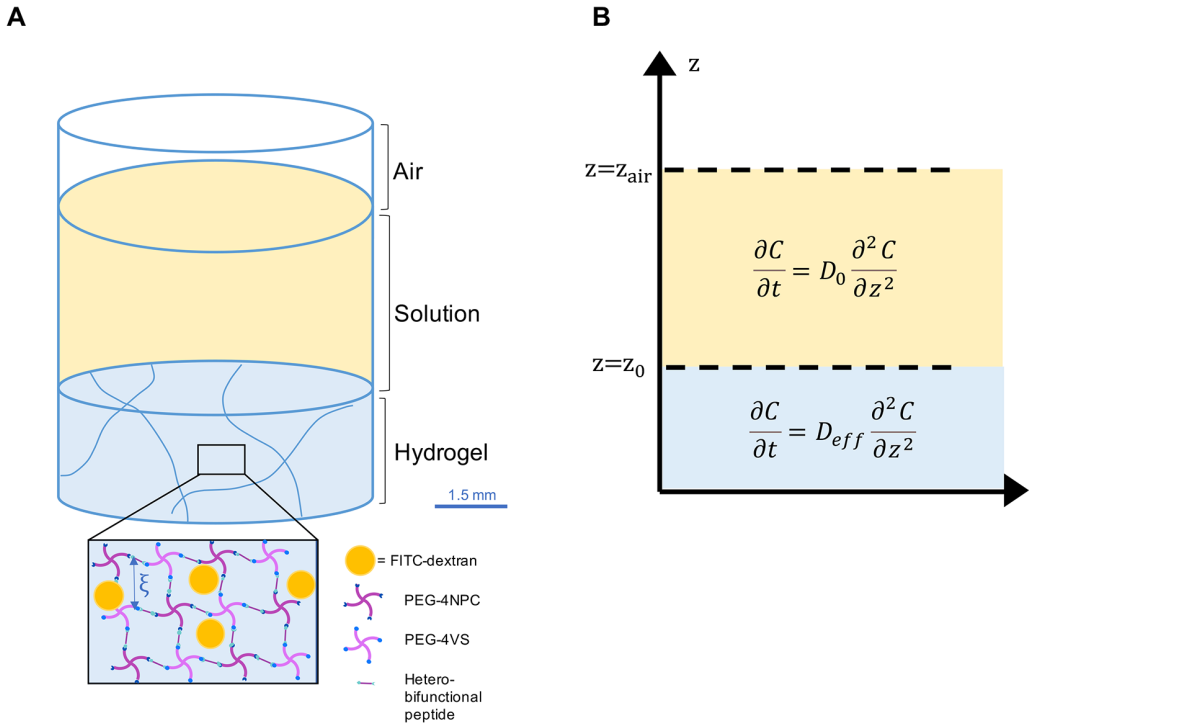


**Figure 2.** (A) Experimental setup showing the two regions through which mass transport of a solute of a given size is mathematically modeled. (B) Schematic representation of the corresponding mathematical model setup in A. Free diffusion is prescribed in the solution region with reduced diffusivity in the hydrogel modeled by altering the diffusion coefficient.


https://doi.org/10.1021/acsbiomaterials.0c01723
ACS Biomater. Sci. Eng. 2021, 7, 4293−4304

Table 2. Table Summarizing the Parameters Used in the Diffusion Model and Their Values

| parameter | explanation | value | parameter sweep value |
|---|---|---|---|
| $k_b$ | Boltzmann constant | $1.381 \times 10^{-23}$ [$m^2$ kg $s^2$ $K^{-1}$] | |
| $T$ | absolute temperature of the solution | 310.15 [K] | |
| $\eta$ | dynamic viscosity (taken to be that of water at 37 °C) | $6.913 \times 10^{-4}$ [Pa s] | |
| $r_s$ | solute hydrodynamic radius | 2.3 [nm] for 10 kDa FITC-dextran, 4.5 [nm] for 40 kDa FITC-dextran, 6.0 [nm] for 70 kDa FITC-dextran | 2.0 [nm], 4.0 [nm], 7.0 [nm], 8.0 [nm] |
| $r_f$ | polymer chain radius | 0.232 [nm][33] | |
| $\xi$ | mesh network size | 8.41 [nm] for 2.5% hydrogels, 7.41 [nm] for 5% hydrogels, 6.43 [nm] for 10% hydrogels. | 4.5 [nm], 5.0 [nm], 6.0 [nm], 7.0 [nm], 8.0 [nm], 10 [nm], 20 [nm] |

and using direct measurements of the mass swelling ratio. The hydrogel domain was modeled to be one-fifth of the height of the media domain above it, which represented a 60 $\mu$L hydrogel under 240 $\mu$L of solution in a well of a 96-well plate (Figure 2A). The diffusion of FITC-labeled dextran molecules of molecular weight 10, 40, and 70 kDa corresponding to hydrodynamic radii of approximately 2.3, 4.5, and 6 nm, respectively, was modeled for hydrogels created at all three polymer concentrations. The Fickian diffusion of a species $C$, representing the FITC-labeled dextran molecule, is described generally using the diffusion equation:

$$\frac{\partial C}{\partial t} = D_{\text{eff}} \frac{\partial^2 C}{\partial z^2} \tag{7}$$

where $C$ is the species concentration in moles per cubic meter, and $D_{\text{eff}}$ in square meters per second is the effective diffusion coefficient (dependent on the properties of the medium through which the species diffuses). We assumed the diffusion coefficient to be constant in space and time, assuming no spatial inhomogeneities and using parameters based on fully swollen hydrogels. We imposed free diffusion in the solution and hindered diffusion (due to the polymer network) in the hydrogel region. We imposed zero flux conditions $\left(\frac{\partial C}{\partial z} = 0\right)$ at the bottom of the culture well ($z = z_0$) and at the media air interface ($z = z_{\text{air}}$; Figure 2B). We prescribe continuity of the concentration and flux at the hydrogel/media interface. An initial concentration $C_0$ was prescribed in the hydrogel region and an initial concentration of 0 in the solution phase. The diffusion coefficient in the solution is approximated as the free diffusion coefficient $D_0$ in water of the solute and is given by the Stokes–Einstein equation:

$$D_0 = \frac{k_b T}{6\pi\eta r_s} \tag{8}$$

Here, $k_b$ is the Boltzmann constant, $T$ the temperature of the solution in Kelvin, $\eta$ is the dynamic viscosity of the medium in Pascal seconds, and $r_s$ is the hydrodynamic radius of the diffusing solute in meters.[36,37] This approach assumes diffusing molecules to be spheres moving in a continuum of solvent.[38]

The impact of the polymer phase on diffusion is modeled through an effective diffusion coefficient that captures the dependence on polymer chain radius and mesh size. The effective diffusion coefficient through the hydrogel is given by

$$\frac{D_{\text{eff}}}{D_0} = \exp\left(-\pi\left(\frac{r_s + r_f}{\xi + 2r_f}\right)^2\right) \tag{9}$$

in which $r_f$ is the polymer chain radius and $\xi$ the mesh size, both in meters.[35,37] All simulations were conducted using the COMSOL Multiphysics finite element solver with the additional microfluidics module. A mesh independence study was conducted to ensure solutions' numerical convergence as mesh element size was decreased. Elements of size 0.001 mm were used for the final simulations resulting in 50 001 elements in the mesh. The parameters in the model and their values are summarized in Table 2.

**Experimental Measurements of FITC–Dextran Diffusion from Hydrogels.** The 10, 40, and 70 kDa fluorescein isothiocyanate (FITC)-labeled dextran molecules (Sigma-Aldrich) were encapsulated at a concentration of 47.62 $\mu$M in 60 $\mu$L of 2.5%, 5%, and 10% hydrogels cast in flat-bottomed 96-well plates and allowed to gel for 60 min at 37 °C. Once gelled, wells were topped up with 240 $\mu$L of 30 mM HEPES buffer (pH 8). A total of 60 $\mu$L of solution was transferred to black bottom 96-well plates, and the absolute fluorescence was measured using a Promega GloMax Discover microplate reader (excitation 475 nm, emission 500–550 nm, peak emission measured). Measurements were made every hour for the first 4 h and then at regular intervals thereafter. Data were tested for significance using a one-way ANOVA with Tukey's multiple comparison correction at 2 h and 24 h. Experimental data were then normalized to steady state fluorescence by first fitting an exponential plateau function of the form $f(x) = Y_m \times e^{-kx}$ where $k$ represents a growth rate constant and $Y_m$ is the maximum fluorescence value ($R^2$ values all >0.92). Fluorescence measurements were then normalized to the end point value to enable comparisons between experimental data and modeling results. These data were then used to parametrize the model for $D_{\text{eff}}$.

## RESULTS AND DISCUSSION

**Tetra-PEG Hydrogel Physical Properties Are Dependent on Polymer Concentration.** To build a model of solute diffusivity, we required baseline experimental parameters for the tetra-PEG hydrogel system. Therefore, we first measured the mass swelling ratio of hydrogels with polymer concentrations of 2.5%, 5%, and 10% (Figure 3). On the basis of these values, we applied the Flory–Rehner model to calculate

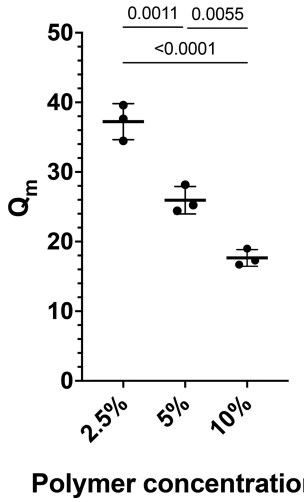


Figure 3. Mass swelling ratio ($Q_m$) for 2.5%, 5%, and 10% hydrogels calculated using the hydrogels' wet weight (at swelling equilibrium) and dry weight ($n$ = 3 independent hydrogels, mean ± SD, one-way Anova with Tukey's multiple comparison test).


https://doi.org/10.1021/acsbiomaterials.0c01723
ACS Biomater. Sci. Eng. 2021, 7, 4293–4304

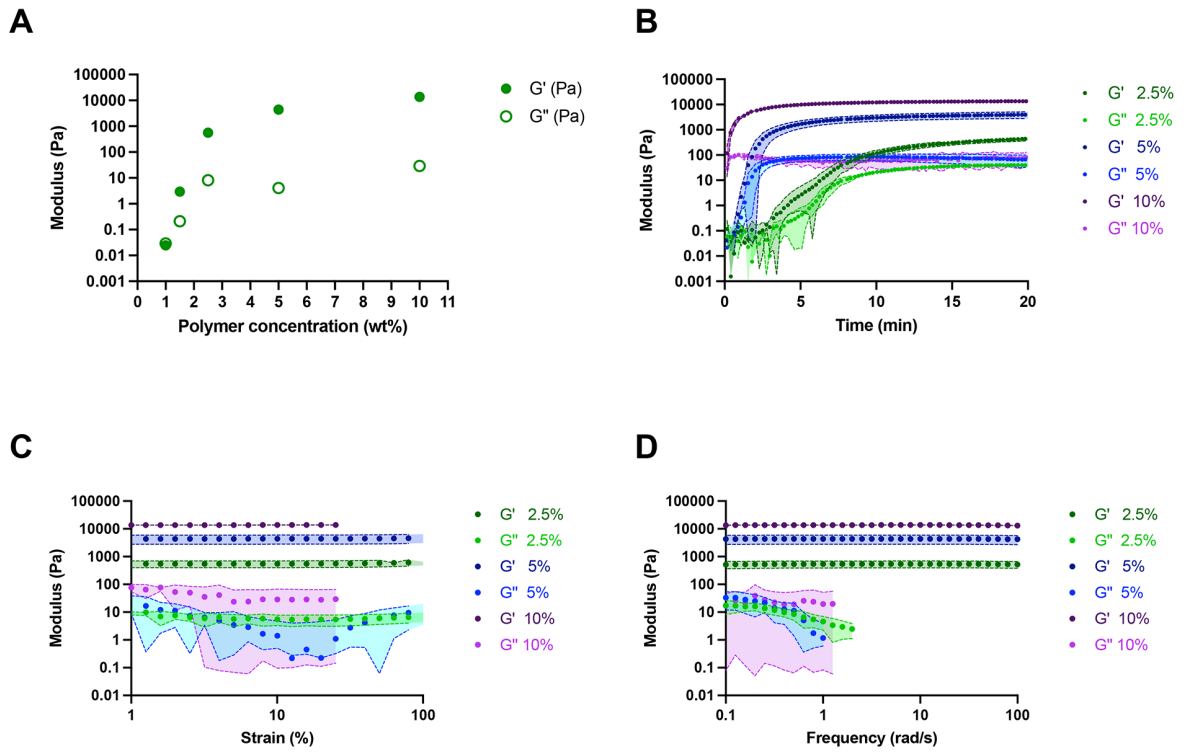


**Figure 4.** Rheological measurements performed on PEG hydrogels. (A) Mean plateau moduli of hydrogels of varying polymer concentrations. Hydrogels form ($G' > G''$) at polymer concentrations ≥ 1.5%. Mean modulus was calculated from data collected for 10 min after plateau values were reached. (B) Time sweep measurements of the gelation reaction. Higher polymer concentration hydrogels have a higher plateau value and form more quickly. (C) Strain sweep measurements, $G'$ was significantly different between all three samples ($p < 0.0001$ for 2.5% vs 5%, 2.5% vs 10% and 5% vs 10%); $G''$ not significant ($p > 0.9999$ for 2.5% vs 5%, $p = 0.2647$ for 2.5% vs 10%, and $p = 0.2659$ for 5% vs 10%), both by one-way ANOVA with Tukey's correction for multiple comparisons. (D) Frequency sweep measurements. The loss modulus could not be determined for the full range of frequencies accessed. In panels A–D, data are shown as means (dots) with the shaded area representing SD; $n = 3$ independent hydrogels for each condition. Some errors are small and not visible.

theoretical mesh sizes, which yielded values of 8.41, 7.41, and 6.43 nm for the 2.5, 5, and 10% hydrogels, respectively. These findings were in line with expected trends that hydrogels formed with higher polymer concentrations have smaller mesh sizes.

Next, we characterized the mechanical behavior of the tetra-PEG hydrogels. Mechanical studies using oscillatory rheology can provide insight into hydrogel gelation kinetics and stiffness.[39] To determine the critical polymer concentration for hydrogel formation, we tested hydrogels formed with varying polymer concentrations and determined gelation from the point at which the storage modulus ($G'$) was greater than the loss modulus ($G''$). These data show that tetra-PEG hydrogels form at polymer concentrations of 1.5% and higher (polymer concentrations of 1% behave as viscous liquids; Figure 4A). Time sweep measurements further revealed that gelation occurs more quickly for higher polymer concentration gels. Ten-percent hydrogels formed in the short time frame between loading the sample and measuring the first data point. Alternatively, 5% hydrogels reached plateau values of $G'$ and $G''$ within 10 min, and 2.5% hydrogels reached plateau values in ∼20 min (Figure 4B). These findings are consistent with theoretical predictions that an increased concentration of reactive groups should drive faster reaction kinetics. We also found that $G'$ was significantly different for all three polymer concentrations ($p < 0.0001$ for 2.5% vs 5%, 2.5% vs 10%, 5% vs 10%). However, the loss moduli did not differ significantly from one another ($p > 0.9999$ for 2.5% vs 5%, $p = 0.2647$ for 2.5% vs 10%, and $p = 0.2659$ for 5% vs 10%). The 10% hydrogel showed strain resistance up to 25%, whereas both the 5% and 2.5% polymer concentrations showed strain resistance within the accessed range (Figure 4C). No frequency dependence in storage moduli was observed for any of the three formulations (Figure 4D). Taken together, these data show that tetra-PEG hydrogels form at polymer concentrations ≥ 1.5% and that their gelation kinetics and resulting equilibrium moduli follow expected patterns based on polymer concentrations.

**Mathematical Models Predict That Mesh Size Plays a Limited Role in Diffusivity for Small Solutes.** With the hydrogels' physical properties well characterized, we next aimed to build a diffusion model treating the polymer chains as an obstruction to diffusing molecules. The hydrodynamic radii of biologically relevant proteins are generally within the range of a few nanometers. Indeed, cytokines such as IFN$\gamma$ and TNF$\alpha$ are reported to have hydrodynamic radii of 1.85 nm[40] and 3 nm,[41] respectively. Bovine serum albumin is reported to be 3.56 nm[42] and MMP-9 4.5 nm.[43] Some secreted proteins, however, have hydrodynamic radii that are considerably larger. For example, the ubiquitous iron-storing protein ferritin has a hydrodynamic radius of 7.17 nm,[44] and the ECM protein fibronectin is 8.7 nm.[45] Large proteoglycans can be as much as an order of magnitude larger (∼80 nm[46]), but these are generally accepted to not diffuse within hydrogels. Therefore,


https://doi.org/10.1021/acsbiomaterials.0c01723
ACS Biomater. Sci. Eng. 2021, 7, 4293−4304

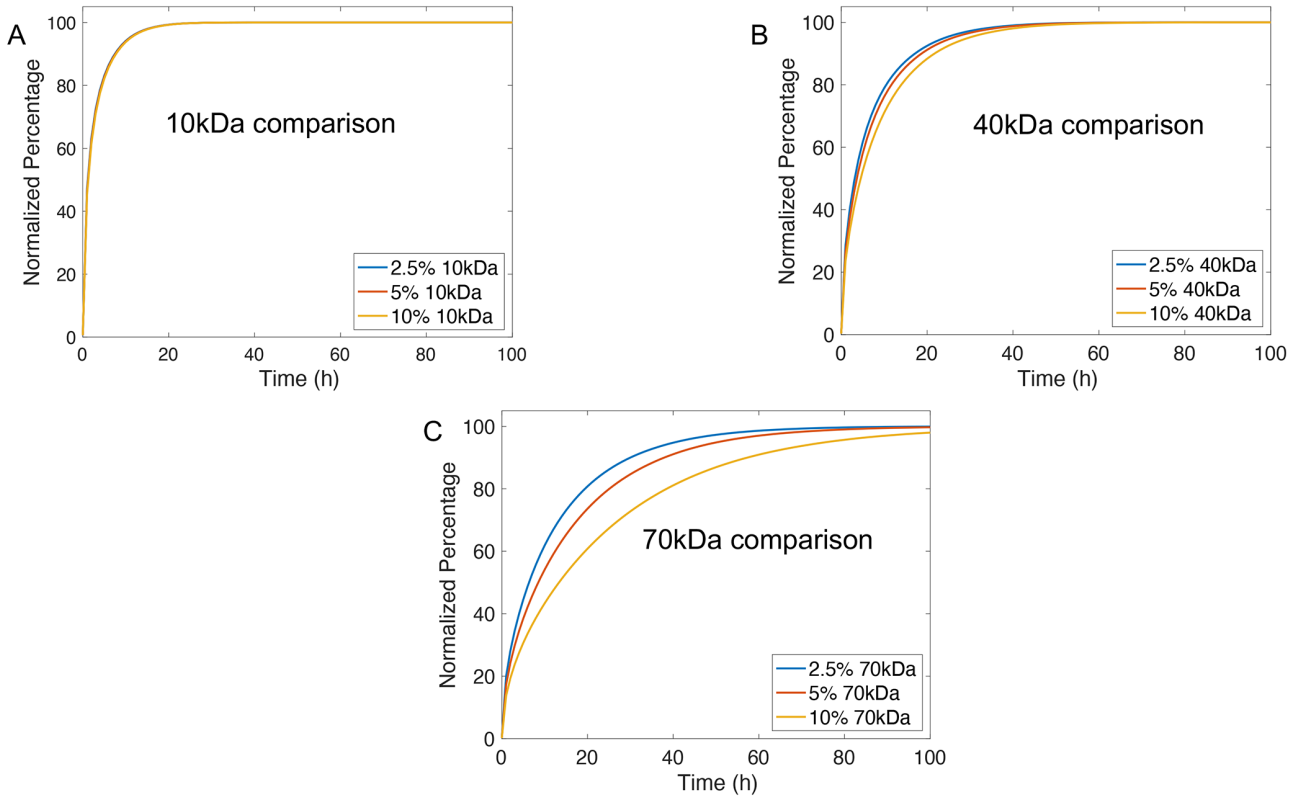


**Figure 5.** Plots generated using mathematical models showing the predicted average concentration of (A) 10 kDa, (B) 40 kDa, and (C) 70 kDa solutes in the solution above the gel normalized to the steady state concentration (to calculate a percentage of endpoint concentration) for 2.5%, 5%, and 10% hydrogels.

we considered solutes with hydrodynamic radii of 2.3, 4.5, and 6 nm, which correspond to the predicted values for 10 kDa, 40 kDa, or 70 kDa FITC-labeled dextran.

Using our model, we predicted the average concentration of 10 kDa, 40 kDa, or 70 kDa solutes over time in the solution above the hydrogel normalized relative to the steady state concentration prediction (Figure 5). We found that in the 10 kDa condition, diffusivity was negligibly impacted by changes in mesh size with a maximum percentage difference between the 2.5% and 10% conditions of 4.6% (Table 3). Changes in diffusivity in the 40 kDa condition were more pronounced between different mesh sizes with the largest difference of 20.8%. For the 70 kDa condition, mesh size had the greatest impact, as in 10% hydrogels we found that diffusivity changed up to 46% between profiles at each time point. In all conditions, models predicted that changing polymer concentration from 2.5% to 5% only resulted in a maximum change in diffusivity of 16%.

The time taken to reach a steady state concentration for all hydrogel compositions for the 10 kDa condition was ~20 h and for 40 kDa solutes was ~50 h. However, for 70 kDa solutes, the smaller mesh size of 10% hydrogels impacted the time to a steady state, extending it beyond the ~100 h found for the 5% and 2.5% conditions. For the 10 kDa solute, the transition to a steady state was faster compared to that of the 40 kDa solute, as half the steady state concentration was reached in <2 h. For the 40 kDa solute, this took <5 h. We then carried out parameter sweeps of solute size from 2 to 8 nm for a fixed mesh size and found that the time to achieve steady state concentration increased dramatically with

**Table 3. Table Summarizing the Maximum Percentage Difference between Diffusion Profiles As Predicted by Modeling Results for All Solute Sizes and Hydrogel Compositions**

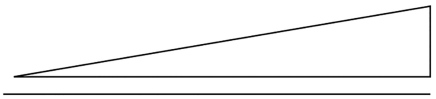

| | Maximum % difference between data sets | | |
|---|---|---|---|
| FITC dextran size | 2.5% vs 5% | 5% vs 10% | 2.5% vs 10% |
| 10kDa | 1.9 | 2.7 | 4.6 |
| 40kDa | 7.8 | 12.1 | 20.8 |
| 70kDa | 15.9 | 25.5 | 45.5 |

increasing solute hydrodynamic radius (Figure 6). In short, our model predicts that in tetra-PEG/$A_4$+$B_4$ hydrogels, mesh size does not have a large influence on the diffusion of small solutes but can have a more dramatic influence on larger solutes.

**Experimental Measurements Confirm That Polymer Concentration Only Minimally Impacts Solute Diffusion.** As our model had predicted that polymer concentration only substantially impacted diffusivity in the 10% condition for



https://doi.org/10.1021/acsbiomaterials.0c01723
ACS Biomater. Sci. Eng. 2021, 7, 4293−4304

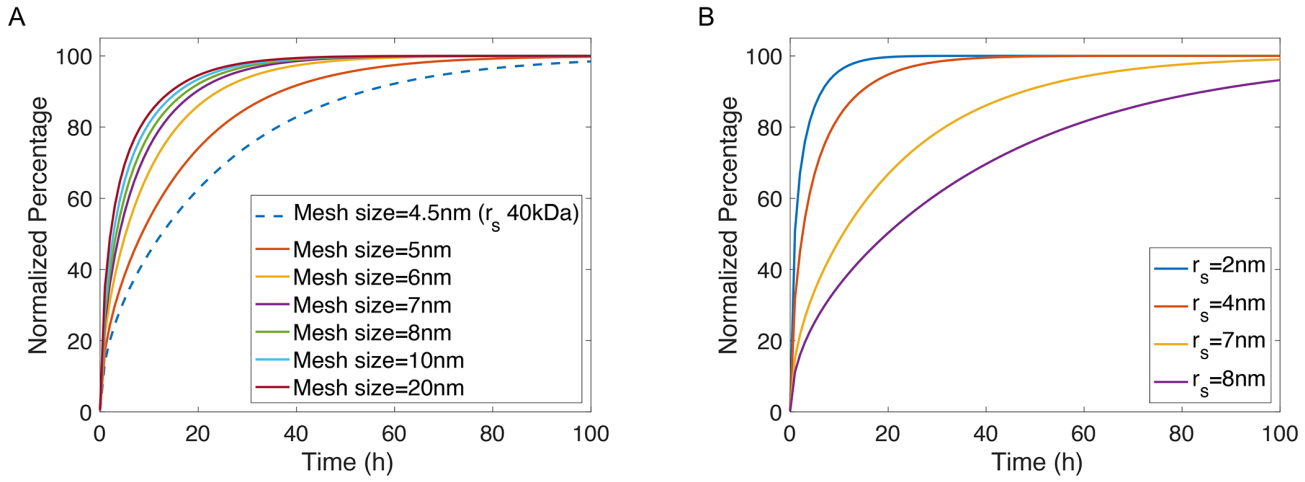


**Figure 6.** Plots generated using mathematical models showing results of parameter sweeps with (A) showing an average concentration of 40 kDa solute in the solution normalized to the steady state concentration above the hydrogel (to calculate a percentage of endpoint concentration) as the mesh network size is altered. (B) Average concentration of solute in the solution above a 2.5% hydrogel for solutes with different hydrodynamic radii ($r_s$). As the solute size increases, the diffusivity is reduced.

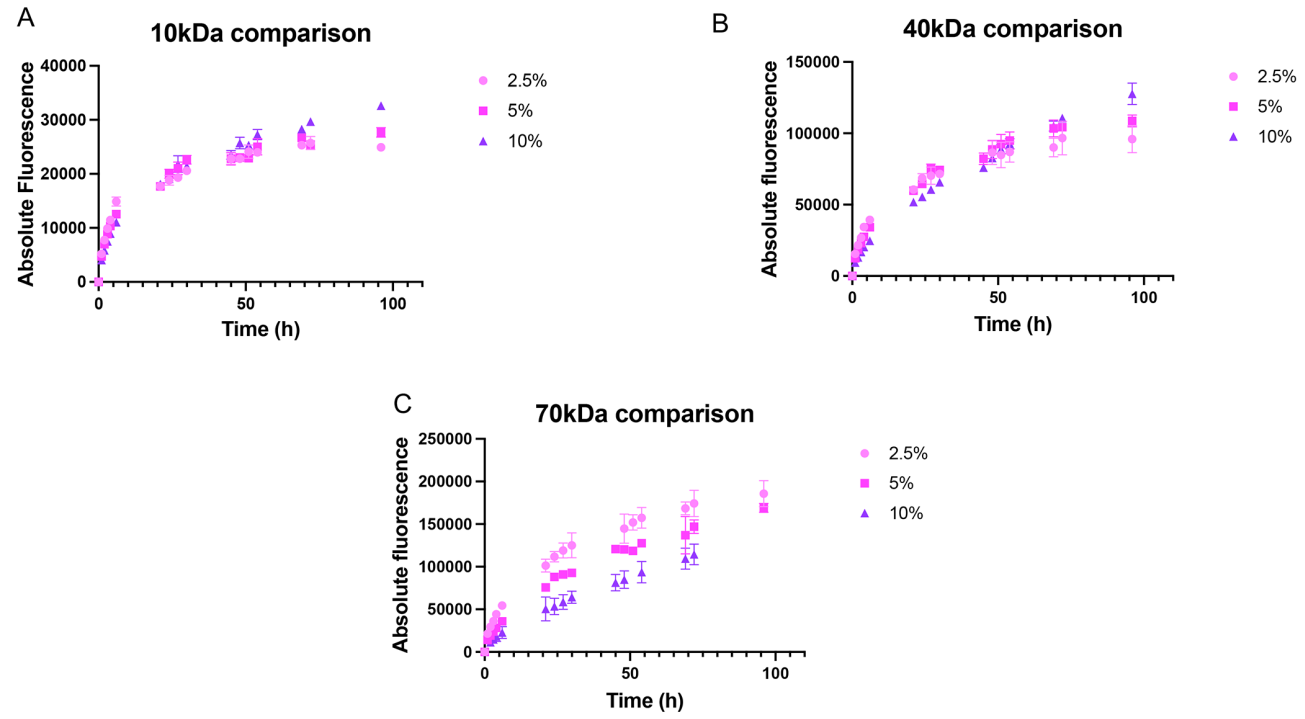


**Figure 7.** Plots showing absolute fluorescence in the media surrounding 2.5%, 5% and 10% hydrogels containing (A) 10 kDa, (B) 40 kDa, and (C) 70 kDa solutes ($n$ = 3, mean ± SD). Some error bars are small and not visible.

the larger solute, we next aimed to measure diffusivity experimentally. We formed 2.5%, 5%, and 10% tetra-PEG hydrogels that contained 10 kDa, 40 kDa, or 70 kDa FITC-labeled dextran molecules. Broadly, we observed that smaller molecules were not differentially hindered from diffusing over 100 h, with larger differences observed between polymer concentrations for the largest molecule. In the 10 kDa condition, the diffusivity profiles for all polymer concentrations were similar, with the time taken to plateau of ∼45 h (Figure 7). Similarly, in the 40 kDa condition, 2.5% and 5% hydrogels behaved similarly, with a time taken to plateau of ∼100 h; however, the 10% profile appeared to be marginally slowed. For 70 kDa solutes, differences between polymer concentration were more apparent, again confirming that changes in mesh size have a larger effect for larger molecules (Figure 7). Statistical analyses comparing fluorescence values in the solution surrounding hydrogels after 2 h revealed significant differences between polymer concentrations for all solute sizes (10 kDa: 2.5% vs 5% $p$ = 0.0035, 5% vs 10% $p$ = 0.0275, 2.5% vs 10% $p$ = 0.0002; 40 kDa: 2.5% vs 5% $p$ = 0.0009, 5% vs 10% $p$ < 0.0001, 2.5% vs 10% $p$ < 0.0001; 70 kDa: 2.5% vs 5% $p$ = 0.0072, 5% vs 10% $p$ = 0.0360, 2.5% vs 10% $p$ = 0.0005).


https://doi.org/10.1021/acsbiomaterials.0c01723
ACS Biomater. Sci. Eng. 2021, 7, 4293−4304

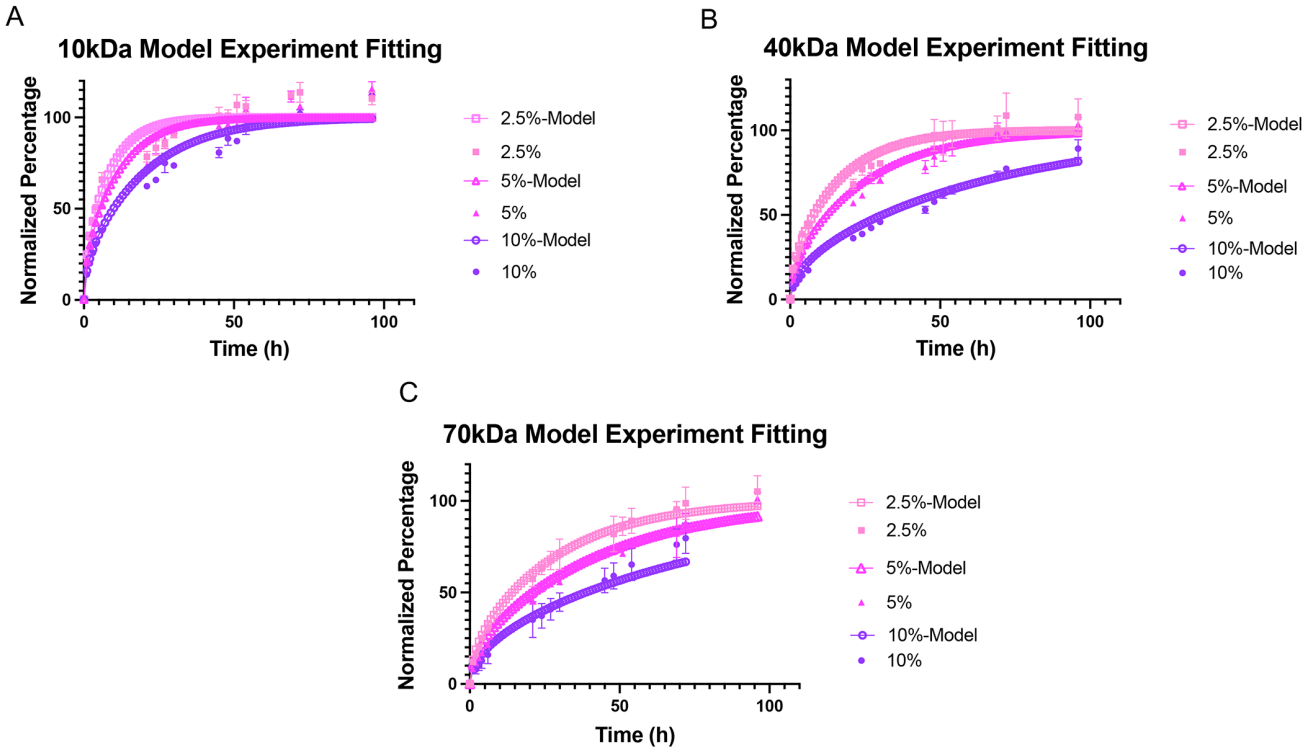


**Figure 8.** Normalized fluorescence from experimentally acquired measurements of (A) 10 kDa, (B) 40 kDa, and (C) 70 kDa FITC-labeled dextran plotted with fitted mathematical model predictions of solutes diffusing out of 2.5%, 5%, and 10% hydrogels. Experimental values are fitted to an exponential plateau function and normalized to the end point fluorescence to calculate a percentage of the total fluorescence for each time point ($n$ = 3, mean ± SD). Some error bars are small and not visible.

However, by 24 h, no significant differences were detected between polymer concentration in the 10 kDa condition. In the 40 kDa condition, we detected higher levels of fluorescence in the 5% and 2.5% conditions compared to the 10% (5% vs 10% $p$ = 0.0056, 2.5% vs 10% $p$ = 0.0008), but the 2.5% and 5% conditions were no different. For the 70 kDa condition, we detected significant differences between polymer concentrations for all comparisons (2.5% vs 5% $p$ = 0.0142, 5% vs 10% $p$ = 0.0022, 2.5% vs 10% $p$ = 0.0001). These observations suggest that the diffusion of larger solutes is far more impacted by changing polymer concentration than that of smaller solutes.

Overall, these data align with trends predicted by our models. They also suggest that doubling the polymer concentration from 2.5 to 5% produces hydrogels with faster gelling kinetics that are an order of magnitude stiffer without greatly affecting diffusivity in the long term. Indeed, increased polymer concentration only appears to affect the diffusion of the largest FITC-dextran molecule at stiffnesses that may not be suitable for cell encapsulation ($G'$> ∼ 10 kPa). These findings alleviate potential concerns surrounding PEG hydrogels that changes in stiffness may impact mass transport. Moreover, our hydrogel system allows us to analyze these impacts independently, thus taking advantage of the tunability of the PEG system while minimizing possible confounding effects from changes in mass transport.

Our experimental and modeling findings both identified that smaller solutes diffuse faster than larger in our tetra-PEG network. Our findings also show that the time required to achieve a steady state is non-negligible. This is of importance for 3D cell cultures in which both delivery of factors to cells from outside the hydrogel (growth factors, e.g.) and detection of biomolecules produced by cells (cytokines, e.g.) in the surrounding media depend on diffusion. In particular, the latter should only be sampled (or interpreted) at time scales that account for these effects. Furthermore, our modeling and experimental data suggest that differences between diffusion profiles tend to occur within the first hours. We suggest that differences in diffusion over this time frame are likely to have a minimal impact on experimental setups, as time scales are often longer.

We fitted our model to experimental results for $D_{eff}$, which depends on both solute size and mesh size ($R^2$ values all > 0.944; Figure 8). In some cases, differences between the polymer concentrations normalized versus experimental fluorescence values appeared more pronounced in models; however, this was likely attributable to our strategy of normalizing experimental data to a predicted steady state value from the data fitting. To determine which parameter plays the larger role in determining diffusivity, we analyzed the sensitivity of the model to both parameters. Our results show that network diffusivity, as initially predicted by our model, was systematically overestimated. This is in agreement with others' findings that obstruction theory overestimates diffusivity.[37] Such overestimations may extend from model assumptions, including that solutes are treated as hard spheres of fixed radius. In reality, molecules like dextran have more nebulous structures, and their hydrodynamic radii are unlikely to remain fixed as they diffuse through the network.[25] Furthermore, our model predictions rely on estimates of mesh size. Mesh sizes are notoriously complex to obtain, and there remains debate concerning the accuracy of different prediction methods.[23] A final limitation of our model is that potential interactions


https://doi.org/10.1021/acsbiomaterials.0c01723
ACS Biomater. Sci. Eng. 2021, 7, 4293−4304

between the polymer and solute molecules is not accounted for; however, others have shown that this simplification is reasonable.[35,37] Nevertheless, despite discrepancies between our predictions and experimental findings, we can have confidence in the trends predicted by our model as fitting only served to scale the value of the effective diffusivity rather than change the predicted diffusion profile.

By performing parameter sweeps changing for mesh size and solute size incrementally, we were able to observe the role of each parameter in determining overall diffusivity. Thus, our model provided additional insight into mechanisms that drive network diffusivity. Indeed, the impact of changing mesh size was negligible and only had an increasingly larger effect as mesh size approached the hydrodynamic radius of the solute. These results are in line with our experimental findings that increasing polymer concentration to 10% had a greater impact on diffusion compared to increasing from 2.5% to 5%. On the other hand, our models predicted that solute size played a far larger role in predicting diffusion, with larger solutes taking longer to diffuse than smaller. For example, our model predicted that solutes with a radius of 7 nm versus 8 nm diffusing out of a 2.5% hydrogel produced a maximum percentage difference between profiles of 36%.

Our theoretical estimates predict that 40 kDa and 70 kDa molecules should remain trapped within hydrogels, as we predicted hydrogel mesh size to be smaller than dextran molecules' hydrodynamic diameter. However, though diffusion was increasingly hindered at higher polymer concentrations for larger molecules, they were still able to escape the hydrogels, in keeping with previous reports.[25] These findings suggest an underestimation of mesh size or an overestimation of solute effective radius. It is also possible that encapsulating FITC-dextran within hydrogels impacts the mesh, driving the inconsistencies. In short, while theoretical predictions are useful for estimating diffusivity, these discrepancies highlight the importance of experimentally measuring diffusion. Parameters from these experiments can then be used to improve models.

## CONCLUSIONS

The diffusivity of solutes in hydrogels is important for the viability and activity of encapsulated cells and will regulate the diffusion and/or local retention of secreted factors, which play important roles in regulating cell behavior.[22,47,48] Here, we show using theoretical estimates of hydrogel mesh size that predictions for the diffusivity of solutes with known hydrodynamic radii reasonably match experimental diffusion behaviors. We also show that altering polymer concentration in our tetra-PEG design allows us to produce hydrogels with different mechanical stiffnesses without significantly impacting diffusivity for hydrogels up to a polymer concentration of 5%. Hydrogels are increasingly used to explore hypotheses regarding the role of mechanical stiffness in regulating cell behaviors. Our findings provide confidence that such questions can be addressed in tetra-PEG hydrogels without introducing the confounding effect of differing transport rates of solutes to and from encapsulated cells. Moreover, as the $A_4$+$B_4$ hydrogel design allows for stiffer hydrogels to be formed at low polymer concentrations compared to $A_2$+$B_4$ designs, stiffer *in vitro* tissue models can be formed without compromising diffusivity. However, our findings also highlight the importance of solute size on diffusion rates, suggesting that it should be an important consideration in experimental designs that aim to deliver factors to encapsulated cells or assay secreted proteins in culture supernatants. Combined with our previous work[11] showing that tetra-PEG designs can also allow for quick gelation at low polymer concentrations, producing hydrogels that are sufficiently soft for encapsulation of human intestinal organoids, we have gone some way to demonstrate that these hydrogels are suitable for a range of applications.

## AUTHOR INFORMATION


### Corresponding Author

**Eileen Gentleman** − *Centre for Craniofacial and Regenerative Biology, King's College London, London SE1 9RT, United Kingdom;* orcid.org/0000-0003-0447-5137; Email: eileen.gentleman@kcl.ac.uk

### Authors

**Suzette T. Lust** − *Centre for Craniofacial and Regenerative Biology, King's College London, London SE1 9RT, United Kingdom; School of Biomedical Engineering and Imaging Sciences, King's College London, London SE1 7EH, United Kingdom;* orcid.org/0000-0002-3399-596X

**Dominique Hoogland** − *Department of Chemistry, King's College London, London SE1 1DB, United Kingdom;* orcid.org/0000-0002-1655-2833

**Michael D. A. Norman** − *Centre for Craniofacial and Regenerative Biology, King's College London, London SE1 9RT, United Kingdom;* orcid.org/0000-0001-8089-9084

**Caoimhe Kerins** − *Centre for Craniofacial and Regenerative Biology, King's College London, London SE1 9RT, United Kingdom;* orcid.org/0000-0001-6418-8776

**Jasmin Omar** − *Institute of Pharmaceutical Science, King's College London, London SE1 9NH, United Kingdom;* orcid.org/0000-0003-0693-4755

**Geraldine M. Jowett** − *Centre for Craniofacial and Regenerative Biology, King's College London, London SE1 9RT, United Kingdom;* orcid.org/0000-0002-8436-6637

**Tracy T. L. Yu** − *Centre for Craniofacial and Regenerative Biology, King's College London, London SE1 9RT, United Kingdom;* orcid.org/0000-0003-4279-5019

**Ziqian Yan** − *Centre for Craniofacial and Regenerative Biology, King's College London, London SE1 9RT, United Kingdom*

**Jessie Z. Xu** − *Centre for Craniofacial and Regenerative Biology, King's College London, London SE1 9RT, United Kingdom;* orcid.org/0000-0003-0333-6127

**Daniele Marciano** − *Centre for Craniofacial and Regenerative Biology, King's College London, London SE1 9RT, United Kingdom*

**Ricardo M. P. da Silva** − *Centre for Craniofacial and Regenerative Biology, King's College London, London SE1 9RT, United Kingdom;* orcid.org/0000-0003-1456-8724

**Cécile A. Dreiss** − *Institute of Pharmaceutical Science, King's College London, London SE1 9NH, United Kingdom;* orcid.org/0000-0002-0578-8090

**Pablo Lamata** − *School of Biomedical Engineering and Imaging Sciences, King's College London, London SE1 7EH, United Kingdom*

**Rebecca J. Shipley** − *Institute of Healthcare Engineering and Department of Mechanical Engineering, University College London, London WC1E 7JE, United Kingdom*

Complete contact information is available at: https://pubs.acs.org/10.1021/acsbiomaterials.0c01723




https://doi.org/10.1021/acsbiomaterials.0c01723
ACS Biomater. Sci. Eng. 2021, 7, 4293−4304

### Notes

The authors declare no competing financial interest.

According to UK research councils' Common Principles on Data Policy and the Wellcome Trust's Policy on data, software and materials management and sharing, all data supporting this study is available within the manuscript.

## ■ ACKNOWLEDGMENTS

S.T.L. gratefully acknowledges the UK Medical Research Council [MR/N013700/1] for funding through the MRC Doctoral Training Partnership in Biomedical Sciences at King's College London. M.D.A.N. is supported by a Ph.D. studentship funded by the BBSRC London Interdisciplinary Doctoral Programme. G.M.J. acknowledges a Ph.D. fellowship from the Wellcome Trust [203757/Z/16/A]. R.M.P.d.S. acknowledges a King's Prize fellowship supported by the Wellcome Trust (Institutional Strategic Support Fund), King's College London and the London Law Trust. R.J.S. gratefully acknowledges funding from the Engineering and Physical Sciences Research Council [EPR004463/1]. PL holds a Wellcome Trust Senior Research Fellowship [209450/Z/17/Z].

## ■ REFERENCES

(1) Discher, D. E.; Mooney, D. J.; Zandstra, P. W. Growth Factors, Matrices, and Forces Combine and Control Stem Cells. *Science* **2009**, *324*, 1673.

(2) Guilak, F.; Cohen, D. M.; Estes, B. T.; Gimble, J. M.; Liedtke, W.; Chen, C. S. Control of Stem Cell Fate by Physical Interactions with the Extracellular Matrix. *Cell Stem Cell.* **2009**, *5*, 17.

(3) Walters, N. J.; Gentleman, E. Evolving Insights in Cell-Matrix Interactions: Elucidating How Non-Soluble Properties of the Extracellular Niche Direct Stem Cell Fate. *Acta Biomater.* **2015**, *11* (1), 3−16.

(4) Blache, U.; Stevens, M. M.; Gentleman, E. Harnessing the Secreted Extracellular Matrix to Engineer Tissues. *Nat. Biomed. Eng.* **2020**, *4* (4), 357−363.

(5) Evans, N. D.; Gentleman, E. The Role of Material Structure and Mechanical Properties in Cell-Matrix Interactions. *J. Mater. Chem. B* **2014**, *2*, 2345.

(6) Baker, B. M.; Chen, C. S. Deconstructing the Third Dimension-How 3D Culture Microenvironments Alter Cellular Cues. *J. Cell Sci.* **2012**, *125* (13), 3015−3024.

(7) Cukierman, E.; Pankov, R.; Stevens, D. R.; Yamada, K. M. Taking Cell-Matrix Adhesions to the Third Dimension. *Science* **2001**, *294* (5547), 1708−1712.

(8) Foyt, D. A.; Norman, M. D. A.; Yu, T. T. L.; Gentleman, E. Exploiting Advanced Hydrogel Technologies to Address Key Challenges in Regenerative Medicine. *Adv. Healthcare Mater.* **2018**, *7* (8), 1700939.

(9) Lutolf, M. P.; Tirelli, N.; Cerritelli, S.; Cavalli, L.; Hubbell, J. A. Systematic Modulation of Michael-Type Reactivity of Thiols through the Use of Charged Amino Acids. *Bioconjugate Chem.* **2001**, *12* (6), 1051−1056.

(10) Lutolf, M. P.; Hubbell, J. A. Synthesis and Physicochemical Characterization of End-Linked Poly(Ethylene Glycol)-Co-Peptide Hydrogels Formed by Michael-Type Addition. *Biomacromolecules* **2003**, *4* (3), 713−722.

(11) Jowett, G. M.; Norman, M. D. A.; Yu, T. T. L.; Rosell Arévalo, P.; Hoogland, D.; Lust, S. T.; Read, E.; Hamrud, E.; Walters, N. J.; Niazi, U.; Chung, M. W. H.; Marciano, D.; Omer, O. S.; Zabinski, T.; Danovi, D.; Lord, G. M.; Hilborn, J.; Evans, N. D.; Dreiss, C. A.; Bozec, L.; Oommen, O. P.; Lorenz, C. D.; da Silva, R. M. P.; Neves, J. F.; Gentleman, E. ILC1 Drive Intestinal Epithelial and Matrix Remodelling. *Nat. Mater.* **2021**, *20*, 250.

(12) Shibayama, M. Small-Angle Neutron Scattering on Polymer Gels: Phase Behavior, Inhomogeneities and Deformation Mechanisms. *Polym. J.* **2011**, *43* (1), 18−34.

(13) Wang, R.; Alexander-Katz, A.; Johnson, J. A.; Olsen, B. D. Universal Cyclic Topology in Polymer Networks. *Phys. Rev. Lett.* **2016**, DOI: 10.1103/PhysRevLett.116.188302.

(14) Saffer, E. M.; Lackey, M. A.; Griffin, D. M.; Kishore, S.; Tew, G. N.; Bhatia, S. R. SANS Study of Highly Resilient Poly(Ethylene Glycol) Hydrogels. *Soft Matter* **2014**, *10* (12), 1905−1916.

(15) Sakai, T.; Matsunaga, T.; Yamamoto, Y.; Ito, C.; Yoshida, R.; Suzuki, S.; Sasaki, N.; Shibayama, M.; Chung, U. I. Design and Fabrication of a High-Strength Hydrogel with Ideally Homogeneous Network Structure from Tetrahedron-like Macromonomers. *Macromolecules* **2008**, *41* (14), 5379−5384.

(16) Wang, R.; Sing, M. K.; Avery, R. K.; Souza, B. S.; Kim, M.; Olsen, B. D. Classical Challenges in the Physical Chemistry of Polymer Networks and the Design of New Materials. *Acc. Chem. Res.* **2016**, *49*, 2786.

(17) Rezakhani, S.; Gjorevski, N.; Lutolf, M. P. Low-Defect Thiol-Michael Addition Hydrogels as Matrigel Substitutes for Epithelial Organoid Derivation. *Adv. Funct. Mater.* **2020**, *30* (48), 2000761.

(18) Phelps, E. A.; Enemchukwu, N. O.; Fiore, V. F.; Sy, J. C.; Murthy, N.; Sulchek, T. A.; Barker, T. H.; García, A. J. Maleimide Cross-Linked Bioactive PEG Hydrogel Exhibits Improved Reaction Kinetics and Cross-Linking for Cell Encapsulation and in Situ Delivery. *Adv. Mater.* **2012**, *24*, 64.

(19) Amsden, B. Solute Diffusion in Hydrogels.: An Examination of the Retardation Effect. *Polym. Gels Networks* **1998**, *6* (1), 13−43.

(20) Ramanujan, S.; Pluen, A.; McKee, T. D.; Brown, E. B.; Boucher, Y.; Jain, R. K. Diffusion and Convection in Collagen Gels: Implications for Transport in the Tumor Interstitium. *Biophys. J.* **2002**, *83* (3), 1650−1660.

(21) Mahadik, B. P.; Bharadwaj, N. A. K.; Ewoldt, R. H.; Harley, B. A. C. Regulating Dynamic Signaling between Hematopoietic Stem Cells and Niche Cells via a Hydrogel Matrix. *Biomaterials* **2017**, *125*, 54.

(22) Ferreira, S. A.; Faull, P. A.; Seymour, A. J.; Yu, T. T. L.; Loaiza, S.; Auner, H. W.; Snijders, A. P.; Gentleman, E. Neighboring Cells Override 3D Hydrogel Matrix Cues to Drive Human MSC Quiescence. *Biomaterials* **2018**, *176*, 13−23.

(23) Tsuji, Y.; Li, X.; Shibayama, M. Evaluation of Mesh Size in Model Polymer Networks Consisting of Tetra-Arm and Linear Poly(Ethylene Glycol)s. *Gels* **2018**, *4* (2), 50.

(24) Richbourg, N. R.; Peppas, N. A. The Swollen Polymer Network Hypothesis: Quantitative Models of Hydrogel Swelling, Stiffness, and Solute Transport. *Prog. Polym. Sci.* **2020**, *105*, 101243.

(25) Rehmann, M. S.; Skeens, K. M.; Kharkar, P. M.; Ford, E. M.; Maverakis, E.; Lee, K. H.; Kloxin, A. M. Tuning and Predicting Mesh Size and Protein Release from Step Growth Hydrogels. *Biomacromolecules* **2017**, *18*, 3131.

(26) Peppas, N. A.; Bures, P.; Leobandung, W.; Ichikawa, H. Hydrogels in Pharmaceutical Formulations. *Eur. J. Pharm. Biopharm.* **2000**, *50* (1), 27−46.

(27) Matsunaga, T.; Sakai, T.; Akagi, Y.; Chung, U. I.; Shibayama, M. Structure Characterization of Tetra-PEG Gel by Small-Angle Neutron Scattering. *Macromolecules* **2009**, *42*, 1344.

(28) McCall, J. D.; Lin, C. C.; Anseth, K. S. Affinity Peptides Protect Transforming Growth Factor Beta during Encapsulation in Poly-(Ethylene Glycol) Hydrogels. *Biomacromolecules* **2011**, *12*, 1051.

(29) Dikovsky, D.; Bianco-Peled, H.; Seliktar, D. The Effect of Structural Alterations of PEG-Fibrinogen Hydrogel Scaffolds on 3-D Cellular Morphology and Cellular Migration. *Biomaterials* **2006**, *27*, 1496.

(30) Russell, L. N.; Lampe, K. J. Oligodendrocyte Precursor Cell Viability, Proliferation, and Morphology Is Dependent on Mesh Size and Storage Modulus in 3D Poly(Ethylene Glycol)-Based Hydrogels. *ACS Biomater. Sci. Eng.* **2017**, *3*, 3459.

(31) Zustiak, S. P.; Leach, J. B. Hydrolytically Degradable Poly(Ethylene Glycol) Hydrogel Scaffolds with Tunable Degradation and Mechanical Properties. *Biomacromolecules* **2010**, *11*, 1348.

(32) Raeber, G. P.; Lutolf, M. P.; Hubbell, J. A. Molecularly Engineered PEG Hydrogels: A Novel Model System for Proteolytically Mediated Cell Migration. *Biophys. J.* **2005**, *89* (2), 1374−1388.
(33) Amsden, B. An Obstruction-Scaling Model for Diffusion in Homogeneous Hydrogels. *Macromolecules* **1999**, *32* (3), 874−879.
(34) Sun, T.; Zhang, L.; Chen, J.; Shen, Y. Elastic Behavior of Short Compact Polymers. *J. Chem. Phys.* **2004**, *120* (11), 5469−5475.
(35) Hadjiev, N. A.; Amsden, B. G. An Assessment of the Ability of the Obstruction-Scaling Model to Estimate Solute Diffusion Coefficients in Hydrogels. *J. Controlled Release* **2015**, *199*, 10−16.
(36) Miller, C. C. The Stokes-Einstein Law for Diffusion in Solution. *Proceedings of the Royal Society of London. Series A, Containing Papers of a Mathematical and Physical Character* **1924**, *106*, 724.
(37) Axpe, E.; Chan, D.; Offeddu, G. S.; Chang, Y.; Merida, D.; Hernandez, H. L.; Appel, E. A. A Multiscale Model for Solute Diffusion in Hydrogels. *Macromolecules* **2019**, *52* (18), 6889−6897.
(38) Cussler, E. L. *Diffusion: Mass Transfer in Fluid Systems*, 3rd ed; Cambridge University Press, 1997.
(39) Zuidema, J. M.; Rivet, C. J.; Gilbert, R. J.; Morrison, F. A. A Protocol for Rheological Characterization of Hydrogels for Tissue Engineering Strategies. *J. Biomed. Mater. Res., Part B* **2014**, *102*, 1063.
(40) Kendrick, B. S.; Carpenter, J. F.; Cleland, J. L.; Randolph, T. W. A Transient Expansion of the Native State Precedes Aggregation of Recombinant Human Interferon-$\gamma$. *Proc. Natl. Acad. Sci. U. S. A.* **1998**, *95*, 14142.
(41) Schoenfeld, H. J.; Poeschl, B.; Frey, J. R.; Loetscher, H.; Hunziker, W.; Lustig, A.; Zulauf, M. Efficient Purification of Recombinant Human Tumor Necrosis Factor $\beta$ from Escherichia Coli Yields Biologically Active Protein with a Trimeric Structure That Binds to Both Tumor Necrosis Factor Receptors. *J. Biol. Chem.* **1991**, *266*, 3863.
(42) Weber, L. M.; Lopez, C. G.; Anseth, K. S. Effects of PEG Hydrogel Crosslinking Density on Protein Diffusion and Encapsulated Islet Survival and Function. *J. Biomed. Mater. Res., Part A* **2009**, *90* (3), 720−729.
(43) Rosenblum, G.; Van den Steen, P. E.; Cohen, S. R.; Grossmann, J. G.; Frenkel, J.; Sertchook, R.; Slack, N.; Strange, R. W.; Opdenakker, G.; Sagi, I. Insights into the Structure and Domain Flexibility of Full-Length Pro-Matrix Metalloproteinase-9/Gelatinase B. *Structure* **2007**, *15*, 1227.
(44) Stetefeld, J.; McKenna, S. A.; Patel, T. R. Dynamic Light Scattering: A Practical Guide and Applications in Biomedical Sciences. *Biophys. Rev.* **2016**, *8*, 409.
(45) Nelea, V.; Nakano, Y.; Kaartinen, M. T. Size Distribution and Molecular Associations of Plasma Fibronectin and Fibronectin Crosslinked by Transglutaminase 2. *Protein J.* **2008**, *27*, 223.
(46) Comper, W. D.; Williams, R. P. Hydrodynamics of Concentrated Proteoglycan Solutions. *J. Biol. Chem.* **1987**, *262*, 13464.
(47) Loebel, C.; Mauck, R. L.; Burdick, J. A. Local Nascent Protein Deposition and Remodelling Guide Mesenchymal Stromal Cell Mechanosensing and Fate in Three-Dimensional Hydrogels. *Nat. Mater.* **2019**, *18*, 883.
(48) Ferreira, S. A.; Motwani, M. S.; Faull, P. A.; Seymour, A. J.; Yu, T. T. L.; Enayati, M.; Taheem, D. K.; Salzlechner, C.; Haghighi, T.; Kania, E. M.; Oommen, O. P.; Ahmed, T.; Loaiza, S.; Parzych, K.; Dazzi, F.; Varghese, O. P.; Festy, F.; Grigoriadis, A. E.; Auner, H. W.; Snijders, A. P.; Bozec, L.; Gentleman, E. Bi-Directional Cell-Pericellular Matrix Interactions Direct Stem Cell Fate. *Nat. Commun.* **2018**, *9* (1), 1−12.
(49) Merrill, E. W.; Dennison, K. A.; Sung, C. Partitioning and Diffusion of Solutes in Hydrogels of Poly(Ethylene Oxide). *Biomaterials* **1993**, *14*, 1117.


https://doi.org/10.1021/acsbiomaterials.0c01723
*ACS Biomater. Sci. Eng.* 2021, 7, 4293−4304

# Chapter 5

# Developing an *in-vitro* Culture of 3D Encapsulated VSMCs

## Chapter Abstract

**Background**: In order to test whether vascular cell-ECM interaction is altered in the presence of flow, we first need a baseline static *in-vitro* culture. This setup should allows us to observe evidence of cell-matrix interaction so we can then infer changes, if any, in these interactions in flow conditions. As discussed in Chapter 1, we concern ourselves specifically with VSCM interactions and we therefore aimed to create a reductionist model in which these cells can be long-term cultured in 3D, seen to interact with their surrounding matrix and eventually treated with interstitial flows. To this end, in lieu of using tissue, a bio-material is used to keep cell cultures in 3D. As previously described, a synthetic PEG based hydrogel was selected for this work in which stiffness, biodegradability and availability of adhesive ligands can be independently tuned.

**Aim**: With data in hand characterising the basic properties of the hydrogel itself (Chapters 3 and 4), the aim of this chapter is to determine the suitability of this material to hosting cell-ECM interactions. The first criteria is to ensure the cells' viability for long-term culture within the hydrogels and thus to obtain the optimum set of hydrogel characteristics for the study. With these optimum conditions identified, the next aim is to show that cells can actively interact with this material and thus recapitulate the basics of cell mediated tissue remodelling. This interaction is two fold: cell-mediated degradation of the matrix as well as synthesis of newly laid proteins, thus demonstrating an active remodelling of the hydrogel by embedded cells.

**Methods**: This chapter introduces both the bovine and human primary cell cultures used in our models. Data assessing VSMC viability exploring the impact of the hydrogel solid content, peptide distribution and cell seeding density, is then presented. Morphology of cells in hydrogels

of different degradabilites is explored looking at cells ability to breakdown the hydrogel and confirming that this is MMP mediated. Finally we present data showing evidence of newly laid ECM proteins by encapsulated human primary cells.

**Conclusion**: The data in this chapter allowed us to identify the optimum encapsulation conditions and confirm the suitability of using our PEG-peptide hydrogel to host vascular cell-ECM interactions including matrix degradation and synthesis of new ECM proteins.

## 5.1 Chapter Aims

The data in this chapter address Aim 2: developing a suitable static *in-vitro* baseline model to study VSCM cell interaction to then compare to in-flow conditions. The specific aims of this chapter were to:

- Assess encapsulated VSMC viability in hydrogels altering stiffness, bioactivity and seeding density
- Assess whether cells can break down the hydrogel via MMP secretion
- Test whether cells can lay down new ECM within the hydrogels
- Assess the possibility of using human primary cells

## 5.2 Methods

### 5.2.1 Tissue Culture

Initially in order to optimise experimental protocols, primary bovine VSMCs were used. These cells were isolated from the adventitia of bovine aortic tissue. This work was conducted primarily by our collaborators in the Shanahan group at Kings College London. Tissue was obtained from an abattoir the same day as the animal was sacrificed and kept on ice until isolation of cells. The Aorta was first thoroughly cleaned in HBSS to remove excess blood. The vessel was then cut open and divided into smaller sections (approx 5 cm long) and stored in media containing antibiotic and anti fungal medication for sterilisation (referred to as sterilisation media). The sterilisation media contains 1% PSG (penicillin-streptomycin-glutamine) and 1% Amphotericin B in DMEM, serum free. The sections were then stored in the fridge in solution awaiting further processing. The tissue can be stored overnight like this.

Scissors were then used to cut away connective tissue, fat and to cut away the Adventitia (the outer most layer of the Aorta containing primarily fibroblasts) from each sample. The inside of the vessel was then gently scraped with bent forceps to denude the endothelial layer. The Aorta was then cut up into 1-2 mm wide chunks in order to maximise surface area for enzyme digestion. The aortic pieces were then transferred to 5 ml tube and incubated in 3 ml Collagenase (Sigma C-0130), 3 mg/ml in sterilisation media and 500 $\mu$l Elastase (Sigma E0127) 1 mg/ml in sterilisation media as shown in Figure 5.1. The pieces were then incubated in this enzyme solution for 4 hours and agitated by pipetting up and down every 30 mins. After 4 hours, the solution was mixed and then centrifuged at 400 rpm for 1 min. The supernatant was then transferred to a new tube before spinning down at 900 rpm for 3 mins. The media was then aspirated and the cell pellet re-suspended in 1 ml of culture medium containing 20% FBS, 1% Antibiotic-Antimycotic (ABAM) (Thermo 15240062) and 1% L-Glutamine in DMEM. Cells were then counted and then re-suspended to a concentration concentration of $4 \times 10^5$ cells/ml. One ml of cell suspension was then plated in a T75 flask with 15 ml of media and then left for undisturbed for 48 hrs.

Subsequently, cells are grown up on standard T75 tissue culture flasks at 37°C in 5% CO2 and grown to confluency of 70-80% before splitting via standard trypsinisation. These cells were observed to proliferate quickly, doubling in population every 24 hours likely on account of the high concentration of FBS in the media. The cells were split in ratios of 1-4 to 1-6 as needed, never below a ratio of 1-10. Media changes were performed every 2-3 days. In culture, they adopt long thin spindle like shape as seen in Figure 5.2. Senescence in these cells occurs at approximately passage 25.

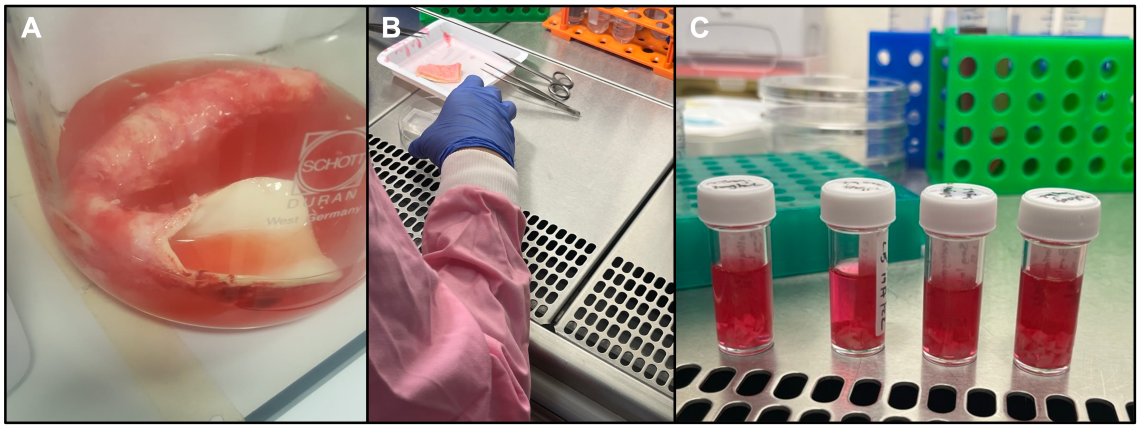


Figure 5.1: Figure showing the process of isolating VSMCs from tissue. In A, the intact Aorta is first washed to remove excess blood. In B, the Aorta is cut into sections and the endothelium denuded before slicing the sample into 1 mm chunks. In C, the sections of Aorta are shown submerged in enzyme solution for digestion.

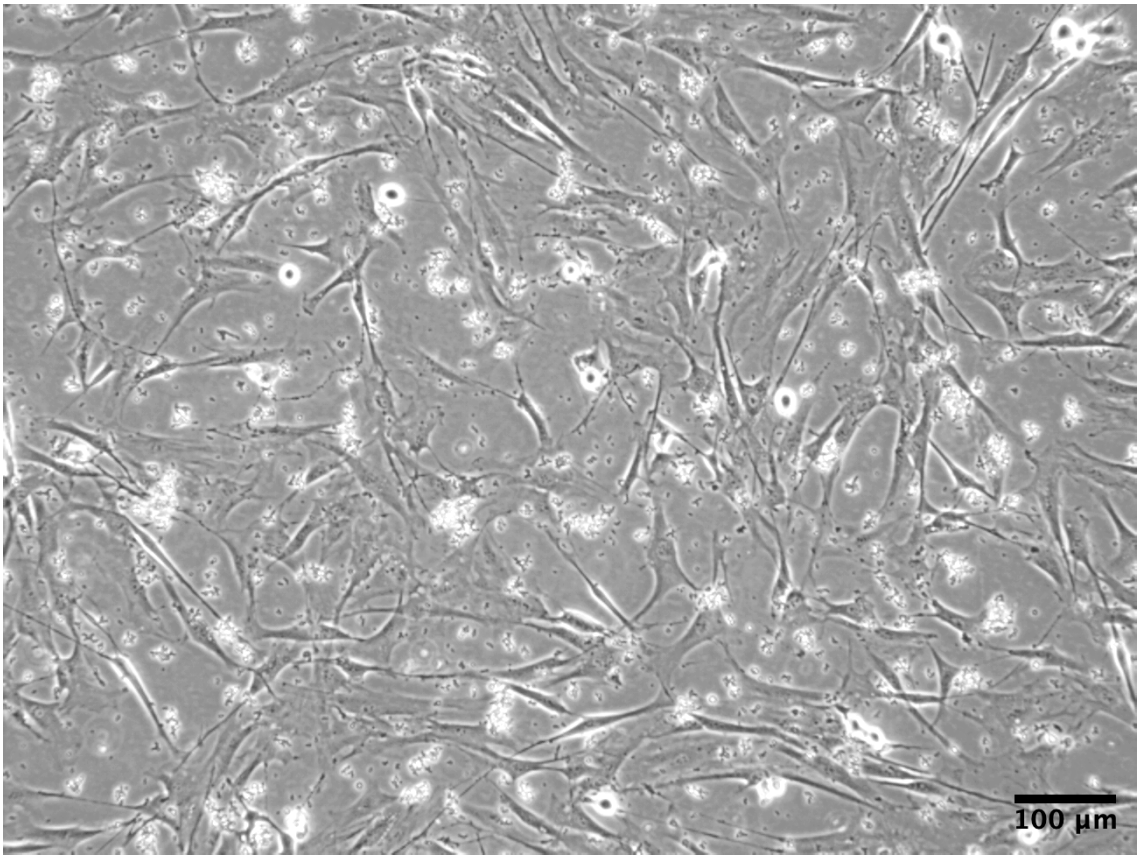


Figure 5.2: Representative bright field image of bovine VSMCS cultured in T75 flasks.

### 5.2.2 VSMC Marker Expression

To confirm the cell type isolated, imunocytochemistry for 3 markers of smooth muscle cells was performed: smooth muscle actin ($\alpha$SMA), smooth muscle protein 22 (SM-22) and calponin at different passage numbers. Cells were seeded at a density of $2\times10^4$ cells/cm$^2$ on autoclaved cover slips of diameter 16 mm in a 24 well plate. After 2-3 days of culture, cells were washed with PBS 3 times and then fixed with 4% PFA 500 $\mu$l per well for 15 mins at room temperature. The wash step was repeated and the cells were permeabilised in 0.5% Triton-X in PBS for 5 mins before an incubation of 30 mins in 1% Bovine Serum Albuminin (BSA) in 0.1% triton-X PBS to block for non specific binding. The respective primary antobodies anti-TAGLN-SM22, anti-Calponin 1 or anti-$\alpha$SMA were then added in blocking buffer solution to a 1:600, 1:600 and 1:333 dilution respectively for overnight incubation at 4 degrees. The coverslips were then washed a further 3 times in 0.1% triton-X PBS before adding a 1:1000 dilution of secondary antibody (either donkey anti-rabbit Alexa Fluor 488 or donkey anti-mouse Alexa Fluor 555) for 2 hrs in the dark at room temperature. A further wash step was then repeated before adding either a 1:1000 Hoescht or 1:500 DAPI incubation for 15 mins. Samples were then washed a final time before mounting onto glass slides using Dako Mounting Medium (Agilent technologies) and then imaged on either a confocal microscope (Zeiss LSM 980) or an apotome microscope (Zeiss Axio Observer). Details of all antibodies are given in Appendix 9.3

### 5.2.3 Cell Encapsulation

Cells are encapsulated into the hydrogel by mixing cell suspensions at desired cell density with solutions of the 2 cross-linking polymers. As before, PEG vinyl sulphone and PEG-peptide conjugate are dissolved to the correct concentration in buffer. When encapsulating cells, all dilutions are made in HEPES buffer PH8 supplemented with 1x Hanks Balanced Salt Solution (HBSS) to ensure correct osmotic balance of the cells. Cells are first peleted, counted and then resuspended in HEPES PH8 buffer to the desired cell/ml concentration. First the PEG-VS, PEG-peptide and cell suspension mixture is allowed to cross-link for 3-5 mins in the 2-2.5% polymer concentration before being pipetted into the final casting receptacle. Pre-mixing of the PEG components allows for some cross-linking to occur to ensure an even distribution of cells within the mixture in the final solid state. Trial encapsulations were run to determine the optimum time to allow the hydrogel to pre-form without resulting in premature cross-linking no longer allowing for pipetting. Higher polymer solid content hydrogels cannot be left for as long to cross-link before cell addition as the cross-linking reaction happens faster compared to in lower solid content hydrogels. Hydrogels are then allowed to fully cross-link for up to 45 mins in the incubator before media is added around the hydrogel to provide encapsulated cells with nutrients. The hydrogels are then placed in the incubator and the media is replaced every 2-3 days as with standard culture.

### 5.2.4 Assessing Encapsulated Cell Viability

Viability was assessed by staining encapsulated cells using the invitrogen LIVE/DEAD™ Viability/Cytotoxicity Kit for mammalian cells (Catalog number: L3224). Calcein AM (green fluorescence) is used to stain cells with intracellular esterase activity whilst ethidium homodimer-1 (red fluorescence) penetrates cells with a compromised cell membrane.

Thirty $\mu L$ samples were cast in Sigmacote-treated glass rings of 6 mm diameter in a 24-well plate and cultured as per normal. To stain, hydrogels are first washed 3 times quickly with PBS before fresh PBS is added and the hydrogels are placed on a shaker (approx 300 rpm) for 20-30 mins to remove phenol from media. Samples are then stained with a solution of 2 $\mu$M ethidium homodimer and 2 $\mu$M calcein AM in PBS and placed on the shaker at room temperature for 45 mins. The stain is then replaced with fresh PBS before shaking for a further 20 mins to remove any excess. Finally the PBS is replaced once more before cells are imaged. For encapsulated cell densities of $2\times10^6$ cells/ml or greater a 10 $\mu$M concentration of both dyes was used instead. Staining of 2D conditions was performed on glass cover slips as before, washing 3 times with PBS before incubating with stain for 10 mins and then repeating the wash step. Negative controls for 2D were prepared with 70% ice-cold IMS for 10 mins before washing with PBS and then staining.

### 5.2.5 Staining Encapsulated Cells

In order to stain encapsulated cells, either whole mount staining of the entire hydrogel or staining of cryopreserved thin sections can be performed. The advantage of whole mount staining is that the spatial distribution of the signal is maintained, however antibodies are relatively large molecules and therefore it can be difficult for them to penetrate the hydrogel fully. Furthermore, imaging relatively large depths of hydrogel can result in loss of resolution and imaging limitations due to lens working distances. Conversely, cryosectioning is a more time consuming process in which spatial detail can be lost but imaging these thinner sections can result in higher resolution images.

For whole mount imaging, hydrogels were placed on the shaker for 30 mins in PBS to remove excess media. Samples were then fixed in 4% PFA for 30 mins at room temperature on the shaker before being washed in PBS once to remove excess PFA. Samples were then permeabilised using 0.5% Triton-X in PBS on the shaker for 5 mins 3 times, replacing the solution for each repeat. Samples were then washed 3 times for 5 mins on the shaker in 0.1% Triton-X replacing the solution for each wash. A blocking step of 1 hr at room temperature on a shaker in 3% BSA was then performed before washing and adding primary antibodies at the manufacturers recommended dilution. The primary antibody incubation was done overnight on a shaker in 4°C. Secondary antibodies were then added for 2 hours at room temperature on the shaker in the dark before adding Hoescht or DAPI stain and performing a final wash step.

For cryosectioning of hydrogels, samples were first washed in PBS for 30 mins to remove media before adding a solution of 30% sucrose in PBS and incubating at least overnight in 4°C to replace the water content in the hydrogel. The sucrose solution was then replaced with Optimal Cutting Temperature compound (OCT) and left at 4 degrees overnight. The samples were then added to fresh OCT in a cryo-mould ensuring the hydrogels did not sink to the bottom of the mould and minimal bubbles are introduced. Finally the OCT was then frozen slowly over dry-ice and the block kept at −80°C until ready to cut. Sections of approximately 20 $\mu$m thickness were cut using the cryostat and attached to statically charged glass slides. Slides were stored at −80°C and then stained as previously described for cells on coverslips. Details of all antibodies are given in Appendix 9.3.

### 5.2.6 Encapsulated Cell Morphology Analysis

Encapsulated cell morphology was assessed using F-actin staining. Hydrogels were first washed, fixed and cells permeabilised as previously described. A dilution of 1:600 of Alexa Fluor™ Plus 647 Phalloidin was then added for 2 hours in the dark on the shaker at room temperature. The 5 min wash step was then repeated 3 further times before adding a 1:1000 dilution of Hoescht or 1:500 DAPI for 15 mins on the shaker at room temperature. A final series of wash steps was performed before adding PBS to the samples and then imaging.

Quantification of cell morphology was performed in FIJI where cells were automatically segmented. Briefly, a threshold was first applied to images to clearly distinguish cell shape before smoothing the edges. The analyse particles function was then applied to all objects above a size of 100 square pixels or 200 square pixels depending on the condition. Metrics for cell shape were then automatically calculated for segmented cells. An example of the segmentation is shown in Panel B of Figure 5.11 for the original image shown in Panel A.

### 5.2.7 MMP Inhibition Assay

The degradable sequence in the hydrogel system is designed to be cleavable by MMPs secreted by cells. The sequence is known to be cleavable by MMPs 1, 2, 8, 9,3 and 7 [Nagase and Fields, 1996]. In order to confirm that this is the mechanism by which cells are interacting with the hydrogel, MMP activity can be inhibited. Samples were incubated with MMP Inhibitor (Sigma GM6001). This is a collagenase inhibitor (Ilomastat or N-[(2R)-2-(hydroxamidocarbonylmethyl)-4-methylpentanoyl]-L-tryptophan methylamide) reported by the manufacturer to act on MMPs 1, 2, 3, 8 and 9. This is therefore not a specific inhibitor but rather reduces or inhibits activity generally. Samples were incubated in a 12.5 $\mu$M solution made up in standard media and replaced with each media change.

### 5.2.8 RNA Extraction from Hydrogels

RNA is extracted from encapsulated cells by first washing hydrogels to remove media before adding 350 $\mu$l of cell lysis buffer (RLT buffer) from the RNeasy Mini Kit (Qiagen). At this stage, multiple hydrogels can be combined into each volume to increase the yield of RNA. Samples were then snap frozen in liquid nitrogen and stored at $-80$°C until RNA extraction is performed. The hydrogels were then thawed in solution and homogenised using a tissue homogeniser (MP Biomedicals FastPrep-24) pulsed at 4.5 m/s for 10 seconds, cooled on ice for 5 mins and then pulsed for a further 10 seconds. The samples were then spun down and the supernatant added to QIAshredder shredding columns (Qiagen) to further homogenise cell lysate and remove potential debris from hydrogels. Steps of the RNeasy mini kit as per the manufacturers recommendations were then performed and collected RNA stored at $-80$°C until needed. All steps were performed using protein low binding tips and ependorfs where possible to ensure maximum RNA retention.

Typically, hydrogels of 30 $\mu L$ are made and therefore seeding densities ranging from $1\times10^6$ to $4\times10^6$ cells/ml correspond to the order of tens of thousands of cells per sample. RNA abundance is therefore relatively low and the process of RNA extraction as described above was optimised in order to minimise losses. Furthermore, traditional methods for RNA quantification and quality control using the Nanodrop methods were not possible as yields were too low to generate reliable data with this method. To address this, samples were measured on a Bioanylser (instrument name DE13805253) using the Agilent RNA 6000 Pico RNA kit. Samples were processed and loaded as prescribed by the manufacturer. Results from the bioanalyser indicate the quality of the obtained RNA by an RNA integrity number (RIN), a score out of 10. Using the above protocol, RIN scores of 9.2 or higher were achieved, indicating high quality RNA can be obtained with this method. Example results of Bioanylser analysis can be found in Appendix 9.4.

### 5.2.9 Human Cell Culture

Once hydrogel conditions and the flow experimental set up (discussed in Chapter 6) had been optimised, we moved to cultures of primary human cells. These cells were kindly donated by the Shanahan group at KCL.

VSMCs were isolated from explants of human aortic tissues from a 35-year-old female (04-35F-11A) donor, hereby referred to as 35-F. All human materials were handled in compliance with the Human Tissue Act (2004, UK) and with ethical approval from the research ethics committee (REC reference: 13/LO/1950). Cells were cultured in M199 medium supplemented with 20% fetal bovine serum (FBS) and 1% penicillin–streptomycin-glutamine (PSG) at 37°C in 5% CO2. When human cells were encapsulated in hydrogels, the media was supplemented with 50 $\mu$g/$\mu$l sodium L-Ascorbate (Sigma A4034) to help accelerate ECM deposition and remodelling. To induce replicative senescence, VSMCs were passaged until their growth was arrested, which occurred

between passages 20 and 25. All cell isolation was performed before the work in this thesis by someone else. Cells were cultured and passaged in the same way as the bovine with the exception of slower speeds for pelleting of 1000 rpm. These cells were slower growing compared to the bovine and needed more time post thawing to grow to confluency.

## 5.3 Results

### 5.3.1 Isolated cells expressed VSMC markers

Figures 5.3, 5.4 and 5.5 show representative images of 2D cell cultures (passage 9 and 10 respectively) seeded on glass coverslips stained for 3 markers of VSMCs: SM-22 (Figure 5.3 Panel B), $\alpha$SMA (Figure 5.3 Panel C) as well calponin (Figure 5.5). These images indicate isolated cells are indeed VSMCs. As expected, calponin, SM-22 and $\alpha$ SMA expression was seen in the cell cytoskeleton with a large degree of overlap seen for co-staining of $\alpha$SMA and SM-22. Panel A in Figure 5.4 shows actin filaments. Calponin staining was performed by I. Guri as part of her MRes rotation in the Gentleman Lab.

To test whether cells expressed these markers when in contact with the peptide cross-linkers used in the PEG hydrogel system, cells were seeded on 2D hydrogels (2% polymer content 1 mM degradable and adhesive). Figure 5.6 shows that although no quantitative comparison can be made with these images due to the different mounting between glass and hydrogel samples, cells on the hydrogel still expressed VSMC markers in a similar pattern to those seen on glass.

Cells seeded on the 2D hydrogel surface qualitatively appeared to adopt a longer, more "spindle-like" morphology akin to that of cells cultured on tissue culture plastic, compared to their shape on the glass surface. Mann-Whitney statistical analysis of the aspect ratio of cells however, revealed no significant differences between the 2 conditions based on 3 technical replicates. The seeding density made separation of individual cell boundaries difficult and thus results may be affected by the shape of cell clusters rather than the morphology of individual cells. The qualitative elongation of cells seen in the hydrogel condition may indicate that the adhesive motifs, absent on the untreated glass surface, may allow cells to spread to a greater degree but repeats are needed with sparser cell seeding to test this hypothesis fully.

### 5.3.2 VSMCs favour soft, highly adhesive and degradable hydrogels, with cells seeded at a density of up to $5 \times 10^6$ cells/ml

During the encapsulation process cells are re-suspended and incubated for 45 mins in HEPES buffer PH8 supplemented with 1x HBSS to allow the hydrogel to fully cross-link before media is added. We therefore wanted to test the impact the buffer's basic PH and the time delay before cells receive nutrients on cell survival. To this end we performed live dead stains on 2D cultures of cells incubated with HEPES for 45 mins compared to media only controls. Panel A of Figure 5.7 shows the impact of the 45 mins HEPES incubation to be negligible on cell viability.

To assess the impact of hydrogel polymer content and hence stiffness on cell viability, VSMCs (passage 16 or lower) were encapsulated in hydrogels of 2%, 2.5%, 3%, 4% and 5% polymer content hydrogels corresponding to $\approx$ 500 Pa, $\approx$ 1.2 kPa, $\approx$ 4 kPa, (4% not measured) and $\approx$

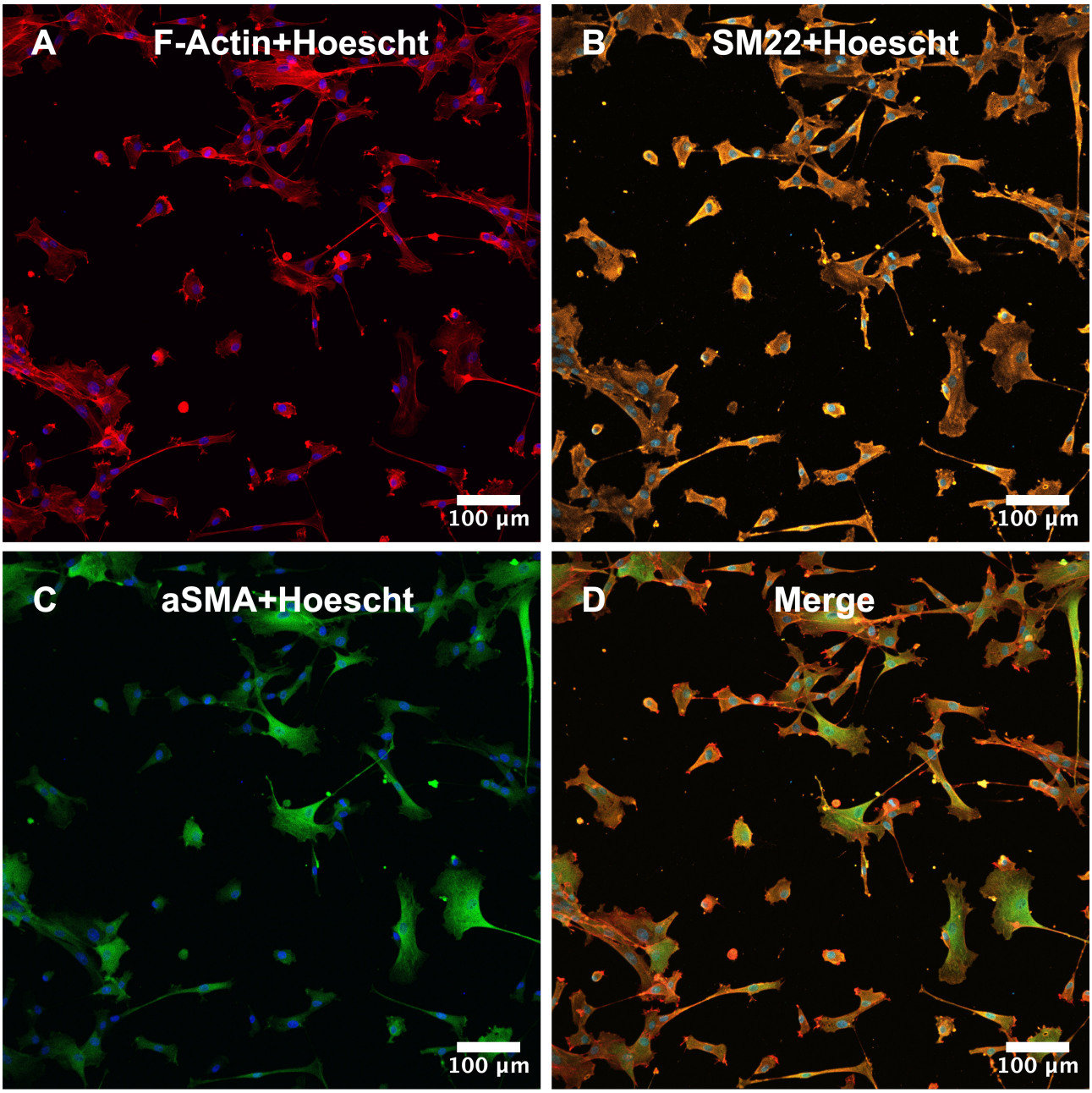


Figure 5.3: Representative image of bovine VSMCs (passage 9) seeded on glass coverslips for 2 days stained for F-actin in red (A), SM22 in orange (B) and $\alpha$SMA in green (C). Nuclear Hoeascht stain is shown in blue. D shows the merge of all stains.

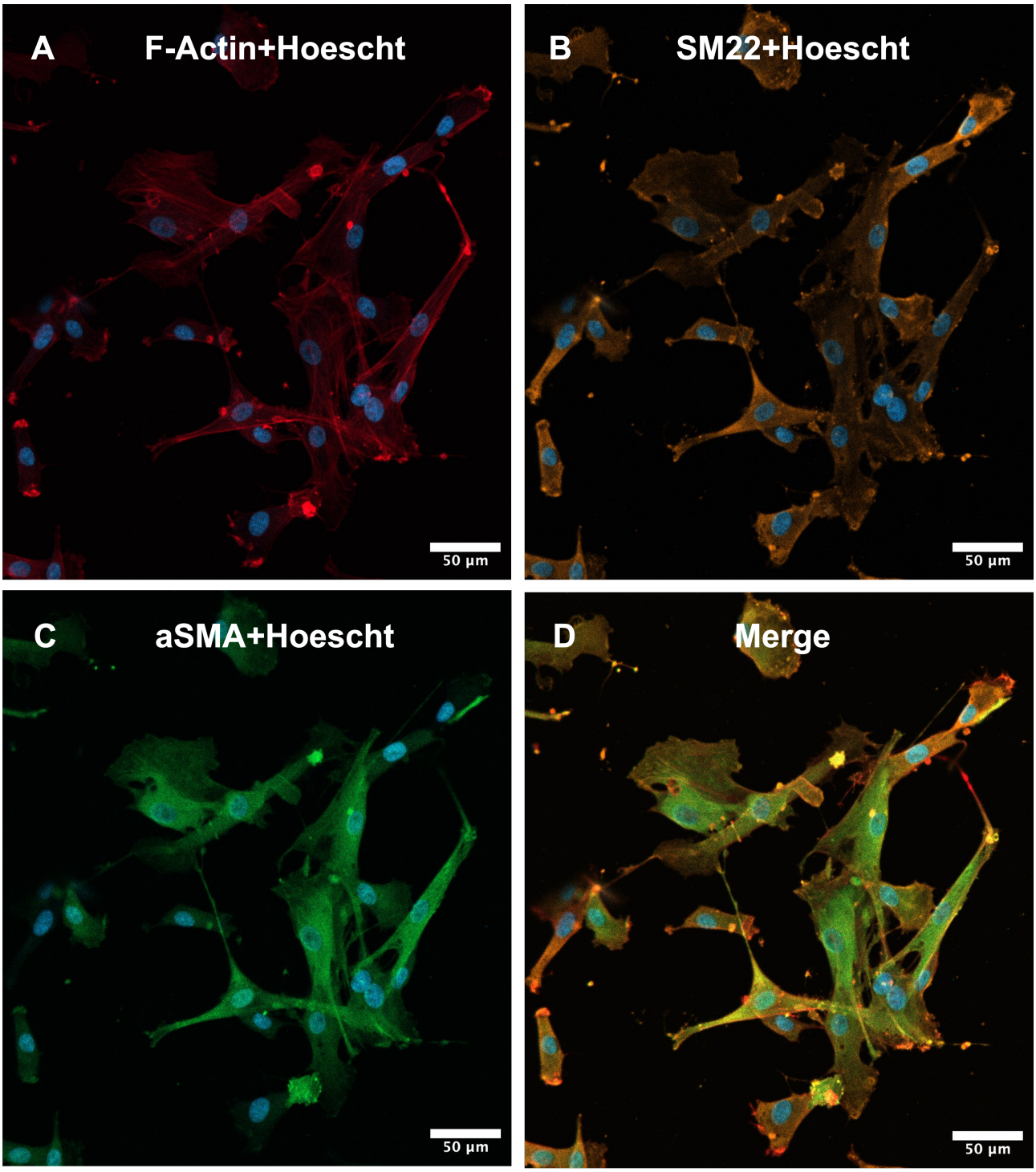


Figure 5.4: Representative close up image of bovine VSMCs (passage 9) seeded on glass coverslips for 2 days stained for F-actin in red (A), SM22 in orange (B) and $\alpha$SMA in green (C). Nuclear Hoeascht stain is shown in blue. D shows the merge of all stains.

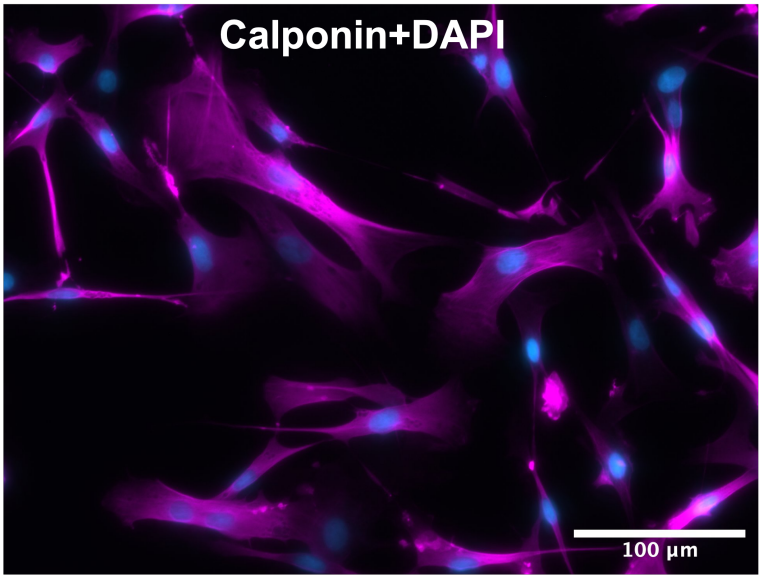


Figure 5.5: Representative image of bovine VSMCs (passage 10) seeded on glass coverslips for 2 days stained for calponin in magenta. Nuclear DAPI stain is shown in blue.

6.5 kPa stiffness as measured previously by AFM (credit M. Norman [Jowett et al., 2021]). Cells were encapsulated at a fixed seeding density of $1 \times 10^6$ cells/ml and fixed concentration of 1 mM MMP-cleavable and 1 mM adhesive peptide for 48 hrs prior to staining. Additional non-functional conjugates were added in to increase polymer content without changing the bioactivity of the hydrogel. Percentage viability was assessed by imaging 9 z planes in 3 hydrogels in each condition. The number of dead and live cells were counted and the proportion of viable cells calculated. All viability data was collected using whole mount imaging. Panel B of Figure 5.7 shows that viability was highest in the 2 softest hydrogels at approximately 75% with a reduction in approximately 10% viability for a polymer solid contents of 3% or higher. The viability of the softest 3 conditions (2 %, 2.5% and 3%) was then assessed at 96 hrs (different samples to those assessed at 48 hrs) as shown in Panel B of Figure 5.7. Viability of approximately 75% was maintained with no significant differences between conditions.

Within the hydrogel system, we are able to alter the number of adhesive and MMP-cleavable cross-links. To explore the impact of these changes on viability, cells (passage 12) were encapsulated in hydrogels of varying concentrations of adhesive and degradable cross-links for fixed seeding density of $1 \times 10^6$ cells/ml and fixed polymer solid content of 2% and assessed for viability at 48 hrs. Panel C of Figure 5.7 shows that there was no clear trend correlating viability with peptide distribution but the highest viability was seen in the 1 mM degradable 1 mM adhesive condition.

The viability of cells encapsulated in hydrogels at different seeding densities was assessed for $1 \times 10^6$ cells/ml, $2 \times 10^6$ cells/ml, $5 \times 10^6$ cells/ml and $10 \times 10^6$ cells/ml. In most instances, hydrogels of 30 $\mu L$ were made and this therefore corresponds to $33 \times 10^4$ cells to $333 \times 10^4$ cells

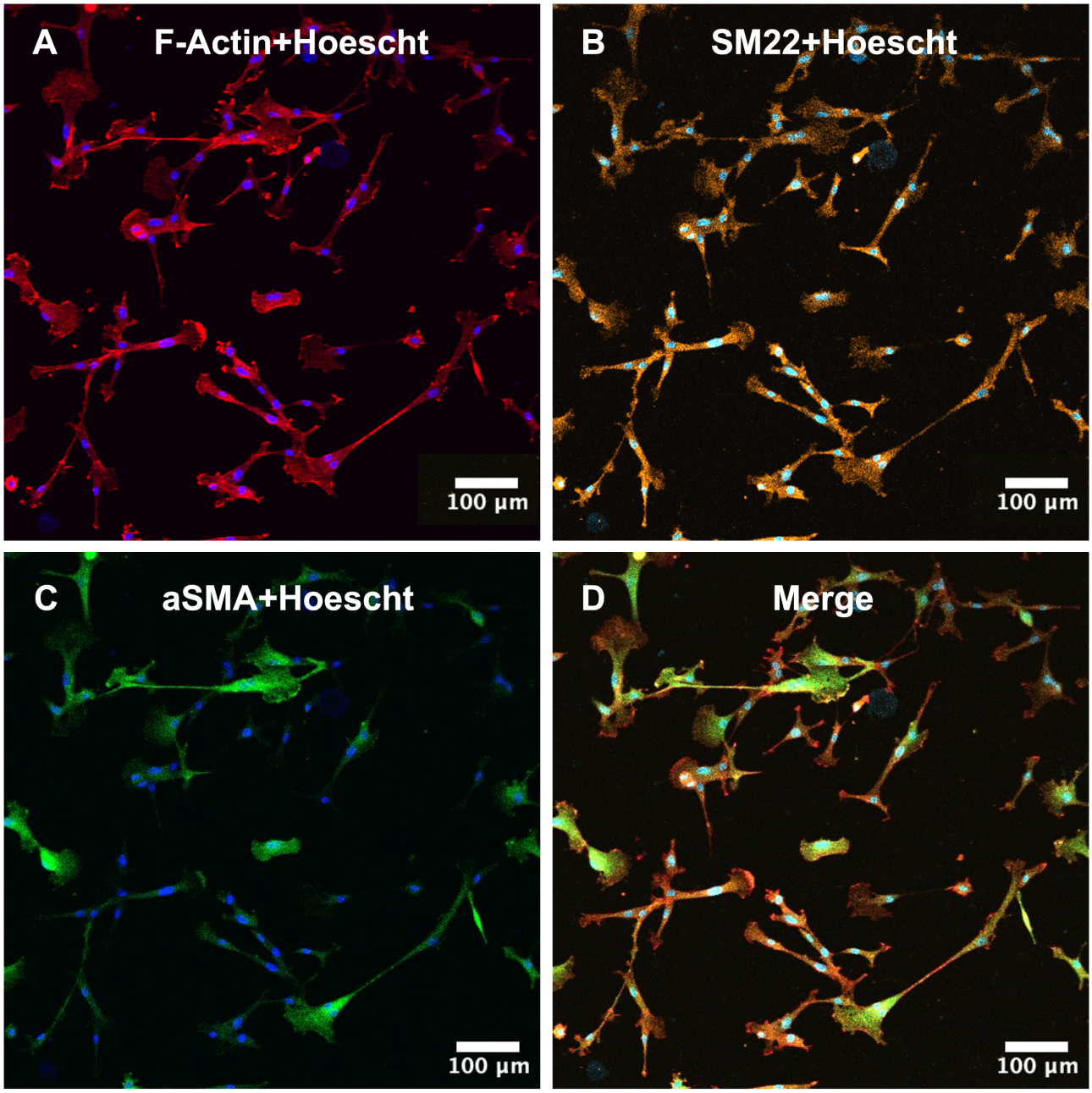


Figure 5.6: Representative image of bovine VSMCs seeded on 2D hydrogel 2% 1mM degradable/adhesive in 24 well plate for 3 days stained for F-actin (A), SM22 (B) and $\alpha$SMA (C). Nuclear Hoeascht stain is shown in blue. D shows the merge of all stains.

per sample. When considering potential downstream assays such as qPCR analysis or staining for nascent proteins, maximising the number of cells in each sample is beneficial to increase RNA or new protein yield. However, the results in Panel D of Figure 5.7 show a sharp decrease in viability in densities $\geq 5 \times 10^6$ cells/ml and therefore $166 \times 10^4$ cells per sample represented a higher limit in 30 $\mu L$ samples. For all conditions hydrogels formed, showing densities of $10 \times 10^6$ cells/ml can be encapsulated without completely disrupting cross-linking.

Data in Panel A as well as some of the data in Panel B of Figure 5.7 were collected by C. Kerins as part of her MRes Rotation project in the Gentleman lab.

### 5.3.3 Cells encapsulated in degradable hydrogels secrete MMPs to breakdown the surrounding matrix and adopt elongated morphologies

We hypothesised that cells would initially interact with the hydrogel by secreting MMPs to break down the material and thus be able to spread. To test this, the morphology of cells encapsulated in hydrogels of varying degradability was assessed. Three conditions were considered, a non, low and high degradable hydrogel the compositions of which are shown in Table 5.1.

Whole mount F-actin staining was used to label cell cytoskeleton and z-stack images of approximately 90 10 $\mu m$ slices at 10x were taken in the centre of the hydrogel. Figure 5.10 shows representative maximum intensity projections of the full z-stack for A) a high degradable , B) a high degradable incubated with MMP inhibitor, C) a low degradable and D) a non degradable hydrogel all of fixed 2% polymer concentration and seeding density 1 $\times 10^6$ cells/ml, 7 days post encapsulation.

Cells appear more spread in the high degradable condition creating elongated structures as seen in Panel A. Comparatively spreading is reduced in the low degradable condition (Panel C) and cells mostly remaining rounded in the non degradable condition (Panel D). The degree of cell spreading was quantified by plotting cell circularity (shown in Panel C of Figure 5.11). Cells were significantly rounder in the non-degradable condition compared all other conditions ($p \leq 0.0001$ for all comparisons), with the lowest circularity observed in the high degradable condition.

Furthermore, to test whether differences between these conditions were down to cells inability to break down hydrogel cross-links via MMP secretion, encapsulated cells in the high degradable condition were incubated with non-specific MMP inhibitor. First the viability of cells in the degradable hydrogel incubated with MMP inhibitor was assessed at day 7. Analysis of images such as in Figure 5.8 found cells to be 66% viable in these conditions based on 2 biological replicates indicating that the MMP inhibitor was not cytotoxic. Cell morphology was also assessed in a 2D control condition plated on glass and incubated with MMP inhibitor and were seen

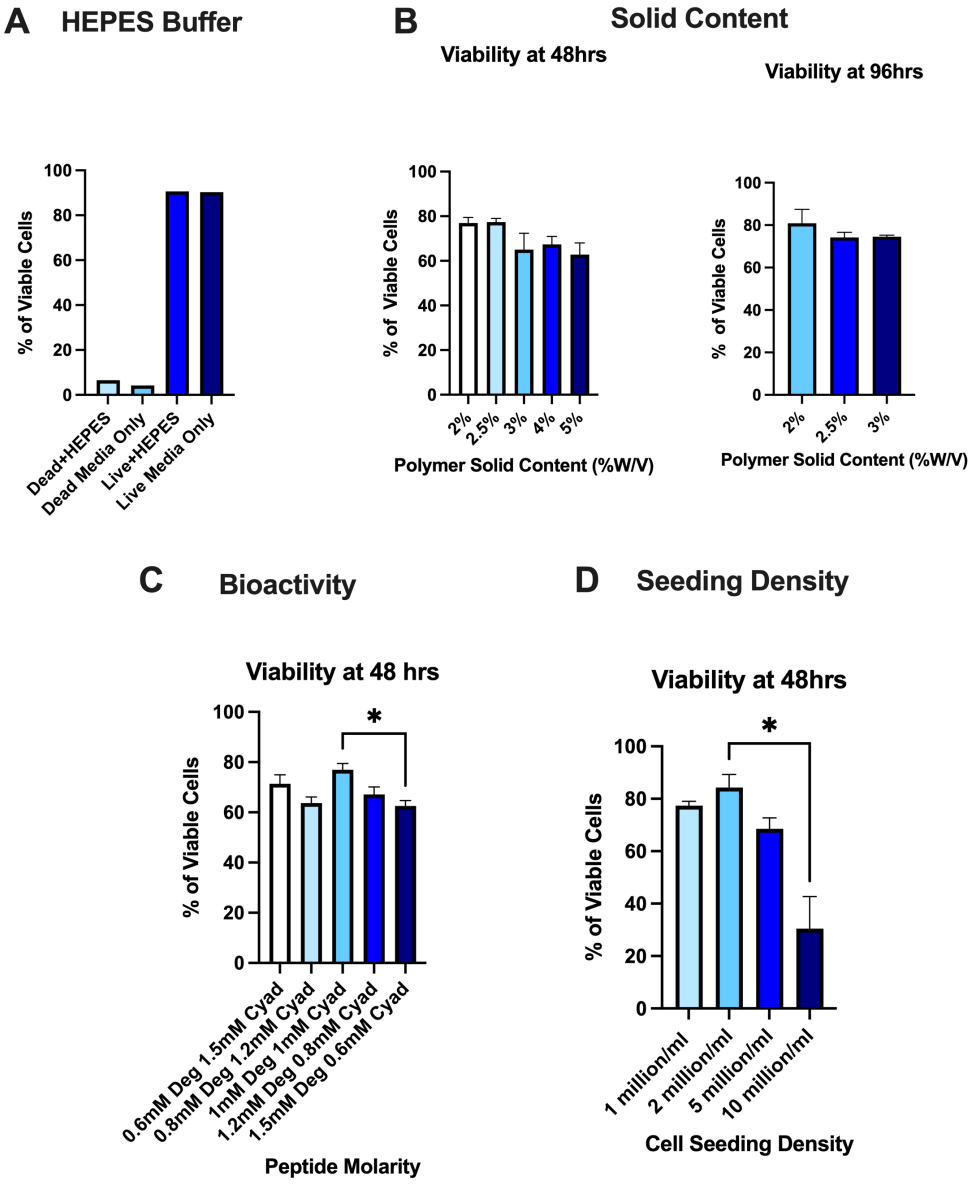


Figure 5.7: A) Figure showing the percentage of viable cells in 2D cultures both with and without HEPES incubation. Negative controls were prepared with 70% ice-cold IMS for 10 mins. Analysis was carried out on 3 images for 1 coverslip in each condition representing 1 technical replicate. B) Figure showing the percentage of viable cells encapsulated at different polymer solid contents at 48 hrs and 96 hrs post encapsulation. C) Figure showing the percentage of viable cells encapsulated for different peptide molarities 48 hrs post encapsulation, Deg for MMP-cleavable and Cyad for adhesive peptide. D) Figure showing the percentage of viable cells encapsulated for different cell seeding densities 48 hrs post encapsulation. All tests were conducted on bovine VSMCs. B-D show data for 3 technical replicates and 1 biological replicate for each condition. Error bars represent standard deviation. Statistical analysis: Kruskal-Wallis with Dunn's multiple comparison test; * $p \leq 0.05$, ** $p \leq 0.01$, *** $p \leq 0.001$, **** $p \leq 0.0001$.

to be able to spread similarly to in media only condition as shown in Figure 5.9. In the 3D encapsulated condition, cell morphology remained rounded as seen in Panel D of Figure 5.10, with cell circularity increased significantly compared to in high degradable hydrogels in media alone and low degradable conditions (Panel C in Figure 5.11)($p \leq 0.0001$). Circularity was significantly lower in the MMP condition compared to the non degradable condition suggesting that MMP activity was not completely blocked and cells were able to spread to some degree ($p \leq 0.0001$).

### 5.3.4 Primary human cells are viable in hydrogels for long-term culture

We assessed the viability of human primary cells encapsulated in 2% polymer content 1 mM degradable and adhesive hydrogel at a density of $4 \times 10^6$ at day 7 and day 20. Quantitative analysis of live (green) vs dead (red) cells in images (Figure 5.12) revealed viability to be 87% at day 7 and 68% at day 20. Assessing viability by day 20 became more difficult as cells form large clumps making it hard to distinguish individual cells, and thus there is likely an underestimation of the number of live cells.

### 5.3.5 Primary human cells secrete ECM proteins in the PEG-peptide hydrogels

All results in this section were achieved in collaboration with M. Antonazzi in the Shanahan lab. The work was split evenly.

Immunostaining on cryosections of human VSMCs cultured for 7 days encapsulated in 2% hydrogels containing 1 mM adhesive and degradable peptides showed cells synthesise collagen 1, 4 and fibronectin (Figures 5.13, 5.14). After 20 days in culture, extensive pericellular matrix was evident around cells (Figures 5.15 and 5.16). Quantification of staining area determined by creating maximum intensity projections of 20 $\mu m$ sections of hydrogel and then calculating the percentage of positive area in each image confirmed that more ECM deposition is seen by day 20 compared to day 7 (Figure 5.17 Panel A-C) (day 7 vs day 20: fibronectin $p \leq 0.0001$, collagen-1

| | Percentage CYAD | CYAD peptide (mM) | Percentage DEG | DEG peptide (mM) | Percentage KDWERC | KDWERC peptide (mM) |
|---|---|---|---|---|---|---|
| Non degradable | 47.5 | 1.04 | 0.00 | 0.00 | 52.50 | 1.15 |
| Low degradable | 48.5 | 1.04 | 24.50 | 0.52 | 27.00 | 0.58 |
| High degradable | 50 | 1.04 | 50.00 | 1.04 | 0.00 | 0.00 |

Table 5.1: Table showing the percentage of cross-links and molarity for each peptide type for non, low and high degradable 2% polymer content hydrogels.

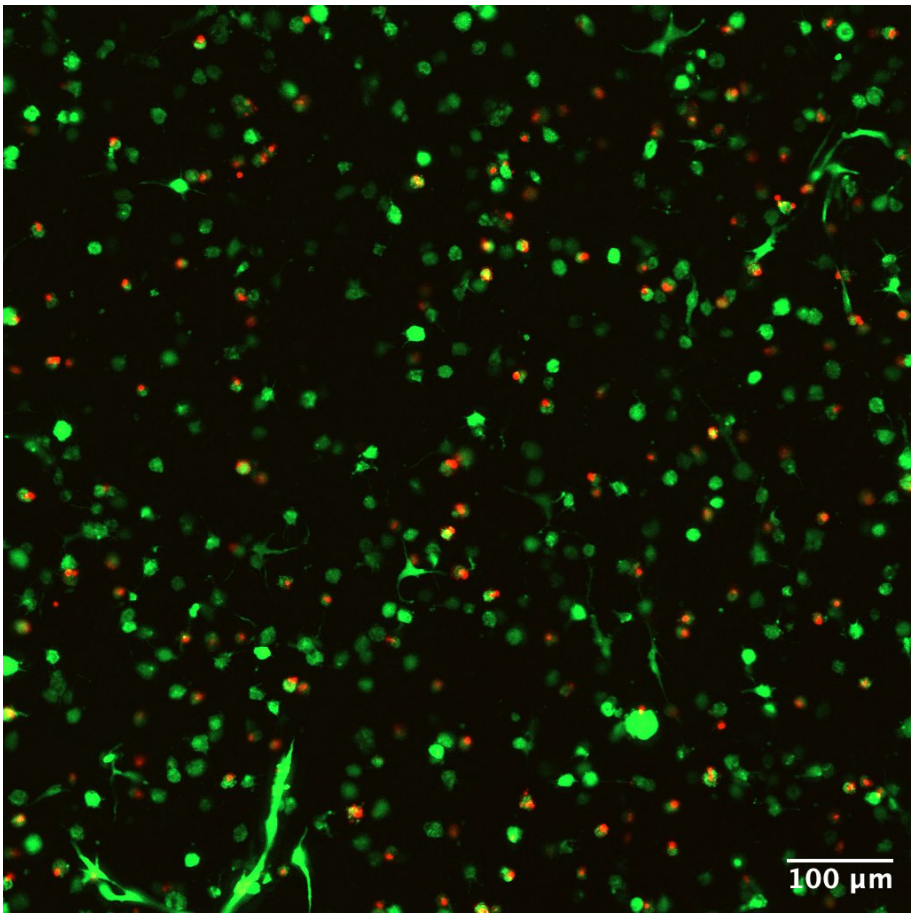


Figure 5.8: Representative images of live (green) dead (red) staining of encapsulated bovine VSMCs in 2% polymer content 1 mM degradable and adhesive hydrogel at a density of $1 \times 10^6$ treated with MMP inhibitor at day 7.

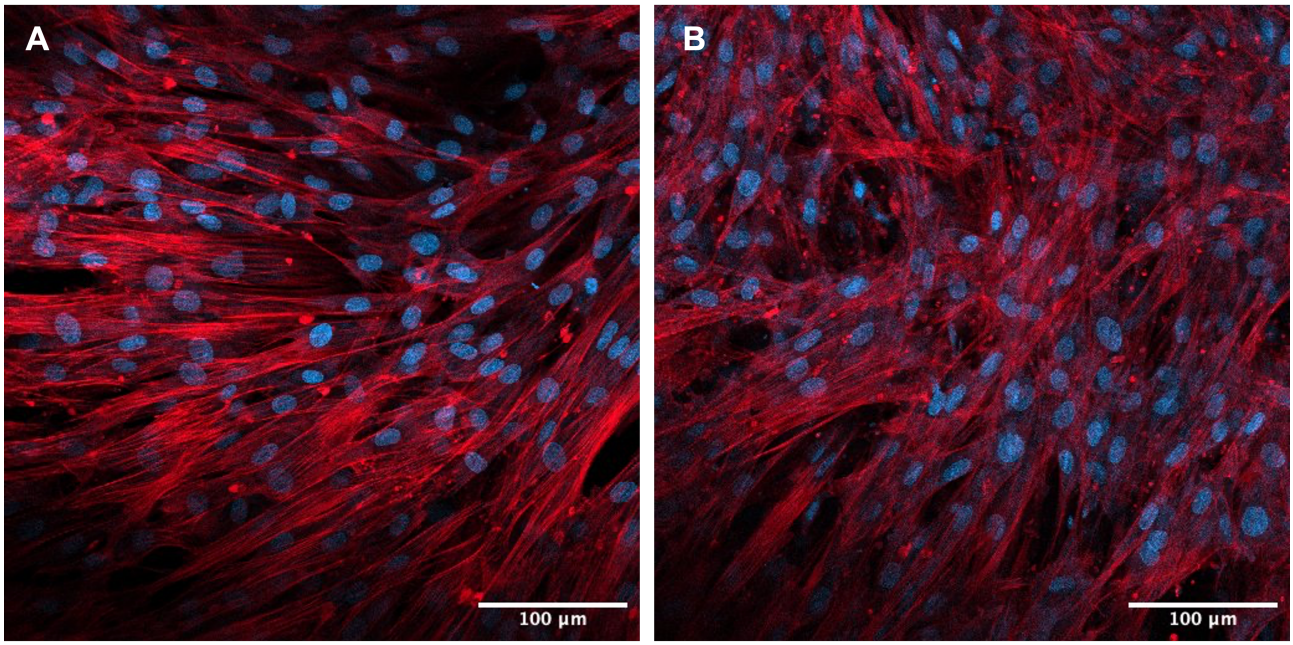


Figure 5.9: Representative images of bovine VSMCs seeded on glass treated with MMP-inhibitor (A) and a negative media only control (B). Cells are stained using Phalloidin (red) for F-actin staining and Hoescht (blue) for nuclear stain at day 7.

$p \leq 0.0001$ and collagen-4 $p \leq 0.001$). Panel D shows a side by side analysis of these results. The number of cells in each section were no different at days 7 and 20 (Mann-Whitney statistical test $p=0.0781$) ((Figure 5.17 Panel E), indicating that the increase in ECM proteins is due to increased production by the cells by day 20.

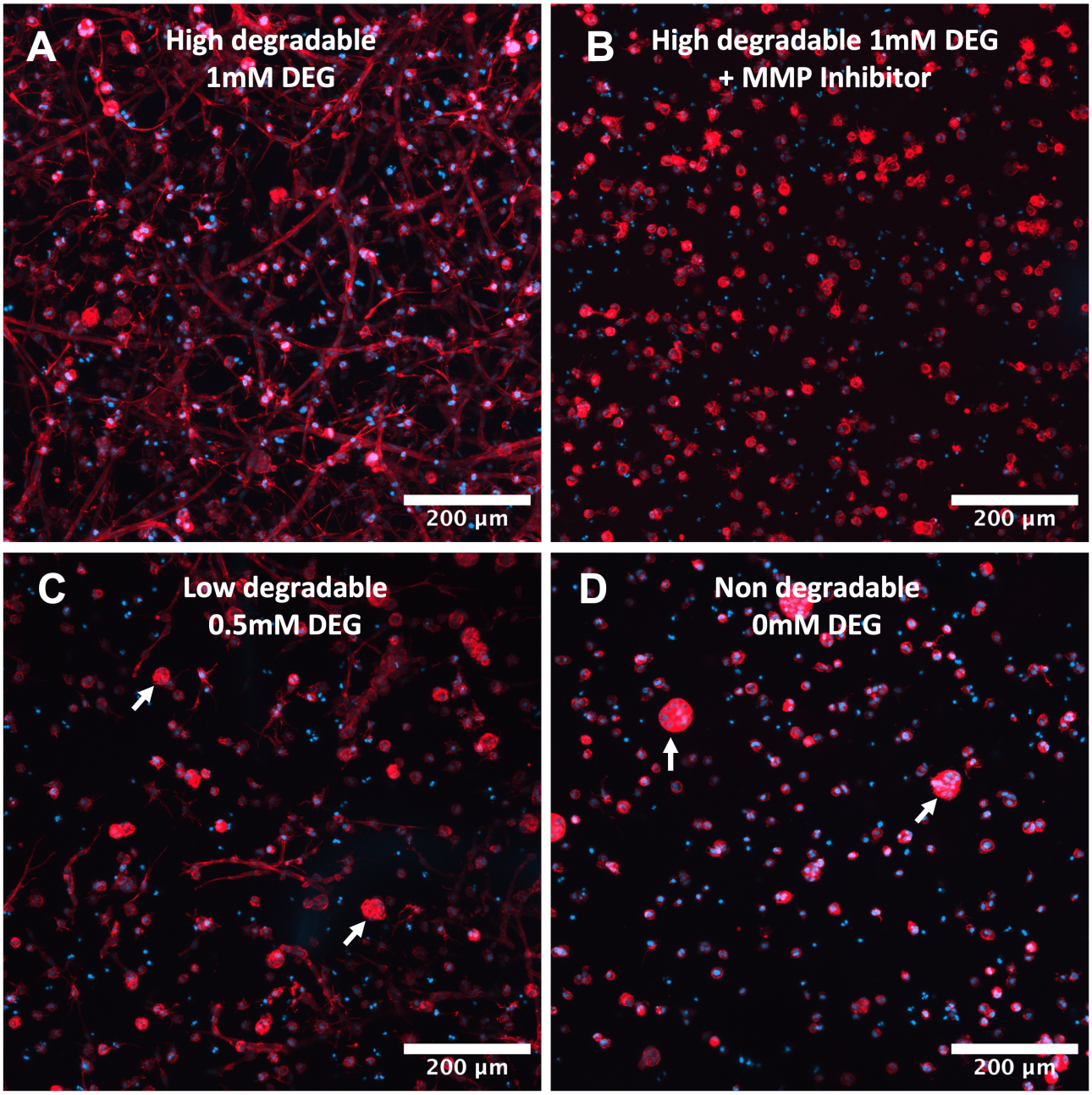


Figure 5.10: Maximum intensity projections of representative z-stack images taken at 10x by confocal microscopy showing morphology of bovine VSMCs encapsulated in A) a high degradable , B) a high degradable incubated with MMP inhibitor, C) a low degradable and D) a non degradable hydrogel all of fixed 2% polymer concentration, seeding density 1 $\times 10^{-6}$ cells/ml, 7 days post encapsulation. Data was collected for 3 biological replicates for each condition with 1 or 2 technical replicates per repeat. Cells are stained using Phalloidin (red) for F-actin staining and Hoescht (blue) for nuclear stain. White arrows indicate clusters of cells.

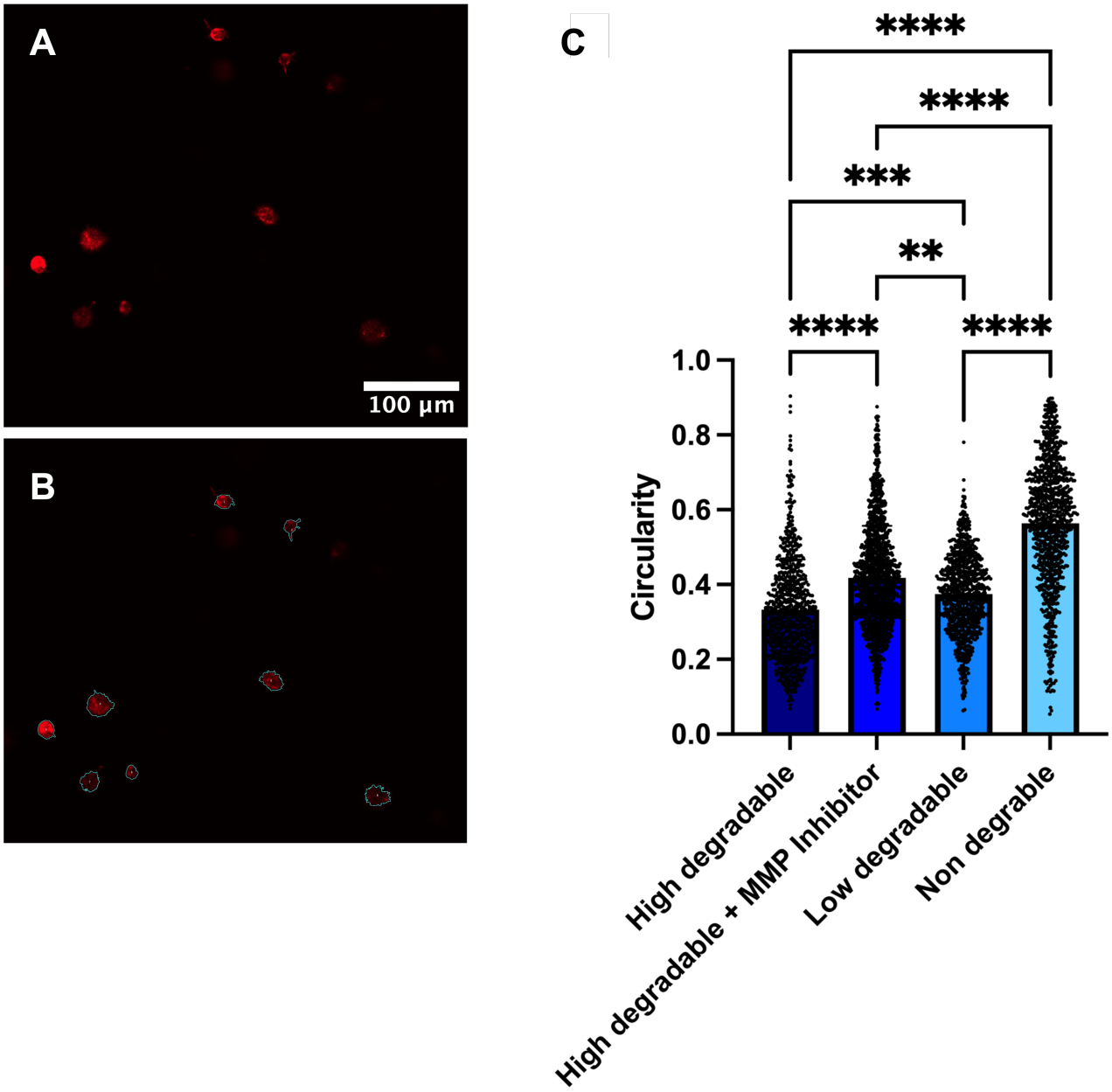


Figure 5.11: A shows a representative image of bovine VSMCs stained for F-actin in the low degradable condition. B shows an example cell segmentation using FIJI image analysis tools to determine cell circularity. C shows a graph of cell circularity for high, high with MMP inhibitor, low and non degradable conditions. Each point represents measurement for 1 cell with results collected for a z-stack taken in the centre of the hydrogel with approximately 90 slices of 10 $\mu m$ thick for 1 or 2 technical replicates per condition and 3 biological replicates. One biological replicate was lost for the low degradable condition. Statistical analysis: Kruskal-Wallis test with Dunn's multiple comparison test; **** $p \leq 0.0001$, *** $p \leq 0.001$, ** $p \leq 0.01$.

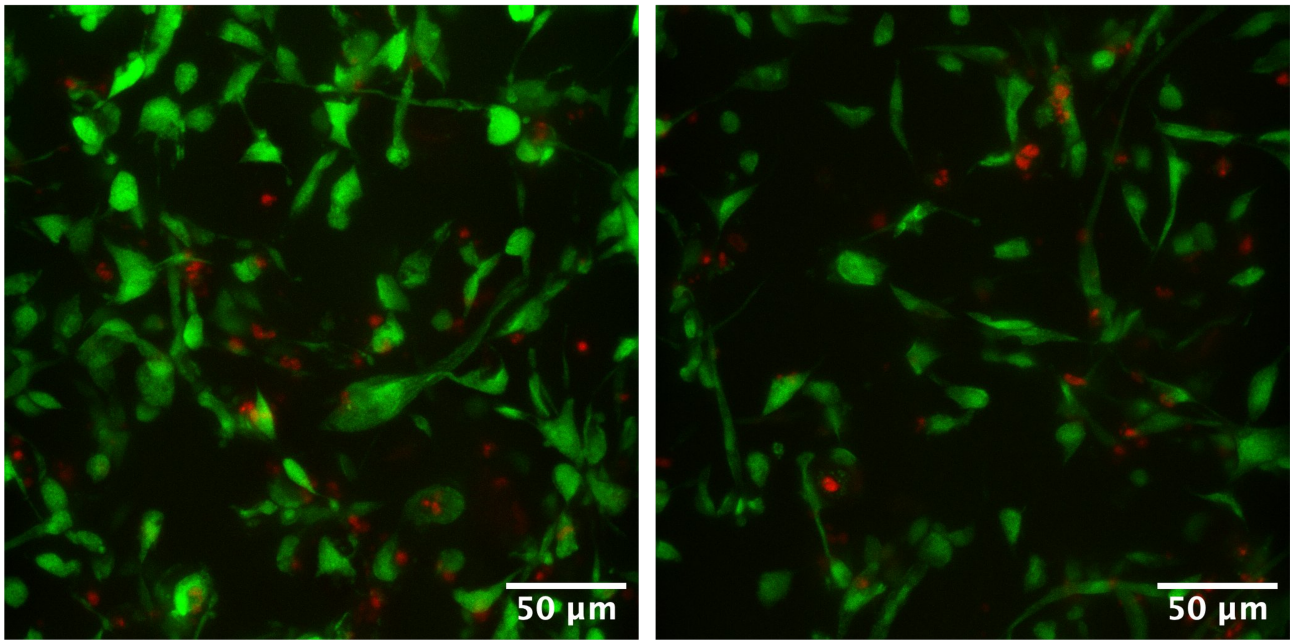


Figure 5.12: Representative images of live (green) dead (red) staining of primary human VSMCs encapsulated in 2% polymer content 1 mM degradable and adhesive hydrogel at a density of $4 \times 10^6$ cells/ml at day 20.

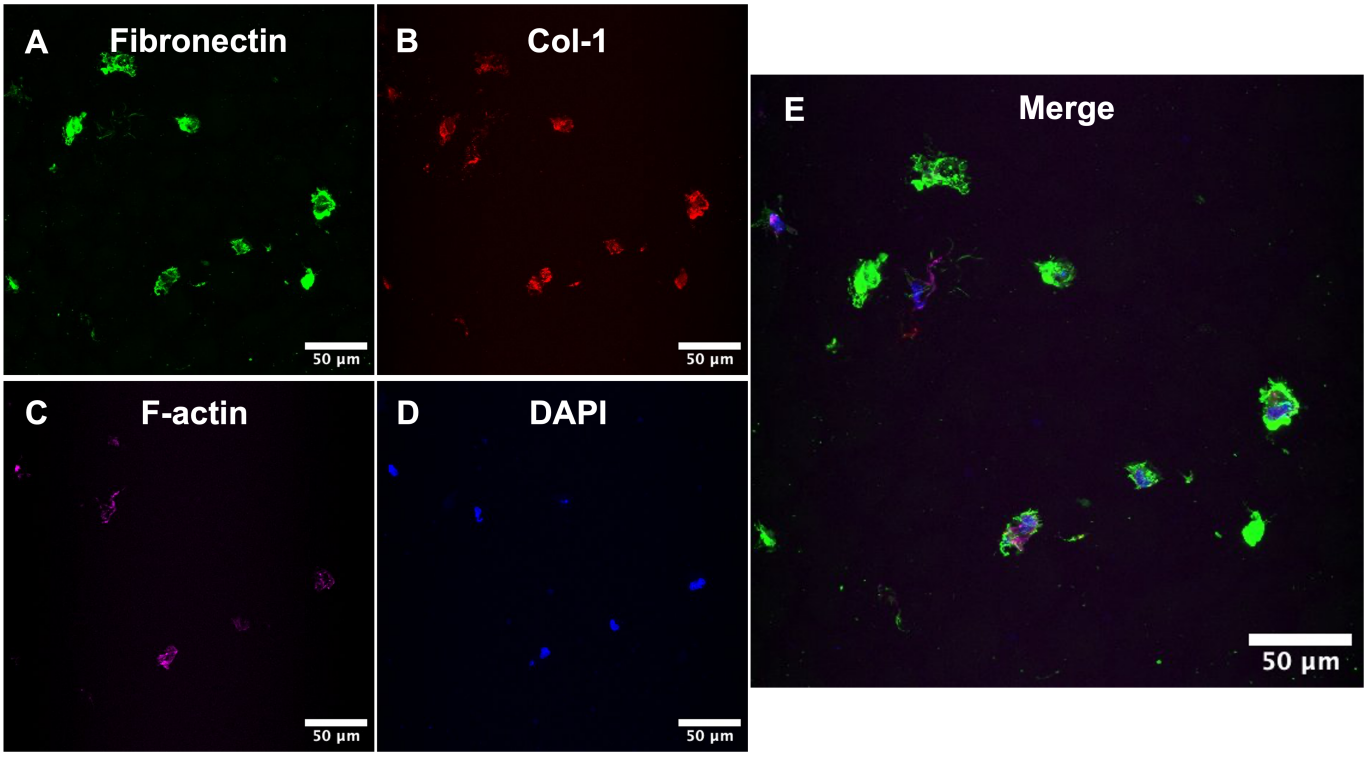


Figure 5.13: Representative maximum projection images of stained 20 $\mu m$ cryosections of primary human VSMCs isolated from a 35 year old female (35-F) encapsulated in 2% polymer content 1 mM degradable and adhesive hydrogel at a density of $4 \times 10^6$ cells/ml, 7 days post encapsulation. A shows fibronectin staining, B collagen-1 staining, C F-actin staining and D nuclear DAPI staining. Finally E shows the merge.

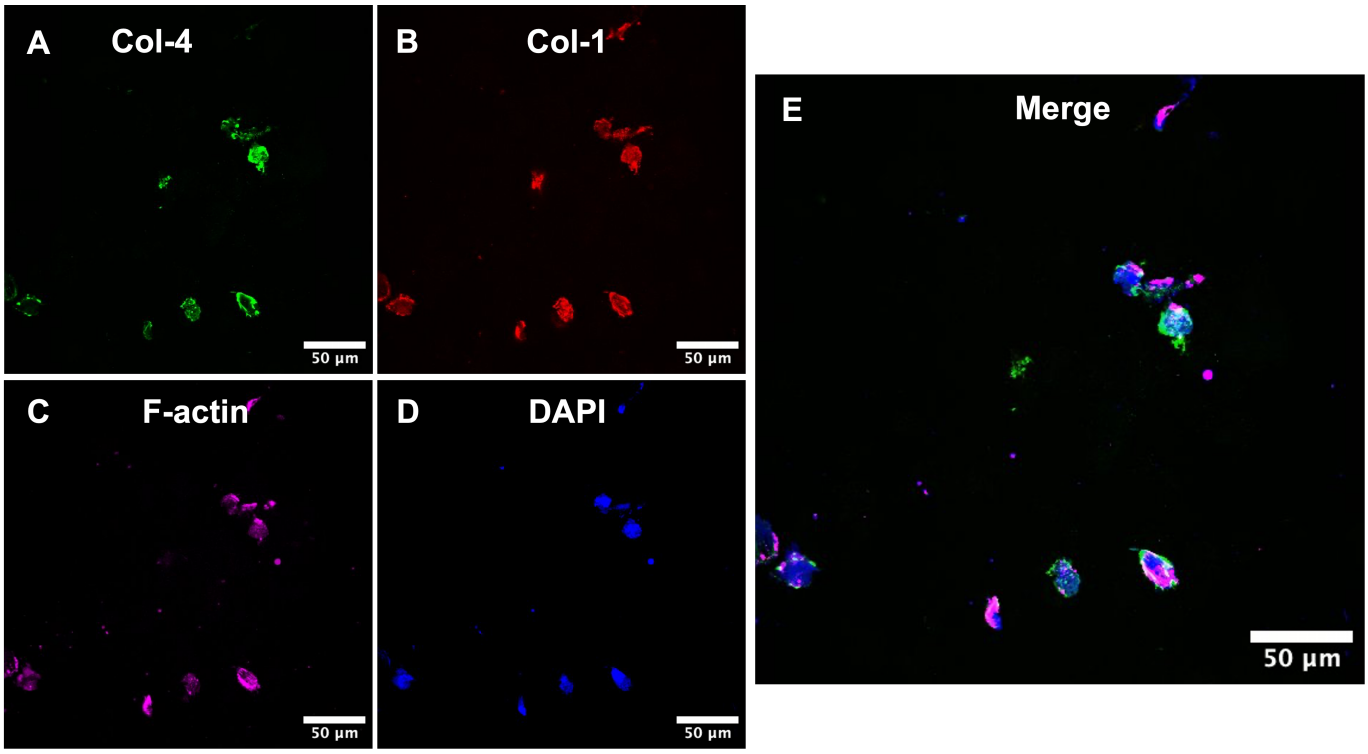


Figure 5.14: Representative maximum projection images of stained 20 $\mu m$ cryosections of primary human VSMCs isolated from a 35 year old female (35-F) encapsulated in 2% polymer content 1 mM degradable and adhesive hydrogel at a density of $4 \times 10^6$ cells/ml, 7 days post encapsulation. A shows collagen-4 staining, B collagen-1 staining, C F-actin staining and D nuclear DAPI staining. Finally E shows the merge.

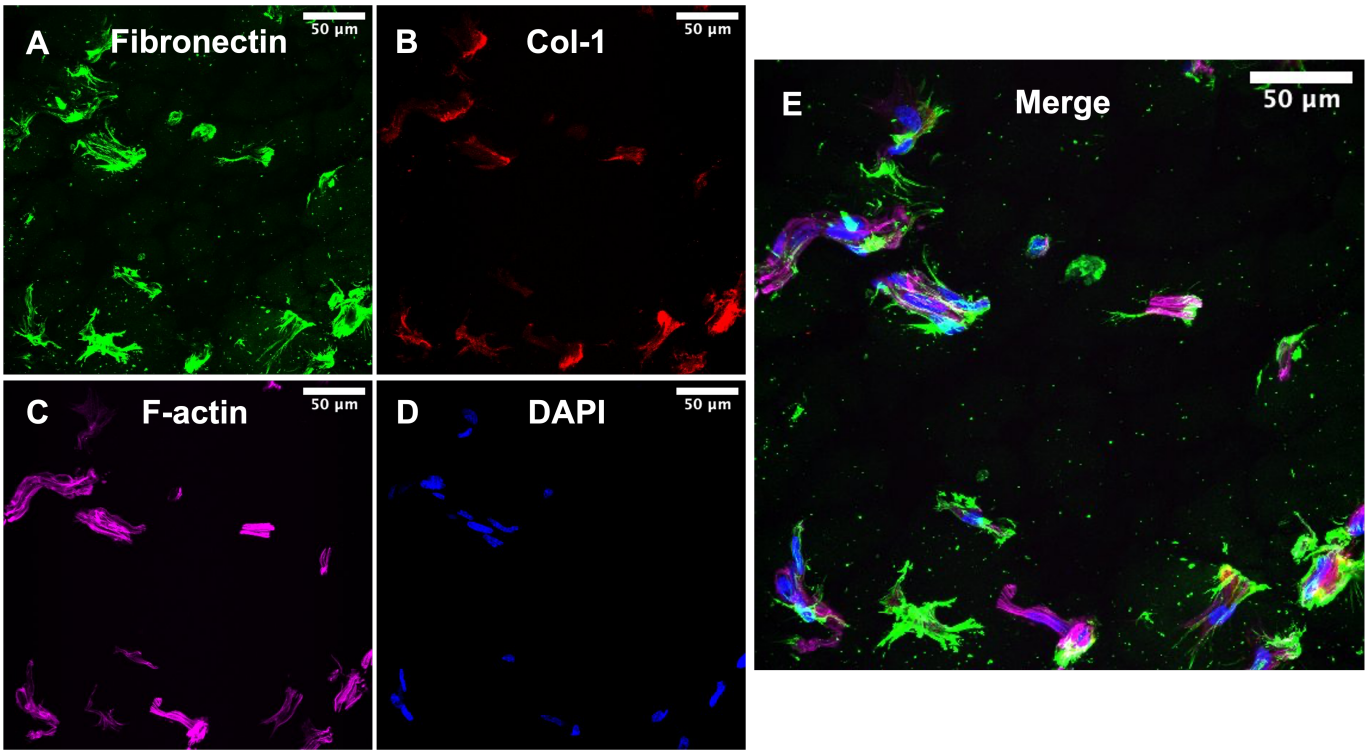


Figure 5.15: Representative maximum projection images of stained 20 $\mu m$ cryosections of primary human VSMCs isolated from a 35 year old female (35-F) encapsulated in 2% polymer content 1 mM degradable and adhesive hydrogel at a density of $4 \times 10^6$ cells/ml, 20 days post encapsulation. A shows fibronectin staining, B collagen-1 staining, C F-actin staining and D nuclear DAPI staining. Finally E shows the merge.

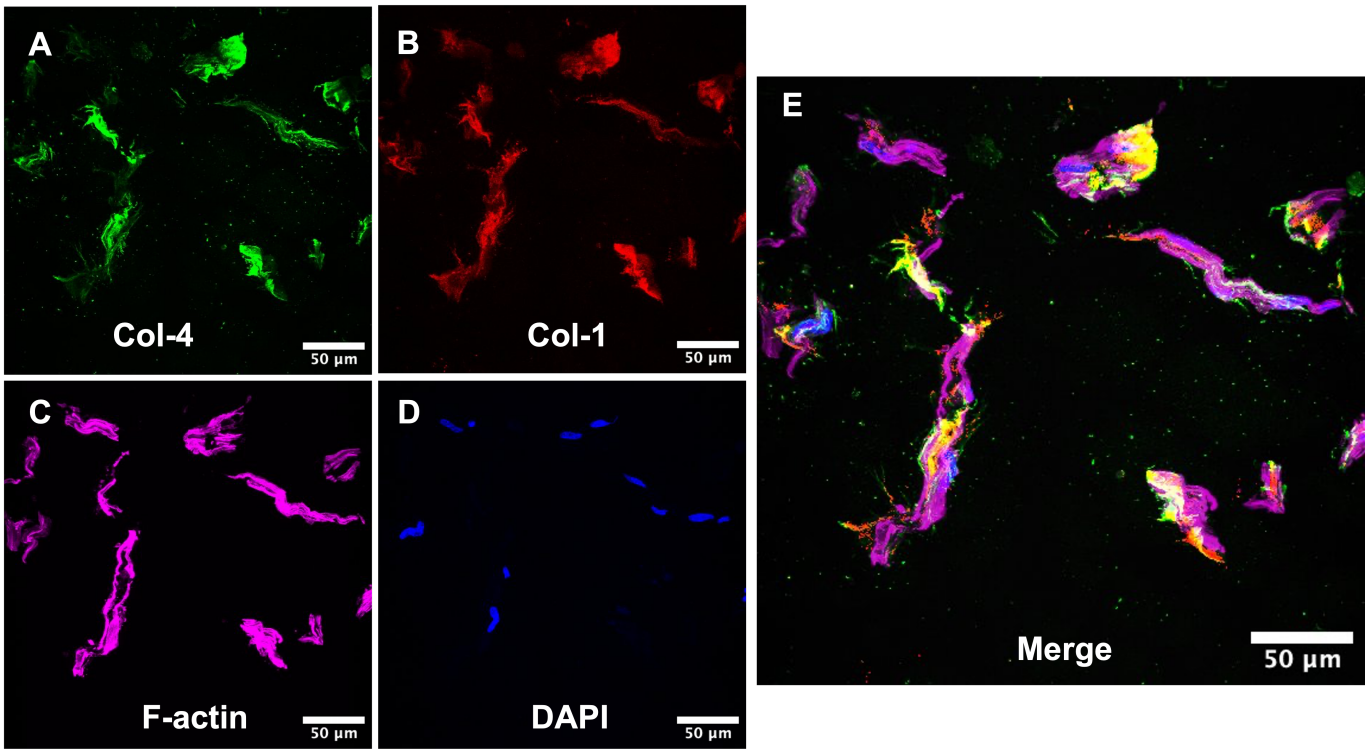


Figure 5.16: Representative maximum projection images of stained 20 $\mu m$ cryosections of primary human VSMCs isolated from a 35 year old female (35-F) encapsulated in 2% polymer content 1 mM degradable and adhesive hydrogel at a density of $4 \times 10^6$ cells/ml, 20 days post encapsulation. A shows collagen-4 staining, B collagen-1 staining, C F-actin staining and D nuclear DAPI staining. Finally E shows the merge.

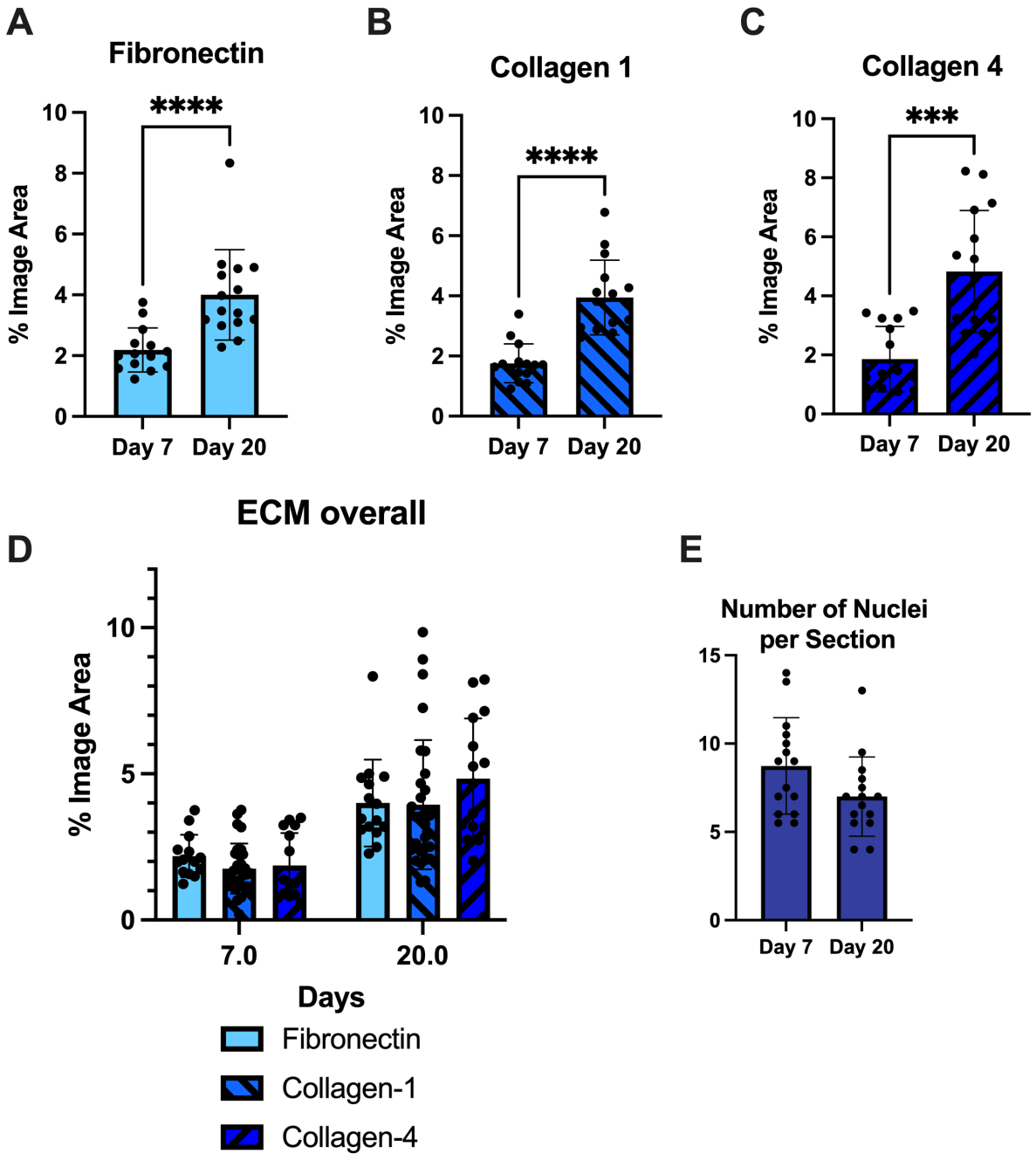


Figure 5.17: Quantitative analysis of the percentage area of images covered by fibronectin (A), collagen-1 (B), collagen-4 (C) and side by side comparison of all stains day 7 and 20 post encapsulation (D). Each dot represents the result for 1 image with 5 images analysed for 3 technical replicates (3 independent hydrogels). E shows the average number of nuclei in each section at day 7 and day 20. Error bars represent standard deviation. Statistical analysis: for A-C and E Mann-Whitney test, D) 2-way Anova with Tukey's multiple comparison test (significance between day 7 and 20 for each protein type in D is omitted for clarity). *** $p \leq 0.001$, **** $p \leq 0.0001$

## 5.4 Discussion

In this chapter we aimed to determine the parameters for our baseline static *in-vitro* culture of VSMCs. Staining in Figures 5.3 and 5.6 showed that primary cells isolated from bovine tissue expressed calponin, $\alpha$SMA and SM-22 indicating that these were indeed the correct cell type and the isolation method suitable.

These cells were then used to identify suitable hydrogel characteristics for 3D encapsulation showing the optimum conditions to be low polymer content of up to 3%, high degradability and adhesive ligand density of 1 mM and seeding density of $5 \times 10^6$ cells/ml or lower. For these conditions, the maximum stiffness of the hydrogel as measured by AFM is of 3 kPa. Estimates for media stiffness also based on AFM measurements are higher at ($22.18 \pm 5.54$ kPa) for human media [Asgari et al., 2022] and 6 kPa for murine aortic arch and descending Aorta [Bae et al., 2016]. In our system, hydrogels of this stiffness would induce cell death and therefore a potential limitation of our model is the inability to match *in-vivo* aortic stiffness. AFM is used to measure the Young's modulus (E) of a material by probing the surface and measuring deformation of a cantilever beam at a micro to nano scale (depending on bead size) [Krieg et al., 2019]. However, whilst AFM was used to measure both the hydrogels and the tissues in these examples, our measurements were made without cells in the system and thus we cannot directly compare these results. Our data estimates the stiffness of the material surrounding the cells at baseline and whilst including cells may change this results, we also hypothesise that as cells remodel their environment these values will further change. Therefore, matching the hydrogel stiffness to estimates based on tissue requires caution. Not only that, but discrepancies in AFM methodology lead to differently reported young's modulus values for a same tissue or material [Norman et al., 2021] and thus direct comparison may not be possible.

Furthermore, the microstructure of aortic tissue compared to that of the hydrogel is very different. The stiffness cells truly feel is dependent on the distribution of adhesive ligands and the range over which cells can "pull" on their surrounding ECM to develop internal stresses. In comparing the structure of our hydrogel compared to medial ECM from tissue, these differ significantly. The cross-links in our hydrogel system are of the range of nanometers long and a tightly packed network of these short range cross-links encapsulate cells. Conversely, the main component of medial ECM is elastin which form long range fibrils of thickness in the order of $\mu$m creating a highly irregular structure [Dingemans et al., 2000]. Whilst a tightly packed ECM may create a relatively stiff environment, the arrangement of fibrils and defects may mean the true peri-cellular environment differs significantly from that of the bulk material. It therefore may not be useful or indeed possible to compare absolute stiffness values between completely different matrices but we may be limited to studying differences within the same material.

The maximum number of cells we were able to encapsulate was limited to up to $5 \times 10^6$ cells/ml.

At this density cells are sparser than in the aortic wall. The reduction in cell viability at higher seeding densities we observed may be due to a reduction in nutrient availability. Indeed, the impact of densely packed cells on network diffusivity has not be explored and cells may hinder transport of nutrients within the matrix. Furthermore, consumption of nutrients by cells nearer to the surrounding media may reduce the availability to cells in the centre. A drawback of this encapsulation limit is a reduced yield of RNA or proteins in the sample for downstream analysis.

By changing the concentration of MMP-cleavable and adhesive motifs included in the hydrogel, the degree to which the cells can interact with their environment is altered. *In-vivo*, VSMC actin filaments bind to surrounding ECM developing dystrophin-glycoprotein complexes to allow cells to develop contractile forces to maintain vessel wall integrity. We therefore hypothesised that we should include a high proportion of adhesive cross-links within our hydrogels. Furthermore, with the aim of exploring cell-ECM interaction, it stands to reason that we should include the highest proportion of MMP-cleavable cross-links possible to maximise possible interactions. Therefore the aim was to use a highly degradable and adhesive hydrogel and the viability data showed these conditions to be favourable to cell survival.

Furthermore the type of peptide motif affects VSMC phenotype as discussed in Chapter 1. Once primary cells are isolated, achieving contractile phenotype in culture is challenging as cells lose their contractile like state almost immediately upon isolation. Different strategies can be employed to "§re-differentiate" cells and the importance of ECM composition has been highlighted as a driver of cell phenotype changes [Stegemann et al., 2005, Assoian et al., 1996, Owens, 1995, Thyberg et al., 1990]. The amino acid sequence of different adhesive motifs drive particular VSMC phenotype driving either a more synthetic or contractile like phenotype. Laminin and collagen-4 are largely accepted to drive a more contractile-like phenotype whilst fibronectin and collagen-1 drive a more synthetic one [Hedin et al., 1988, Hayward et al., 1995, Thyberg et al., 1997, Huo et al., 2000]. Indeed our adhesive RGD ligand is based on fibronectin and therefore may not be the best sequence to facilitate the contractile phenotype most relevant for a healthy baseline model. However, Beamish et al test the ability of fibronectin, laminin and PEGDA hydrogel modified with pendant RGD surfaces to support differentiation of human coronary artery SMCs in 2D culture to contractile like phenotype [Beamish et al., 2009]. Unexpectedly, they show that at a transcriptional and translational level no differences in expression of contractile markers between surface conditions was found for a 6 day culture. The authors suggest that RGD doped hydrogels can indeed then support correct differentiation of these cells at least as well as seeding on laminin coatings. Furthermore, they tested hydrogels containing peptides based on other ECM componants including collagen-1, laminin and elastin but were unable to achieve cell attachement with these motifs. In the discussion, the authors highlight that the cell type, the way in which the peptides are presented to the cells and indeed the density of adhesive ligands all play a role in how well cells attach and their phenotype, thus making clear cut conclusions on which peptides

drive which phenotype complex.

The results of phenotype marker staining of cells seeded on hydrogel surfaces shown in Figure 5.6 do show expression of these markers in the presence of our adhesive and MMP-cleavable peptides. However, these results alone cannot be used to determine the phenotype of the VSMCs. Rather, relative expression of these markers along side others such as myosin heavy chain and smoothelin need to be compared between conditions to determine which conditions drive more contractile like state [Yap et al., 2021]. For this study we have not considered VSMC phenotype closely and this is a limitation of this model as phenotype indeed does heavily influence cell matrix remodelling. However, this model would be used to compare static versus flow conditions for the same hydrogel characteristics and thus the comparison would be made between cells of the same phenotype (unless flow itself mediates a change).

The results of the morphology analysis in different percentage degradable hydrogels showed evidence of cells interacting with the hydrogel actively through secretion of MMPs. Cells are therefore able to breakdown their surrounding matrix showing this material to be suitable for our goal of studying ECM breakdown by vascular cells. Furthermore, staining for ECM proteins revealed that by day 7, encapsulated human primary cells were able to synthesise new matrix, showing deposition of collagen-1, collagen-4 and fibronectin. The media wall is densely packed with elastins and collagens, with elastin arranged in sheets separated by collagen fibres and proteoglycan-rich ECM [Wagenseil and Mecham, 2009]. Indeed, type 1 and type 3 collagens are the most abundant in media [Xu and Shi, 2014], and collagen-4 in the sub-intimal basement membrane [Sariola et al., 1986, Murata et al., 1986]. Furthermore, fibronectin is identified as playing an important role in modulating elastic modulus of the vessel wall as well as mediating the deposition and stability of other proteins, including collagen-1 and collagen-3 [Sottile and Hocking, 2002]. Although not exhaustive, the stains we have performed are therefore relevant to study ECM deposition by VSMCs. However, one gap is the absence of elastin staining. Previous work in the Shanahan group showed elastin staining in 3D tissues to yield non specific results with large amounts of background stain using Verhoeff staining (personal communication). Furthermore, proteomics data performed on matrices produced by 2D cultures of human VSMCs showed low levels of elastin [Whitehead et al., 2023]. This is therefore a limitation to the current model, with elastin loss being an important marker of aortic aneursysm and loss of vessel function in general. We will next work on optimising elastin detection in our system looking at alternative staining methods as well as using RNA expression to infer changes in this protein expression. We chose to seed cells at the highest possible density without impacting viability in order to maximise potential new synthesis and samples were left for up to 20 days to allow new proteins to form. Indeed greater amounts of ECM were seen at day 20 compared to day 7.

We were able to see new proteins at day 7 in cryosectioned samples but not in whole mount stained ones. This suggests that primary and secondary antibodies are unable to penetrate the

hydrogel sufficiently with the time frames in the current protocol. Indeed antibodies are relatively large molecules of approximate size 150 kDa [Janeway Jr et al., 2001]. A 150 kDa FITC dextran molecule corresponds to a stokes radius of approximately 8 nm (based on manufacturers data). The estimated diameter then of a typical antibody is much larger than the mesh network size estimates in Chapter 4. As discussed in this chapter, molecules are not rigid and it may therefore be able to penetrate, however we would expect it to take significant time to fully permeate. Indeed, with whole mount staining of VSMC markers we were able to detect some fluorescence on the edges of the hydrogel (data not shown) but not sufficient signal throughout to analyse these data. In order to perform whole mount staining further optimisation of the protocol is required to try and maximise diffusion into the hydrogel. By comparison Phalloidin molecules have a diameter of approximately 1-2 nm and therefore we were able to perform whole mount staining for all morphology analysis.

## 5.5 Conclusion

The data in this chapter show the PEG-based hydrogel system to be a suitable material for a reductionist *in-vitro* model of the aortic wall. We were able to achieve high cell viability and observe evidence of cells interacting with their matrix within our synthetic material. Cells were shown to both degrade and synthesise within the matrix. In summary the data from this chapter showed:

- Both bovine and human cells can be encapsulated in 3D with a viability of up to 85%
- Encapsulated cells are able to secrete MMPs to break down hydrogel cross-links
- Cells can adopt elongated spindle like morphologies inside the hydrogels
- MMP inhibitors can be used to reduce cell-mediated hydrogel breakdown
- Cells can lay down newly synthesised ECM proteins inside the hydrogel
- We are able to make human cell *in-vitro* models thus increasing the impact of our findings for studying aortic disease

At this stage, we have thoroughly characterised a highly controllable and reproducible synthetic hydrogel system and shown it to be capable of hosting cultures of vascular cells and cell-mediated remodelling. We have gone some way in showing that we can recapitulate function of the cells within this reductionist system. This synthetic *in-vitro* system allows a higher degree of control over the mechanical environment and the ability to alter parameters independently as opposed to tissue studies. This therefore makes it amenable to introducing interstitial flow as is discussed in the next chapter.

# Chapter 6

# Incorporating Flow

## Chapter Abstract

**Background**: Vascular cells are subject to 3 main types of mechanical stimulation from flow, cyclic strains as the wall is distended by puslatile flow, lumminal shear stresses on the endothelium and interstitial stresses due to flow driven into the wall itself. For this work, we are focused on the impact of interstitial fluid stresses and therefore a fluidic system in which flow can be driven through 3D cultures of cells needs to be established. Building on the work in previous chapters, this chapter presents preliminary flow experiments to demonstrate the feasibility of using our *in-vitro* model combined with a microfluidics setup to interrogate the role of flow in matrix remodelling. Further to this, an initial design for a novel bioreactor which may be able to incorporate a more complete vascular mechanical environment is presented.

**Aim**: The aim of this chapter is to present the microfluidics setup used for stimulating 3D cultures of cells, show evidence that cells indeed respond to flow cues and to validate in theory the novel bioreactor design.

**Methods**: Flow was passed through 3D cultures of encapsulated cells housed in Ibidi channel slides using a compressor and pressure controller to drive flow from a reservoir through the culture of cells. Cells were then stained using Phalloidin and DAPI to assess cell morphology and orientation with respect to flow direction. A novel bioreactor design was drawn using computer aided design (CAD) and simulations of flow in the chamber were run using computational fluid dynamics (CFD). Flow velocities and pressures were resolved for using both free flow and porous medium flow governing equations.

**Results**: VSMCs subjected to flow are rounder in morphology compared to those cultured under static conditions. Cells align parallel to the direction of flow. Results from CFD simulations on the novel bioreactor indicate that this design may be suitable to stimulate cultures of cells with luminal and interstitial stresses with the ability to independently control these factors. Results

from simulations are validated against analytical results and shown to be mesh independent.

**Conclusion**: The preliminary flow experiments in this chapter indicate that this setup is suitable for imparting interstitial stresses to encapsulated cells in 3D. Together with results from previous chapters we have shown that we have developed a reductionist *in-vitro* model which can be used to interrogate the role flow in aberrant ECM remodelling. Furthermore, in this chapter we have presented a validated theoretical design for a novel bioreactor which may be used in the future to extend the model we have presented here.

## 6.1 Introduction

In the previous chapters, properties of the PEG-peptide hydrogel have been characterised and the ability to encapsulate vascular cells within these hydrogels has been assessed. Now that we know the material to be permeable to flow and able to host cell-mediated breakdown and the laying of nascent proteins, we are now able to introduce flow into the system.

Chapter 1 covers the different types of mechanostimulation present in the vascular wall, the impact these have on cellular behaviours and the main methods of incorporating these mechanical cues into *in-vitro* cultures. Briefly, the aortic wall is subject to 3 main mechanical forces imparted by pulsatile blood flow: cyclic strains due to vessel wall distention, luminal shear stresses on the endothelium and interstitial stresses caused by flow driven into the wall itself [Lehoux and Tedgui, 2003, Hahn and Schwartz, 2009, White and Frangos, 2007, Shi and Tarbell, 2011]. For this study, we are focused on the impact of fluid stresses on VSMCs interaction with their surrounding ECM. Therefore the main type of mechanostimulation to include is fluid stresses from interstitial flows. Importantly, VSMCs are known to interact with surrounding ECM differently in 3D compared to 2D and thus it is important to include these stresses within a 3D culture. There is historically a paucity of studies incorporating flows in 3D due to an underestimation of the potential importance of these mechanical cues and limitations in biomaterial choice. Therefore the aim in this study is to stimulate 3D cultures of encapsulated VSMCs with fluid stresses by driving flow through the hydrogel in which they are embedded. In this chapter we present the fluidics setup used to stimulate our 3D cultures as well as the impact these flows have on cell morphologies.

Whilst the focus of this thesis has been solely on VSMCs, another aspect which is highlighted in Chapter 1 is the important interactions between ECs and VSMCs in regulating vessel tone. Furthermore, the other mechanostimulation pathways, pulsatile stretch and luminal shear stresses are crucial to ECs and thus for recapitulating the full mechanical environment of the vascular wall. Therefore, we also include in this chapter, a novel design of a bioreactor which may be used to incorporate co-cultures of ECs and VSMCs and the 3 axes of mechanical stimulation. At this stage the work is theoretical however this serves as an introduction for how the work in this thesis may be extended to create more complete vascular wall models.

### 6.1.1 Shear and Normal Fluid Stresses

The purpose of introducing flow into the model is to impart fluids stresses on cells. When fluid passes over a surface, stresses due to friction occur. These are governed both by the relative velocity of the fluid to the surface and the rate of change of direction of the flow. Fluid stresses therefore have both a component in the direction of the flow, shear stress and perpendicular to the direction, normal stresses. For example, in the Aorta, lumen flow imparts shear stresses on

endothelial cells but interstitial flow driven into the wall and around embedded cells has both a normal and shear component.

By considering flow as a continuous medium, these stresses occur due to the relative motion of different layers of fluid and is highly dependent on the rate of change of velocity of the fluid but also it's viscosity. If we consider a 3 dimensional volume of fluid, stresses act on the fluid surfaces in 3 spatial directions. Since the deformation of the fluid is dependent on the magnitude but also the direction of the force applied, stress in a fluid is defined by a stress tensor defined in 3 space coordinates. Expressions for the resultant stresses on the fluid in terms of velocities and pressures of the flow can be established by considering the constitutive laws which relate properties of the flow (for example viscosity) to its response to external forces. Throughout this thesis, stresses are imparted using cell culture medium which is approximated as water and thus treated as an incompressible newtonian fluid. The density of the fluid is therefore treated as constant and the viscosity independent of the strain rate. For such materials the stress tensor is given by:

$$\begin{bmatrix} \tau_{xx} = -p + 2\mu\frac{\partial u_x}{\partial x} & \tau_{xy} = \tau_{yx} = \mu(\frac{\partial u_x}{\partial y} + \frac{\partial u_y}{\partial x}) \\ \tau_{yy} = -p + 2\mu\frac{\partial u_y}{\partial y} & \tau_{xz} = \tau_{zx} = \mu(\frac{\partial u_x}{\partial z} + \frac{\partial u_z}{\partial x}) \\ \tau_{zz} = -p + 2\mu\frac{\partial u_z}{\partial z} & \tau_{yz} = \tau_{zy} = \mu(\frac{\partial u_y}{\partial z} + \frac{\partial u_z}{\partial y}) \end{bmatrix}, \tag{6.1}$$

where $\tau_{xy}$ for example denotes the stress acting on the y plane in the x direction, $\mu$ is the viscosity, $p$ pressure and $u_x$ is for example the x component of the velocity.

In summary, the force imparted by flow is dependent on the viscosity of the fluid, the velocity magnitude of the flow but also the rate of change of direction of flow. Therefore, to fully describe fluid stresses the properties of the flow itself but also the geometry through which it is flowing needs to be fully understood. Stresses are therefore complex to estimate and importantly cannot be directly measured experimentally. For estimates from lumen flow in the Aorta they are inferred from flow profiles and morphological data using methods such as 4D MRI as discussed in Chapter 1. Luminal shear is estimated to be on the order of 0.5-0.8 Pa approximately for healthy patients [Bissell et al., 2013, Van Ooij et al., 2017]. In disease, these values are increased with peak estimates for BAV disease patients at approximately 1.3-1.7 Pa dependant on valve fusion type, severity of stenosis and location within the Aorta [Bissell et al., 2013, Van Ooij et al., 2017]. Estimates for intersitial shear are far more complex to obtain due to the complexity of the vessel wall microstructure and measuring flow pressures and velocities. As discussed in Chapter 2, mathematical models have been used to estimate these at around 0.1 Pa [Wang and Tarbell, 1995].

### 6.1.2 Chapter Aims

The data in this chapter address Aim 3: including mechanostimulation into the *in-vitro* model to be able to test the impact, if any, on cell-matrix interactions. The specific aims of this chapter

were to:

- Develop a fluidics setup to incorporate physiologically relevant levels of interstitial flows in 3D cultures of VSMCs in the PEG-peptide hydrogel
- Explore the impact of flow on encapsulated cell morphology
- Design and validate a theoretical design for a bioreactor to deliver a more complex mechanical environment to a co-culture of ECs and vascular wall cells (VSMCs and Fibroblasts)

## 6.2 Methods

### 6.2.1 Flow setup

Encapsulated cells were stimulated by flow by driving standard cell culture medium through hydrogels cast in Ibidi channel slide ($\mu$-Slide VI 0.4), the same ones used for the permeability PTV assay in Chapter 3, as shown in Figure 6.1. Each channel in the slide has a working volume of 30 $\mu$L of hydrogel cell mixture and has the following dimensions: length 17 mm, width 3.8 mm and depth 0.4 mm.

The system used to drive flow was the Fluigent lineup series and includes: a compressor (Fluigent FLPG plus SMF Pressure generator) with a maximum pressure supply of 2.3 Bar, an airfilter to sterilise air driven into the system (10001001 Air filter for <0.01 $\mu$m particles), a pressure controller (LineUP Flow EZ 2000), a pressure manifold to divide the pressure into separate channels (CTQ-MANI 10 Position Pressure Manifold) and 15 ml falcon tube reservoirs (P-CAP15-HP- PCK 15mL pressure CAP HP PACKAGE). Air above the medium in the reservoirs is then pressurised at a desired level and the medium is then driven into tubing to the chips as shown in Figure 6.1.

Hydrogels were formed as before and cast into the channels. Once the hydrogel formed, a pressure of 30 mBar was set on the pump to drive air out of connecting tubes before connecting the tubing with media to the inlet port on the chip. The outlet is open to atmosphere but pre-filled with media to prevent the hydrogel from drying up before flow is driven to the end. The hanging drop method was used to connect the chip in which a drop is created in the inlet and connected to a hanging drop on the end of the tubing before tubing is plugged in to avoid trapping air into the system.

### 6.2.2 Culturing Cells under Flow

Primary Bovine VSMCs were cultured under flow in 2% W/V hydrogels with 1 mM adhesive and degradable peptide at a density of $1 \times 10^6$ cells/ml. The driving pressure was set to 600 mBar for all flow experiments. For a permeability of $1.65 \times 10^{-16} \mathrm{m}^2$ (data from Chapter 3), from Darcy's law this gives a flow velocity of $6.54 \times 10^{-5}$cm/s and a volumetric flow rate through the hydrogel of 59.7 nl/min. Cells were cultured in these conditions for up to 7 days. Media was pumped through continuously from the same reservoir for the whole length of the experiment. Static control hydrogels were made at the same time from the same cell pellet in sigma coated glass rings as previously.

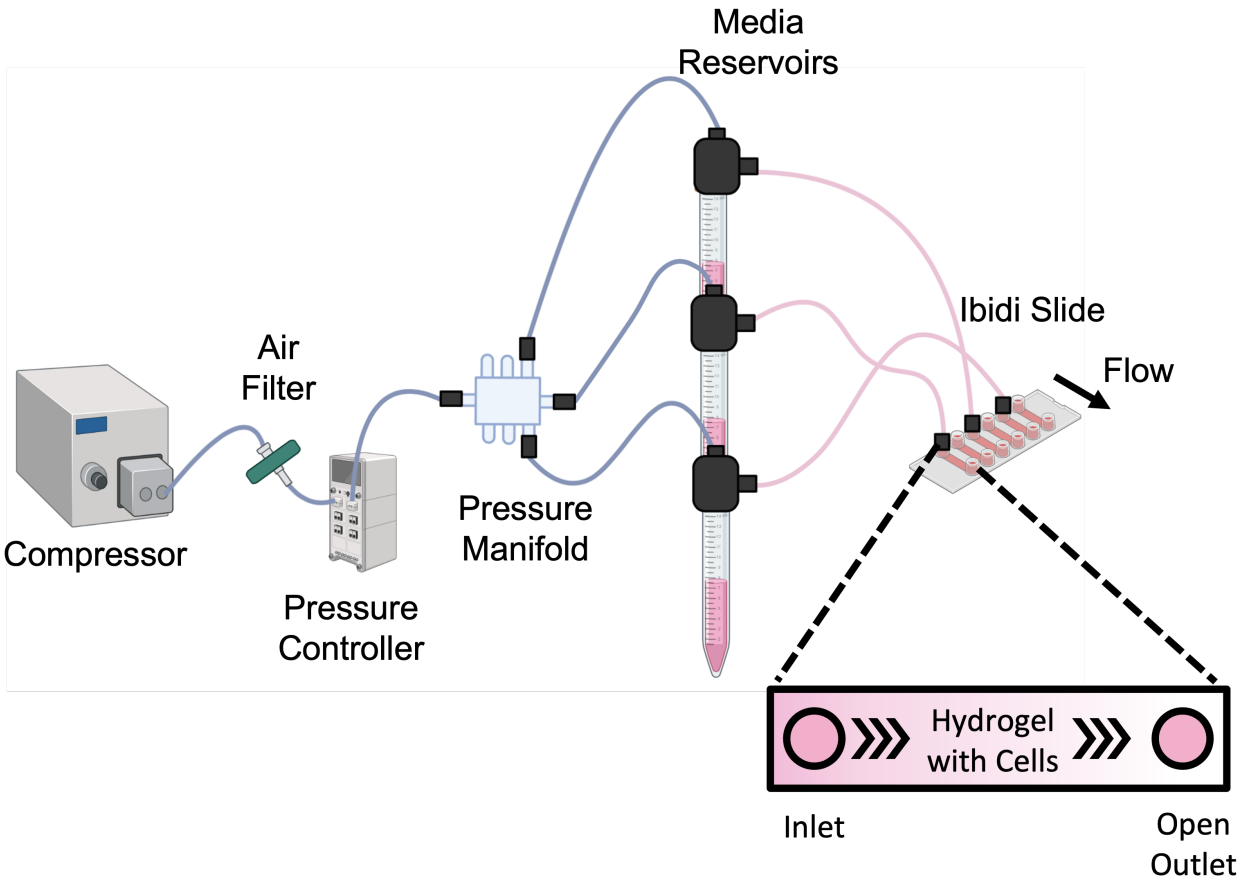


Figure 6.1: Figure showing flow setup used to drive flow through 3D cultures of VSMCS. A compressor is used to generate pressurised air which is filtered before being split into multiple channels. The air in reservoirs of cell culture medium is then pressurised and drives medium into flow slides and through the hydrogel inside the channel. The outlet of the channel is left open.

### 6.2.3 Staining Encapsulated Cells in Flow Chips

Due to the relatively low permeability of the PEG-peptide hydrogel, it takes approximately 8 hrs at a driving pressure of 600 mBar to fully replace the volume of the channel. These time frames are not suitable for immuno staining in which multiple incubations and wash steps are needed. To overcome this, the sample was cut free by running a scalpel on the underside of the Ibidi chip. The plastic layer on the bottom of the channel was then removed to expose the hydrogel which can then be stained similarly to sections of tissue due to the 400 $\mu$m depth of the channel. The hydrogel samples were relatively soft and stick to the underside of the chip so it is challenging to do this process with no damage to the samples. Care was taken to ensure that the hydrogel sections of most interest are the least damaged but some cell hydrogel mixture is lost.

### 6.2.4 Bioreactor Design and Computational Fluid Mechanics

Potential designs for different bioreactors were tested by running flow simulations on different geometries. Computer Aided Design (CAD) software CATIA (D'Assault System) was used to created 3D models of different bioreactors. The resulting fluid domain (volume occupied by flow) was also drawn in CAD. To simulate the movement of flow in these designs, we used a computational fluid mechanics (CFD) package COMSOL Multiphysics. The baseline mulitphysics package with additional CAD import and microfluidics modules were used for this work.

CFD allows the user to solve for fluid pressures and velocities over geometries for which governing flow equations cannot be resolved analytically. This is achieved by discretising the geometry into a mesh of elements for which the solutions can be obtained. Numerical methods are then used to compute values of pressures and velocities at the nodes of the elements by interpolating over small incremental coordinate changes as defined by the mesh, to obtain results over the entire geometry. For this simmulation, there are 2 distinct flow regions to consider. Flow outside of the hydrogel is free laminar flow but flow within the hydrogel is governed by equations for flow through porous media.

The governing equations to be solved in the free flow regions are the Navier Stokes equations given for an incompressible newtonian fluid by:

$$\rho\left(\frac{\partial \mathbf{u}}{\partial t} + \mathbf{u}\cdot\nabla)\mathbf{u}\right) = \rho F - \nabla p + \mu\nabla^2\mathbf{u}, \tag{6.2}$$

where $\rho$ is the fluid density, $\mathbf{u}$ is the flow velocity, $F$ are the external forces applied to the fluid, $p$ is the fluid pressure and $\mu$ the fluid viscosity. This is combined with the continuity of mass equation given by:

$$\frac{\partial \rho}{\partial t} + \nabla\cdot(\rho\mathbf{u}) = 0, \tag{6.3}$$

In the porous region the continuity and momentum equations are combined to give the Brinkman equations which adapt to include the solid phase of the medium and hence the extra flow obstacle:

$$\rho\frac{\partial \mathbf{u}}{\partial t} - \nabla \cdot \mu(\nabla \mathbf{u} + (\nabla \mathbf{u})^T) - (\frac{\mu}{k}\mathbf{u} + \nabla p - F) = 0, \tag{6.4}$$

where k is the permeability of the porous phase and F represents any external body forces.

Simulations were set up by first defining the geometry over which you want to resolve, applying material properties to the fluid regions and then defining which type of flows are needed for each region in the geometry. Initial and boundary conditions were then prescribed in order to define the problem. The geometry was then meshed using a combination of prescribing element size and shapes and finally the simulation was run and the results visualised.

## 6.3 Results

### 6.3.1 Preliminary data shows VSMCs align to the direction of flow

Viability of cells in the presence of flow at day 3 was assessed using the invitrogen LIVE/DEAD™ Viability/Cytotoxicity Kit as before. Figure 6.2 shows representative images of viability both near the inlet and the outlet of the flow chip. Viability was seen to vary along the length of the channel with an average viability in the front half of the channel of 68%. The viability was significantly worse in the half of the channel nearest the outlet with an average of 22% (based on 1 biological replicate and 3 technical replicates). We hypothesise that this is due to the extended time taken for media to reach the end half of the channel. At these flow rates 8 hrs is needed for the full volume to be replaced and therefore cells at distance of more than 4 mm have been without media for at least 2 hrs. This estimation assumes that passive diffusion of nutrients is slower than the active mass transport due to flow but to remain cautious, we excluded cells beyond 4 mm from the inlet from our analyses going forward as these cells are likely dead or else impacted by the lack of nutrients. These viability data suggest that the presence of flow itself does not cause cell death and thus cells can be cultured under flow.

Cell morphology was assessed using F-actin staining as previously. Briefly a threshold was applied to the image to segment cells before analysing for predefined measurements set in the FIJI image analysis software. The parameters of interest in this study were cell circularity and cell alignment. Based on previous work in Chapter 5 showing cells remain rounder in non degradable conditions, we hypothesise that cell morphology could be an indicator of the degree to which cells are degrading their surrounding matrix in order to spread. Alignment was used as a marker that cells are sensing the flow delivered. Cell circularity was compared to that of cells in static conditions. Figure 6.4 shows a representative image of Phalloidin and DAPI staining of cells cultured under flow. Analysis of these images (Figure 6.5) shows cells are significantly rounder under flow conditions compared to in static culture.

To test cells for alignment to flow direction, the feret angle was computed for each cell. This is defined as the angle between the largest distance between 2 points on the cell perimeter (the feret distance) and the x-axis. In the images, the flow direction was parallel to the y axis so the angle between the feret distance and flow was computed by taking the modulus of the 90 degrees minus the feret angle. Figure 6.6 shows cells under flow had a smaller angle to the y-axis compared to static conditions. Cells with an angle of less than 45 degrees to flow are classified as aligned and the average proportion of cells that met this condition under flow was 75.6% under flow compared to 45.5% in static conditions.

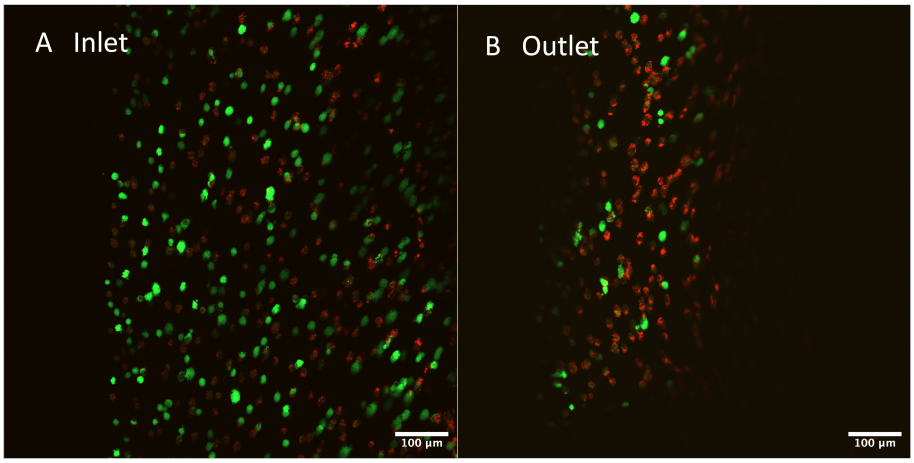


Figure 6.2: Representative images of live (green) dead (red) staining on bovine VSMCs encapsulated in 2% polymer content 1 mM degradable and adhesive hydrogels at a density of $1 \times 10^6$ cells/ml and cultured under flow at a driving pressure of 600 mBar for 3 days. Panel A shows an image taken near the flow chip inlet and Panel B near the outlet. The viability of cells in Panel A is approximately 64% whereas in Panel B it is 37%. Direction of flow from top to bottom.

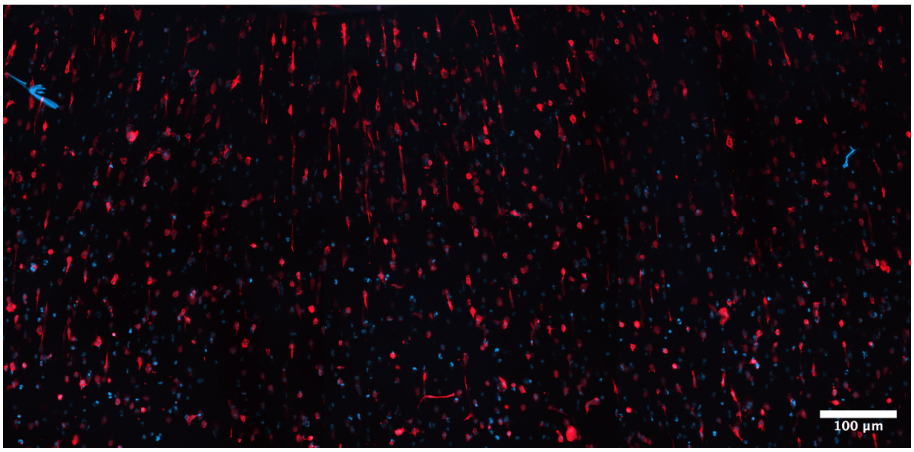


Figure 6.3: Representative images of F-actin staining on bovine VSMCs encapsulated in 2% polymer content 1 mM degradable and adhesive hydrogels at a density of $1 \times 10^6$ cells/ml and cultured under flow at a driving pressure of 600 mBar for 7 days. This image is a maximum projection of the 5 image z-stack over the 400 $\mu$m Ibidi Channel depth taken at the inlet of one channel. Direction of flow from top to bottom.

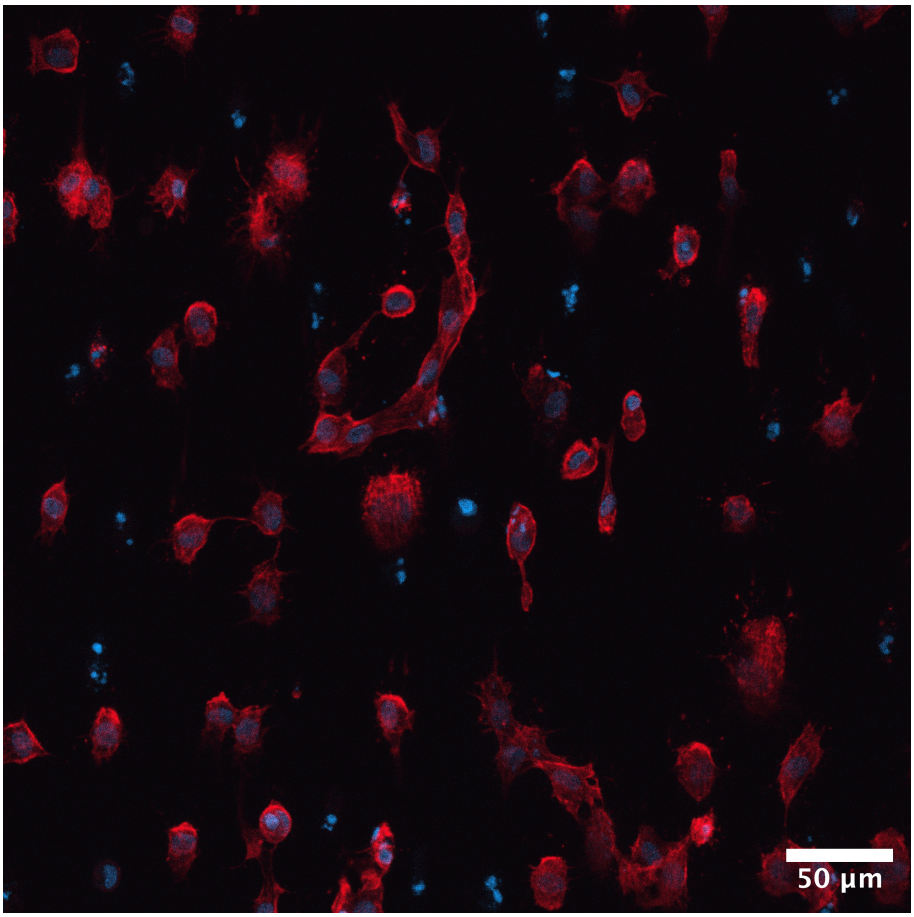


Figure 6.4: Representative images of F-actin staining on bovine VSMCs encapsulated in in 2% polymer content 1 mM degradable and adhesive hydrogels at a density of $1 \times 10^6$ cells/ml and cultured under flow at a driving pressure of 600 mBar for 7 days. This image shows a cells in one plane taken near the inlet. Direction of flow from top to bottom.

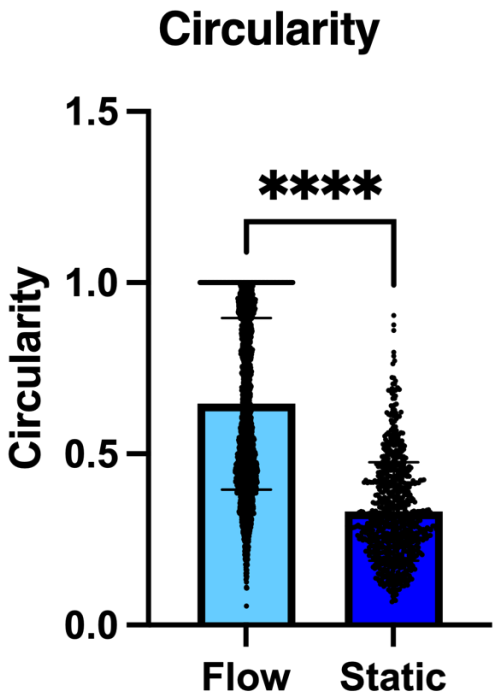


Figure 6.5: Figure showing the circularity of cells cultured in 2% W/V hydrogels with 1 mM adhesive and degradable peptide at a density of $1 \times 10^6$ cells/ml under flow (applied pressure 600 mBar, average flow rate 59.7 nl/min) and in static conditions. Each point represents measurement for 1 cell with results collected from maximum intensity projections of a z-stack taken at 10x in the centre of the hydrogel for static condition or 10x images of the first 4 mm of the hydrogel channel for flow conditions. Results are based on 3 biological replicates (1 technical for each) for the static condition and 2 biological replicates (at least 2 technical for each) for the flow condition. Statistical analysis: Mann-Whitney test; **** $p \leq 0.0001$.

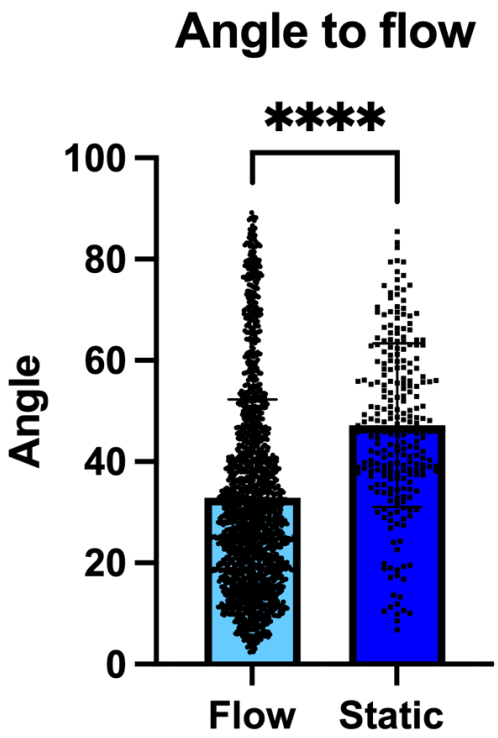


Figure 6.6: Figure showing the angle between cells and flow direction for cells cultured in 2% W/V hydrogels with 1 mM adhesive and degradable peptide at a density of $1 \times 10^6$ cells/ml under flow (applied pressure 600 mBar, average flow rate 59.7 nl/min) and in static conditions. The angle with the y axis is taken in the static condition. Each point represents measurement for 1 cell with results collected from maximum intensity projections of a z-stack taken at 10x in the centre of the hydrogel for static condition or 10x images of the first 4 mm of the hydrogel channel for flow conditions. Results are based on 3 biological replicates (1 technical for each) for the static condition and 2 biological replicates (at least 2 technical for each) for the flow condition. Statistical analysis: Mann-Whitney test; **** $p \leq 0.0001$.

### 6.3.2 Novel Bioreactor Design

In this section we present a potential bioreactor design which could be used to create a more complete model of the aortic wall in the future. It can include monolayers of ECs combined with the 3D cultures of VSCMs (with the possibility of including fibroblasts) and crucially allows for both luminal and interstitial stimulation by flow.

Figure 6.7 shows a schematic of the concept for the bioreactor. Flow through a cylindrical lumen above the hydrogel is used to stimulate a monolayer of ECs seeded on the top of the hydrogel VSMC mixture which is set above a porous membrane. A second outlet is made underneath the hydrogel where a pressure sync can be used to draw flow from the lumen down through the hydrogel cell mixture. Therefore the proportion of flow moving interstitially depends on the relative pressure drop between the inlet and the 2 outlets.

The aim was to create a design that could give rise to physiological stresses. Stresses of approximately 1 Pa are required to stimulate cells seeded on the surface of the cell hydrogel mixture to mimic *in-vivo* values. The cross section of the lumen flow part of the bioreactor was selected to be circular to mimic the shape of the Aorta. However one edge was kept flat to avoid issues with evenly pipetting cells and hydrogels onto curved surfaces as shown in Figure 6.8. An important factor to consider is that the viscosity of blood is approximately one order of magnitude larger than that of cell culture medium, the fluid for the bioreactor. It therefore follows that to obtain the same values of shear stress through the bioreactor, faster flow through a smaller channel size is required. It is essential however, that maximum flow rates into the lumen remain in the laminar flow regime in order to keep flows from becoming turbulent. A measure of the flow regime in a circular cross section pipe is given by the Reynolds number:

$$Re = \frac{\rho u D}{\mu}, \tag{6.5}$$

where $\rho$ is the density of the fluid, D the diameter of the pipe, u the velocity and $\mu$ the viscosity. Values of Re lower than 2000 indicate a laminar flow regime.

The lumen can be considered as standard flow in a pipe for which the velocity profile is known and described by:

$$u(y) = 2u_{max}(1 - \frac{y^2}{r^2}), \tag{6.6}$$

where $u_{max}$ is the centre-line velocity and r is the pipe radius.

From the stress tensor give in Equation 6.1, the expression for wall shear assuming symmetry around the axis through the pipe, is given by:

$$\tau_{zx} = \mu \frac{\partial u}{\partial y}|_{y=D/2} \tag{6.7}$$

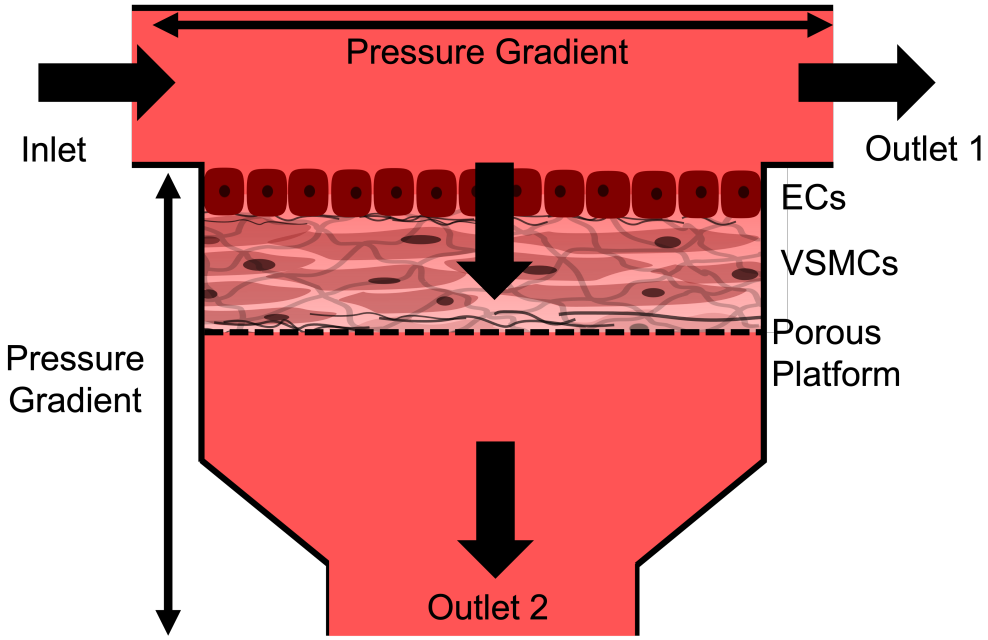


Figure 6.7: Schematic of the concept for the bioreactor. Flow through a lumen above the hydrogel is used to stimulate a monolayer of ECs seeded on the top of the hydrogel VSMC mixture which is set above a porous membrane. A second outlet is made underneath the hydrogel where a pressure sink can be used to draw flow from the lumen down through the hydrogel cell mixture.

By combining the above 2 expressions shear on the wall of the lumen can also be given as:

$$\tau_{zx} = \frac{4\overline{U}\mu}{r}, \tag{6.8}$$

where $\overline{U}$ is the mean velocity.

The diameter of the lumen was chosen to be 4 mm for which with an inlet average velocity of 0.4 m/s theoretical estimates of shear stress at the lumen wall are at 0.7 Pa with the Reynolds number at 1792 and thus still in the laminar regime.

Since the hydrogel is composed of a solid phase surrounded by water, the hydrogel was modelled as a porous medium. Therefore there were 2 distinct regions of flow in this computation as shown in Figure 6.8. Laminar free flow in the lumen region and the flow region below the hydrogel and porous medium flow within the hydrogel.

The COMSOL model was set up for a steady state solution assuming an incompressible fluid and a no slip boundary condition at the interface of the fluid-wall interface. Continuity of pressure and velocity is imposed at the boundary of the hydrogel and the lumen and the hydrogel and outlet region. Fully developed parabolic flow was imposed at the lumen inlet with a mean velocity of 0.4 m/s. The outlet of the lumen was set at 0 gauge pressure and the outlet under the hydrogel was set to -1000 Pa simulating a connected pump pulling the fluid through by means of a negative

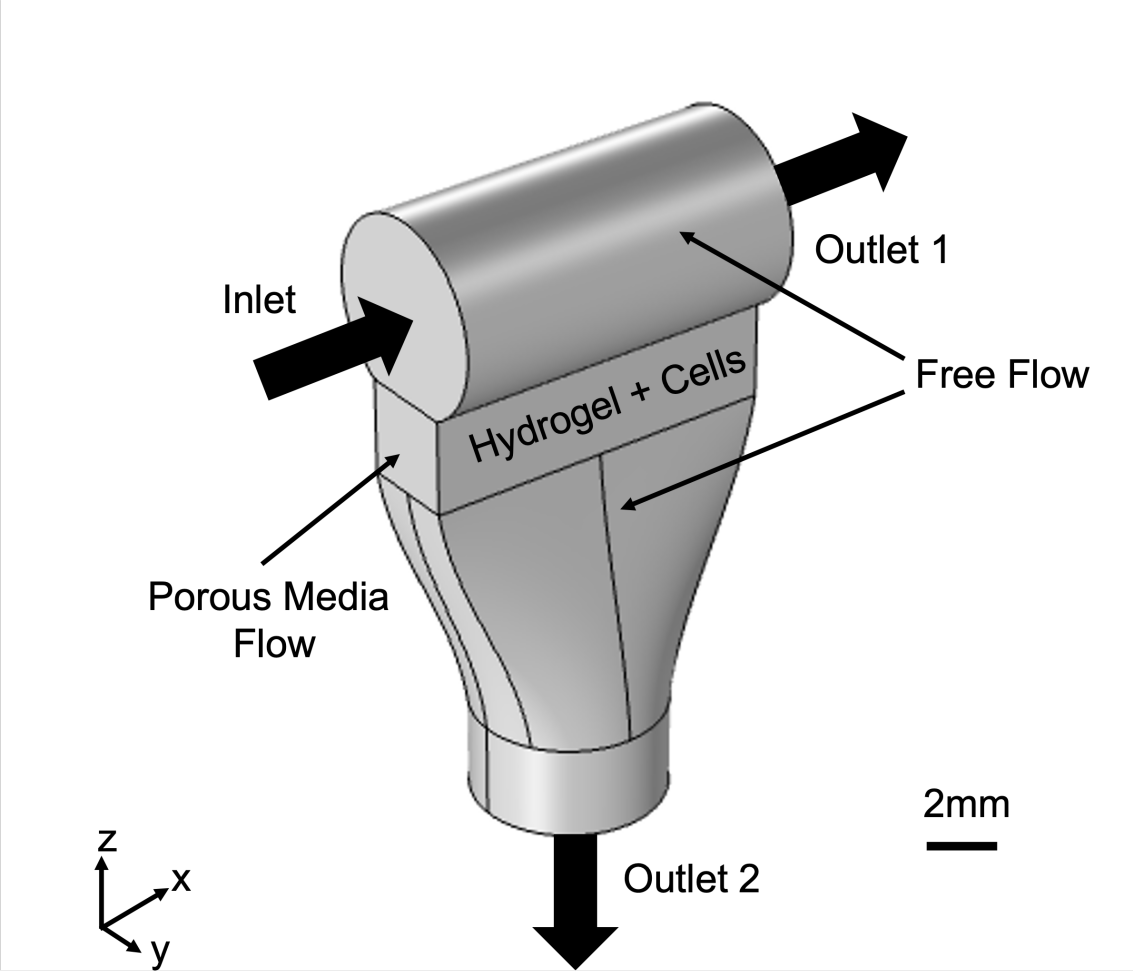


Figure 6.8: Figure showing the fluid domain for the bioreactor design. The regions above and below the hydrogel is modelled using free flow whereas in the hydrogel region, porous media flow is modelled. As before 2 outlets direct flow through the lumen to impart shear stresses to cells seeded on top of the hydrogel with some flow drawn down through the hydrogel to generate interstitial shears.

pressure gradient. These values were arbitrarily chosen and can be altered to achieve the required flow rates. The hydrogel permeability was set to $1.65\times10^{-16}\text{m}^2$ from the PTV permeability assay in Chapter 3 for pressures of 600 mBar with this setup.

Results from the simulations are shown in Figure 6.9 and Table 6.1. With this design we were able to achieve 2 directions of flow as shown in Panel A of Figure 6.9 in which flow streamlines (red) show flow through the lumen and down into the hydrogel drawn by the negative pressure gradient applied at the outlet. Luminal flow stimulates the hydrogel surface with shear stress as shown in Panel B. This is where the EC layer would sit and therefore the simulations predict the majority of cells would be exposed approximately to between 0.8-1.1 Pa for this inlet velocity, with a small border under lower stress. The magnitude the luminal shear can be altered by changing the inlet velocity as shown in Figure 6.10. Futhermore, the velocity field shown in Figure 6.9 Panel B show the characteristic parabolic flow profile found in pipes with the fastest velocities in the pipe centre.

The interstitial flow is controlled by altering the outlet pressure. The average velocity inside the hydrogel is computed at the hydrogel centre. Average values are given for different outlet pressure in Table 6.1. Importantly shear and interstitial velocities can be independently tuned as average velocity in the hydrogel did not change for changing inlet velocity at fixed outlet pressure.

| Applied Pressure at Outlet 2 [Pa] | Mean Velocity [m/s] |
|---|---|
| -2000 | $1.86\times10^{-7}$ |
| -1000 | $9.30\times10^{-8}$ |
| -500 | $4.66\times10^{-8}$ |
| -200 | $1.88\times10^{-8}$ |
| -100 | $9.55\times10^{-9}$ |

Table 6.1: Table showing mean velocity values in the hydrogel centre values obtained using COMSOL for different applied pressures across the hydrogel.

### 6.3.3 Model validation

#### Simulation Results are Shown to be Mesh Independent

The way in which the mesh is constructed for CFD simulations can greatly affect the accuracy and precision of the results achievable and can therefore incorrectly bias results. In general the finer the mesh the more accurate a result should be, however this is dependent on the distribution and shape of mesh elements relative to that of the domain over which you wish to resolve. Furthermore the more elements included in the mesh, the more intensive the computations are and therefore it is a balancing act of creating a mesh with enough elements to capture the result and being efficient

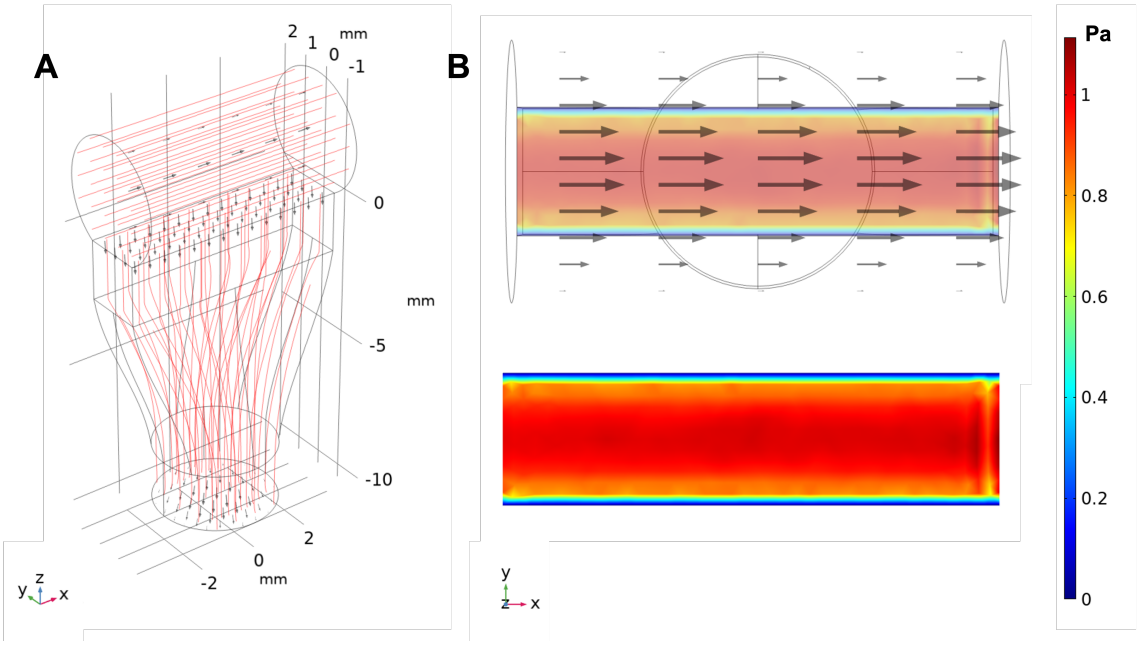


Figure 6.9: Figure showing the results obtained from the COMSOL simulations of flow in the bioreactor. In A flow streamlines are shown in red. Black arrows represent the direction of the velocity vector field but are not drawn to scale for clarity due to the comparatively small velocity magnitudes in the hydrogel compared to the lumen. In B, a heat map of the shear stress on the surface of the hydrogel. Black arrows show the velocity vector field and in this Panel, arrow size depicts velocity magnitude.

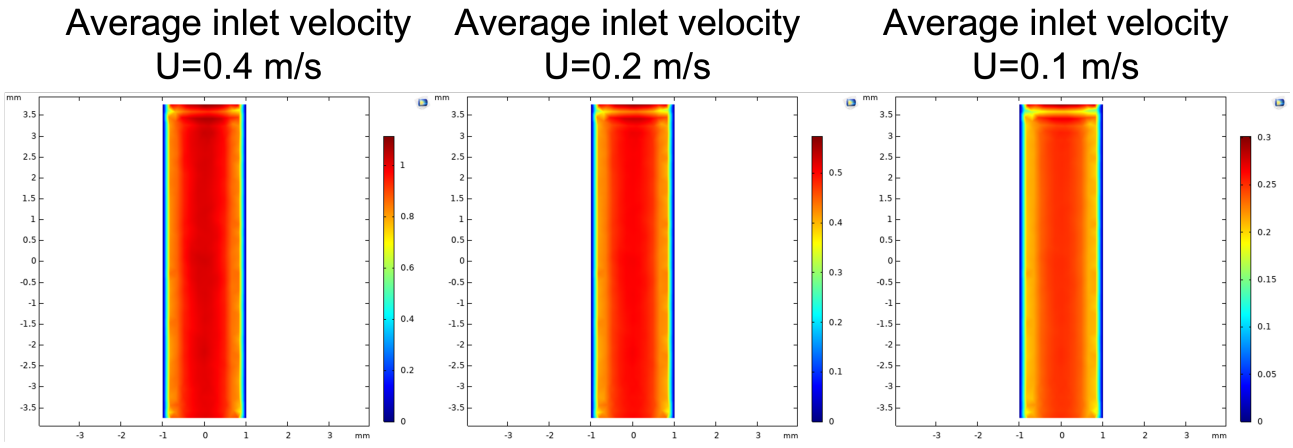


Figure 6.10: Figure showing heat maps of shear stress on the surface of the hydrogel for different inlet average velocity conditions.

with how many are actually needed. When making a mesh it is important to consider the location of the results of interest. Finer elements or boundary refinements can be implemented in these regions and areas of less importance far away from regions of interest can have coarser elements thereby removing the need to resolve to the same precision everywhere and reducing computation time. It is extremely important to ensure that the mesh construction does not artificially impact the results of the simulation. This is achieved my conducting a mesh independence study where by the elements in a mesh are made progressively smaller and a value of interest is recorded to ensure that as the mesh becomes finer the results converge to a solution.

A free tetrahedral mesh with a 3 layer boundary refinement on domain edges was used. The average size of the elements was altered by prescribing the maximum element size in the mesh applied to all domains. A point velocity in the centre of the hydrogel and the centre of the surface were taken as markers of convergence and their values were recorded as the element number was increased from 4539 to 509325 elements. The results are shown in Panel A of Figure 6.11 and show the mesh to converge on values for both velocities and hence suitable to obtain stable solutions.

**Comparison to Expected Theoretical Results Show Simulations to Give Accurate Results**

In order to validate the simulations, results were compared to those obtained using analytical expressions where possible. For this validation step, the lumen and interstitial flows are considered separately. The lumen can be considered as standard flow in a pipe. Panel B in Figure 6.11 shows that the expected parabolic velocity profiles for flow in a pipe were obtained and that the COMSOL results match closely to theoretical ones.

For the interstitial flow, equations describing flow through a porous medium were used. The Darcy's law describes this given as:

$$\overline{U} = -\frac{k}{\mu}\Delta p \tag{6.9}$$

where $\Delta p$ is the pressure drop across the hydrogel. If we assume the flow to be uni-directional through down the hydrogel, the predicted mean velocities in the z direction can be compared to those obtained in COMSOL for different pressure drops imposed across the hydrogel, ie the pressure differential between the lumen inlet and outlet 2.

Mean velocities through the hydrogel in COMSOL were recorded at the hydrogel centre-point and compared to values predicted by theory for different pressure drops as shown in Table 6.2. The results show that COMSOL predicts values within 3% of theoretical estimates.

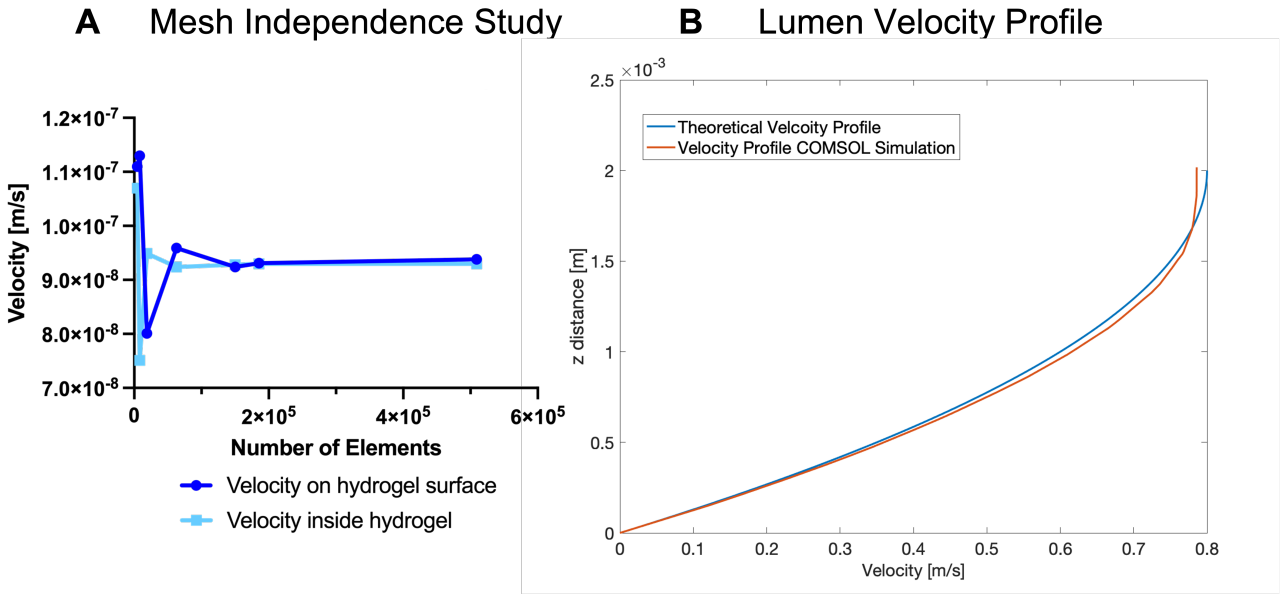


Figure 6.11: Figure showing validation of simulation results. In A the results of the Mesh independence study are shown displaying velocity values as element size is increased. In B a comparison between the theoretical parabolic flow profile through a pipe and that achieved in the lumen of the bioreactor.

| **COMSOL** | | **Analytical Solution** | |
|---|---|---|---|
| Applied Pressure at Outlet 2 [Pa] | Mean Velocity [m/s] | Mean Velocity [m/s] | Percentage Difference in Velocities |
| -2000 | $1.86\times10^{-7}$ | $1.85\times10^{-7}$ | 0.15 |
| -1000 | $9.30\times10^{-8}$ | $9.27\times10^{-8}$ | 0.30 |
| -500 | $4.66\times10^{-8}$ | $4.63\times10^{-8}$ | 0.61 |
| -200 | $1.88\times10^{-8}$ | $1.85\times10^{-8}$ | 1.52 |
| -100 | $9.55\times10^{-9}$ | $9.27\times10^{-9}$ | 3.04 |

Table 6.2: Table showing the comparison and percentage difference for mean velocity values in the centre of the hydrogel predicted using Darcy's law and values obtained using COMSOL for different applied pressures across the hydrogel.

### 6.3.4 Prototype Model

Figure 6.12 shows a potential prototype design for the bioreactor. The design is in 3 parts which allows the hydrogel to be formed in a tray which can be easily removed for downstream analysis. The lumen is long enough to ensure that flow entering has time to become fully developped over the hydrogel. Inlet and outlets can be connected to tubing and then to pumps and reservoirs as needed. The whole system could be bolted together. Depending on manufacturing cost, the hydrogel tray could be disposable to help with sterility.

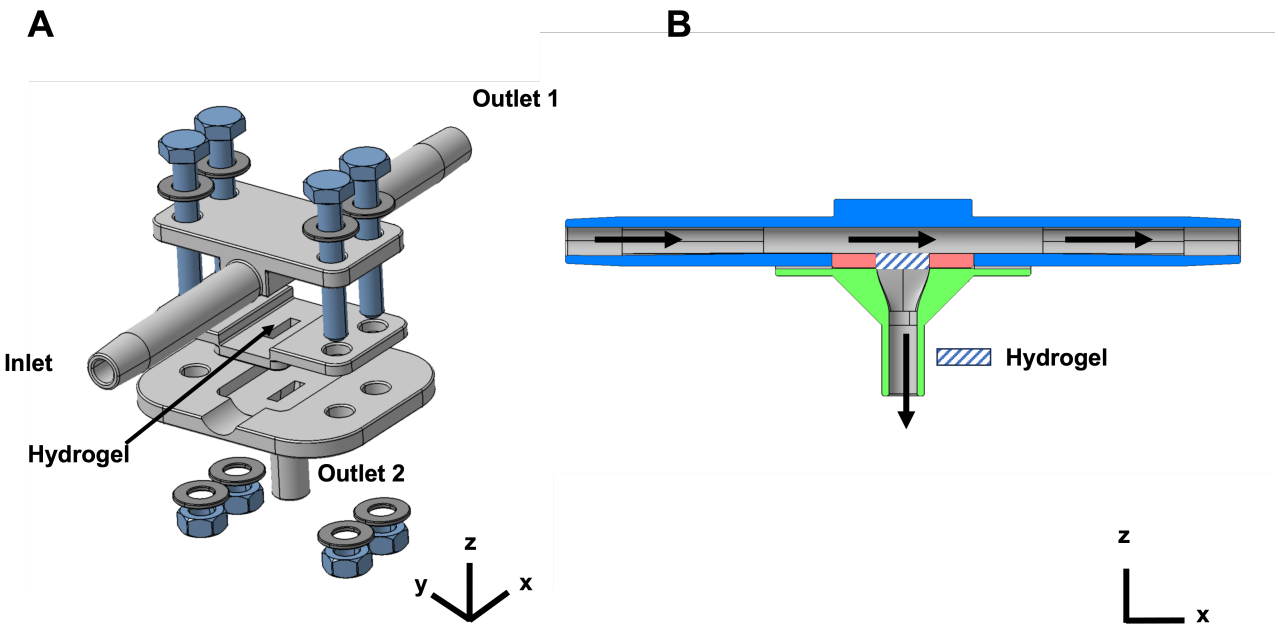


Figure 6.12: Figure showing a potential prototype design of the bioreactor design in Panel A and a cross-section in Panel B. The design is in 3 separate layers bolted together which allow for easy removal of the hydrogel tray.

## 6.4 Discussion

In this chapter the aim was to setup a suitable flow system to stimulate encapsulated cells with interstitial flow. VSMCs were cultured for 7 days under flow and were seen to align parallel to the flow direction indicating cells respond to interstitial cues. Some cells became elongated in the flow direction, but on average, the circularity of the cells was greater compared to that of cells in static culture. This may possibly indicate that cells are producing fewer MMPs under flow and are thus not destroying the matrix and spreading as much as in static conditions. Indeed their rounder morphology is akin to that seen when encapsulating cells in hydrogels with fewer degradable cross-links as shown in Chapter 5.

These preliminary results show this system to be suitable for future experiments exploring the impact of these flow on cell behaviours as is discussed in the planning of future work in Chapter 7. Stresses are complex variables which depend on the rate of change of flow through the matrix as well as the fluid properties itself. Differences in our model such as hydrogel microstructure compared to ECM or indeed that we stimulate our cells with culture medium in place of non-newtonian blood mean we cannot recapitulate these factors from the *in-vivo* environment individually. However, we aim to recapitulate the resultant forces on these cells by modulating flows to give rise to relevant levels of shear within the confines of our model.

Estimates of the velocities through the hydrogel for the applied pressures in our experiments

are on the order of $10^{-5}$ cm/s, close to estimates for interstitial flow velocities through the aortic wall [Wang and Tarbell, 1995]. Wang et al developped a model to estimate levels of shear stress on VSMCs embedded in the vascular wall by modelling the arterial wall as an array of cells in a fibre matrix. Cells are modelled as impermeable and are arranged in an idealised square array surrounded by an even "grid" of matrix. Estimates of shear stress are made my considering the direction of flow on the cell boundary and are given by:

$$\tau = \frac{B\mu\frac{Q}{A}}{\sqrt{k}}, \tag{6.10}$$

where B is a constant with value $4/\pi$ or $3/\pi$ depending in whether cells are treated as cylinders or spheres, $\mu$ viscosity in Pa·s, Q is the volumetric flow rate in $m^3/s$, A is the surface area in $m^2$ and $\kappa$ is the Darcy permeability in $m^2$. Indeed the Tarbell group apply these estimates to their own flow experiments on VSMCs and Fibroblasts embedded in collagen hydrogels [Wang and Tarbell, 2000, Shi et al., 2009]. For the values of pressure and permeability in our experiments we estimate from these equations that the shear acting on embedded cells are approximately 0.04 Pa, close to physiologically relevant levels of 0.1 Pa as estimated by Wang et al [Wang and Tarbell, 1995]. One limitation in our estimates using this method is that permeability values were obtained without including cells within the hydrogel and these likely have a significant impact on the permeability of the material as a whole. Plans to improve on these are presented in the future work section in Chapter 7. Furthermore, we assume that the pressure drop across the hydrogel is that applied with the pump but the system does not yet include a pressure gauge across the hydrogel to more precisely determine the true pressure drop. Indeed we have neglected the resistance contribution of the connecting pipes but given its relatively low permeability, we hypothesise that the resistance of the hydrogel itself far outweighs that of the tubing. In the future, a gauge or flow rate sensor could be used to improve on this.

Whilst these estimates are useful they are derived from highly simplified models of the wall. To obtain this relation between pressure and shear Wang et al greatly simplify the microstructure vascular matrix. Furthermore, they assume cells to be evenly distributed but *in-vivo* the density of VSMCs depends on artery type and location in the wall. Indeed *in-vivo* VSMCs form confluent sheets in the media with spaces between layers. Thus the cell volume fraction used in these models is likely underestimated and may result in an underestimation of the levels of shear [Wang and Tarbell, 1995]. Indeed these are estimates based on bulk material properties but the specific microstructure of each matrix will heavily influence the stress felt by cells. Using average velocities and flow rates to calculate shear over simplifies more complex flow patterns within the ECM which also in turn give non-uniform shear stresses. In [Pedersen et al., 2007], flow through idealised matrices are simulated using CFD in place of analytical relations as in [Wang and Tarbell, 1995]. The authors show that fiber diameter and spacing strongly affect the

flow around cells and indeed estimates of peak shear stresses using CFD are higher than predictions using Brinkman equations using the average matrix properties. In short, bulk permeability does not have the resolution to capture the full shear variation at the single cell scale. The authors further predict however that discrepancies between analytical and numerical estimates may be lower in the case of matrices with permeabilities lower than $10^{-18}$ $m^2$ where continuum approximations with bulk properties may be more accurate [Pedersen et al., 2007]. With enough resolution of the matrix microstructure and the position of cells within it, CFD may yield more accurate estimates of shear. However as previously mentioned obtaining high detailed images of hydrogel microstructure is not simple. Furthermore, these models cannot be validated experimentally as shear cannot be measured.

Given the dependency of shear on so many factors and difficulties in characterising these properties we are likely only ever to achieve estimates of varying accuracy. In our hydrogel system, we as of yet do not have enough resolution on the matrix microstructure to improve upon estimates using the analytical relations presented in [Wang and Tarbell, 1995], although ideas on how we might obtain these are discussed in the future work presented in Chapter 7. Furthermore, shear stresses are likely to vary significantly *in-vivo* with vessel position or even between tissue samples given the variation in tissue microstructure and interstitial pressures. This means truly defining physiological shear may not only be hampered by inability to make direct measurements but also by tissue variability. Nonetheless, estimating shear levels proves useful to obtain rough estimates of the order of magnitude of forces we are exposing cells to and to decide on flow pressures to apply or compare between samples.

The setup described so far can only be used to impart interstitial shears on embedded cells within the hydrogel. As described in [Lust et al., 2021b] in Chapter 1, vessel maintenance is regulated by inter-cellular communications between different vascular cells and fluid stimulation both lumininally and interstitially. It stands to reason that a complete disease model requires the need to include all of these factors. Particularly, understanding the relative contributions of luminal and interstitial shear stresses in aberrant ECM remodelling for aneurysms may prove key in determining which blood flow characteristics are most important for risk of aneurysm. To this end, we present a potential novel bioreactor design which could be used to interrogate the relative contribution of these mechanical forces as well as including the intercommunication between ECs and VSMCs. The top of hydrogels with embedded VSMCs can be seeded with monlayers of ECs in the bioreactor. The lumen can then be used to stimulate these ECs with shear stress whilst a negative pressure gradient under the hydrogel draws flow interstitially through the hydrogel to stimulate VSMCs. Importantly we demonstrated with our simulations that we can independently control the magnitude of luminal shear and interstitial shear by controlling the inlet velocities and outlet pressure. Results of our simulations were validated using analytical predictions and we are able to show the results are mesh independent.

At this stage, all the work is theoretical and we have not manufactured the design to test in the lab. Manufacturing a device to this precision on this scale is not trivial and may indeed be the more complex part of the task. The complex geometry may prevent the use of certain techniques like machining and most likely, high tolerance 3D printing is the best approach to make these components. Different materials need to be tested for this purpose and the components need to fit together well enough for the system to seal under high pressures. Setting up a system with a commercial chip required optimisation and thus with a custom design this process should not be underestimated. However, we have at least shown the early stages of achieving such as design with the view of creating more complex vascular *in-vitro* models in the future.

## 6.5 Conclusion

Preliminary results in this chapter show we have a suitable microfluidics setup for interrogating the role of interstitial flow on embedded VSCMs behaviour. We demonstrated that cells embedded in the hydrogel can be cultured under flow for 7 days and respond to fluid forces by aligning in the direction of flow. Whilst this data is only preliminary at this stage, the system is now optimised to be used for future experiments as discussed later in Chapter 7. Furthermore in this chapter we present a potential design to create more relevant *in-vitro* models in the future. In summary:

- Cells can be cultured under flow and stimulated with approximately 0.04 Pa of interstitial shear
- Cells remain rounder in flow versus static conditions
- Cells under flow align to the direction of fluid travel
- CFD simulations have been used to validate a potential novel bioreactor design to introduce both luminal and interstitial shear to vascular cells
- The results from these simulations have been validated against theory and are mesh independent
- Luminal and intersititial shear can be in theory independently controlled in this system

At this stage in this thesis we have demonstrated that we have a biomaterial which can be used to study human primary cell matrix interactions in 3D and a system with which to stimulate these cultures with flow. In the next chapter we present the future experiments we propose to build on this work in the aim of understanding the role of flow in aneurysm development.

# Chapter 7

# Discussion

The goal of this PhD project was to develop a novel reductionist model to study vascular cell ECM interactions in the presence of flow. This was achieved by combining a synthetic PEG-peptide hydrogel system encapsulating cultures of primary cells with microfluidics. The methods were devised using experimental data enhanced with predictive models. This was a new project conceived during the MRes rotation year of the MRC DTP program. My first rotation was in Prof. Lamata's group analysing patient 4D MRI data. We looked at abnormal flow patterns and assessed these for characteristics which could be used to improve on current clinical disease markers. My final rotation was in the Gentleman lab studying the impact of hydrogel properties on stem cell behaviours. Specifically we were looking to combine biological data with models of the hydrogel microstructure using molecular dynamics. With these projects I realised fluid dynamics of the diseased vascular system was my area of interest but that I wanted to focus on the cellular scale. Particularly I wanted to look at what prompts the structural changes in the blood vessel we see in disease by trying to understand how the cells remodel their environment. To attempt this we setup a new collaboration between the 2 groups, combining the expertise of Prof. Lamata in cardiac imaging and disease markers with those of Prof. Gentleman in cell matrix interactions and biomaterials. As a starting point we had 4D MRI data predicting abnormal fluid stresses in patients with aneurysms and the PEG-peptide hydrogel system which had successfully been used in other disease models where ECM remodelling is a key component. Therefore this was a new *in-vitro* model of vascular disease and the majority of our efforts in this thesis have been spent optimising techniques to develop the platform. Indeed, this project was highly ambitious and we faced a number of challenges. After the first year of experiments we reduced the scope of the work by focusing on the interstitial flow stimulation of VSMCs specifically with the goal of extending the model down the line to include more factors as discussed in the future work section. As previously highlighted there is both a paucity of vascular *in-vitro* models in 3D cultures and focus on interstitial wall flow in the literature and so this became our area of focus. Our more specific aim was then to develop a platform to stimulate 3D cultures of primary cells with interstitial flow

mimicking that in the vessel wall.

In order to address this aim we have demonstrated that primary VSMCs can be cultured in the PEG-peptide hydrogel which they can actively remodel and lay new matrix within. We have also demonstrated that these cells can be cultured under flow in 3D and that they respond to the resultant stresses by aligning in the direction of flow. These flows have also been shown to approximate physiological estimates. Furthermore we have demonstrated that this platform allows for standard techniques for downstream analysis such as immunofluorescence staining. We have therefore developed a suitable platform to study the impact of interstitial flow on VSMC ECM remodelling and addressed the majority of the goals laid out for this thesis. Although we have made substantial progress in this model there are a number of limitations which need to be addressed in the future as is outlined in the next section.

## 7.1 Model Limitations

In our review paper in Chapter 1 we lay out the main considerations for designing 3D models to study vascular disease *in-vitro*. We address 3 main areas: choice of biomaterials, cellular arrangement and inclusion of mechanical cues [Lust et al., 2021b]. We are now able appraise our own model against these criteria.

We opted for a fully synthetic PEG based hydrogel system incorporating bio-active peptides to render the matrix hospitable to cells. Whilst this allowed us to tightly and independently control key hydrogel characteristics such as stiffness or degradability, the synthetic material presents a much simpler bio-chemical environment to cells compared to tissue. Indeed material choices such as Matrigel and other naturally derived hydrogels offer a greater diversity of proteins to encapsulated cells. Furthermore, the microstructure of our synthetic system is made up of short range cross-links which are likely different to the longer range bonds seen in hydrogels such as collagen and we saw this reflected in the comparatively low permeability to flow of our material.

The "regularity" we create in our hydrogel is useful for tightly controlling our experimental variables however it pulls away from the natural defects and variability seen in tissue. Certainly in our model, we prioritised the ability to modulate hydrogel properties over recapitulating the full complexity of the native tissue. The main justification of this decision was that we wanted to study the specific impact of mechano-stimulation from flow and thus we needed to keep the other mechanical cues in the model fixed. Furthermore, decreased variability within the system allows more representative models to be made as these rely on bulk characteristics of the material which may be more accurately captured in a synthetic system. Finally, in our system we show the material is able to withstand relatively high pressure flows without breaking and this material strength is not as easily achieved in naturally derived hydrogels [Weinberg and Bell, 1986, Berglund et al., 2003]. The major limitation in our work however is that we did not assess the impact of this synthetic

environment on cell behaviour. Most notably, ECM proteins are a driver of VSMC phenotype and may drive a more synthetic or contractile state in these cells. Thus we have not assessed our baseline model for how well it recapitulates the healthy contractile like state of VSMCs. Whilst significant challenges exist in achieving contractility in any isolated primary VSMCs, it would be useful to assess this in our system to understand how it compares to in other materials. More specifically this may help to make improvements down the line by incorporating different peptide motifs as is addressed in the future work section.

Importantly, we can only exercise control over the initial environment in which the cells reside. Our data has highlighted the ability of encapsulated cells to remodel their environment and thus, properties of the material such as stiffness and protein makeup will vary with time as PEG is gradually replaced by nascent proteins. Indeed, we aim to create an environment which most easily facilitates cell-mediated changes to encourage remodelling and thus it may make more sense to track cell phenotype changes over time instead of comparing the baseline model to *in-vivo* tissue.

In our model, we focused solely on VSMC-ECM interactions. VSMCs are largely accepted to be primarily responsible for ECM regulation in the vessel wall with pathological remodelling seen in aneurysm attributed to changes in their phenotype and or apoptosis of these cells [Losenno et al., 2012, Fedak et al., 2002, Wilson et al., 2006, Davis et al., 1998]. Furthermore, these are the cells exposed to interstitial stresses and thus the main focus of our experiments. Whilst undoubtedly VSMCs play a central role in aortic disease, there are a myriad of factors that contribute and our model is limited by their exclusion.

As discussed in Chapter 1, in the first instance, ECs are known to regulate VSMC proliferation, quiescence, morphology, and by extension are involved in healthy vasodilation and or disease progression [Battiston et al., 2014, Ganesan et al., 2017, Xia et al., 2012, Nam et al., 2011, Nackman et al., 1996, Truskey, 2010, van Buul-Wortelboer et al., 1986, Ziegler et al., 1995, Wang et al., 2007, Powell et al., 1996, Powell et al., 1998]. ECs communicate with VSMCs both through cell-cell junctions and by secreted molecules and therefore including this interaction relies on correctly positioning ECs within the model [Hirase and Node, 2012, Bazzoni and Dejana, 2004]. In Chapter 6, we proposed to include ECs by seeding a monolayer on top of the 3D culture of VSMCs. With this method, we would need to ensure a confluent monolayer is formed by the ECs with enough proximity to the VSMCs to form inter-cellular junctions and mass transport to the VSMCs of secreted molecules.

Another much less studied factor, is the importance of Fibroblasts (FBs) in disease. These cells make up the majority of the adventitia and changes in this layer have been historically overlooked compared to the intima and media [Mackay et al., 2022, Coen et al., 2011]. The exact role of FBs is not fully understood however much like with the media, a phenotype change

in these cells associated with subsequent ECM remodelling is observed during aneurysm development [Shen et al., 2020, Niestrawska et al., 2019, Coen et al., 2011, Sakata et al., 2007]. FBs are seen to differentiate into a myofibroblast state characterised by increased contractility, migration, proliferation, and production of cytokine and chemokines [Haurani and Pagano, 2007, Coen et al., 2011, Suh et al., 2011, Jones et al., 2009, Tinajero and Gotlieb, 2020]. This results in aberrant remodelling of the adventitia layer with increased collagen deposition [Han et al., 2018, Coen et al., 2011]. Considering the often reduced integrity of the medial layer in aneurysms, this poses a further strain on the adventitia layer which then bears more of the haemodynamic load [Mackay et al., 2022, Jones et al., 2009]. Furthermore, myofibroblasts are seen to infiltrate the media and intima layer [Tinajero and Gotlieb, 2020, Coen et al., 2011, Han et al., 2018].

Indeed whilst delineation between the FBs and VSCM cell populations is largely classified by the distinct structural layers of the wall, the boundary between these cell types in disease is blurred. When vascular cells de-differentiate, overlap between activated FBs and VSMC phenotype is observed [Tinajero and Gotlieb, 2020, Yap et al., 2021]. Defining the exact phenotype of these cells is complex but with the aid of techniques such as RNA-seq, further distinctions between sub populations of de-differentiated cells is possible, highlighting the overlap between different vascular cells [Tinajero and Gotlieb, 2020, Yap et al., 2021]. In short, including FBs into the model to understand their contribution to the overall changes in vascular ECM may be key in understanding aneurysm development.

Another important factor in aneurysm development is the presence of immune cells. Indeed regardless of the stimulus which initiates the structural changes in the vessel wall, chronic transmural inflammation is a key marker of disease [Thompson et al., 2002]. Although inflammation is predominantly associated with abdominal aneurysms, including immune cells may be useful to extend the scope of our model. Furthermore, the role of inflammation in thoracic aneurysms is not well understood and therefore may still be an important factor to model. In aneurysm, immune cells predominantly infiltrate the media and adventitia [Thompson et al., 2002]. Cells can either be recruited or resident, with the healthy aventitia hosting a small population of macrophages, dendritic cells, T cells and B cells [Tinajero and Gotlieb, 2020, Galkina et al., 2006, Jongstra-Bilen et al., 2006]. These immune cells are known to secrete matrix degrading enzymes and thus mediate ECM remodelling [Rateri et al., 2011, Rizas et al., 2009]. The immune cells themselves are a source of MMPs but also release cytokines such as interleukin (IL)-6, MCP-1, osteopontin, whose release recruits even more immune cells creating a feedback loop [Curci et al., 1998, McCormick et al., 2007]. Importantly, this can also lead to activation of cell death pathways in VSMCs which not only reduces the amount of new ECM protein synthesised but dying VSMCs are also known to release MMPs [McCormick et al., 2007]. Thus immune cells are an integral part of mediating ECM breakdown and potential changes in their activation or recruitment in response to flow cues needs to be considered.

Finally, in our current model we mechanically stimulate cells only with the stiffness of the matrix around them and interstitial flow. Aside from viability studies, we fixed the hydrogel stiffness at the value which yielded highest cell survival and thus did not explore the impact of stiffness on cell behaviour. As previously highlighted the blood vessel wall is mechanically complex with cyclic strain from pulsatile arterial flow stimulating cells with compressive stresses as well as luminal and interstitial shear [Hahn and Schwartz, 2009, Lehoux and Tedgui, 2003, Ku, 1997]. These forces impact all the different layers of the vascular wall and therefore may need to be included in a model with multiple cells types exploring inter-cellular interactions. Incorporating lumen flow into the model may be possible using a more complex bioreactor design as highlighted in Chapter 6. Furthermore, specialised pumps for cardiac research can deliver pulsatile flows based on the cardiac cycle which could then be used to make this luminal flow closer to the physiological regime.

The question arises then, can our model without all these factors, truly capture VSMC-ECM interactions in response to interstitial flow? Undoubtedly VSMC-ECM interactions are dependent on the whole feedback loop of mechanical forces, matrix and inter-cellular interactions and to build a more complete aneurysm model our current setup is too simplified. However our reductionist approach is important to first isolate the role, if any, of interstitial flow in VSMC-ECM remodelling. To the best of our knowledge, this is the first 3D model of human VSMCs combining synthetic hydrogels with flow. We hope with the model we have implemented, experiments will show that interstitial flow is an important mediator of aberrant ECM remodeling. Whilst elucidating the true impact it has may require the inclusion of more factors into the model, we hope to be able to highlight that it is an important consideration that should not be ignored in the understanding of disease progression.

## 7.2 Future Work

The majority of the work in this thesis has been focused on optimising the setup and so the next stages of work are the experiments which would allow us to test our hypothesis on the role of interstitial flow.

The first experiment would be to pass flow through cultures of the primary human cells we demonstrated produced new ECM within the static hydrogel cultures. By running side by side flow and static controls we would then be able to quantify the area covered by different ECM proteins and thus the impact of fluid stresses on cell matrix synthesis. Thus far we have stained for collagen-1, 4 and fibronectin but we could expand the list of proteins we stain for. Another approach could be to use fluorescent non-canonical amino acid tagging (FUNCAT) assay in which all newly synthesised protein is fluorescently tagged and thus this would allow us to visualise the overall changes in protein synthesis without needing to specifically target the right proteins. The assay could also be used to assess the impact of the hydrogel and of flow on VSMC phenotype by staining for markers of contractility in different conditions.

Furthermore, at this stage we have only tested the end stage of protein synthesis but it may be possible to measure transcriptional changes at an earlier stage by running genomic assays such as qPCR, looking at regulation of matrix related genes. Indeed we have already demonstrated that we are able to extract high quality RNA from encapsulated cells. Similarly to with FUNCAT staining, this could be extended to RNAseq analysis to compare the full spectrum of transcriptional changes. Indeed Chou et al have recently performed single nuclear RNA seq analysis on 13 samples from human donors, 6 with thoracic aortic aneurysm, and 7 healthy [Chou et al., 2022]. They identified 11 cell types with 7 VSMC and 6 FB sub-populations. Interestingly, the majority of deferentially expressed genes were in the VSMC population and include: $HDAC9$ (histone deactylase 9) which is known to regulate the expression of contractile VSMC proteins [Lino Cardenas et al., 2018], $ACTN4$ a gene encoding for $\alpha$-actinin involved in cell contractility and $KLF4$ (Krüppel-like factor 4) encoding for a transcription factor important in regulating VSMC phenotype [Yap et al., 2021]. $TGF\beta_2$ and $TGF\beta R_3$ were also differentially expressed with these genes, part of the TGF$\beta$ cascade associated with governing the contractile function of VSMCs [Lino Cardenas et al., 2018, Chou et al., 2022]. Furthermore $LM07$ and $LTPB1$ were upregulated in aneurysm, the former involved in the regulation of TGF$\beta$ expression in VSMCs [Xie et al., 2019] and the later encoding for a protein which is known to bind with TGF$\beta$ isoforms [Pottie et al., 2021]. Importantly, TGF$\beta$ signalling has been implicated in matrix destruction in aortic aneurysm, affecting cell proliferation, differentiation, apoptosis, recruitment of inflammatory cells and synthesis of matrix proteins [Holm et al., 2011, Biros et al., 2012, Wang et al., 2013].

Disrupted TGF$\beta$ signalling has also been implicated specifically in flow induced vascular remodeling [Gao et al., 2014]. Furthermore, fluid stresses are known to activate the TGF$\beta$ pathway

in ECs [Egorova et al., 2009, Ohno et al., 1995] which in turn regulates VSMC behaviour. Not only that, but shear induced TGF$\beta$ is also know to affect VSMC proliferation and differentiation into myofibroblast like state [Qiu et al., 2014]. With this published RNA-seq data set we may be able to compare our own gene analysis in flow conditions to see if any of these aneurysm associated gene expression changes are seen under flow.

All flow experiments so far have all been under a pressure of 600 mBar. A possible extension to this work would be to test flows of different pressures to try and identify a threshold of stimulation needed to invoke a change or if indeed the degree of ECM synthesis change is proportional to the degree of shear.

Whilst we have proposed plans to extend our model to include monolayers of ECs, in the immediate short term, we could either use media from cultured ECs or else include them in a direct co-culture with the VSMCs in the hydrogel. ECs could be cultured under luminal flow with the same device we currently have and thus stimulated with luminal shear. The endothelial cell conditioned medium could be collected and then used in the interstitial flow model to expose the VSMCs to any EC secreted molecules in the medium as in [Stegemann and Nerem, 2003]. In this study EC conditioned medium was used to culture both 2D and 3D rat aortic SMCs. The authors observed that the VSMCs expressed lower levels of contractile markers in the conditioned media however acknowledge that this may be due to the fact that ECs were cultured statically and that treating them with shear may alter the effect of the conditioned media. An assay which would allow EC-VSMC contact would be a mixed co-culture of the 2 cell types within the same hydrogel however, both cell types would then be indiscriminately treated with interstitial shear and the ECs would not be able to form a confluent layer.

Finally experimentally, an important extension to our model would be to include aneurysm patient cells to understand whether genetic mutations affect the way in which VSMCs respond to flow. To this end we have identified a potential collaboration with a vascular surgeon Prof. Yeung at Amsterdam University Medical Centers. Prof Yeung has access to healthy and patient primary VSCM cells as well as a protocol to differentiate "VSMC like" cells from dermal fibroblasts. We are working towards setting up this collaboration.

The ultimate aim of this work was to develop an *in-vitro* model of cell-matrix interactions underpinned by predictive mathematical models. There are essentially 3 main mechanisms underpinning matrix changes, mass transport of molecules through the hydrogel, cellular breakdown of the cross-links and synthesis of newly laid proteins. To build a predictive mathematical model of matrix properties, all of these factors need to be modelled taking into consideration changes in the parameters describing the material properties as they occur. For example, as the hydrogel breaks down, parameters such as material diffusivity change as a function of the number of cross-links broken down. With our work presented in Chapter 4, we have successfully modelled mass

transport through the hydrogels using experimental data to parameterise the governing equations. The next steps are to try and model ECM breakdown and eventually include the presence of new matrix in the models. Parameterising models to describe these behaviours would be extremely challenging as we may not be able to single out these effects with individual experiments as easily as we were able to looking just at diffusion. Indeed, cells likely degrade and synthesise matrix in concert and so isolating a particular interaction is difficult. However, we may be able to improve on some of our assays to readout hydrogel changes to include continuous measurements which might allow us to determine bulk parameters for our models. For example, continuously tracking permeability changes in the hydrogel may serve to predict the rate of breakdown by cells of the matrix and eventually the increase in path tortuosity for the flow as new matrix is synthesised. However this would likely rely on obtaining highly precise readouts and this is discussed further in the following section.

All of our modelling so far has been using partial differential equations, treating the hydrogel as a bulk material. A different modelling approach which may be useful would be to model on the individual PEG monomer scale using techniques such as molecular dynamics. Indeed we used this approach in [Jowett et al., 2021] to predict the rate of cross-linking bonds in 2 different hydrogel designs. This type of modelling may be used to predict the hydrogel microstructure which could be used then to make more accurate estimates of the fluid stresses acting on cells. This work would need to be conducted along side experimental techniques to visualise the hydrogel microstructure as discussed in Chapter 3.

### 7.2.1 Ongoing Collaborations

Throughout this project we have had the opportunity of wonderful collaborations without which this project would not have been possible. Some of the experiments we have conducted with collaborators could also be extended to enhance our model.

The MEMS assay that we used to determine hydrogel permeability in collaboration with Dr Cacheux and Professor Matsunaga at the University of Tokyo allowed us to make precise measurements by continuously measuring pressure increases due to flow through the hydrogel. The first extension to this work would be to repeat the assay and include cells in the hydrogels to see how these change the overall permeability of the matrix. However, the MEMS system also allows for long-term tracking of the permeability and the pressure gauge can be placed in the cell culture incubator. We therefore propose to use permeability as a readout of cell-mediated ECM remodelling. We will assemble our models and measure, in real time, changes in permeability as cells modulate their surrounding matrix in response to interstitial fluid shear. If we are able to measure small enough changes in permeability we may be able to infer the full time scale of matrix changes rather than only using endpoint samples. Furthermore, we may be able to detect

changes in the hydrogel on a shorter time scale than we see newly synthesised proteins by staining. We hypothesise that we may first see an increase in permeability as the hydrogel is broken down before eventually seeing a decrease as new proteins are synthesised.

Our collaboration with M. Antonazzi in the Shanahan group at KCL has been key for us to develop techniques to interrogate ECM synthesis in the hydrogels and to be able to include primary human cells. Whilst our emphasis is on aneurysms, we may be able to use the platform for investigating their groups area of interests as well. In particular, M. Antonazzi's work focuses on vascular dementia and understanding whether the transport of Amyloid Beta, the main component of the amyloid plaques found in the brains of people with Alzheimer's disease, is altered in aging tissue. In short he hypothesises that with age, vascular ECM is altered and thus movement of Amyloid Beta proteins in the tissue is slowed leading to an accumulation. To test this, M. Antonazzi uses both senescent VSMCs and young ones to compare the ECM they synthesise. With the work we have conducted on mass transport within our hydrogels combined with the flow setup, we potentially have a powerful platform with which to test this hypothesis. By allowing embedded cells to lay down their own matrix, we could then introduce Amyloid Beta proteins into the flow media to observe if transport through the hydrogel is altered when using senescent cells.

Although the context for our work was aortic aneurysms, the platform we have made may be used to try and model many different vascular diseases. One of the goals of this PhD was to develop an assay which could be of broader use in the future and we are very grateful to all our collaborators and colleagues who have given us ideas of how we could put this work to best use in the future!

# Chapter 8

# Conclusion

In this thesis we have presented a reductionist *in-vitro* model with which to study vascular cell-ECM interactions in 3D in the presence of fluid stresses. In particular we have concerned ourselves with developing a platform to interrogate the role of interstitial fluid stresses on VSMC mediated remodelling in the context of aortic aneurysms. We have combined a synthetic PEG-based hydrogel with cultures of both primary bovine and human VSMCs with a microfluidic setup. We have characterised the diffusivity, degradability and permeability of the hydrogel. Once the material had been suitably characterised we then determined the optimum hydrogel conditions in which to encapsulate our cultures of VSMCs. With these data in hand, we were then able to demonstrate that VSMCs are able to breakdown the hydrogel and lay down nascent proteins whilst encapsulated. Finally we were able to show that these 3D cultures can then be stimulated with interstitial flows to expose cells to fluid stresses.

This work addresses some of the current gaps in the literature by first considering vascular cell-ECM interactions in 3D but also by including interstitial flows, a component of mechanotransduction of the blood vessel wall which historically has largely been overlooked. We have combined both *in-vitro* and *in-silico* techniques in this work to try and augment our experimental findings as well as using them to parameterise predictive models. By further elucidating the interaction of vascular cells with interstitial flow, we hope to understand whether haemodynamics play a role in aneurysm development and ultimately whether abnormal blood flow can be used as a stratification for disease risk. Of course there is still a long way to go to determine the impact of fluid stresses in aberrant ECM remodelling but by combining understanding of their role with techniques such as 4D MRI there is an opportunity to non-invasively diagnose patients.

Whilst the majority of the work in this thesis has been building and optimising the platform we have gone some way to develop assays which can be used not only to interrogate our specific biological hypotheses on aortic aneurysms but also for a broad spectrum of applications in vascular disease. This type of reductionist *in-vitro* model is a powerful tool to elucidate some of the mechanisms behind multi-factor disease progression. The ability to use human cells not only

serves to reduce the number of animals used in research but also avoids inter-species variability which can limit the applicability of animal *in-vivo* work. Furthermore, *in-vitro* models may be combined with vascular cells differentiated from patient-derived induced pluripotent stem cells (iPSCs) which offer obvious advantages in disease modelling, considering both the role of genetics and external stimuli in disease. Ultimately we hope these types of models will help highlight the relative impact of different contributors in disease and thus elucidate alternative therapeutic targets.

# Chapter 9

# Appendices

## 9.1 MATLAB Code Used to Calculate Hydrogel Quantities

```
%Gel making calculator
% Started by Suzie 21/11/18

%Variables nomenclature
%-------------------------------------------------------------------------

%Gel Properties
%------------------
%SC=Solid content [mg/ul]
%e=Margin extra for experiment
%V_e=End volume desired
%V_a=(1+e)*V_e actual volume for experiment
%Per_KDWERK=Percentage of KDWERK peptide
%Per_CYAD=Percentage of CYAD peptide
%Per_DEG=Percentage of DEG peptide
%m_total=Total solid mass in desired amount of gel


%Molecular masses
%------------------
%M_PEG_NPC=Theoretical Molecular mass of 1 PEG4NPC [mg/mMol]
%M_KDWERC=Theoretical Molecular mass of 1 KDWERK sequence [g/mol]
%M_CYAD=Theoretical Molecular mass of 1 CYAD sequence [g/mol]
%M_DEG=Theoretical Molecular mass of 1 DEG sequence [g/mol]
%M_PEG_VS=Theoretical Molecular mass of 1 PEG4NPC [g/mMol]
%M_t_g_unit=Theoretical Molecular mass of 1 gel unit
%Pur_NPC=purity of NPC PEG
%Pur_VS=purity of VS PEG
%Pur_P_KDWERK=purity of KDWERK
%Pur_P_CYAD=purity of CYAD
%Pur_P_DEG=purity of DEG

%number of moles  [nMol]
%denonated by n_{previous naming}

%volume [ul]
%v_{previous naming}


%Gel properties
prompt = 'Please enter the concentration of gel: ';
SC=input(prompt);

prompt_1='What volume of gel do you want to make excluding extra margin: ';
v_e=input(prompt_1);

prompt_4='What size VS PEG do you want?: ';
T=input(prompt_4);

prompt_2= 'What percentage KDWERK do you want?: ';
Per_KDWERK=input(prompt_2);

prompt_3= 'What percentage CYAD do you want?: ';
Per_CYAD=input(prompt_3);

 prompt_4= 'What percentage DEG do you want?: ';
Per_DEG=input(prompt_4);
```

```
e=10/100;
%SC=2.5;
%v_e=30;
v_a=v_e*(1+e);
m_total=(SC/100)*v_e;
%Per_KDWERK=100;
%Per_CYAD=0;
%Per_DEG=0;
Pur_NPC=89/100;

if T==10
    Pur_VS=99.2/100;
else
    Pur_VS=95.7/100;
end

Per_total=Per_KDWERK+Per_CYAD+Per_DEG;


%Molar masses
M_PEG_NPC=10275;
M_KDWERK=876.972;
%M_CREWERC=1022.155;
M_CYAD=1848.952;
M_DEG=1872.033;

if T==10
M_PEG_VS=10275;
else
        M_PEG_VS=20784;
    end

M_t_g=M_PEG_NPC+((Per_KDWERK*0.01)*4*M_KDWERK)+((Per_CYAD/100)*4*M_CYAD)+
((Per_DEG/100)*4*M_DEG)+M_PEG_VS;


%number of moles of each componant
n_PEG_VS=m_total/M_t_g;
n_PEG_NPC=m_total/M_t_g;
n_peptide_KDWERK=(Per_KDWERK/100)*m_total/M_t_g;
n_peptide_CYAD=(Per_CYAD/100)*m_total/M_t_g;
n_peptide_DEG=(Per_DEG/100)*m_total/M_t_g;


%masses of each componant
m_PEG_NPC=(n_PEG_NPC*M_PEG_NPC)*(1+e);
m_PEG_VS=(n_PEG_VS*M_PEG_VS/Pur_VS)*(1+e);
m_KDWERK=(n_peptide_KDWERK*4*M_KDWERK)*(1+e);
m_CYAD=(n_peptide_CYAD*4*M_CYAD)*(1+e);
m_DEG=(n_peptide_DEG*4*M_DEG)*(1+e);
m_conj_KDWERK=m_PEG_NPC+m_KDWERK;
m_conj_CYAD=m_PEG_NPC+m_CYAD;
m_conj_DEG=m_PEG_NPC+m_DEG;



%concentration in HEPES of each componant change these around until you get
%the left over volumes
%as a starting point with 100% of one conj conc=0.03 works 50%
```

```
%0.04
c_PEG_VS=0.04;
%c_PEG_VS=0.03015;
c_conj_KDWERK=0.005074061;
%c_conj_KDWERK=0.007290513;
%c_conj_DEG=0.015;
c_conj_DEG=0.015;
c_conj_CYAD=0.015;



%volume of HEPES for each componant
%Calculate the volume taken up from the conjugates and the VS and then say
%the remainder is eith00er for cells or for straight HEPES
v_PEG_VS=m_PEG_VS/c_PEG_VS;
v_conj_KDWERK=m_KDWERK/c_conj_KDWERK;
v_conj_CYAD=m_CYAD/c_conj_CYAD;
v_conj_DEG=m_DEG/c_conj_DEG;
v_cells=v_a-v_conj_KDWERK-v_conj_DEG-v_conj_CYAD-v_PEG_VS


filename=[datestr(now, 'yyyy-mm-dd'),'Experiment Title]
fid = fopen(filename,'wt');
fprintf(fid, 'You need %f mg of PEG_VS in %f ul of HEPES, giving a
concentration of %f mg/ul\n',m_PEG_VS, v_PEG_VS, c_PEG_VS')
fprintf(fid,'You need %f mg of KDWERK conjugate in %f ul of HEPES, giving a
concentration of %f mg/ul\n',m_KDWERK, v_conj_KDWERK, c_conj_KDWERK)
fprintf(fid,'You need %f mg of DEG conjugate in %f ul of HEPES, giving a
concentration of %f mg/ul\n',m_DEG, v_conj_DEG, c_conj_DEG)
fprintf(fid,'You need %f mg of CYAD conjugate in %f ul of HEPES, giving a
concentration of %f mg/ul\n',m_CYAD, v_conj_CYAD, c_conj_CYAD)
fprintf(fid,'This leaves you with %f ml of HEPES or cell suspension to
add\n',v_cells)
fprintf(fid,'Total volume of gel made, EXCLUDING margin %f',v_e)
fclose(fid);


%Molar concentrations
mc_CYAD=(m_CYAD/M_CYAD)/(v_a/10^6)
mc_DEG=(m_DEG/M_DEG)/(v_a/10^6)
mc_KDWERK=(m_KDWERK/M_KDWERK)/(v_a/10^6)
```

## 9.2 MATLAB Code Used to Analyse Trackmate Results for PVT

```
%add path for FIJI scripts
 addpath('/Applications/Fiji.app/scripts')
close all
clear all
scaleT = true;
file_path_tracks ='2_5_per_p600-gel2_Tracks.xml';
clipZ = true;
tracks = importTrackMateTracks(file_path_tracks, clipZ, scaleT);
n_tracks = numel( tracks );
pressure=600; %mbar

for i=1:length(tracks)
   track{i}=tracks{i};

%exclude tracks that don't go length of recording
   if isequal(size(track{i}),[60,3])
   %find end data and start data
  last=track{i}(1,:);
  first=track{i}(60,:);
  %subtract to get difference
  xdistance=last-first
  %Store all values in a matrix
  m(i,:) = [xdistance];

  %isolating x values from matrix
  m2 = m(:, [2]);

  %excluding zeros from soltuion
  v = nonzeros(m2');
  Mean_x_velocity=mean(v)/60

  viscosity=8.9*10^-4; %[pa]
  path_length=1.7*10^-2; %m
  k=(Mean_x_velocity*0.000001*path_length*viscosity)/(pressure*100)
   else end

end
```

## 9.3 Table Showing Details of Antibodies Used for Immunofluorescence

| Antibody name | Manufacturer | Catalogue Number |
|---|---|---|
| rabbit polyclonal anti-TAGLN-SM22 | Abcam | ab 14106 |
| rabbit monoclonal anti-Calponin 1 | Abcam | ab 46794 |
| mouse monoclonal anti-$\alpha$ SMA | Sigma Aldrich | A5228 |
| donkey anti-rabbit Alexa Fluor 488 | Invitrogen | A-21206 |
| donkey anti-mouse Alexa Fluor 555 | Invitrogen | A-31570 |
| Alexa Fluor™ Plus 647 Phalloidin | Invitrogen | A-30107 |
| Mouse monoclonal anti-Collagen I | Abcam | ab 6308 |
| Rabbit polycolonal anti Fibronectin | Sigma Aldrich | f3648 |
| Rabbit polyclonal anti-Collagen 4 | Abcam | ab 6586 |

Table 9.1: Table showing details of antibodies used for immunofluorescence.

## 9.4 Results From Bioanlyser Analysis of RNA Extracted from Cells Encapsulated PEG-peptide Hydrogels

Assay Class: Eukaryote Total RNA Pico
Data Path: C:\...Eukaryote Total RNA Pico_DE13805253_2021-08-11_11-23-18.xad

Created: 8/11/2021 11:23:18 AM
Modified: 8/11/2021 11:39:12 AM

## Electrophoresis File Run Summary

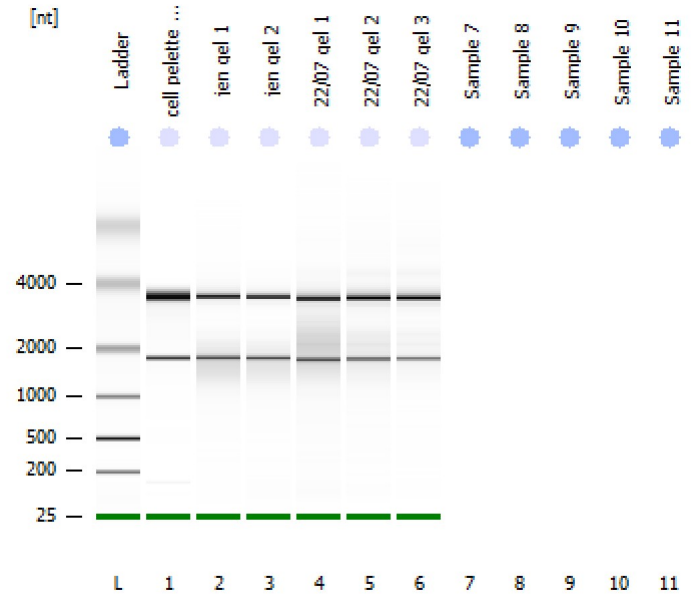


Instrument Information:

Instrument Name: DE13805253 Firmware: C.01.069
Serial#: DE13805253 Type: G2939A

Assay Information:

Assay Origin Path: C:\Program Files (x86)\Agilent\2100 bioanalyzer\2100 expert\assays\RNA\Eukaryote Total RNA Pico Series II.xsy

Assay Class: Eukaryote Total RNA Pico

Version: 2.6

Assay Comments: Total RNA Analysis pg sensitivity (Eukaryote)



Chip Information:

Chip Lot #:

Reagent Kit Lot #:

Chip Comments:

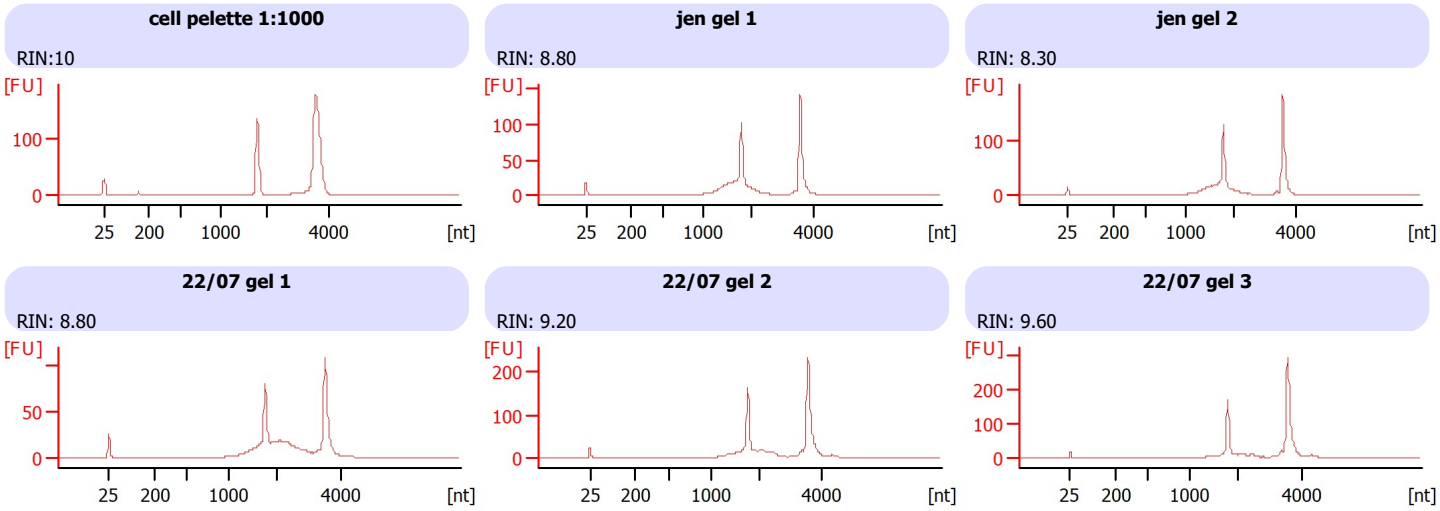

Assay Class: Eukaryote Total RNA Pico
Data Path: C:\...Eukaryote Total RNA Pico_DE13805253_2021-08-11_11-23-18.xad

Created: 8/11/2021 11:23:18 AM
Modified: 8/11/2021 11:39:12 AM

## Electrophoresis File Run Summary (Chip Summary)

| Sample Name | Sample Comment | Status | Result Label | Result Color |
|---|---|---|---|---|
| cell pelette 1:1000 | | ✔ | RIN:10 | |
| jen gel 1 | | ✔ | RIN: 8.80 | |
| jen gel 2 | | ✔ | RIN: 8.30 | |
| 22/07 gel 1 | | ✔ | RIN: 8.80 | |
| 22/07 gel 2 | | ✔ | RIN: 9.20 | |
| 22/07 gel 3 | | ✔ | RIN: 9.60 | |
| Sample 7 | | | | |
| Sample 8 | | | | |
| Sample 9 | | | | |
| Sample 10 | | | | |
| Sample 11 | | | | |
| Ladder | | ✔ | All Other Samples | |

**Chip Lot #**

**Reagent Kit Lot #**

**Chip Comments :**

Assay Class: Eukaryote Total RNA Pico
Data Path: C:\...Eukaryote Total RNA Pico_DE13805253_2021-08-11_11-23-18.xad

Created: 8/11/2021 11:23:18 AM
Modified: 8/11/2021 11:39:12 AM

## Electrophoresis Assay Details

### General Analysis Settings

Number of Available Sample and Ladder Wells (Max.) : 12
Minimum Visible Range [s] : 17
Maximum Visible Range [s] : 70
Start Analysis Time Range [s] : 18
End Analysis Time Range [s] : 69
Ladder Concentration [pg/µl] : 1000
Lower Marker Concentration [pg/µl] : 0
Upper Marker Concentration [pg/µl] : 0
Used Lower Marker for Quantitation
Standard Curve Fit is Logarithmic
Show Data Aligned to Lower Marker

### Integrator Settings

Integration Start Time [s] : 18
Integration End Time [s] : 69
Slope Threshold : 0.6
Height Threshold [FU] : 0.5
Area Threshold : 0.2
Width Threshold [s] : 0.3
Baseline Plateau [s] : 6

### Filter Settings

Filter Width [s] : 0.5
Polynomial Order : 4

### Ladder

| Ladder Peak | Size |
|---|---|
| 1 | 25 |
| 2 | 200 |
| 3 | 500 |
| 4 | 1000 |
| 5 | 2000 |
| 6 | 4000 |

Assay Class: Eukaryote Total RNA Pico
Data Path: C:\...Eukaryote Total RNA Pico_DE13805253_2021-08-11_11-23-18.xad

Created: 8/11/2021 11:23:18 AM
Modified: 8/11/2021 11:39:12 AM

## Electropherogram Summary

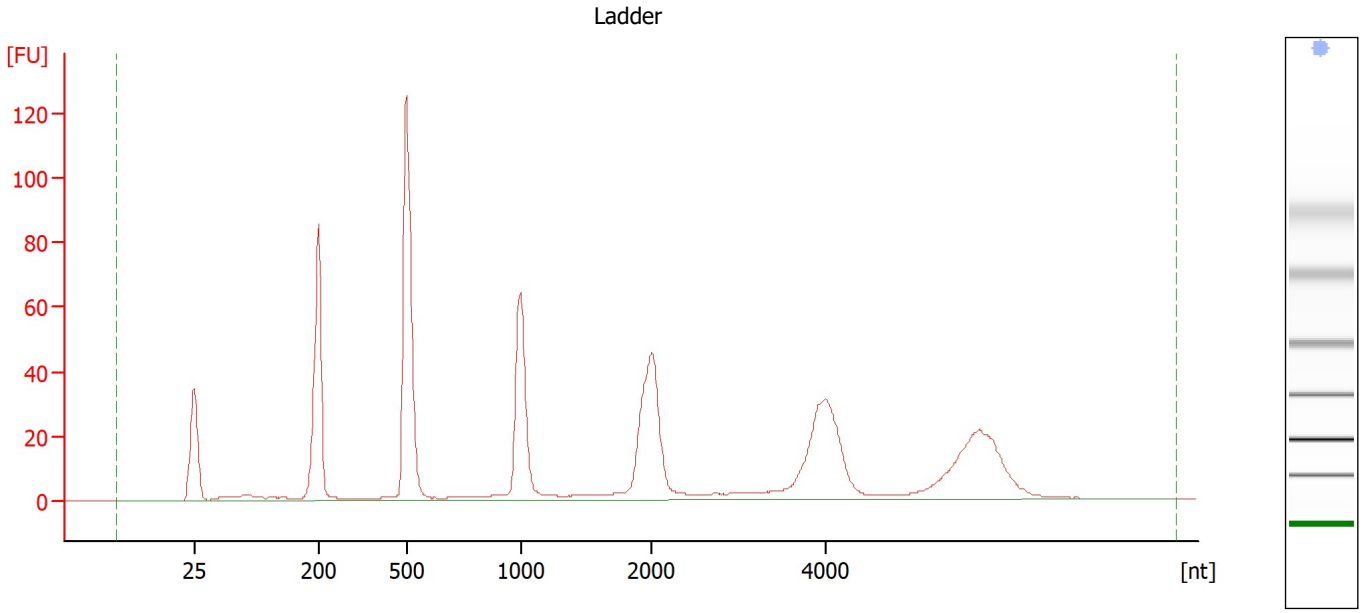


## Overall Results for Ladder

| | | | |
|---|---|---|---|
| RNA Area: | 741.5 | Result Flagging Color: | |
| RNA Concentration: | 1,000 pg/µl | Result Flagging Label: | All Other Samples |

Assay Class: Eukaryote Total RNA Pico
Data Path: C:\...Eukaryote Total RNA Pico_DE13805253_2021-08-11_11-23-18.xad

Created: 8/11/2021 11:23:18 AM
Modified: 8/11/2021 11:39:12 AM

**Electropherogram Summary Continued ...**

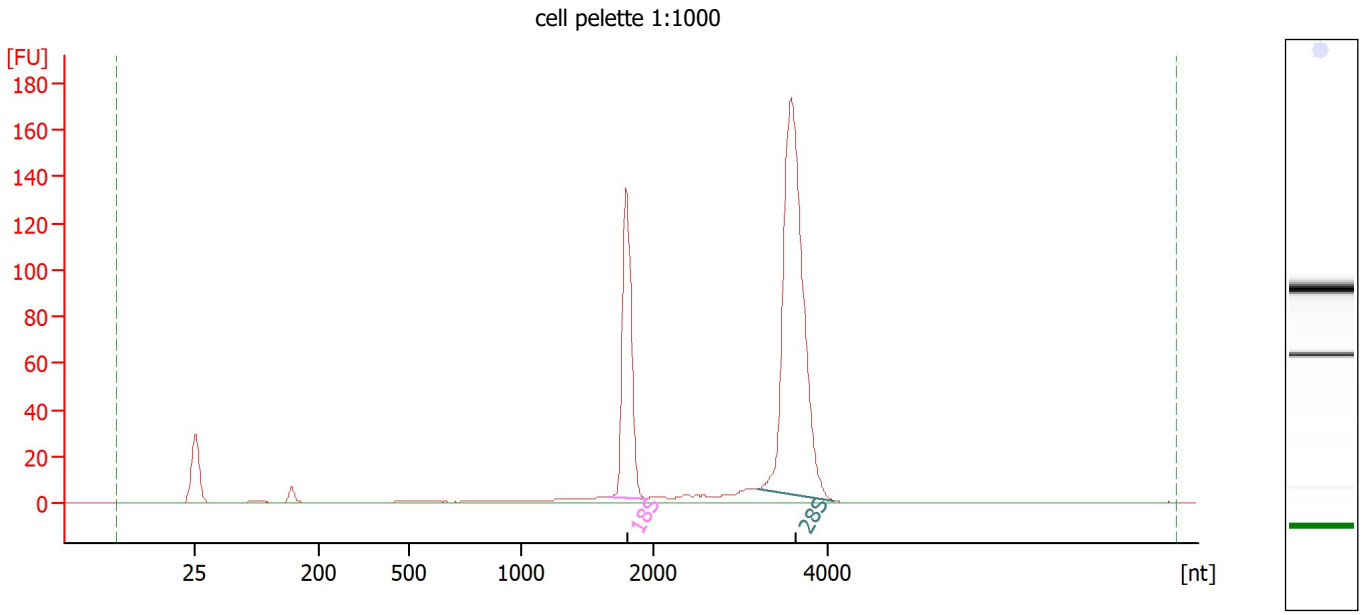


**Overall Results for sample 1 : cell pelette 1:1000**

| | | | |
|---|---|---|---|
| RNA Area: | 610.6 | RNA Integrity Number (RIN): | 10 (B.02.10) |
| RNA Concentration: | 824 pg/µl | Result Flagging Color: | |
| rRNA Ratio [28s / 18s]: | 2.4 | Result Flagging Label: | RIN:10 |

**Fragment table for sample 1 : cell pelette 1:1000**

| Name | Start Size [nt] | End Size [nt] | Area | % of total Area |
|---|---|---|---|---|
| 18S | 1,643 | 1,943 | 148.8 | 24.4 |
| 28S | 3,195 | 4,082 | 354.7 | 58.1 |

Assay Class: Eukaryote Total RNA Pico
Data Path: C:\...Eukaryote Total RNA Pico_DE13805253_2021-08-11_11-23-18.xad

Created: 8/11/2021 11:23:18 AM
Modified: 8/11/2021 11:39:12 AM

**Electropherogram Summary Continued ...**

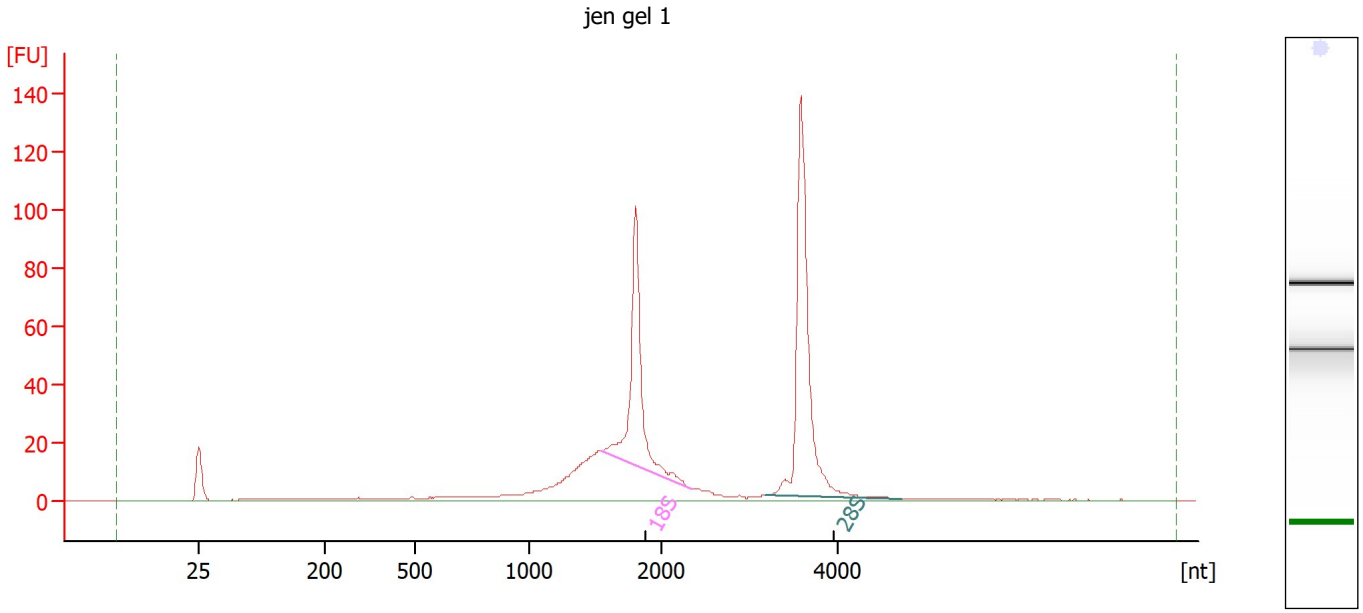


**Overall Results for sample 2 : jen gel 1**

| | | | |
|---|---|---|---|
| RNA Area: | 522.6 | RNA Integrity Number (RIN): | 8.8 (B.02.10) |
| RNA Concentration: | 705 pg/µl | Result Flagging Color: | |
| rRNA Ratio [28s / 18s]: | 1.4 | Result Flagging Label: | RIN: 8.80 |

**Fragment table for sample 2 : jen gel 1**

| Name | Start Size [nt] | End Size [nt] | Area | % of total Area |
|---|---|---|---|---|
| 18S | 1,536 | 2,346 | 116.3 | 22.3 |
| 28S | 3,189 | 4,740 | 160.9 | 30.8 |

Assay Class: Eukaryote Total RNA Pico
Data Path: C:\...Eukaryote Total RNA Pico_DE13805253_2021-08-11_11-23-18.xad

Created: 8/11/2021 11:23:18 AM
Modified: 8/11/2021 11:39:12 AM

**Electropherogram Summary Continued ...**

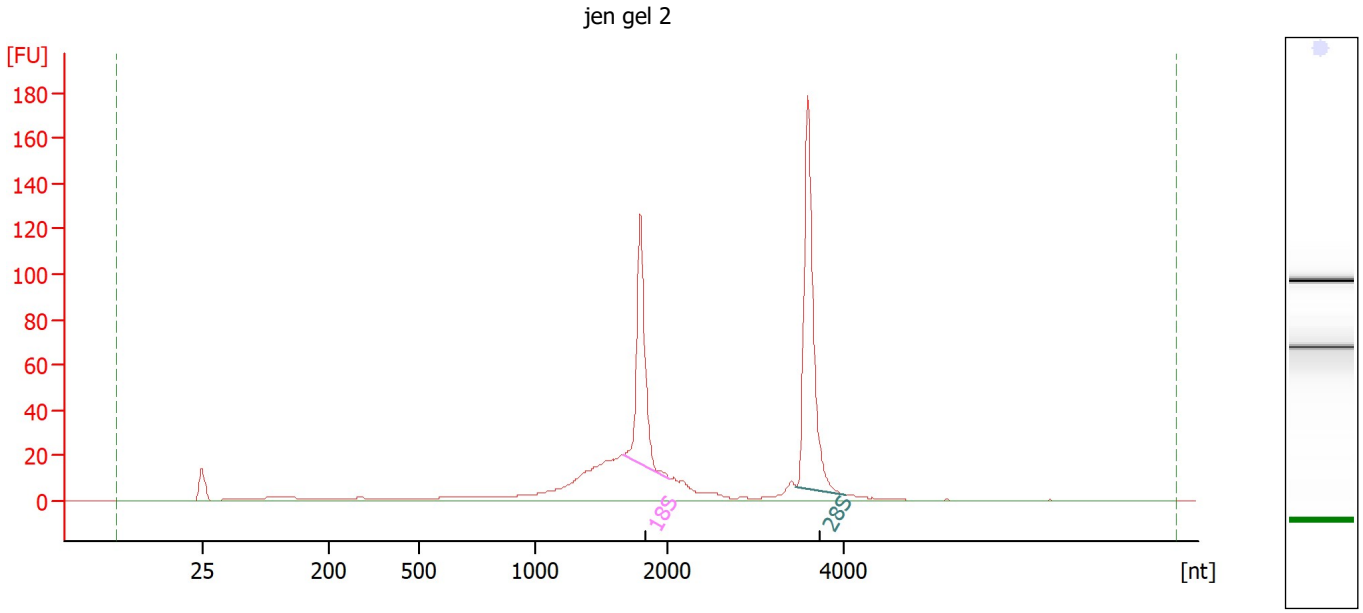


**Overall Results for sample 3 : jen gel 2**

| | | | |
|---|---|---|---|
| RNA Area: | 592.8 | RNA Integrity Number (RIN): | 8.3 (B.02.10) |
| RNA Concentration: | 800 pg/µl | Result Flagging Color: | |
| rRNA Ratio [28s / 18s]: | 1.5 | Result Flagging Label: | RIN: 8.30 |

**Fragment table for sample 3 : jen gel 2**

| Name | Start Size [nt] | End Size [nt] | Area | % of total Area |
|---|---|---|---|---|
| 18S | 1,661 | 2,019 | 111.0 | 18.7 |
| 28S | 3,451 | 4,009 | 165.0 | 27.8 |

Assay Class: Eukaryote Total RNA Pico
Data Path: C:\...Eukaryote Total RNA Pico_DE13805253_2021-08-11_11-23-18.xad

Created: 8/11/2021 11:23:18 AM
Modified: 8/11/2021 11:39:12 AM

**Electropherogram Summary Continued ...**

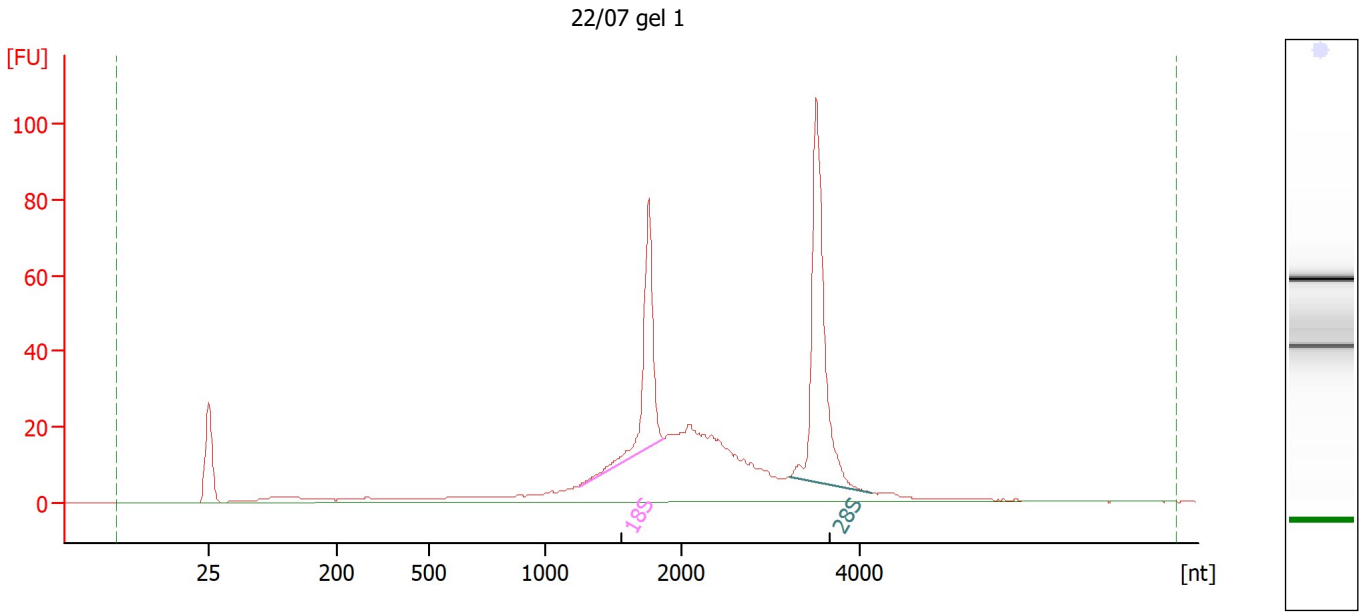


**Overall Results for sample 4 : 22/07 gel 1**

| | | | |
|---|---|---|---|
| RNA Area: | 574.9 | RNA Integrity Number (RIN): | 8.8 (B.02.10) |
| RNA Concentration: | 775 pg/µl | Result Flagging Color: | |
| rRNA Ratio [28s / 18s]: | 1.7 | Result Flagging Label: | RIN: 8.80 |

**Fragment table for sample 4 : 22/07 gel 1**

| Name | Start Size [nt] | End Size [nt] | Area | % of total Area |
|---|---|---|---|---|
| 18S | 1,250 | 1,866 | 72.4 | 12.6 |
| 28S | 3,222 | 4,133 | 126.0 | 21.9 |

Assay Class: Eukaryote Total RNA Pico
Data Path: C:\...Eukaryote Total RNA Pico_DE13805253_2021-08-11_11-23-18.xad

Created: 8/11/2021 11:23:18 AM
Modified: 8/11/2021 11:39:12 AM

**Electropherogram Summary Continued ...**

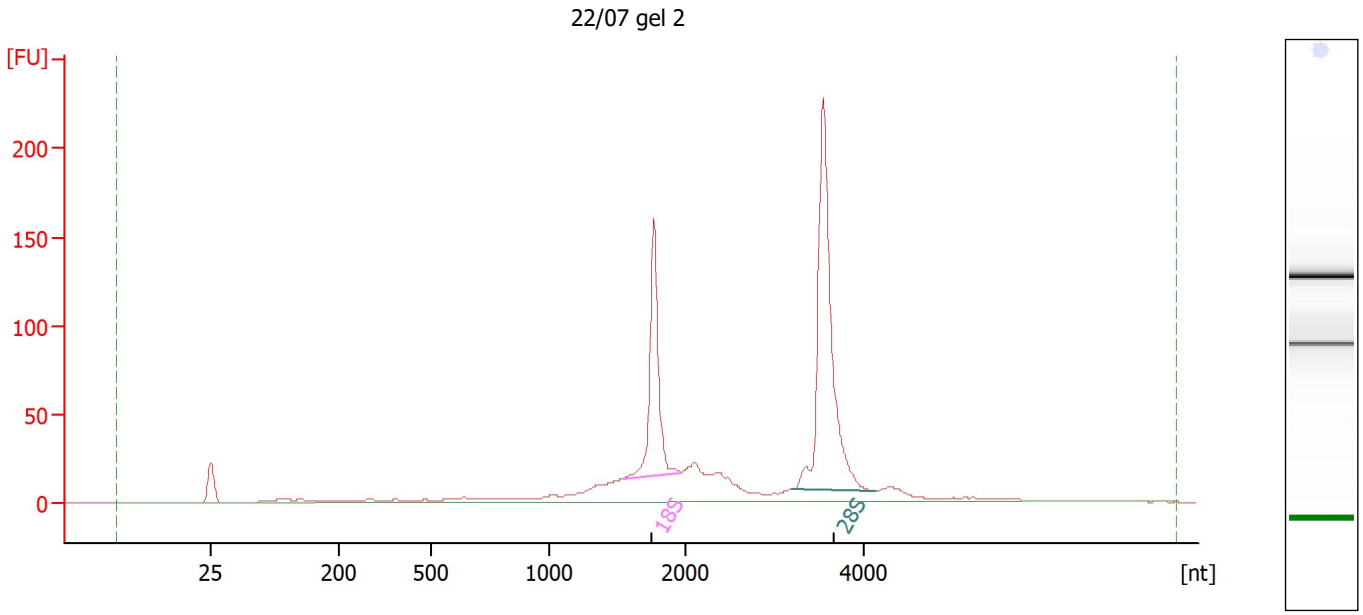


**Overall Results for sample 5 : 22/07 gel 2**

| | | | |
|---|---|---|---|
| RNA Area: | 889.0 | RNA Integrity Number (RIN): | 9.2 (B.02.10) |
| RNA Concentration: | 1,199 pg/µl | Result Flagging Color: | |
| rRNA Ratio [28s / 18s]: | 2.0 | Result Flagging Label: | RIN: 9.20 |

**Fragment table for sample 5 : 22/07 gel 2**

| Name | Start Size [nt] | End Size [nt] | Area | % of total Area |
|---|---|---|---|---|
| 18S | 1,553 | 1,977 | 149.5 | 16.8 |
| 28S | 3,183 | 4,138 | 299.0 | 33.6 |

Assay Class: Eukaryote Total RNA Pico
Data Path: C:\...Eukaryote Total RNA Pico_DE13805253_2021-08-11_11-23-18.xad

Created: 8/11/2021 11:23:18 AM
Modified: 8/11/2021 11:39:12 AM

**Electropherogram Summary Continued ...**

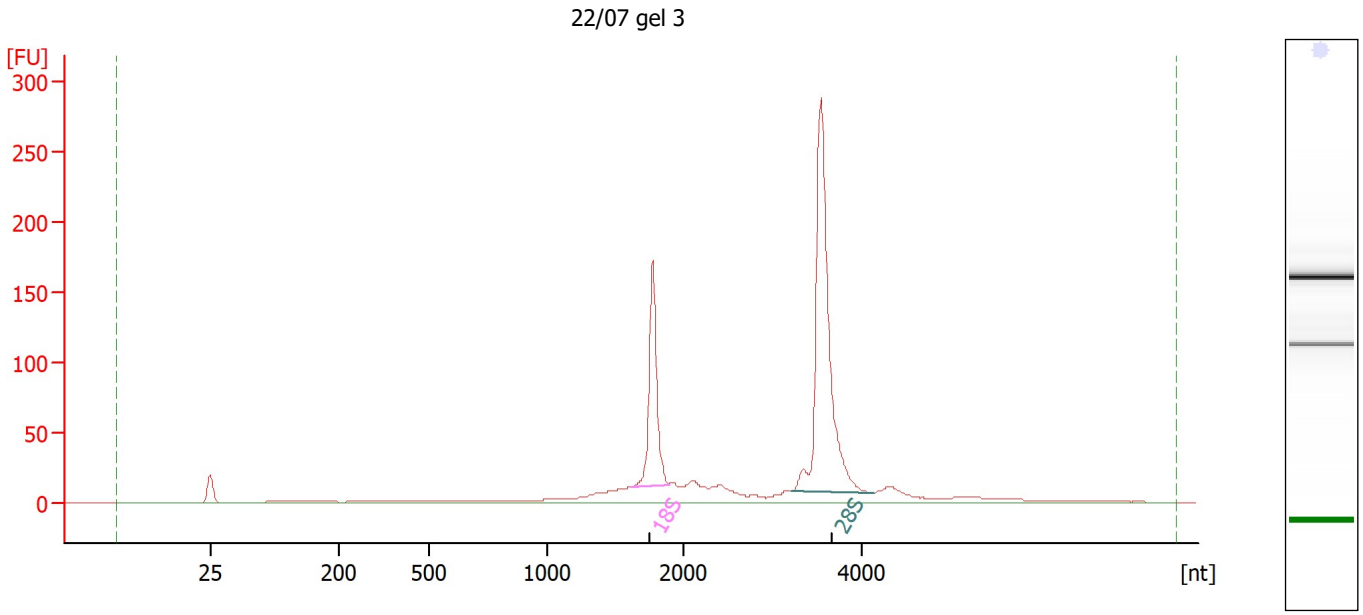


**Overall Results for sample 6 : 22/07 gel 3**

| | | | |
|---|---|---|---|
| RNA Area: | 887.2 | RNA Integrity Number (RIN): | 9.6 (B.02.10) |
| RNA Concentration: | 1,197 pg/µl | Result Flagging Color: | |
| rRNA Ratio [28s / 18s]: | 2.4 | Result Flagging Label: | RIN: 9.60 |

**Fragment table for sample 6 : 22/07 gel 3**

| Name | Start Size [nt] | End Size [nt] | Area | % of total Area |
|---|---|---|---|---|
| 18S | 1,622 | 1,898 | 152.0 | 17.1 |
| 28S | 3,220 | 4,129 | 363.6 | 41.0 |

Assay Class: Eukaryote Total RNA Pico
Data Path: C:\...Eukaryote Total RNA Pico_DE13805253_2021-08-11_11-23-18.xad

Created: 8/11/2021 11:23:18 AM
Modified: 8/11/2021 11:39:12 AM

**Gel Image**

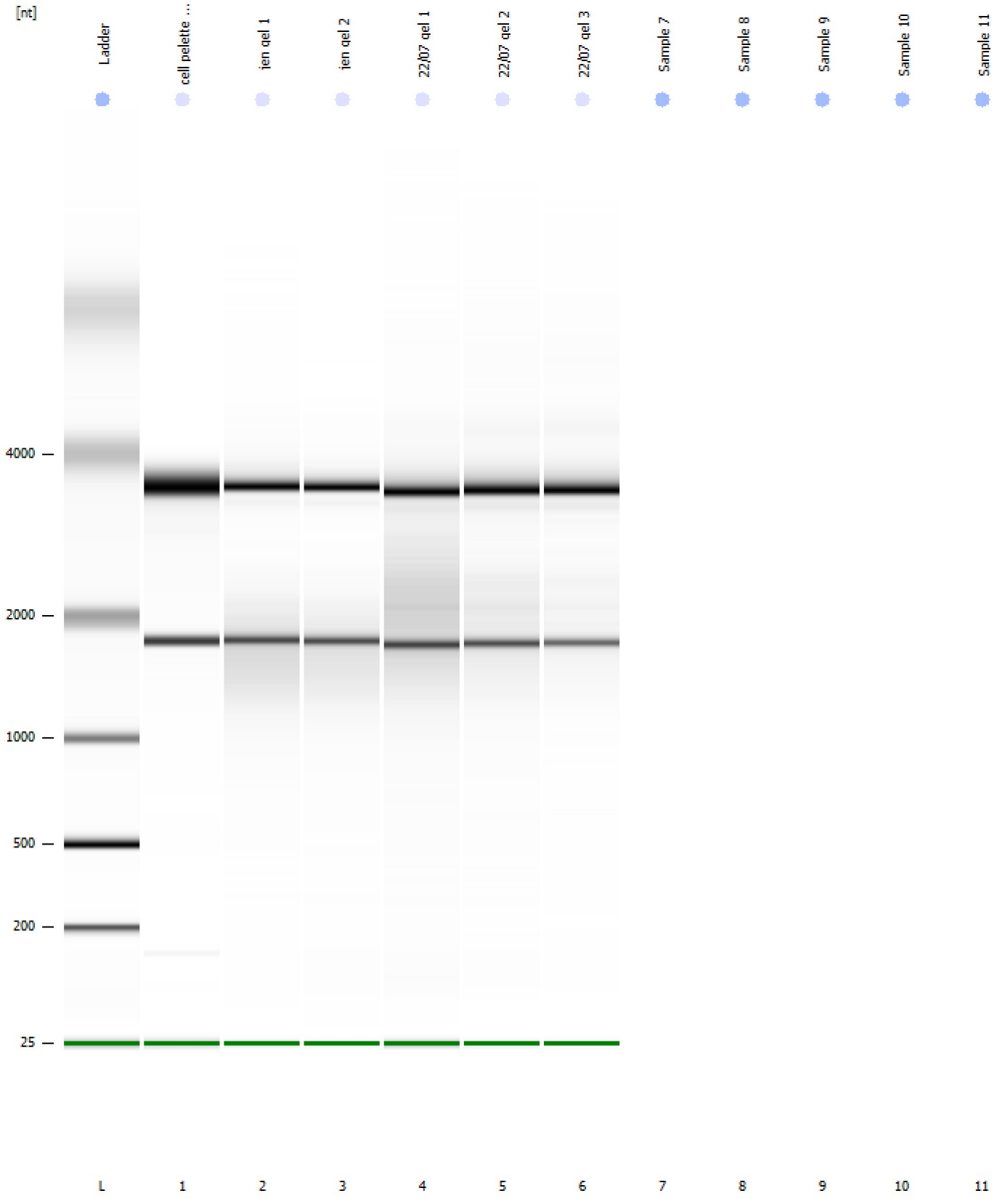

Assay Class: Eukaryote Total RNA Pico
Data Path: C:\...Eukaryote Total RNA Pico_DE13805253_2021-08-11_11-23-18.xad

Created: 8/11/2021 11:23:18 AM
Modified: 8/11/2021 11:39:12 AM

**Invalid Samples**

Sample 7 has not been run, no results available.

Sample 8 has not been run, no results available.

Sample 9 has not been run, no results available.

Sample 10 has not been run, no results available.

Sample 11 has not been run, no results available.

# Bibliography

[Ahmad et al., 2022] Ahmad, F. B., Cisewski, J. A., and Anderson, R. N. (2022). Provisional mortality data—united states, 2021. *Morbidity and Mortality Weekly Report*, 71(17):597.

[Andreassi and Della Corte, 2016] Andreassi, M. G. and Della Corte, A. (2016). Genetics of bicuspid aortic valve aortopathy. *Current opinion in cardiology*, 31(6):585–592.

[Annabi et al., 2002] Annabi, B., Shédid, D., Ghosn, P., Kenigsberg, R. L., Desrosiers, R. R., Bojanowski, M. W., Beaulieu, É., Nassif, E., Moumdjian, R., and Béliveau, R. (2002). Differential regulation of matrix metalloproteinase activities in abdominal aortic aneurysms. *Journal of vascular surgery*, 35(3):539–546.

[Asgari et al., 2022] Asgari, M., Latifi, N., Giovanniello, F., Espinosa, H. D., and Amabili, M. (2022). Revealing layer-specific ultrastructure and nanomechanics of fibrillar collagen in human aorta via atomic force microscopy testing: Implications on tissue mechanics at macroscopic scale. *Advanced NanoBiomed Research*, 2(5):2100159.

[Assoian et al., 1996] Assoian, R. K., Marcantonio, E. E., et al. (1996). The extracellular matrix as a cell cycle control element in atherosclerosis and restenosis. *The Journal of clinical investigation*, 98(11):2436–2439.

[Azhar et al., 2003] Azhar, M., Schultz, J. E. J., Grupp, I., Dorn II, G. W., Meneton, P., Molin, D. G., Gittenberger-de Groot, A. C., and Doetschman, T. (2003). Transforming growth factor beta in cardiovascular development and function. *Cytokine & growth factor reviews*, 14(5):391–407.

[Bae et al., 2016] Bae, Y. H., Liu, S.-l., Byfield, F. J., Janmey, P. A., and Assoian, R. K. (2016). Measuring the stiffness of ex vivo mouse aortas using atomic force microscopy. *Journal of visualized experiments: JoVE*, (116).

[Bagarello et al., 2004] Bagarello, V., Iovino, M., and Elrick, D. (2004). A simplified falling-head technique for rapid determination of field-saturated hydraulic conductivity. *Soil Science Society of America Journal*, 68(1):66–73.

[Battiston et al., 2014] Battiston, K. G., Cheung, J. W., Jain, D., and Santerre, J. P. (2014). Biomaterials in co-culture systems: towards optimizing tissue integration and cell signaling within scaffolds. *Biomaterials*, 35(15):4465–4476.

[Bazzoni and Dejana, 2004] Bazzoni, G. and Dejana, E. (2004). Endothelial cell-to-cell junctions: molecular organization and role in vascular homeostasis. *Physiological reviews*, 84(3):869–901.

[Beamish et al., 2009] Beamish, J. A., Fu, A. Y., Choi, A.-j., Haq, N. A., Kottke-Marchant, K., and Marchant, R. E. (2009). The influence of rgd-bearing hydrogels on the re-expression of contractile vascular smooth muscle cell phenotype. *Biomaterials*, 30(25):4127–4135.

[Berglund et al., 2003] Berglund, J. D., Mohseni, M. M., Nerem, R. M., and Sambanis, A. (2003). A biological hybrid model for collagen-based tissue engineered vascular constructs. *Biomaterials*, 24(7):1241–1254.

[Bertoli-Avella et al., 2015] Bertoli-Avella, A. M., Gillis, E., Morisaki, H., Verhagen, J. M., De Graaf, B. M., Van De Beek, G., Gallo, E., Kruithof, B. P., Venselaar, H., Myers, L. A., et al. (2015). Mutations in a tgf-$\beta$ ligand, tgfb3, cause syndromic aortic aneurysms and dissections. *Journal of the American College of Cardiology*, 65(13):1324–1336.

[Biros et al., 2012] Biros, E., Walker, P. J., Nataatmadja, M., West, M., and Golledge, J. (2012). Downregulation of transforming growth factor, beta receptor 2 and notch signaling pathway in human abdominal aortic aneurysm. *Atherosclerosis*, 221(2):383–386.

[Bissell et al., 2013] Bissell, M. M., Hess, A. T., Biasiolli, L., Glaze, S. J., Loudon, M., Pitcher, A., Davis, A., Prendergast, B., Markl, M., Barker, A. J., et al. (2013). Aortic dilation in bicuspid aortic valve disease: flow pattern is a major contributor and differs with valve fusion type. *Circulation: Cardiovascular Imaging*, 6(4):499–507.

[Boyum et al., 2004] Boyum, J., Fellinger, E. K., Schmoker, J. D., Trombley, L., McPartland, K., Ittleman, F. P., and Howard, A. B. (2004). Matrix metalloproteinase activity in thoracic aortic aneurysms associated with bicuspid and tricuspid aortic valves. *The Journal of thoracic and cardiovascular surgery*, 127(3):686–691.

[Brauer, 2006] Brauer, P. R. (2006). Mmps-role in cardiovascular development and disease. *Frontiers in Bioscience-Landmark*, 11(1):447–478.

[Byun et al., 2008] Byun, H., Hong, B., Nam, S. Y., Jung, S. Y., Rhim, J. W., Lee, S. B., and Moon, G. Y. (2008). Swelling behavior and drug release of poly (vinyl alcohol) hydrogel cross-linked with poly (acrylic acid). *Macromolecular Research*, 16:189–193.

[Cacheux et al., 2023] Cacheux, J., Ordonez-Miranda, J., Bancaud, A., Jalabert, L., Alcaide, D., Nomura, M., and Matsunaga, Y. T. (2023). Asymmetry of tensile versus compressive elasticity and permeability contributes to the regulation of exchanges in collagen gels. *Science Advances*, 9(31):eadf9775.

[Cacheux et al., 2022] Cacheux, J., Ordonez-Miranda, J., Bancaud, A., Jalabert, L., Nomura, M., and Matsunaga, Y. T. (2022). Asymmetry of tensile vs. compressive elasticity and permeability contributes to the regulation of exchanges in collagen gels. *arXiv preprint arXiv:2212.00915*.

[Chandra et al., 2012] Chandra, S., Rajamannan, N. M., and Sucosky, P. (2012). Computational assessment of bicuspid aortic valve wall-shear stress: implications for calcific aortic valve disease. *Biomechanics and modeling in mechanobiology*, 11:1085–1096.

[Chase and Newby, 2003] Chase, A. J. and Newby, A. C. (2003). Regulation of matrix metalloproteinase (matrixin) genes in blood vessels: a multi-step recruitment model for pathological remodelling. *Journal of vascular research*, 40(4):329–343.

[Chen et al., 1997] Chen, C.-H., Nevo, E., Fetics, B., Pak, P. H., Yin, F. C., Maughan, W. L., and Kass, D. A. (1997). Estimation of central aortic pressure waveform by mathematical transformation of radial tonometry pressure: validation of generalized transfer function. *Circulation*, 95(7):1827–1836.

[Chor and Li, 2006] Chor, M. V. and Li, W. (2006). A permeability measurement system for tissue engineering scaffolds. *Measurement Science and Technology*, 18(1):208.

[Chou et al., 2022] Chou, E. L., Chaffin, M., Simonson, B., Pirruccello, J. P., Akkad, A.-D., Nekoui, M., Lino Cardenas, C. L., Bedi Jr, K. C., Nash, C., Juric, D., et al. (2022). Aortic cellular diversity and quantitative genome-wide association study trait prioritization through single-nuclear rna sequencing of the aneurysmal human aorta. *Arteriosclerosis, Thrombosis, and Vascular Biology*, 42(11):1355–1374.

[Coen et al., 2011] Coen, M., Gabbiani, G., and Bochaton-Piallat, M.-L. (2011). Myofibroblast-mediated adventitial remodeling: an underestimated player in arterial pathology. *Arteriosclerosis, thrombosis, and vascular biology*, 31(11):2391–2396.

[Cripe et al., 2004] Cripe, L., Andelfinger, G., Martin, L. J., Shooner, K., and Benson, D. W. (2004). Bicuspid aortic valve is heritable. *Journal of the American College of Cardiology*, 44(1):138–143.

[Cross et al., 2010] Cross, V. L., Zheng, Y., Choi, N. W., Verbridge, S. S., Sutermaster, B. A., Bonassar, L. J., Fischbach, C., and Stroock, A. D. (2010). Dense type i collagen matrices

that support cellular remodeling and microfabrication for studies of tumor angiogenesis and vasculogenesis in vitro. *Biomaterials*, 31(33):8596–8607.

[Curci et al., 1998] Curci, J. A., Liao, S., Huffman, M. D., Shapiro, S. D., Thompson, R. W., et al. (1998). Expression and localization of macrophage elastase (matrix metalloproteinase-12) in abdominal aortic aneurysms. *The Journal of clinical investigation*, 102(11):1900–1910.

[Daugherty et al., 2017] Daugherty, A., Chen, Z., Sawada, H., Rateri, D. L., and Sheppard, M. B. (2017). Transforming growth factor-$\beta$ in thoracic aortic aneurysms: good, bad, or irrelevant?

[Davis et al., 1998] Davis, V., Persidskaia, R., Baca-Regen, L., Itoh, Y., Nagase, H., Persidsky, Y., Ghorpade, A., and Baxter, B. T. (1998). Matrix metalloproteinase-2 production and its binding to the matrix are increased in abdominal aortic aneurysms. *Arteriosclerosis, thrombosis, and vascular biology*, 18(10):1625–1633.

[Della Corte et al., 2007] Della Corte, A., Bancone, C., Quarto, C., Dialetto, G., Covino, F. E., Scardone, M., Caianiello, G., and Cotrufo, M. (2007). Predictors of ascending aortic dilatation with bicuspid aortic valve: a wide spectrum of disease expression. *European Journal of Cardio-Thoracic Surgery*, 31(3):397–405.

[den Reijer et al., 2010] den Reijer, P. M., Sallee, D., van der Velden, P., Zaaijer, E. R., Parks, W. J., Ramamurthy, S., Robbie, T. Q., Donati, G., Lamphier, C., Beekman, R. P., et al. (2010). Hemodynamic predictors of aortic dilatation in bicuspid aortic valve by velocity-encoded cardiovascular magnetic resonance. *Journal of Cardiovascular Magnetic Resonance*, 12(1):1–13.

[Dessalles et al., 2021] Dessalles, C. A., Ramón-Lozano, C., Babataheri, A., and Barakat, A. I. (2021). Luminal flow actuation generates coupled shear and strain in a microvessel-on-chip. *Biofabrication*, 14(1):015003.

[Dewey Jr et al., 1981] Dewey Jr, C., Bussolari, S., Gimbrone Jr, M., and Davies, P. F. (1981). The dynamic response of vascular endothelial cells to fluid shear stress.

[Dias et al., 2012] Dias, M., Fernandes, P., Guedes, J., and Hollister, S. (2012). Permeability analysis of scaffolds for bone tissue engineering. *Journal of biomechanics*, 45(6):938–944.

[Dingemans et al., 2000] Dingemans, K. P., Teeling, P., Lagendijk, J. H., and Becker, A. E. (2000). Extracellular matrix of the human aortic media: an ultrastructural histochemical and immunohistochemical study of the adult aortic media. *The Anatomical Record: An Official Publication of the American Association of Anatomists*, 258(1):1–14.

[Dobrin and Mrkvicka, 1994] Dobrin, P. and Mrkvicka, R. (1994). Failure of elastin or collagen as possible critical connective tissue alterations underlying aneurysmal dilatation. *Cardiovascular surgery*, 2(4):484–488.

[Dolan et al., 2013] Dolan, J. M., Kolega, J., and Meng, H. (2013). High wall shear stress and spatial gradients in vascular pathology: a review. *Annals of biomedical engineering*, 41:1411–1427.

[Dušková-Smrčková et al., 2021] Dušková-Smrčková, M., Zavřel, J., Bartoš, M., Kaberova, Z., Filová, E., Zárubová, J., Šlouf, M., Michálek, J., Vampola, T., and Kubies, D. (2021). Communicating macropores in phema-based hydrogels for cell seeding: Probabilistic open pore simulation and direct micro-ct proof. *Materials & Design*, 198:109312.

[Egorova et al., 2009] Egorova, A. D., de Ruiter, M. C., van de Pas, S., ten Dijke, P., Poelmann, R. E., and Hierck, B. P. (2009). Shear stress modulates tgf-beta signaling and emt in endothelial cells. *The FASEB Journal*, 23:830–8.

[Ershov et al., 2022] Ershov, D., Phan, M.-S., Pylvänäinen, J. W., Rigaud, S. U., Le Blanc, L., Charles-Orszag, A., Conway, J. R., Laine, R. F., Roy, N. H., Bonazzi, D., et al. (2022). Trackmate 7: integrating state-of-the-art segmentation algorithms into tracking pipelines. *Nature methods*, 19(7):829–832.

[Fedak et al., 2002] Fedak, P. W., Verma, S., David, T. E., Leask, R. L., Weisel, R. D., and Butany, J. (2002). Clinical and pathophysiological implications of a bicuspid aortic valve. *Circulation*, 106(8):900–904.

[Fiori et al., 2022] Fiori, M., Pramanik, S., and MacMinn, C. W. (2022). Flow and deformation due to periodic loading in a soft porous material. *arXiv preprint arXiv:2212.12166*.

[Galis et al., 1994] Galis, Z. S., Muszynski, M., Sukhova, G. K., Simon-Morrissey, E., Unemori, E. N., Lark, M. W., Amento, E., and Libby, P. (1994). Cytokine-stimulated human vascular smooth muscle cells synthesize a complement of enzymes required for extracellular matrix digestion. *Circulation research*, 75(1):181–189.

[Galkina et al., 2006] Galkina, E., Kadl, A., Sanders, J., Varughese, D., Sarembock, I. J., and Ley, K. (2006). Lymphocyte recruitment into the aortic wall before and during development of atherosclerosis is partially l-selectin dependent. *The Journal of experimental medicine*, 203(5):1273–1282.

[Ganesan et al., 2017] Ganesan, M. K., Finsterwalder, R., Leb, H., Resch, U., Neumüller, K., de Martin, R., and Petzelbauer, P. (2017). Three-dimensional coculture model to analyze the cross talk between endothelial and smooth muscle cells. *Tissue Engineering Part C: Methods*, 23(1):38–49.

[Gao et al., 2014] Gao, F., Chambon, P., Tellides, G., Kong, W., Zhang, X., and Li, W. (2014). Disruption of tgf-$\beta$ signaling in smooth muscle cell prevents flow-induced vascular remodeling. *Biochemical and Biophysical Research Communications*, 454(1):245–250.

[Garanich et al., 2005] Garanich, J. S., Pahakis, M., and Tarbell, J. M. (2005). Shear stress inhibits smooth muscle cell migration via nitric oxide-mediated downregulation of matrix metalloproteinase-2 activity. *American Journal of Physiology-Heart and Circulatory Physiology*, 288(5):H2244–H2252.

[Gibbons and Dzau, 1994] Gibbons, G. H. and Dzau, V. J. (1994). The emerging concept of vascular remodeling. *New England Journal of Medicine*, 330(20):1431–1438.

[Girdauskas et al., 2011] Girdauskas, E., Borger, M. A., Secknus, M.-A., Girdauskas, G., and Kuntze, T. (2011). Is aortopathy in bicuspid aortic valve disease a congenital defect or a result of abnormal hemodynamics? a critical reappraisal of a one-sided argument. *European Journal of Cardio-Thoracic Surgery*, 39(6):809–814.

[Goh et al., 2002] Goh, D., Han, L., Judge, D., Geutbner, J., McIntosh, I., Patel, A., Thomas, G., Basson, C., Milewicz, D., and Dietz, H. (2002). Linkage of familial bicuspid aortic valve with aortic aneurysm to chromosome 15q. In *AMERICAN JOURNAL OF HUMAN GENETICS*, volume 71, pages 211–211. CELL PRESS 600 TECHNOLOGY SQUARE, 5TH FLOOR, CAMBRIDGE, MA 02139 USA.

[Guzzardi et al., 2015] Guzzardi, D. G., Barker, A. J., Van Ooij, P., Malaisrie, S. C., Puthumana, J. J., Belke, D. D., Mewhort, H. E., Svystonyuk, D. A., Kang, S., Verma, S., et al. (2015). Valve-related hemodynamics mediate human bicuspid aortopathy: insights from wall shear stress mapping. *Journal of the American College of Cardiology*, 66(8):892–900.

[Hadjiev and Amsden, 2015] Hadjiev, N. A. and Amsden, B. G. (2015). An assessment of the ability of the obstruction-scaling model to estimate solute diffusion coefficients in hydrogels. *Journal of Controlled Release*, 199:10–16.

[Hahn and Schwartz, 2009] Hahn, C. and Schwartz, M. A. (2009). Mechanotransduction in vascular physiology and atherogenesis. *Nature reviews Molecular cell biology*, 10(1):53–62.

[Han et al., 2018] Han, X., Wu, A., Wang, J., Chang, H., Zhao, Y., Zhang, Y., Mao, Y., Lou, L., Gao, Y., Zhang, D., et al. (2018). Activation and migration of adventitial fibroblasts contributes to vascular remodeling. *The Anatomical Record*, 301(7):1216–1223.

[Hassanizadeh and Gray, 1979] Hassanizadeh, M. and Gray, W. G. (1979). General conservation equations for multi-phase systems: 1. averaging procedure. *Advances in water resources*, 2:131–144.

[Haurani and Pagano, 2007] Haurani, M. J. and Pagano, P. J. (2007). Adventitial fibroblast reactive oxygen species as autacrine and paracrine mediators of remodeling: bellwether for vascular disease? *Cardiovascular research*, 75(4):679–689.

[Hayward et al., 1995] Hayward, I., Bridle, K., Campbell, G., Underwood, P. A., and Campbell, J. (1995). Effect of extracellular matrix proteins on vascular smooth muscle cell phenotype. *Cell biology international*, 19(9):727–734.

[Hedin et al., 1988] Hedin, U., Bottger, B. A., Forsberg, E., Johansson, S., and Thyberg, J. (1988). Diverse effects of fibronectin and laminin on phenotypic properties of cultured arterial smooth muscle cells. *The Journal of cell biology*, 107(1):307–319.

[Hinz, 2015] Hinz, B. (2015). The extracellular matrix and transforming growth factor-$\beta$1: Tale of a strained relationship. *Matrix biology*, 47:54–65.

[Hirase and Node, 2012] Hirase, T. and Node, K. (2012). Endothelial dysfunction as a cellular mechanism for vascular failure. *American Journal of Physiology-Heart and Circulatory Physiology*, 302(3):H499–H505.

[Holm et al., 2011] Holm, T. M., Habashi, J. P., Doyle, J. J., Bedja, D., Chen, Y., Van Erp, C., Lindsay, M. E., Kim, D., Schoenhoff, F., Cohn, R. D., et al. (2011). Noncanonical tgf$\beta$ signaling contributes to aortic aneurysm progression in marfan syndrome mice. *Science*, 332(6027):358–361.

[Hope et al., 2010] Hope, M. D., Hope, T. A., Meadows, A. K., Ordovas, K. G., Urbania, T. H., Alley, M. T., and Higgins, C. B. (2010). Bicuspid aortic valve: four-dimensional mr evaluation of ascending aortic systolic flow patterns. *Radiology*, 255(1):53–61.

[Huang and Tarbell, 1997] Huang, Z. and Tarbell, J. (1997). Numerical simulation of mass transfer in porous media of blood vessel walls. *American Journal of Physiology-Heart and Circulatory Physiology*, 273(1):H464–H477.

[Huo et al., 2000] Huo, Y., Hafezi-Moghadam, A., and Ley, K. (2000). Role of vascular cell adhesion molecule-1 and fibronectin connecting segment-1 in monocyte rolling and adhesion on early atherosclerotic lesions. *Circulation research*, 87(2):153–159.

[Ikonomidis et al., 2006] Ikonomidis, J. S., Jones, J. A., Barbour, J. R., Stroud, R. E., Clark, L. L., Kaplan, B. S., Zeeshan, A., Bavaria, J. E., Gorman III, J. H., Spinale, F. G., et al. (2006). Expression of matrix metalloproteinases and endogenous inhibitors within ascending aortic aneurysms of patients with marfan syndrome. *Circulation*, 114(1_supplement):I–365.

[Ikonomidis et al., 2012] Ikonomidis, J. S., Ruddy, J. M., Benton Jr, S. M., Arroyo, J., Brinsa, T. A., Stroud, R. E., Zeeshan, A., Bavaria, J. E., Gorman III, J. H., Gorman, R. C., et al. (2012). Aortic dilatation with bicuspid aortic valves: cusp fusion correlates to matrix metalloproteinases and inhibitors. *The Annals of thoracic surgery*, 93(2):457–463.

[Isselbacher, 2005] Isselbacher, E. M. (2005). Thoracic and abdominal aortic aneurysms. *Circulation*, 111(6):816–828.

[Jaffe et al., 2012] Jaffe, M., Sesti, C., Washington, I. M., Du, L., Dronadula, N., Chin, M. T., Stolz, D. B., Davis, E. C., and Dichek, D. A. (2012). Transforming growth factor-$\beta$ signaling in myogenic cells regulates vascular morphogenesis, differentiation, and matrix synthesis. *Arteriosclerosis, thrombosis, and vascular biology*, 32(1):e1–e11.

[Janeway Jr et al., 2001] Janeway Jr, C. A., Travers, P., Walport, M., and Shlomchik, M. J. (2001). The structure of a typical antibody molecule. In *Immunobiology: The Immune System in Health and Disease. 5th edition*. Garland Science.

[Jones et al., 2009] Jones, J. A., Beck, C., Barbour, J. R., Zavadzkas, J. A., Mukherjee, R., Spinale, F. G., and Ikonomidis, J. S. (2009). Alterations in aortic cellular constituents during thoracic aortic aneurysm development: myofibroblast-mediated vascular remodeling. *The American journal of pathology*, 175(4):1746–1756.

[Jongstra-Bilen et al., 2006] Jongstra-Bilen, J., Haidari, M., Zhu, S.-N., Chen, M., Guha, D., and Cybulsky, M. I. (2006). Low-grade chronic inflammation in regions of the normal mouse arterial intima predisposed to atherosclerosis. *The Journal of experimental medicine*, 203(9):2073–2083.

[Jowett et al., 2021] Jowett, G. M., Norman, M. D., Yu, T. T., Rosell Arevalo, P., Hoogland, D., Lust, S. T., Read, E., Hamrud, E., Walters, N. J., Niazi, U., et al. (2021). Ilc1 drive intestinal epithelial and matrix remodelling. *Nature materials*, 20(2):250–259.

[Kamiya et al., 1984] Kamiya, A., Bukhari, R., and Togawa, T. (1984). Adaptive regulation of wall shear stress optimizing vascular tree function. *Bulletin of mathematical biology*, 46(1):127–137.

[Kappetein et al., 1991] Kappetein, A., Gittenberger-de Groot, A., Zwinderman, A., Rohmer, J., Poelmann, R., and Huysmans, H. (1991). The neural crest as a possible pathogenetic factor in coarctation of the aorta and bicuspid aortic valve. *The Journal of thoracic and cardiovascular surgery*, 102(6):830–836.

[Keane et al., 2000] Keane, M. G., Wiegers, S. E., Plappert, T., Pochettino, A., Bavaria, J. E., and Sutton, M. G. S. J. (2000). Bicuspid aortic valves are associated with aortic dilatation out of proportion to coexistent valvular lesions. *Circulation*, 102(suppl_3):Iii–35.

[Krieg et al., 2019] Krieg, M., Fläschner, G., Alsteens, D., Gaub, B. M., Roos, W. H., Wuite, G. J., Gaub, H. E., Gerber, C., Dufrêne, Y. F., and Müller, D. J. (2019). Atomic force microscopy-based mechanobiology. *Nature Reviews Physics*, 1(1):41–57.

[Ku, 1997] Ku, D. N. (1997). Blood flow in arteries. *Annual review of fluid mechanics*, 29(1):399–434.

[Langlois et al., 2010] Langlois, D., Hneino, M., Bouazza, L., Parlakian, A., Sasaki, T., Bricca, G., and Li, J. Y. (2010). Conditional inactivation of tgf-$\beta$ type ii receptor in smooth muscle cells and epicardium causes lethal aortic and cardiac defects. *Transgenic research*, 19:1069–1082.

[Lehoux and Tedgui, 2003] Lehoux, S. and Tedgui, A. (2003). Cellular mechanics and gene expression in blood vessels. *Journal of biomechanics*, 36(5):631–643.

[Lewin and Otto, 2005] Lewin, M. B. and Otto, C. M. (2005). The bicuspid aortic valve: adverse outcomes from infancy to old age.

[Lino Cardenas et al., 2018] Lino Cardenas, C. L., Kessinger, C. W., Cheng, Y., MacDonald, C., MacGillivray, T., Ghoshhajra, B., Huleihel, L., Nuri, S., Yeri, A. S., Jaffer, F. A., et al. (2018). An hdac9-malat1-brg1 complex mediates smooth muscle dysfunction in thoracic aortic aneurysm. *Nature communications*, 9(1):1009.

[Liu et al., 2015] Liu, S.-L., Bae, Y. H., Yu, C., Monslow, J., Hawthorne, E. A., Castagnino, P., Branchetti, E., Ferrari, G., Damrauer, S. M., Puré, E., et al. (2015). Matrix metalloproteinase-12 is an essential mediator of acute and chronic arterial stiffening. *Scientific Reports*, 5(1):17189.

[Longo et al., 2002] Longo, G. M., Xiong, W., Greiner, T. C., Zhao, Y., Fiotti, N., Baxter, B. T., et al. (2002). Matrix metalloproteinases 2 and 9 work in concert to produce aortic aneurysms. *The Journal of clinical investigation*, 110(5):625–632.

[Lopez-Quintero et al., 2009] Lopez-Quintero, S. V., Amaya, R., Pahakis, M., and Tarbell, J. M. (2009). The endothelial glycocalyx mediates shear-induced changes in hydraulic conductivity. *American Journal of Physiology-Heart and Circulatory Physiology*, 296(5):H1451–H1456.

[Losenno et al., 2012] Losenno, K. L., Goodman, R. L., Chu, M. W., et al. (2012). Bicuspid aortic valve disease and ascending aortic aneurysms: gaps in knowledge. *Cardiology Research and Practice*, 2012.

[Lu et al., 2021] Lu, H., Du, W., Ren, L., Hamblin, M. H., Becker, R. C., Chen, Y. E., and Fan, Y. (2021). Vascular smooth muscle cells in aortic aneurysm: from genetics to mechanisms. *Journal of the American Heart Association*, 10(24):e023601.

[Lust et al., 2021a] Lust, S. T., Hoogland, D., Norman, M. D., Kerins, C., Omar, J., Jowett, G. M., Yu, T. T., Yan, Z., Xu, J. Z., Marciano, D., et al. (2021a). Selectively cross-linked tetrapeg hydrogels provide control over mechanical strength with minimal impact on diffusivity. *ACS biomaterials science & engineering*, 7(9):4293–4304.

[Lust et al., 2021b] Lust, S. T., Shanahan, C. M., Shipley, R. J., Lamata, P., and Gentleman, E. (2021b). Design considerations for engineering 3d models to study vascular pathologies in vitro. *Acta biomaterialia*, 132:114–128.

[Mackay et al., 2022] Mackay, C. D., Jadli, A. S., Fedak, P. W., and Patel, V. B. (2022). Adventitial fibroblasts in aortic aneurysm: unraveling pathogenic contributions to vascular disease. *Diagnostics*, 12(4):871.

[MacMinn et al., 2015] MacMinn, C. W., Dufresne, E. R., and Wettlaufer, J. S. (2015). Fluid-driven deformation of a soft granular material. *Physical Review X*, 5(1):011020.

[MacMinn et al., 2016] MacMinn, C. W., Dufresne, E. R., and Wettlaufer, J. S. (2016). Large deformations of a soft porous material. *Physical Review Applied*, 5(4):044020.

[Martin et al., 2007] Martin, L. J., Ramachandran, V., Cripe, L. H., Hinton, R. B., Andelfinger, G., Tabangin, M., Shooner, K., Keddache, M., and Benson, D. W. (2007). Evidence in favor of linkage to human chromosomal regions 18q, 5q and 13q for bicuspid aortic valve and associated cardiovascular malformations. *Human genetics*, 121:275–284.

[Mathur et al., 2016] Mathur, A., Mohan, V., Ameta, D., Gaurav, B., and Haranahalli, P. (2016). Aortic aneurysm. *Journal of translational internal medicine*, 4(1):35–41.

[McBride et al., 2005] McBride, K. L., Pignatelli, R., Lewin, M., Ho, T., Fernbach, S., Menesses, A., Lam, W., Leal, S. M., Kaplan, N., Schliekelman, P., et al. (2005). Inheritance analysis of congenital left ventricular outflow tract obstruction malformations: segregation, multiplex relative risk, and heritability. *American journal of medical genetics Part A*, 134(2):180–186.

[McCormick et al., 2007] McCormick, M. L., Gavrila, D., and Weintraub, N. L. (2007). Role of oxidative stress in the pathogenesis of abdominal aortic aneurysms. *Arteriosclerosis, thrombosis, and vascular biology*, 27(3):461–469.

[Medline, 1997] Medline, P. (1997). Bicuspid aortic valve: Medlineplus medical encyclopedia.

[Michel et al., 2018] Michel, J.-B., Jondeau, G., and Milewicz, D. M. (2018). From genetics to response to injury: vascular smooth muscle cells in aneurysms and dissections of the ascending aorta. *Cardiovascular research*, 114(4):578–589.

[Murata et al., 1986] Murata, K., Motayama, T., and Kotake, C. (1986). Collagen types in various layers of the human aorta and their changes with the atherosclerotic process. *Atherosclerosis*, 60(3):251–262.

[Nackman et al., 1996] Nackman, G. B., Bech, F. R., Fillinger, M. F., Wagner, R. J., and Cronenwett, J. L. (1996). Endothelial cells modulate smooth muscle cell morphology by inhibition of transforming growth factor-beta1 activation. *Surgery*, 120(2):418–426.

[Nagase and Fields, 1996] Nagase, H. and Fields, G. B. (1996). Human matrix metalloproteinase specificity studies using collagen sequence-based synthetic peptides. *Peptide Science*, 40(4):399–416.

[Nam et al., 2011] Nam, M.-H., Lee, H.-S., Seomun, Y., Lee, Y., and Lee, K.-W. (2011). Monocyte-endothelium-smooth muscle cell interaction in co-culture: proliferation and cytokine productions in response to advanced glycation end products. *Biochimica et Biophysica Acta (BBA)-General Subjects*, 1810(9):907–912.

[Nataatmadja et al., 2003] Nataatmadja, M., West, M., West, J., Summers, K., Walker, P., Nagata, M., and Watanabe, T. (2003). Abnormal extracellular matrix protein transport associated with increased apoptosis of vascular smooth muscle cells in marfan syndrome and bicuspid aortic valve thoracic aortic aneurysm. *Circulation*, 108(10_suppl_1):II–329.

[Newby, 2006] Newby, A. C. (2006). Matrix metalloproteinases regulate migration, proliferation, and death of vascular smooth muscle cells by degrading matrix and non-matrix substrates. *Cardiovascular research*, 69(3):614–624.

[Ng and Pun, 2008] Ng, C. P. and Pun, S. H. (2008). A perfusable 3d cell–matrix tissue culture chamber for in situ evaluation of nanoparticle vehicle penetration and transport. *Biotechnology and bioengineering*, 99(6):1490–1501.

[Niestrawska et al., 2019] Niestrawska, J. A., Regitnig, P., Viertler, C., Cohnert, T. U., Babu, A. R., and Holzapfel, G. A. (2019). The role of tissue remodeling in mechanics and pathogenesis of abdominal aortic aneurysms. *Acta biomaterialia*, 88:149–161.

[Norman et al., 2021] Norman, M. D., Ferreira, S. A., Jowett, G. M., Bozec, L., and Gentleman, E. (2021). Measuring the elastic modulus of soft culture surfaces and three-dimensional hydrogels using atomic force microscopy. *Nature Protocols*, 16(5):2418–2449.

[O'Brien et al., 2007] O'Brien, F. J., Harley, B. A., Waller, M. A., Yannas, I. V., Gibson, L. J., and Prendergast, P. J. (2007). The effect of pore size on permeability and cell attachment in collagen scaffolds for tissue engineering. *Technology and Health Care*, 15(1):3–17.

[Ochoa et al., 2009] Ochoa, I., Sanz-Herrera, J. A., García-Aznar, J. M., Doblaré, M., Yunos, D. M., and Boccaccini, A. R. (2009). Permeability evaluation of 45s5 bioglass®-based scaffolds for bone tissue engineering. *Journal of biomechanics*, 42(3):257–260.

[Offeddu et al., 2016] Offeddu, G., Ashworth, J., Cameron, R., and Oyen, M. (2016). Structural determinants of hydration, mechanics and fluid flow in freeze-dried collagen scaffolds. *Acta biomaterialia*, 41:193–203.

[Offeddu et al., 2018] Offeddu, G., Axpe, E., Harley, B., and Oyen, M. (2018). Relationship between permeability and diffusivity in polyethylene glycol hydrogels. *AIP advances*, 8(10):105006.

[Ohno et al., 1995] Ohno, M., Cooke, J. P., Dzau, V. J., Gibbons, G. H., et al. (1995). Fluid shear stress induces endothelial transforming growth factor beta-1 transcription and production. modulation by potassium channel blockade. *The Journal of clinical investigation*, 95(3):1363–1369.

[Olgac et al., 2008] Olgac, U., Kurtcuoglu, V., and Poulikakos, D. (2008). Computational modeling of coupled blood-wall mass transport of ldl: effects of local wall shear stress. *American Journal of Physiology-Heart and Circulatory Physiology*, 294(2):H909–H919.

[Owens, 1995] Owens, G. K. (1995). Regulation of differentiation of vascular smooth muscle cells. *Physiological reviews*, 75(3):487–517.

[Pape et al., 2007] Pape, L. A., Tsai, T. T., Isselbacher, E. M., Oh, J. K., O'Gara, P. T., Evangelista, A., Fattori, R., Meinhardt, G., Trimarchi, S., Bossone, E., et al. (2007). Aortic diameter 5.5 cm is not a good predictor of type a aortic dissection: observations from the international registry of acute aortic dissection (irad). *Circulation*, 116(10):1120–1127.

[Pedersen et al., 2007] Pedersen, J. A., Boschetti, F., and Swartz, M. A. (2007). Effects of extracellular fiber architecture on cell membrane shear stress in a 3d fibrous matrix. *Journal of biomechanics*, 40(7):1484–1492.

[Pennella et al., 2013] Pennella, F., Cerino, G., Massai, D., Gallo, D., Falvo D'Urso Labate, G., Schiavi, A., Deriu, M., Audenino, A., and Morbiducci, U. (2013). A survey of methods for the evaluation of tissue engineering scaffold permeability. *Annals of Biomedical Engineering*, 41:2027–2041.

[Pottie et al., 2021] Pottie, L., Adamo, C. S., Beyens, A., Lütke, S., Tapaneeyaphan, P., De Clercq, A., Salmon, P. L., De Rycke, R., Gezdirici, A., Gulec, E. Y., et al. (2021). Bi-allelic premature truncating variants in ltbp1 cause cutis laxa syndrome. *The American Journal of Human Genetics*, 108(6):1095–1114.

[Powell et al., 1998] Powell, R. J., Bhargava, J., Basson, M. D., and Sumpio, B. E. (1998). Coculture conditions alter endothelial modulation of tgf-$\beta$1 activation and smooth muscle growth morphology. *American Journal of Physiology-Heart and Circulatory Physiology*, 274(2):H642–H649.

[Powell et al., 1996] Powell, R. J., Cronenwett, J. L., Fillinger, M. F., Wagner, R. J., and Sampson, L. N. (1996). Endothelial cell modulation of smooth muscle cell morphology and organizational growth pattern. *Annals of vascular surgery*, 10(1):4–10.

[Prakash et al., 2014] Prakash, S. K., Bossé, Y., Muehlschlegel, J. D., Michelena, H. I., Limongelli, G., Della Corte, A., Pluchinotta, F. R., Russo, M. G., Evangelista, A., Benson, D. W., et al. (2014). A roadmap to investigate the genetic basis of bicuspid aortic valve and its complications: insights from the international bavcon (bicuspid aortic valve consortium). *Journal of the American College of Cardiology*, 64(8):832–839.

[Prosi et al., 2005] Prosi, M., Zunino, P., Perktold, K., and Quarteroni, A. (2005). Mathematical and numerical models for transfer of low-density lipoproteins through the arterial walls: a new methodology for the model set up with applications to the study of disturbed lumenal flow. *Journal of biomechanics*, 38(4):903–917.

[Qiu et al., 2014] Qiu, J., Zheng, Y., Hu, J., Liao, D., Gregersen, H., Deng, X., Fan, Y., and Wang, G. (2014). Biomechanical regulation of vascular smooth muscle cell functions: from in vitro to in vivo understanding. *Journal of The Royal Society Interface*, 11(90):20130852.

[Quintana and Taylor, 2019] Quintana, R. A. and Taylor, W. R. (2019). Cellular mechanisms of aortic aneurysm formation. *Circulation research*, 124(4):607–618.

[Rabkin, 2017] Rabkin, S. W. (2017). The role matrix metalloproteinases in the production of aortic aneurysm. *Progress in molecular biology and translational science*, 147:239–265.

[Raffetto and Khalil, 2008] Raffetto, J. D. and Khalil, R. A. (2008). Matrix metalloproteinases and their inhibitors in vascular remodeling and vascular disease. *Biochemical pharmacology*, 75(2):346–359.

[Rahman et al., 2013] Rahman, C. V., Kuhn, G., White, L. J., Kirby, G. T., Varghese, O. P., McLaren, J. S., Cox, H. C., Rose, F. R., Müller, R., Hilborn, J., et al. (2013). Plga/peg-hydrogel composite scaffolds with controllable mechanical properties. *Journal of Biomedical Materials Research Part B: Applied Biomaterials*, 101(4):648–655.

[Rateri et al., 2011] Rateri, D. L., Howatt, D. A., Moorleghen, J. J., Charnigo, R., Cassis, L. A., and Daugherty, A. (2011). Prolonged infusion of angiotensin ii in apoe-/- mice promotes macrophage recruitment with continued expansion of abdominal aortic aneurysm. *The American journal of pathology*, 179(3):1542–1548.

[Rhoads et al., 2000] Rhoads, D. N., Eskin, S. G., and McIntire, L. V. (2000). Fluid flow releases fibroblast growth factor-2 from human aortic smooth muscle cells. *Arteriosclerosis, thrombosis, and vascular biology*, 20(2):416–421.

[Richards et al., 2004] Richards, K. E., Deserranno, D., Donal, E., Greenberg, N. L., Thomas, J. D., and Garcia, M. J. (2004). Influence of structural geometry on the severity of bicuspid aortic

stenosis. *American Journal of Physiology-Heart and Circulatory Physiology*, 287(3):H1410–H1416.

[Rizas et al., 2009] Rizas, K. D., Ippagunta, N., and Tilson III, M. D. (2009). Immune cells and molecular mediators in the pathogenesis of the abdominal aortic aneurysm. *Cardiology in review*, 17(5):201–210.

[Rizzo et al., 1989] Rizzo, R. J., McCarthy, W. J., Dixit, S. N., Lilly, M. P., Shively, V. P., Flinn, W. R., and Yao, J. S. (1989). Collagen types and matrix protein content in human abdominal aortic aneurysms. *Journal of vascular surgery*, 10(4):365–373.

[Robinson et al., 2013] Robinson, W. P., Schanzer, A., Li, Y., Goodney, P. P., Nolan, B. W., Eslami, M. H., Cronenwett, J. L., and Messina, L. M. (2013). Derivation and validation of a practical risk score for prediction of mortality after open repair of ruptured abdominal aortic aneurysms in a us regional cohort and comparison to existing scoring systems. *Journal of vascular surgery*, 57(2):354–361.

[Roos-Hesselink et al., 2003] Roos-Hesselink, J., Schölzel, B., Heijdra, R., Spitaels, S., Meijboom, F., Boersma, E., Bogers, A., and Simoons, M. (2003). Aortic valve and aortic arch pathology after coarctation repair. *Heart*, 89(9):1074–1077.

[Saeyeldin et al., 2019] Saeyeldin, A. A., Velasquez, C. A., Mahmood, S. U. B., Brownstein, A. J., Zafar, M. A., Ziganshin, B. A., and Elefteriades, J. A. (2019). Thoracic aortic aneurysm: unlocking the "silent killer" secrets. *General thoracic and cardiovascular surgery*, 67:1–11.

[Sakata et al., 2007] Sakata, N., Nabeshima, K., Iwasaki, H., Tashiro, T., Uesugi, N., Nakashima, O., Ito, H., Kawanami, T., Furuya, K., and Kojima, M. (2007). Possible involvement of myofibroblast in the development of inflammatory aortic aneurysm. *Pathology-Research and Practice*, 203(1):21–29.

[Sanz-Herrera et al., 2008] Sanz-Herrera, J. A., Kasper, C., van Griensven, M., Garcia-Aznar, J. M., Ochoa, I., and Doblare, M. (2008). Mechanical and flow characterization of sponceram® carriers: evaluation by homogenization theory and experimental validation. *Journal of Biomedical Materials Research Part B: Applied Biomaterials: An Official Journal of The Society for Biomaterials, The Japanese Society for Biomaterials, and The Australian Society for Biomaterials and the Korean Society for Biomaterials*, 87(1):42–48.

[Sariola et al., 1986] Sariola, H., Viljanen, T., and Luosto, R. (1986). Histological pattern and changes in extracellular matrix in aortic dissections. *Journal of clinical pathology*, 39(10):1074–1081.

[Serpooshan et al., 2013] Serpooshan, V., Quinn, T. M., Muja, N., and Nazhat, S. N. (2013). Hydraulic permeability of multilayered collagen gel scaffolds under plastic compression-induced unidirectional fluid flow. *Acta biomaterialia*, 9(1):4673–4680.

[Shapiro and Senior, 1999] Shapiro, S. D. and Senior, R. M. (1999). Matrix metalloproteinases: matrix degradation and more. *American journal of respiratory cell and molecular biology*, 20(6):1100–1102.

[Shen et al., 2020] Shen, Y. H., LeMaire, S. A., Webb, N. R., Cassis, L. A., Daugherty, A., and Lu, H. S. (2020). Aortic aneurysms and dissections series. *Arteriosclerosis, thrombosis, and vascular biology*, 40(3):e37–e46.

[Shi et al., 2009] Shi, Z.-D., Ji, X.-Y., Qazi, H., and Tarbell, J. M. (2009). Interstitial flow promotes vascular fibroblast, myofibroblast, and smooth muscle cell motility in 3-d collagen i via upregulation of mmp-1. *American Journal of Physiology-Heart and Circulatory Physiology*, 297(4):H1225–H1234.

[Shi and Tarbell, 2011] Shi, Z.-D. and Tarbell, J. M. (2011). Fluid flow mechanotransduction in vascular smooth muscle cells and fibroblasts. *Annals of biomedical engineering*, 39:1608–1619.

[Shimko and Nauman, 2007] Shimko, D. A. and Nauman, E. A. (2007). Development and characterization of a porous poly (methyl methacrylate) scaffold with controllable modulus and permeability. *Journal of Biomedical Materials Research Part B: Applied Biomaterials: An Official Journal of The Society for Biomaterials, The Japanese Society for Biomaterials, and The Australian Society for Biomaterials and the Korean Society for Biomaterials*, 80(2):360–369.

[Shimko et al., 2005] Shimko, D. A., Shimko, V. F., Sander, E. A., Dickson, K. F., and Nauman, E. A. (2005). Effect of porosity on the fluid flow characteristics and mechanical properties of tantalum scaffolds. *Journal of Biomedical Materials Research Part B: Applied Biomaterials: An Official Journal of The Society for Biomaterials, The Japanese Society for Biomaterials, and The Australian Society for Biomaterials and the Korean Society for Biomaterials*, 73(2):315–324.

[Sill et al., 1995] Sill, H. W., Chang, Y. S., Artman, J. R., Frangos, J., Hollis, T., and Tarbell, J. M. (1995). Shear stress increases hydraulic conductivity of cultured endothelial monolayers. *American Journal of Physiology-Heart and Circulatory Physiology*, 268(2):H535–H543.

[Sinha and Frishman, 1998] Sinha, S. and Frishman, W. H. (1998). Matrix metalloproteinases and abdominal aortic aneurysms: a potential therapeutic target. *The Journal of Clinical Pharmacology*, 38(12):1077–1088.

[Siu and Silversides, 2010] Siu, S. C. and Silversides, C. K. (2010). Bicuspid aortic valve disease. *Journal of the American College of Cardiology*, 55(25):2789–2800.

[Sottile and Hocking, 2002] Sottile, J. and Hocking, D. C. (2002). Fibronectin polymerization regulates the composition and stability of extracellular matrix fibrils and cell-matrix adhesions. *Molecular biology of the cell*, 13(10):3546–3559.

[Stegemann et al., 2005] Stegemann, J. P., Hong, H., and Nerem, R. M. (2005). Mechanical, biochemical, and extracellular matrix effects on vascular smooth muscle cell phenotype. *Journal of applied physiology*, 98(6):2321–2327.

[Stegemann and Nerem, 2003] Stegemann, J. P. and Nerem, R. M. (2003). Altered response of vascular smooth muscle cells to exogenous biochemical stimulation in two-and three-dimensional culture. *Experimental cell research*, 283(2):146–155.

[Suh et al., 2011] Suh, J.-H., Yoon, J.-S., Kim, H.-W., and Jo, K.-H. (2011). Adventitial fibroblast abormality in thoracic aortic aneurysms and aortic dissections. *Journal of Chest Surgery*, 44(6):406–412.

[Sun et al., 2006] Sun, N., Wood, N. B., Hughes, A. D., Thom, S. A., and Xu, X. Y. (2006). Fluid-wall modelling of mass transfer in an axisymmetric stenosis: effects of shear-dependent transport properties. *Annals of biomedical engineering*, 34:1119–1128.

[Tada and Tarbell, 2002] Tada, S. and Tarbell, J. M. (2002). Flow through internal elastic lamina affects shear stress on smooth muscle cells (3d simulations). *American Journal of Physiology-Heart and Circulatory Physiology*, 282(2):H576–H584.

[Tadros et al., 2009] Tadros, T. M., Klein, M. D., and Shapira, O. M. (2009). Ascending aortic dilatation associated with bicuspid aortic valve: pathophysiology, molecular biology, and clinical implications. *Circulation*, 119(6):880–890.

[Takazawa et al., 2007] Takazawa, K., Kobayashi, H., Shindo, N., Tanaka, N., and Yamashina, A. (2007). Relationship between radial and central arterial pulse wave and evaluation of central aortic pressure using the radial arterial pulse wave. *Hypertension Research*, 30(3):219–228.

[Talk, 2014] Talk, U. H. (2014). Aortic aneurysms: The silent killer. https://healthtalk.unchealthcare.org/aneurysms-the-silent-killer/ [Accessed: May 2023].

[Thompson and Baxter, 1999] Thompson, R. W. and Baxter, B. T. (1999). Mmp inhibition in abdominal aortic aneurysms: rationale for a prospective randomized clinical trial. *Annals of the New York Academy of Sciences*, 878(1):159–178.

[Thompson et al., 2002] Thompson, R. W., Geraghty, P. J., and Lee, J. K. (2002). Abdominal aortic aneurysms: basic mechanisms and clinical implications. *Current problems in surgery*, 39(2):110–230.

[Thyberg et al., 1997] Thyberg, J., Blomgren, K., Roy, J., Tran, P. K., and Hedin, U. (1997). Phenotypic modulation of smooth muscle cells after arterial injury is associated with changes in the distribution of laminin and fibronectin. *Journal of Histochemistry & Cytochemistry*, 45(6):837–846.

[Thyberg et al., 1990] Thyberg, J., Hedin, U., Sjölund, M., Palmberg, L., and Bottger, B. (1990). Regulation of differentiated properties and proliferation of arterial smooth muscle cells. *Arteriosclerosis: An Official Journal of the American Heart Association, Inc.*, 10(6):966–990.

[Tinajero and Gotlieb, 2020] Tinajero, M. G. and Gotlieb, A. I. (2020). Recent developments in vascular adventitial pathobiology: the dynamic adventitia as a complex regulator of vascular disease. *The American Journal of Pathology*, 190(3):520–534.

[Truscello et al., 2012] Truscello, S., Kerckhofs, G., Van Bael, S., Pyka, G., Schrooten, J., and Van Oosterwyck, H. (2012). Prediction of permeability of regular scaffolds for skeletal tissue engineering: a combined computational and experimental study. *Acta biomaterialia*, 8(4):1648–1658.

[Truskey, 2010] Truskey, G. A. (2010). Endothelial cell vascular smooth muscle cell co-culture assay for high throughput screening assays for discovery of anti-angiogenesis agents and other therapeutic molecules. *International journal of high throughput screening*, 2010(1):171.

[Ueba et al., 1997] Ueba, H., Kawakami, M., and Yaginuma, T. (1997). Shear stress as an inhibitor of vascular smooth muscle cell proliferation: role of transforming growth factor-$\beta$1 and tissue-type plasminogen activator. *Arteriosclerosis, thrombosis, and vascular biology*, 17(8):1512–1516.

[van Buul-Wortelboer et al., 1986] van Buul-Wortelboer, M., Brinkman, H., Dingemans, K., De Groot, P. G., Van Aken, W., and Van Mourik, J. (1986). Reconstitution of the vascular wall in vitro: a novel model to study interactions between endothelial and smooth muscle cells. *Experimental cell research*, 162(1):151–158.

[Van Ooij et al., 2017] Van Ooij, P., Markl, M., Collins, J. D., Carr, J. C., Rigsby, C., Bonow, R. O., Malaisrie, S. C., McCarthy, P. M., Fedak, P. W., and Barker, A. J. (2017). Aortic valve stenosis alters expression of regional aortic wall shear stress: New insights from a 4-dimensional flow magnetic resonance imaging study of 571 subjects. *Journal of the American Heart Association*, 6(9):e005959.

[Varley et al., 2016] Varley, M., Neelakantan, S., Clyne, T., Dean, J., Brooks, R., and Markaki, A. (2016). Cell structure, stiffness and permeability of freeze-dried collagen scaffolds in dry and hydrated states. *Acta biomaterialia*, 33:166–175.

[Wagenseil and Mecham, 2009] Wagenseil, J. E. and Mecham, R. P. (2009). Vascular extracellular matrix and arterial mechanics. *Physiological reviews*, 89(3):957–989.

[Wang and Tarbell, 1995] Wang, D. and Tarbell, J. (1995). Modeling interstitial flow in an artery wall allows estimation of wall shear stress on smooth muscle cells.

[Wang et al., 2007] Wang, H.-Q., Bai, L., Shen, B.-R., Yan, Z.-Q., and Jiang, Z.-L. (2007). Co-culture with endothelial cells enhances vascular smooth muscle cell adhesion and spreading via activation of $\beta$1-integrin and phosphatidylinositol 3-kinase/akt. *European journal of cell biology*, 86(1):51–62.

[Wang and Tarbell, 2000] Wang, S. and Tarbell, J. M. (2000). Effect of fluid flow on smooth muscle cells in a 3-dimensional collagen gel model. *Arteriosclerosis, thrombosis, and vascular biology*, 20(10):2220–2225.

[Wang and Khalil, 2018] Wang, X. and Khalil, R. A. (2018). Matrix metalloproteinases, vascular remodeling, and vascular disease. *Advances in pharmacology*, 81:241–330.

[Wang et al., 2013] Wang, Y., Krishna, S., Walker, P. J., Norman, P., and Golledge, J. (2013). Transforming growth factor-$\beta$ and abdominal aortic aneurysms. *Cardiovascular pathology*, 22(2):126–132.

[Wang et al., 2022] Wang, Z., You, Y., Yin, Z., Bao, Q., Lei, S., Yu, J., Xie, C., Ye, F., and Xie, X. (2022). Burden of aortic aneurysm and its attributable risk factors from 1990 to 2019: An analysis of the global burden of disease study 2019. *Frontiers in Cardiovascular Medicine*, 9:1272.

[Weber et al., 2009] Weber, L. M., Lopez, C. G., and Anseth, K. S. (2009). Effects of peg hydrogel crosslinking density on protein diffusion and encapsulated islet survival and function. *Journal of Biomedical Materials Research Part A: An Official Journal of The Society for Biomaterials, The Japanese Society for Biomaterials, and The Australian Society for Biomaterials and the Korean Society for Biomaterials*, 90(3):720–729.

[Weinberg and Bell, 1986] Weinberg, C. B. and Bell, E. (1986). A blood vessel model constructed from collagen and cultured vascular cells. *Science*, 231(4736):397–400.

[White and Frangos, 2007] White, C. R. and Frangos, J. A. (2007). The shear stress of it all: the cell membrane and mechanochemical transduction. *Philosophical Transactions of the Royal Society B: Biological Sciences*, 362(1484):1459–1467.

[Whitehead et al., 2023] Whitehead, M., Yusoff, S., Ahmad, S., Schmidt, L., Mayr, M., Madine, J., Middleton, D., and Shanahan, C. M. (2023). Vascular smooth muscle cell senescence ac-

celerates medin aggregation via small extracellular vesicle secretion and extracellular matrix reorganization. *Aging Cell*, 22(2):e13746.

[Wilson et al., 2006] Wilson, W. R. W., Anderton, M., Schwalbe, E. C., Jones, J. L., Furness, P. N., Bell, P. R., and Thompson, M. M. (2006). Matrix metalloproteinase-8 and-9 are increased at the site of abdominal aortic aneurysm rupture. *Circulation*, 113(3):438–445.

[Wise et al., 2015] Wise, E. S., Hocking, K. M., and Brophy, C. M. (2015). Prediction of in-hospital mortality after ruptured abdominal aortic aneurysm repair using an artificial neural network. *Journal of vascular surgery*, 62(1):8–15.

[Xia et al., 2012] Xia, Y., Bhattacharyya, A., Roszell, E. E., Sandig, M., and Mequanint, K. (2012). The role of endothelial cell-bound jagged1 in notch3-induced human coronary artery smooth muscle cell differentiation. *Biomaterials*, 33(8):2462–2472.

[Xie et al., 2019] Xie, Y., Ostriker, A. C., Jin, Y., Hu, H., Sizer, A. J., Peng, G., Morris, A. H., Ryu, C., Herzog, E. L., Kyriakides, T., et al. (2019). Lmo7 is a negative feedback regulator of transforming growth factor $\beta$ signaling and fibrosis. *Circulation*, 139(5):679–693.

[Xu and Shi, 2014] Xu, J. and Shi, G.-P. (2014). Vascular wall extracellular matrix proteins and vascular diseases. *Biochimica et Biophysica Acta (BBA)-Molecular Basis of Disease*, 1842(11):2106–2119.

[Yap et al., 2021] Yap, C., Mieremet, A., de Vries, C. J., Micha, D., and de Waard, V. (2021). Six shades of vascular smooth muscle cells illuminated by klf4 (krüppel-like factor 4). *Arteriosclerosis, thrombosis, and vascular biology*, 41(11):2693–2707.

[Yener et al., 2002] Yener, N., Oktar, G. L., Erer, D., Yardimci, M. M., and Yener, A. (2002). Bicuspid aortic valve. *Annals of thoracic and cardiovascular surgery*, 8(5):264–267.

[Ziegler et al., 1995] Ziegler, T., Alexander, R., and Nerem, R. (1995). An endothelial cell-smooth muscle cell co-culture model for use in the investigation of flow effects on vascular biology. *Annals of biomedical engineering*, 23:216–225.

[Zustiak and Leach, 2010] Zustiak, S. P. and Leach, J. B. (2010). Hydrolytically degradable poly (ethylene glycol) hydrogel scaffolds with tunable degradation and mechanical properties. *Biomacromolecules*, 11(5):1348–1357.